Computational Investigations of the Electronic Structure of Molecular Actinide Compounds

Submitted by:

L. Jonasson

For the degree of:

Doctor of Philosophy

Supervisor:

Professor N. Kaltsoyannis

University College London, 2009

Abstract

In this PhD thesis the electronic structure of a range of actinide compounds has been investigated using density functional theory. The reason for using DFT instead of other methods is mainly due to the size of the compounds which makes multireference calculations prohibitively expensive, but also to make comparisons with previously calculated DFT results.

The first chapter presents the basic concepts of electronic structure theory and the chemical properties of the actinides and lanthanides. The theoretical foundation of DFT and the consequences of relativity are also introduced.

In the second chapter the bonding in mixed $MUCl_6$, $MUCl_8^{2-}$, $NpReCl_8^{2-}$ and $PuOsCl_8^{2-}$ (M = Mo, W) systems is investigated and compared with previous work on the M_2Cl_6, $M_2Cl_8^{2-}$, U_2Cl_6 and $U_2Cl_8^{2-}$ systems. The study shows that the total bonding energy in the mixed compounds is the average of the two "pure" compounds.

The third chapter deals with systems of plenary or lacunary Keggin phosphomolybdate coordination to actinide (Th), lanthanide (Ce, La, Lu) and transition metal (Hf, Zr) cations: $[PMo_{12}O_{40}]^{3-}$, $[PMo_{11}O_{39}]_2^{14-}$, $[PMo_{12}O_{40}]_2^{6-}$ and $[PMo_{11}O_{39}][PMo_{12}O_{40}]^{10-}$. These large, highly anionic systems proved to be very challenging computationally. The main result of the study confirms that the bonding is ionic and that there are few differences in the behaviour of the transition metals.

In the fourth chapter the electronic spectrum of NpO_2^{2+}, $NpO_2Cl_4^{2-}$ and $NpO_2(OH)_4^{2-}$ is calculated using time dependent DFT. TDDFT has proved adequate for the uranium analogues of these systems and this extends previous work on f^0 systems to f^1 systems. The results show that TDDFT is in poor agreement with both experimental results and multireference calculations for these compounds.

In chapter five, group 15 and 16 uranyl analogues have been investigated. For the UE_2 (E = O, S, Se, Te) analogues the geometry bends for all chalcogens heavier than O. The UE_2^{2+} analogues remain linear all the way down group 16. In $U(NCH_3)_2^{2+}$ the formation of a π "back bone" along the axis of the molecule was noted. The σ-bonding valence MOs stabilize while the π MOs are destabilized down group 15 and 16.

Chapter six is a summary of the results in this thesis and an outlook on potential future work.

Acknowledgements

I would first like to thank my supervisor Nik Kaltsoyannis for his patience and support in helping me finish this PhD project. There were times when results were not forthcoming or needed explanations but he provided stability, calm and guidance at those times.

I would like to thank Jonas Häller for letting me know about UCL and this PhD project as well as the continuous support in my research and being a fellow Swede abroad. Still need to work a bit on the nationalism but overall a very good friend. I would also like to thank Rosie, Luke, Kieran, Amy, Andrea, German, Andy, Ross, Zoso, Matt, Laura and everyone, past and present, who has been working in G19 for their support and interesting discussions about a lot of different topics, be they scientific or otherwise. We are all proof that natural light is vastly overrated!

I have met a lot of people in London who have made the last three years enjoyable. It would be impossible to name them all here. You know who you are. I would like to mention a few people I have spent a lot of time with during my time here, Mike, Sophie, Marta, Zbig and Kasia, who have been flatmates with me. Having to hunt new accommodation every autumn definitely brings you closer and we have had some great times together.

My parents, sister, niece and grandparents in Sweden have not seen me that often during my time in the UK but, thanks to modern technology, I have been able to keep in touch with them all regularly. I have been home enough each year to rest, relax and enjoy the incredible nature we take for granted. Their encouragement and backing have helped me greatly.

Contents

Chapter 1

Introduction

Actinides

Introduction

All of the projects in this thesis are connected to the actinides, a group of elements usually confined to the outskirts of chemistry. Many of the actinides are radioactive and, when moving across the series, increasingly short-lived, making experimental investigations of them difficult and expensive. However, the field of actinide chemistry does exist and the following section will give a brief overview of the chemical properties of the actinides and the f-block elements in general. A more in depth introduction into the electronic structure of uranium and neptunium containing systems will follow in Chapter 4, relating to the investigation of the electronic structure of species containing these atoms.

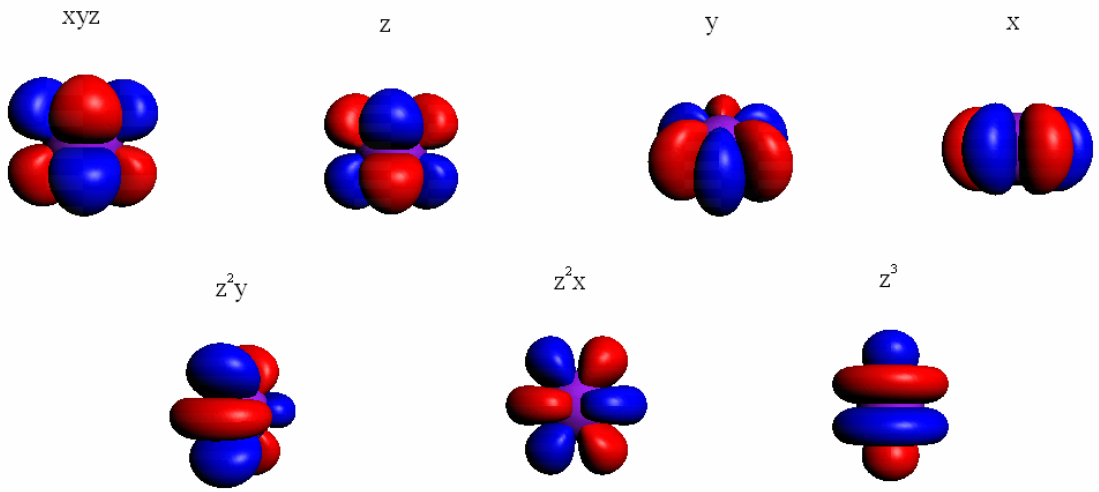

Figure 1.1. The general set of 5f orbitals as calculated in ADF

General features of the actinides and lanthanides

The elements in the periodic table with atomic number 57-71 are known as the lanthanides after the first element of the series, lanthanum. Similarly, elements 89-103 are referred to as the actinides, named for actinium. Moving across both series the primary shell being filled is the f shell, 4f for the lanthanides and 5f for the actinides, with the 5f orbitals displayed in Figure 1.1.

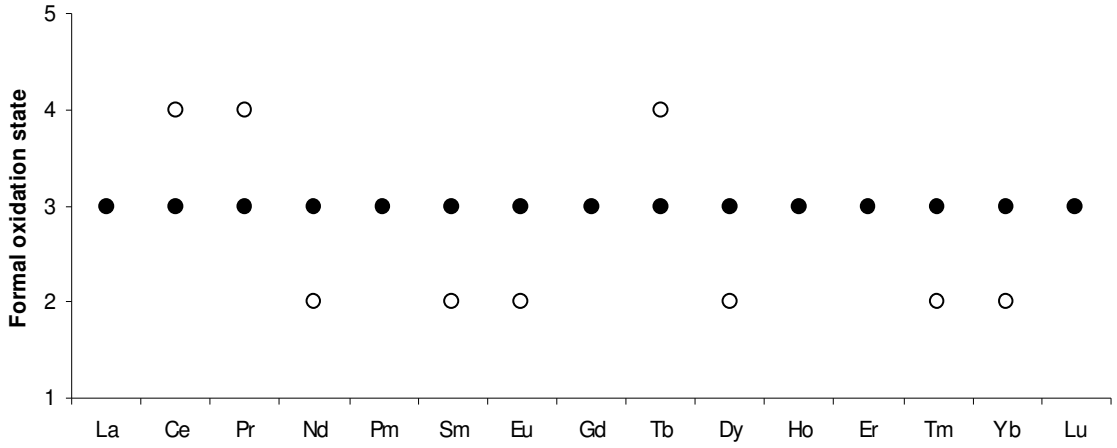

Figure 1.2. The formal oxidation states of the lanthanides. Filled circles represent the most common oxidation states, open circle indicate other possible oxidation states

In neutral lanthanides the valence electrons are distributed in the 4f, 5d and 6s orbitals. As the lanthanides are ionized, these orbitals are stabilized due to experiencing an increased effective nuclear charge, with the 4f orbitals being the most stabilized orbital. After three ionizations the 5d and 6s orbitals are emptied and the 4f orbitals so stabilized that the energy of removing additional electrons exceeds the energetic gain of forming a bond in the +4 oxidation state; thus the 4f is rendered inaccessible for chemical reactions. This is one of the main characteristics of lanthanide chemistry; almost all the lanthanides prefer the +3 oxidation state, with a few exceptions such as when the f shell can become empty (f^0), half-filled (f^7) or full (f^{14}). One example of this is Ce which has been found at +4.[1]

Lanthanides				Actinides			
Element	Symbol	Atomic number	Electronic configuration	Element	Symbol	Atomic number	Electronic configuration
Lanthanum	La	57	$[Xe]5d^16s^2$	Actinium	Ac	89	$[Rn]6d^17s^2$
Cerium	Ce	58	$[Xe]4f^15d^16s^2$	Thorium	Th	90	$[Rn]6d^27s^2$
Praseodymium	Pr	59	$[Xe]4f^36s^2$	Protactinium	Pa	91	$[Rn]5f^26d^17s^2$
Neodymium	Nd	60	$[Xe]4f^46s^2$	Uranium	U	92	$[Rn]5f^36d^17s^2$
Promethium	Pm	61	$[Xe]4f^56s^2$	Neptunium	Np	93	$[Rn]5f^46d^17s^2$
Samarium	Sm	62	$[Xe]4f^66s^2$	Plutonium	Pu	94	$[Rn]5f^67s^2$
Europium	Eu	63	$[Xe]4f^76s^2$	Americium	Am	95	$[Rn]5f^7s^2$
Gadolinium	Gd	64	$[Xe]4f^75d^16s^2$	Curium	Cm	96	$[Rn]5f^76d^17s^2$
Terbium	Tb	65	$[Xe]4f^96s^2$	Berkelium	Bk	97	$[Rn]5f^97s^2$
Dysprosium	Dy	66	$[Xe]4f^{10}6s^2$	Californium	Cf	98	$[Rn]5f^{10}7s^2$
Holmium	Ho	67	$[Xe]4f^{11}6s^2$	Einsteinium	Es	99	$[Rn]5f^{11}7s^2$
Erbium	Er	68	$[Xe]4f^{12}6s^2$	Fermium	Fm	100	$[Rn]5f^{12}7s^2$
Thulium	Tm	69	$[Xe]4f^{13}6s^2$	Mendelevium	Md	101	$[Rn]5f^{13}7s^2$
Ytterbium	Yb	70	$[Xe]4f^{14}6s^2$	Nobelium	No	102	$[Rn]5f^{14}7s^2$
Lutetium	Lu	71	$[Xe]4f^{14}5d^16s^2$	Lawrencium	Lr	103	$[Rn]5f^{14}6d^17s^2$

Table 1.1. The ground state electronic configuration of the lanthanides and the actinides

A corresponding study of the actinide ionisation energies is not possible, due to the radioactive and short-lived nature of the late actinides. Other experimental techniques show that the number of oxidation states available for the early actinides is much greater (Figure 1.3), indicating that the 5f orbitals are relatively destabilised and close in energy to the 6d and more involved in the chemical properties of the actinides. As a consequence, all valence electrons in actinides, up to Np, are available for covalent bonding. The rationale for this is that the 5f orbitals have one radial node while the 4f has none, destabilizing the 5f orbitals. In the lanthanides only cerium is able to remove all its valence electrons and achieve "group valence". In contrast, this is something all the early actinides, up to Np are able to do. The behaviour of the early actinides is sometimes compared with the transition metals, with many oxidation states and the shift from this behaviour to a more lanthanide like behaviour has been the focus of much study.[2]

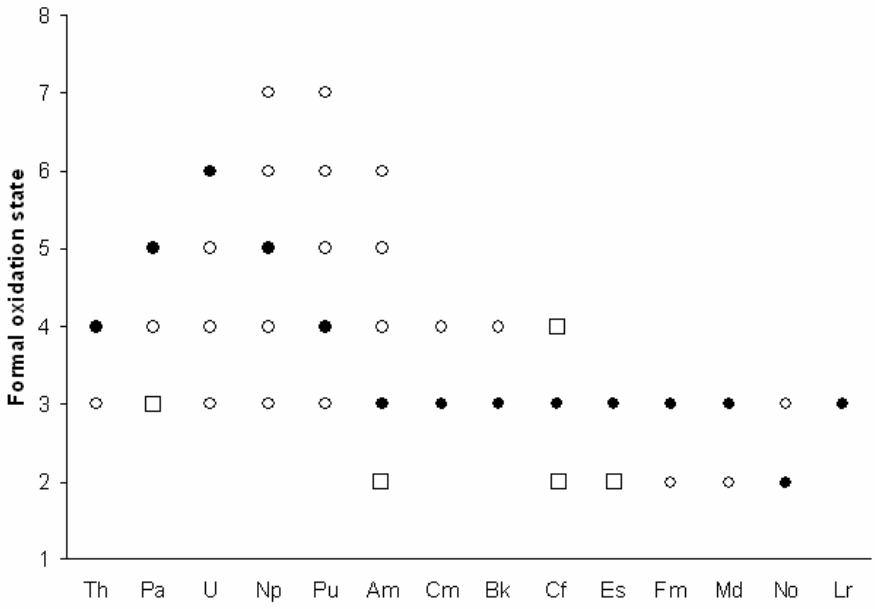

Figure 1.3. The oxidation states found in the actinides. The filled circles are the most common oxidation states, open circles are other available oxidation states and the open squares indicate oxidations states only found in solids.

The 6p orbital of the early actinides has been found to be rather diffuse and have a radial extension close to that of the 6d and 5f. Among transition metals the p orbitals would be considered core orbitals that have no role in chemical bonding, but as will be explained in Chapter 4, the valence electronic structure of, for example, uranyl is very much affected by the influence of the 6p orbital. Due to this role in the valence electronic structure, the 6p is often referred to as a semi-core orbital.

Moving across the period, the actinides become more lanthanide-like, displaying an increased localisation of the f orbitals. The 4f orbitals are less radially extended and participate to a lesser degree in chemical bonds. Relativistic effects play a very important role in the energy ordering of the valence orbitals in the actinides, something that will be discussed further in the theory section below.

The radial extension of the 5f atomic orbitals vary significantly down the actinide series, with the radial extension being close to the other valence orbitals for Th to Pu and thus

allowing the 5f orbitals to be involved in bonding of the early actinides. Moving across the series the 5f orbitals become increasingly lanthanide like.

The atomic and ionic radii of the lanthanides (Ln) and the actinides (An) decrease across the respective rows (Figure 1.4). This is attributed to the poor nuclear shielding of the f electrons, increasing the effective nuclear charge felt by all valence electrons, thus contracting the system. The effect is called actinide and lanthanide contraction, for the actinides and lanthanides respectively.

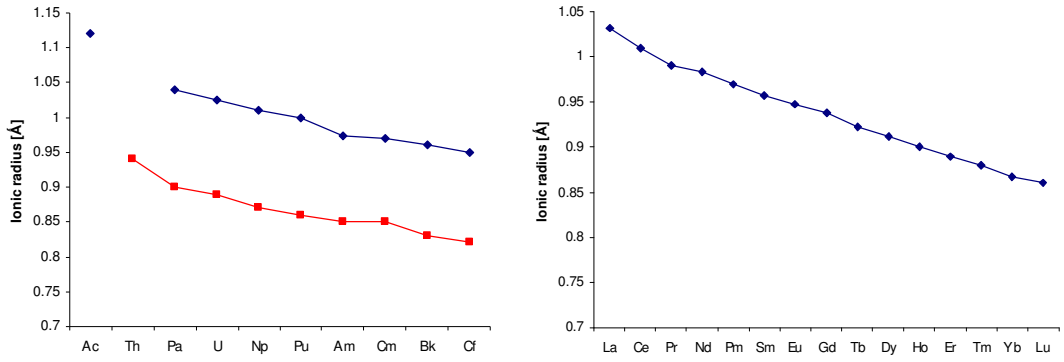

Figure 1.4. The ionic radii of the actinides (left) and the lanthanides (right). In the actinide graph the red line is for An^{4+} and the blue An^{3+}.[3]

Electronic structure theory

Introduction

There are several equivalent ways to formulate quantum mechanics. At the present time two approaches to theoretical chemistry dominate; wave mechanics and density functional theory. Both have their origin in the 1920s and 1930s when quantum mechanics was developed and it was realised that chemical problems could be addressed using the new quantum models of the atoms. However, the problem with these methods has always been that without the aid of computers they are impractical on real systems due to the amount of integrals which must be evaluated. In the last 30 years though, the rise of powerful, inexpensive computers have made it possible to investigate chemical problems, even for the heaviest elements in the periodic table, with good accuracy, accounting for relativistic effects. There are numerous books that describe this field in great detail.[4-6] The following sections will provide a brief description of the basic concepts of wave function based methods and density functional methods that have been used in the course of this PhD.

The Schrödinger equation

Both density functional theory and wave function mechanics start with the formulation of the time-independent Schrödinger equation[7]:

$$\mathbf{H}\Psi = E\Psi \qquad (1.1)$$

Ψ is the wave function, which contains all the information on the system described. **H** is the Hamiltonian operator which operates on the wave function and presents an output E, the total energy of the system, as its eigenvalue. There are several other operators available, for example for spin, electric dipole moments and so on. These can be used to obtain expectation values of physical observables from the wave function.

The Schrödinger equation appears relatively straight forward to solve but is in reality unsolvable without approximations for non-hydrogenic systems. The most fundamental approximation is the Born-Oppenheimer (BO) approximation, which uncouples the motion of the nuclei in the system from the motion of the electrons.[8] The BO approximation states that any change in the positions of the nuclei corresponds to an immediate restructuring of the electronic configuration, i.e. the nuclei are viewed as stationary at each geometry with respect to the motion of the electrons and the interactions between electron-nucleus, nucleus-nucleus and the nuclear kinetic energy can more readily be evaluated. A common way of looking at the approximation is to note that the mass difference between the electrons and the nucleus is so large that the electrons quickly realign when the nuclei have moved. As approximations go the Born-Oppenheimer (BO) approximation is very mild. Only in exceptional cases is it necessary to work without it.

$$(H_{el} + V_N)\Psi_{el} = E_{el}\Psi_{el} \tag{1.2}$$

$$H_{el} = T_e + V_{en} + V_{ee} \tag{1.3}$$

The operators in the electronic Schrödinger equation (1.2) consist of the electronic interactions, H_{el} and the nuclear-nuclear interactions, V_N. H_{el} in (1.3) consists of the kinetic energy of the electrons, T_e, the electron-nuclear potential energy, V_{en}, and the electron-electron potential energy, V_{ee}. V_N is constant at each geometry according to the BO approximation and can therefore be removed from the equation and added as a parameter. In the vast majority of quantum chemistry codes the electronic Schrödinger equation is solved.

Most, if not all, difficulties in electronic structure theory stem from the interactions of the electrons. The many-body problem crops up in fields of science quite remote from one another. Astronomers calculating the orbit of planets face some of the same problems with the interaction of the planets. Similar to atoms, a system of planets orbiting a star under the influence of its gravitational pull interact with each other simultaneously just as

all electrons in an atom do. The easy solution is of course to ignore the many body interactions, which all are significantly weaker than the interaction with the central star (or nucleus in the case of an atom). The effect on the total energy of an atom or the orbit of a planet is relatively small, which makes it a reasonable approximation. However, in the case of atoms the chemically interesting effects are hidden in the error introduced by such an approximation. The solution used in simple quantum chemical methods is to replace the simultaneous interactions of the individual electrons with a mean field approximation, where the interactions between all electrons are replaced by a mean interaction experienced by all electrons.

The variational principle

There exist an infinite number of solutions to the electronic Schrödinger equation, with the accurate solution being the one which minimizes the energy of the system, i.e. which gives the lowest energy solution to the equation. Working within the Born-Oppenheimer approximation the goal is to find the ground state energy of the system by finding the wave function that minimises the energy of the entire system.

Φ is an arbitrary function of the electronic and nuclear coordinates solving the Schrödinger equation. It is possible to define Φ as a linear combination of orthonormal wave functions Ψ_i without loss of generality. The coefficients, c_i, are restricted by requiring the wave function to be normalized.

$$\Phi = \sum_i c_i \Psi_i \tag{1.4}$$

$$\int \Phi^2 dr = \sum_i c_i^2 \tag{1.5}$$

The energy of the wave function Φ is then evaluated. Among all possible E_i that are the eigenvalues of equation 1.2 there is a lower boundary, E_0, which is the ground state

energy of the system. Equations 1.5 and 1.6 are combined and rearranged to produce the inequality in equation 1.7.

$$\int \Phi H \Phi dr = \sum_i c_i^2 E_i \qquad (1.6)$$

$$\int \Phi H \Phi dr - E_0 \int \Phi^2 dr \geq 0 \qquad (1.7)$$

Equation 1.7 is usually rearranged to give the more familiar form of the variational principle.

$$\frac{\int \Phi H \Phi dr}{\int \Phi^2 dr} \geq E_0 \qquad (1.8)$$

The variational principle formulated in equation 1.8 states that if a wave function exists that produce a lower total energy for the system than an arbitrary trial wave function, then that wave function is a better representation of the ground state of the system. The exact solution to the Schrödinger equation for the system is the wave function which gives the lowest ground state energy.

Linear combination of atomic orbitals

To produce trial wave functions used to initialise the process of finding an energy minimum a representation of the wave function must be established. There are several different ways of doing this. In computational chemistry the most common way of describing the wave function is by using orbitals, located on atomic centres. It is entirely possible to work without orbitals located on the atoms in the molecule but the atomic centred orbitals produce chemically sensible output data and are thus the most frequently used model. Through the LCAO (linear combination of atomic orbitals) basis set approach, the atomic orbitals are used to form linear combinations, i.e. to construct molecular orbitals.

$$\phi = \sum_{i=1}^{N} a_i \varphi_i \tag{1.9}$$

The coefficients, a_i, used to describe the contribution of each atomic orbital, φ_i, to the molecular orbitals, ϕ, are what is solved for.

Basis sets

Atomic orbitals are mathematical functions that describe the behaviour of the electron density of the different orbitals, 1s, 2s, 2p and so on, of an atom. They consist of functions, a basis set, that are combined to accurately represent the way electrons behave in space as well as ideally being reasonably quick to use in calculations.

Ideally all orbitals would be expressed using an infinite number of basis functions, which is clearly not possible. Therefore basis sets have been developed that are a reasonable trade off between computational cost and computational results. There are two basic types of basis functions: Slater type orbitals (STOs) and Gaussian type orbitals (GTOs). The qualitative radial behaviour of STOs and GTOs is shown in Figure 1.5. The Slater type orbitals' radial behaviour is modelled on the electron distribution of the hydrogen atom, since it is the only atom that can be solved exactly with the Schrödinger equation. The radial extension of hydrogenic orbitals decays exponentially. Computationally this is not ideal since it takes a fair amount of computational power to calculate the integral of an exponential. Also, the exponential produces a cusp on the atomic centre which creates problems computationally.

$$\varphi(r,\theta,\phi;\zeta,n,l,m) = \frac{(2\zeta)^{n+1/2}}{[(2n)!]^{1/2}} r^{n-1} e^{-\zeta r} Y_l^m(\theta,\phi) \tag{1.10}$$

Equation 1.10 is a normalized, atom centred Slater type orbital, using polar coordinates. ζ is a fitting parameter, n is the principal quantum number, l and m are the angular momentum quantum numbers and $Y(\theta,\phi)$ are the spherical harmonic functions.

$$\varphi(x,y,z;\alpha,i,j,k)=\left(\frac{2\alpha}{\pi}\right)^{3/4}\left[\frac{(8\alpha)^{i+j+k}\,i!\,j!k!}{(2i)!(2j)!(2k)!}\right]^{1/2}x^i y^j z^k e^{-\alpha(x^2+y^2+z^2)} \qquad (1.11)$$

Equation 1.11 presents a normalized, atom centred GTO in Cartesian coordinates. α is a fitting exponent for the width of the Gaussian, i, j, and k are factors determining the shape and nature of the orbital. For example, in an s-type orbital $i = j = k = 0$, while for a d-type orbital $i + j + k = 2$.

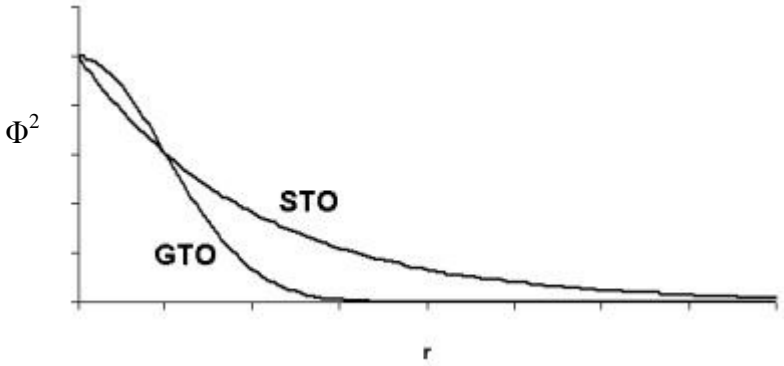

Figure 1.5. The radial distribution of Slater type orbitals and uncontracted Gaussian type orbitals.

One way around the difficulties with the cusp at the nucleus and the computational difficulty in solving integrals with exponentials is to employ Gaussian type functions as the orbital representations. The advantage of using GTOs is that there exist analytical solutions to integrals containing Gaussian functions whereas STOs almost always have to be evaluated numerically. A single Gaussian function does not have the correct radial behaviour, the cusp at the nucleus is missing and the long range behaviour is wrong. To alleviate these problems, M primitive Gaussian functions are contracted to form linear combinations, equation 1.12. The coefficients c_a are fit to give good agreement with the radial behaviour of hydrogenic atomic orbitals. It has been found by Pople *et al.*[9] that M

= 3, i.e. a contraction of three primitive Gaussians, is a good compromise between speed and accuracy.

$$\varphi(x, y, z; \alpha, i, j, k) = \sum_{a=1}^{M} c_a \phi(x, y, z; \alpha_a, i, j, k) \tag{1.12}$$

It is possible to use one STO or one contracted Gaussian function per atomic orbital and create a minimal basis set. Another way of constructing the basis set is to use more than one basis functions per atomic orbital. One basis function per orbital is a minimal or single-ζ basis set, using two creates a double- ζ basis set and so on.

To get a more accurate description on the bonding of a molecule it may be necessary to include polarization functions in the basis set. These are functions which describe orbitals with a higher angular momentum quantum number than is necessary for a minimum description of the electronic structure. For example, hydrogen can be reasonably well described using only a 1s orbital. To improve the description of the bonding behaviour it is useful to include p orbitals in the hydrogen basis set. Similarly for oxygen, d orbitals improve the accuracy of the calculations.

Chemical bonds are usually considered to consist of paired electrons from the valence regions of the atoms in the molecule. Orbitals in the core region of atoms do not change much in chemical bonding and thus the explicit treatment of core electrons is often removed from calculations and replaced by electronic core potentials fitted to high level all electron calculations.

The basis sets used in this thesis are mostly STOs, triple- ζ or higher, with polarization functions included. In some calculations quadruple- ζ all-electron basis sets have been used.

Pauli principle

Spin is an inherent property of electrons, and each electron is characterised by a spin quantum number, ±1/2, frequently called α and β. Spin can be introduced in many different ways into quantum theory, the most common being through the application of relativity, where the concept is introduced in a natural way as a result of the Dirac equations.[10] Relativity also introduces the Pauli principle, which states that no electrons can have the exact same quantum numbers. The consequence of this for quantum mechanics is that any wave function must be anti-symmetric or the Pauli principle is violated. An anti-symmetric wave function is one in which the sign of the wave function changes when two electrons exchange coordinates. A useful tool in constructing wave functions with the correct anti-symmetric properties is Slater determinants.

Slater determinants

For single reference calculations the easiest way to represent the anti-symmetrical wave function using the atomic orbitals of a molecule is a Slater determinant, the general form of which is shown in equation 1.13. N is the number of electrons and χ is a spin-orbital, the product of a spatial orbital and a spin eigenfunction. This notation gives both a mathematically useful expression as well as a representation that is consistent with the Pauli principle.[11]

$$\Psi_{SD} = \frac{1}{\sqrt{N!}} \begin{vmatrix} \chi_1(1) & \cdots & \chi_N(1) \\ \vdots & \ddots & \vdots \\ \chi_1(N) & \cdots & \chi_N(N) \end{vmatrix} \qquad (1.13)$$

The Hartree-Fock method

The Hartree-Fock method is a way of iteratively finding the lowest energy of the molecular system. First formulated in 1928 by Hartree[12] and then corrected to include the Pauli principle in 1930 by Fock and Slater, the method is the way in which many quantum chemical problems are solved, even though it is usually carried out in the matrix formulation proposed by Roothaan in 1951.[13] The procedure consists of a few distinct

steps; starting with the Slater determinant for an electronic configuration the Hartree-Fock equations are set up. The Fock operator and the secular equation is formulated and solved iteratively until self consistency is achieved. A ground state energy minimum should thus have been found. The Slater determinants have already been discussed and the remaining steps will be discussed below.

The one electron Fock operator (f_i in equation 1.14) consists of the one-electron kinetic energy, the nucleus-electron interaction and the Hartree-Fock potential, V_i. The HF potential consists of the Coulomb operator (J) and exchange operator (K).

$$\begin{aligned} f_i &= -\frac{1}{2}\nabla_i^2 - \sum_k^{nuclei} \frac{Z_k}{r_{ik}} + V_i^{HF}\{j\} \\ V_i^{HF} &= 2J_i - K_i \\ J_i &= \iint \phi_\mu(1)\phi_\upsilon(1)\frac{1}{r_{12}}\phi_\lambda(2)\phi_\sigma(2)dr(1)dr(2) \\ K_i &= \iint \phi_\mu(1)\phi_\lambda(1)\frac{1}{r_{12}}\phi_\upsilon(2)\phi_\sigma(2)dr(1)dr(2) \end{aligned} \qquad (1.14)$$

The secular equation, 1.15, formulated below, with the matrix elements defined in equations 1.16 to 1.17, is solved to find its various roots. S is the overlap integral, calculating the orbital overlap between the atomic basis functions in the calculation, and P is the density matrix. The density matrix elements determine how important the exchange and Coulomb effects are for the total energy of the molecular system by weighting the exchange and Coulomb integrals according to the size of the atomic orbital coefficients a of the occupied orbitals.

$$\begin{vmatrix} F_{11} - ES_{11} & \cdots & F_{1N} - ES_{1N} \\ \vdots & \ddots & \vdots \\ F_{N1} - ES_{N1} & \cdots & F_{NN} - ES_{NN} \end{vmatrix} = 0 \qquad (1.15)$$

$$F_{\mu\upsilon} = \left\langle \mu \left| -\frac{1}{2}\nabla^2 \right| \upsilon \right\rangle - \sum_{k}^{nuclei} Z_k \left\langle \mu \left| \frac{1}{r_k} \right| \upsilon \right\rangle + \sum_{\lambda\sigma} P_{\lambda\sigma} \left[(\mu\upsilon|\lambda\sigma) - \frac{1}{2}(\mu\lambda|\upsilon\sigma) \right] \tag{1.16}$$

$$S_{\mu\upsilon} = \int \phi_\mu \phi_\upsilon \tag{1.17}$$

The notation <μ|g|υ>, where g is an operator using basis function ϕ_υ as an argument, specifies a particular type of integration and all terms of this type are referred to as one-electron integrals, 1.18.

$$\langle \mu | g | \upsilon \rangle = \int \phi_\mu (g \phi_\upsilon) dr \tag{1.18}$$

Similarly, the (μυ|λσ) notation in equation 1.16 and 1.19 implies a particular integration where ϕ_μ and ϕ_υ is the probability distribution of one electron and ϕ_λ and ϕ_σ the other. The exchange integrals, (μλ|υσ), in equation 1.16 are divided by two as exchange only affects same-spin electrons while the Coulomb interaction exists between all electrons regardless of spin.

$$(\mu\upsilon \mid \lambda\sigma) = \iint \phi_\mu(1)\phi_\upsilon(1)\frac{1}{r_{12}}\phi_\lambda(2)\phi_\sigma(2)dr(1)dr(2) \tag{1.19}$$

$$P_{\lambda\sigma} = \sum_{i}^{occupied} a_{\lambda i} a_{\sigma i} \tag{1.20}$$

As can be seen in equation 1.20 the atomic orbital coefficients, $a_{\lambda i}$ and $a_{\sigma i}$, are needed to formulate the density matrix element. To be able to solve the secular equation for the total energy an initial guess of the coefficients is needed. From the initial guess, the secular equation is solved and a new density matrix is constructed. If the new density matrix, constructed from the occupied orbitals in the solution of the secular equation, is close enough to the old the calculation has converged. If not, the new density matrix is used in the next iteration of the process.

Electron exchange and correlation

Exchange is a non-classical outcome of the Hartree-Fock equations and the introduction of electronic spin. Electrons interact through classical electronic Coulomb interactions, but the addition of spin adds an extra mode of interaction, electron exchange, for electrons with the same spin. The Pauli principle states that electrons can not have the same quantum numbers, and a visible effect of this is the reduced probability of finding same spin electrons close to each other, producing a so-called Fermi hole around the electrons.

Electron correlation, as defined in HF theory, is the difference between the real energy, E_{real}, and the calculated energy of the system, E_{calc}. Usually this elusive energy term is broken down into two components, dynamic electron correlation energy and non-dynamic correlation energy. Dynamic correlation is the difference in energy between the instantaneous electron-electron interaction (real system) and the average electron-electron interaction (HF system) of the system. Non-dynamic correlation is due to how well the system can be described in terms of a single determinant. Some systems have several Slater determinants of electronic configurations that are equally representative of the system (or very close in energy) and using a single determinant method, such as Hartree-Fock or DFT, can in those cases fail to recover large non-dynamic correlation effects.

Post-Hartree-Fock methods

The major flaw in HF theory is the difficulty the equations have in dealing with electron-electron interactions. In terms of the total energy, this contribution is relatively small. However, for the use of theory in practical chemistry the failure to take electron correlation and exchange into account can result in large errors. HF theory states that the electrons are only exposed to an average, constant interaction with each other. This approximation works in surprisingly many cases. However, there are many methods for improving on this, configuration interaction, perturbation and coupled cluster theories among others, which will be briefly discussed in the following section.

Configuration interaction

In the configuration interaction method (CI) more Slater determinants, representing other electronic configurations, are introduced and the total wave function consists of a linear combination of the different possible configurations.[5] If all possible configurations are included in the calculations, full CI, the exact solution to the non-relativistic time independent Schrödinger equation would be obtained within the accuracy of the basis set. Full CI is all but impossible for any large systems due to bad computational scaling.

Multireference methods

In CI the total wave function consists of a linear combination of the ground state Slater determinant and a number of excitations from this ground state. Multireference method wave functions consist of a linear combination of different electronic configurations, each of which has been optimized. The computational cost of multireference methods is very high and methods such as the complete active space calculation (CASSCF) method have been developed which partition the electronic structure in different "spaces" treated at different levels of theory.[14] Systems with a high density of states, such as open-shell actinides, are very well described using multireference methods, but the calculations are limited to small or highly symmetric systems.

Perturbation theory

The basic precept of Møller-Plesset perturbation theory is that the electronic correlation effects are a small perturbation of the basic HF calculation.[15] By assuming the perturbation to be relatively small it is possible to estimate the perturbation from the HF system. Depending on the order to which corrections are included the method is called MP2, MP3 etc, with MP1 being equal to the original HF result. MP theory is a single reference method. Depending on how many corrections are included the result may vary. Due to the nature of the MP equations MP3 is not much of an improvement to MP2 making MP4 the next logical step in improving the level of theory.

Coupled cluster

Coupled cluster (CC) is another method for including electronic correlation in the calculations.[16] In CC the initial assumption is that the full CI can be calculated as in 1.21:

$$\Psi_{CC} = e^{\mathbf{T}}\Psi_{HF} \tag{1.21}$$

$$\mathbf{T}_2 = \sum\sum t_{ij}\Psi_{ij} \tag{1.22}$$

The **T** cluster operator is expanded in a Taylor series. If this is cut off after two terms the CCSD, coupled cluster singles and doubles, method is created. The amplitude, t, of the **T** operator is solved for. The $\mathbf{T}_2$ term, equation 1.22, is for the doubles, i.e. the second term. Using CCSD it is possible to obtain very good results at a slightly higher computational cost than CI. For smaller systems the CCSD(T) method is possible. This method includes the triple excitations through MP perturbation theory.

The problem is that the formal scaling of these methods is N^4 for regular HF theory to N^8 or higher for the most accurate methods such as CCSDT, where N is the number of basis functions.

Relativistic effects

Relativity is not directly compatible with the Schrödinger equation. Reformulating the quantum mechanical problem Dirac[17] managed to mathematically incorporate the effects of relativity with wave mechanics (equation 1.23).

$$[c\alpha \cdot p + \beta m_e c^2]\Psi = i\frac{\partial \Psi}{\partial t} \tag{1.23}$$

α and β are 4x4 matrices, formulated in equations 1.24 and 1.25. c is the speed of light and p is the momentum operator. The electron rest energy, defined as $m_e c^2$ in the relativistic Dirac equation and zero in the non-relativistic equations, is usually subtracted to align the relativistic and non-relativistic energy scales. In terms of the Dirac equation, this is equivalent to replacing β with β'. σ are representations of the spin-operators.

$$\alpha_{x,y,z} = \begin{pmatrix} 0 & \sigma_{x,y,z} \\ \sigma_{x,y,z} & 0 \end{pmatrix} \quad \beta = \begin{pmatrix} I & 0 \\ 0 & I \end{pmatrix} \quad \beta' = \begin{pmatrix} 0 & 0 \\ 0 & 2I \end{pmatrix} \tag{1.24}$$

$$\sigma_x = \begin{pmatrix} 0 & 1 \\ 1 & 0 \end{pmatrix} \quad \sigma_y = \begin{pmatrix} 0 & -i \\ i & 0 \end{pmatrix} \quad \sigma_z = \begin{pmatrix} 1 & 0 \\ 0 & -1 \end{pmatrix} \tag{1.25}$$

The solution to the time-dependent Dirac equation (1.23) results in some fundamental insights into the way nature is designed. A continuum of positronic states, found below $-2mc^2$, is found in the solution. This result pre-dates the discovery of positrons and is usually thought to have predicted the existence of anti-matter.

The time-independent Dirac equation is shown in equation 1.26, where V is an electric potential.

$$[c\alpha \cdot p + \beta' mc^2 + V]\Psi = E\Psi \tag{1.26}$$

The equation can be factorised into two equations, a large and a small component, Ψ_L and Ψ_S.

$$\begin{aligned} c(\sigma \cdot p)\Psi_S + V\Psi_L &= E\Psi_L \\ c(\sigma \cdot p)\Psi_L + (-2mc^2 + V)\Psi_S &= E\Psi_S \end{aligned} \tag{1.27}$$

Ψ_S is solved for and the inverse term in equation 1.28 is factorised to produce *K*, a factor which determines the size of the relativistic contribution to the calculation. For non-relativistic calculations *K* is 1, reducing the equations to their non-relativistic form.

$$\begin{aligned} \Psi_S &= (E + 2mc^2 - V)^{-1} c(\sigma \cdot p)\Psi_L \\ (E + 2mc^2 - V)^{-1} &= (2mc^2)^{-1}\left(1 + \frac{E - V}{2mc^2}\right)^{-1} = (2mc^2)^{-1} K \end{aligned} \tag{1.28}$$

Rewriting equation 1.28 then gives

$$\Psi_S = K \frac{\sigma \cdot p}{2mc} \Psi_L \tag{1.29}$$

Inserting this result in equation 1.27 gives equation 1.30:

$$\left[\frac{1}{2m}(\sigma \cdot p)K(\sigma \cdot p) + (V - E)\right]\Psi_L = 0 \tag{1.30}$$

In the non-relativistic limit this equation reduces to the Schrödinger equation.

$$\left[\frac{p^2}{2m} + V\right]\Psi_L = E\Psi_L \tag{1.31}$$

Still working in the non-relativistic limit, the small component of the wave function is given as:

$$\Psi_S = \frac{\sigma \cdot p}{2mc}\Psi_L \tag{1.32}$$

Assuming a hydrogenic wave function this reduces to:

$$\Psi_S \approx \frac{Z}{2c}\Psi_L \tag{1.33}$$

From this equation it is quite clear that the heavier the nucleus, Z, the larger the relativistic correction to the wave function, Ψ_S, will be. About 0.4% of the total wave function of a hydrogen 1s electron and 10^{-3}% of the density is accounted for by the small component term, compared to about a third of the wave function and 10% of the density for a uranium 1s electron.

Going back to equation 1.28 to try to calculate the relativistic correction, K can be expanded. However, this expansion is only valid when $E\text{-}V \ll 2mc^2$, a valid approximation for most regions of the atom except the nuclear region.

$$K = \left(1 + \frac{E-V}{2mc^2}\right)^{-1} = 1 - \frac{E-V}{2mc^2} + \ldots \tag{1.34}$$

Using this K factor in equation 1.30, assuming a Coulomb potential and doing some rearranging of the equations results in the Pauli equation. The Pauli Hamiltonian expands the normal Hamiltonian into a relativistic Hamiltonian with the following relativistic terms:

$$H + H_{Pauli} = H + \left(H_{MV} + H_{SO} + H_D\right) = \frac{p^2}{2m} + V - \frac{p^4}{8m^3c^3} + \frac{Zs \cdot I}{2m^2c^2r^3} + \frac{Z\pi\delta(r)}{2m^2c^2} \tag{1.35}$$

H_{MV}, the p^4 term, is due to the relativistic increase in electron mass as a result of the electron velocity. H_{SO} is the spin-orbit term, where s is the electron spin and I is the angular momentum operator. This describes the interaction between the electron magnetic spin and the magnetic field produced by the electron motion. H_D is the Darwin term, a non-classical term for the oscillations of the electrons around their average position (Zwitterbewegung).

As mentioned above, the *K* factor is divergent close to the nucleus. An alternative way of doing the factorising in equation 1.29, which avoids the divergent behaviour, is shown in equation 1.36.

$$K = (E + 2mc^2 - V)^{-1} = (2mc^2 - V)^{-1}\left(1 + \frac{E}{2mc^2 - V}\right)^{-1} = (2mc^2 - V)^{-1} K' \qquad (1.36)$$

K' can be expanded in powers of $E/(2mc^2-V)$, in a manner similar to the expansion of *K*. As $E/(2mc^2-V)$ is always $<<0$, only the zeroth order term in the expansion will be significant, i.e. $K' \approx 1$, giving the Zero Order Regular Approximation (ZORA)[18], equation 1.37, the relativistic method used in this thesis.

$$\left[\frac{c^2 p^2}{2mc^2 - V} + \frac{2c^2}{(2mc^2 - V)^2} - \frac{Zs \cdot I}{r^3} + V\right]\Psi_L = E\Psi_L \qquad (1.37)$$

There are direct and indirect effects of including the relativistic corrections in chemical calculations. The direct relativistic effect on atoms is that orbitals close to the nucleus, mainly the s orbitals but to some extent also the p orbitals, contract. This is mainly seen in heavier elements and must be included in any theoretical treatment of the actinides as the ordering of the valence orbitals are affected by this.[19] The electrons thus come closer to the nucleus.

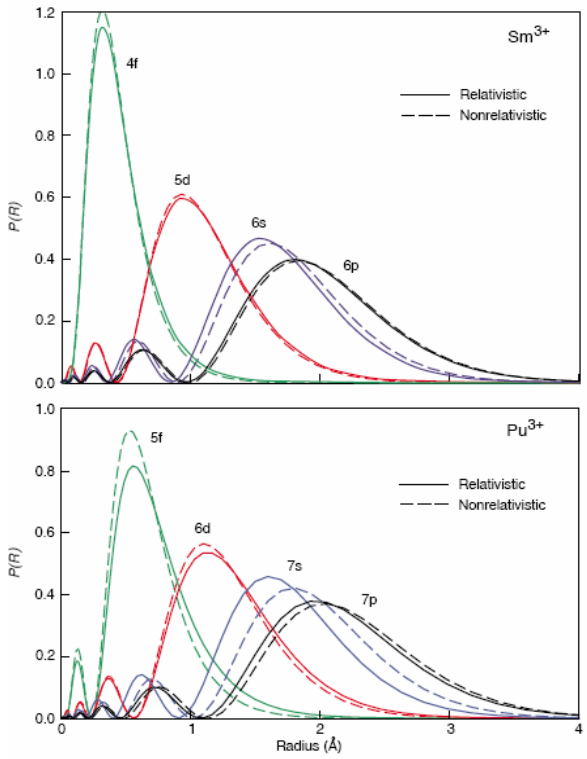

Figure 1.6. A comparison of relativity on the radial extension of the valence orbitals in Sm^{3+} and Pu^{3+}.[20]

The effects on outer orbitals are somewhat different; as the electron density closer to the nucleus increases, more of the nuclear charge is shielded from the outer electrons, meaning that the effective charge felt by these electrons are smaller. The result is an orbital expansion of the d and f orbitals from what the classical models predict. Figure 1.6 shows the behaviour of the valence electron radial distribution of a lanthanide, Sm^{3+}, and an actinide, Pu^{3+}, demonstrating how the s orbitals contract and the orbitals with higher angular momentum quantum number expand.

Of course, to talk about relativistic effects is a bit misleading as the effects are always there in nature but only produce noticeable differences to expected calculated results for heavy elements. The classic example of the colour of gold being a relativistic effect is thus a good argument for including these effects but in reality it only points out the shortcomings of non-relativistic methods.

Density Functional Theory

Density functional theory has its roots in the 1920s, the same time at which the wave mechanical approach was developed. An equation derived independently by both Thomas and Fermi gave the kinetic energy of electrons in a molecule using only the electron density as a parameter.[21, 22] The drawback is that this equation makes chemical bonding impossible (overestimating the kinetic energy of the electrons) which makes the equation of little practical use. However, the notion of using the electron density, a physical observable, instead of the wave function appealed to many and the theory continued to see use in solid state chemistry calculations in the following decades, with some substantial improvements by Slater through the introduction of the X_α-exchange functional.[23, 24]

Kohn-Sham density functional theory

In the 1960s, papers by Kohn and Hohenberg and Kohn and Sham made DFT into a viable method for use in computational chemistry. Kohn and Hohenberg[25] proved the existence of a ground state that could be found from only one electron density, i.e. the electron density uniquely determines the external potential of the system, and that there exists a variational principle by which this lowest energy could be determined. That a variational principle existed had been speculated on in years previous to Kohn and Hohenberg's work but they were able to prove it. This paper, however, only proved the existence of these properties. Kohn and Sham[26] demonstrated how such a calculation might actually be carried out.

The Kohn-Hohenberg theorems

The electronic Hamiltonian of a system, H, can be formulated as is shown in equation 1.38.

$$H = -\sum_{i}^{N} \frac{1}{2}\nabla_i^2 + \sum_{i}^{N} v(r_i) + \sum_{i<j}^{N} \frac{1}{r_{ij}} \qquad (1.38)$$

$$\upsilon(r_i) = -\sum_{Ai} \frac{Z_A}{r_{Ai}} \tag{1.39}$$

The external potential, $\upsilon(r_i)$, is defined in equation 1.39 and the first Hohenberg-Kohn theorem proves that it is uniquely defined by the electron density. The proof itself assumes that two densities lead to the same external potential, which leads to a nonsense result thus proving the theorem *reductio ad absurdum*. The number of electrons in the system, N, is trivially calculated from the electron density.

$$N = \int \rho(r) dr \tag{1.40}$$

Thus the first Hohenberg-Kohn theorem proves that an electron density uniquely determines the external potential, which in turn allows a Hamiltonian to be formulated and ultimately allows a wave function, from which all information of the system can be accessed, to be constructed.

The second Hohenberg-Kohn theorem follows quite readily from the first. Any new density results in a new external potential and thus a new wave function. Inserting the resulting wave function in the usual variational principle results in the DFT formulation of the variational principle:

$$\left\langle \tilde{\Psi} \middle| H \middle| \tilde{\Psi} \right\rangle = E[\tilde{\rho}] \geq E_0[\rho] \tag{1.41}$$

Calculating the electronic energy

The electronic energy of a system can be formulated as shown in equation 1.42. The basis of this formulation is the so-called Levy constrained search formulation of DFT, a formulation which ensures N-representable densities, i.e. densities that can be associated

with anti-symmetric N-electron wave functions. F is a universal functional, defined in equation 1.43, which in Kohn-Sham-DFT includes the kinetic energy of a system of non-interacting electrons, T_s, and J, the traditional inter-electronic Coulomb repulsion found in HF theory. The exchange-correlation energy, E_{XC}, is defined as the difference in kinetic energy between the real system, T, and the non-interacting system together with the difference in the electron-electron interactions between the real, V_{ee}, and non-interacting systems.

$$E[\rho] = F[\rho] + \int \upsilon(r)\rho(r)dr \tag{1.42}$$

$$F[\rho] = T_s[\rho] + J[\rho] + E_{XC}[\rho] \tag{1.43}$$

$$E_{XC}[\rho] = T[\rho] - T_s[\rho] + V_{ee}[\rho] - J[\rho] \tag{1.44}$$

Finding the ground state energy of the system consists of minimising the energy expression in equation 1.42 with respect to the density, under the restraint of keeping the number of electrons, N, in the system constant (1.45).

$$\frac{\partial}{\partial\rho(r)}\left(E[\rho] - \mu\left[\int \rho(r)dr - N\right]\right) = 0 \tag{1.45}$$

$$\frac{\partial E[\rho]}{\partial\rho(r)} - \mu = 0 \tag{1.46}$$

Inserting equation 1.42 into equation 1.46 results in the Euler-Lagrange equation, 1.47, minimising the energy of the non-interacting system with the same external potential, $\upsilon_{eff}(r)$, and therefore same electron density, as the real system.

$$\mu = \upsilon_{eff}(r) + \frac{\partial Ts[\rho]}{\partial\rho(r)} \tag{1.47}$$

$$\upsilon_{eff} = \upsilon(r) + \frac{\partial J[\rho]}{\partial \rho(r)} + \frac{\partial E_{XC}[\rho]}{\partial \rho(r)} \tag{1.48}$$

The Hamiltonian of the non-interacting system with the external potential υ_{eff}(r), equation 1.48, can be formulated and treated as any HF Hamiltonian. The wave functions associated with this Hamiltonian can be constructed using a single determinant, consisting of orbitals solving equation 1.49.

$$\left(-\frac{1}{2}\nabla^2 + \upsilon_{eff}(r)\right)\varphi_i(r) = \varepsilon_i \varphi_i(r) \tag{1.49}$$

Finding the density and kinetic energy of this non-interacting system is straight forward.

$$\rho(r) = \sum_i^N \left|\varphi_i(r)\right|^2 \tag{1.50}$$

$$T_s[\rho] = \sum_i^N \left\langle \varphi_i \left| -\frac{1}{2}\nabla^2 \right| \varphi_i \right\rangle \tag{1.51}$$

To find the electron density of a system, the Kohn-Sham equations, 1.49, are solved using equation 1.48 as the effective external potential. Since υ_{eff} contains functionals of the density the process needs to be performed using an initial, guessed density. The density and the kinetic energy are then found using equations 1.50 and 1.51. The final step of finding the total energy of the system is to use equation 1.42 to add all the energy terms together. The process is then performed iteratively using the new density and repeated until self-consistency.

The reintroduction of orbitals to describe the electronic density was what made KS DFT practically applicable. The manner in which the calculations are set up is very similar to how HF equations are solved, with an initial guess of the density matrix, which enables

the construction of a trial wave function or density depending on the method employed, being the first step in both calculations.

Density functional theory, it must be emphasized, would be exact was it not for the unknown exchange-correlation functional, E_{XC}. There have been many proposed exchange and correlation functionals, all with different areas of application and accuracy. Much of the development in DFT is focused on finding ever better functionals, with the exact exchange-correlation being the ultimate goal. Realistically though, this goal will never be attained as the exchange-correlation functional consists of several very different terms added together, where the behaviour of each of them is only known at certain extremes, e.g. when there is a uniform electron gas.

Exchange-correlation functionals

The development and rise of DFT has occurred in a step-wise fashion, where each step is the result of a significant breakthrough in the formulation of the exchange-correlation functional. The first step was introduced by Kohn and Sham in their paper, the local density approximation (LDA). Later, in the late 80s and early 90s, the introduction of the generalized gradient approximations (GGA) significantly improved the results of DFT and meant that more computational researchers began using DFT. Also, around the same time the hybrid functionals were introduced, with elements of exact (or Hartree-Fock) exchange included. Among the hybrid functionals is B3LYP, a functional that at the moment is the most widely used and is somewhat of a benchmark often used for functional comparisons.

The E_{XC} is frequently divided into two parts, an exchange energy part, E_X, and a correlation energy part, E_C. In terms of contributions, E_X is the dominant term in E_{XC}. As in *ab initio* methods the correlation energy is small as a part of the total energy of the system. However, the range of the correlation energy is where chemically interesting processes take place.

Local density approximation

The LDA is frequently used in DFT for the exchange part of the exchange-correlation.

$$E_X = -\frac{1}{4}\int \frac{\left|\rho_1(r_1, r_2)\right|^2}{r_{12}} dr_1 dr_2 \tag{1.52}$$

The electron exchange energy is defined in equation 1.52. In the LDA the exchange at each point is calculated using the electron density at that point and assuming that this density is constant throughout the system. The equation for calculating the LDA exchange is based on the fictitious uniform electron gas, a medium in which an infinite number of electrons are uniformly distributed in an infinite volume around a uniformly distributed positive charge. Evaluating the integral in equation 1.52, using a uniform gas produces:

$$E_X = C_X \int \rho^{4/3}(r) dr \tag{1.53}$$

$$C_X = -\frac{3}{4}\left(\frac{3}{\pi}\right)^{1/3} \tag{1.54}$$

Using high level Monte Carlo simulations it is possible to parameterise the correlation part, as was done in the work of Vosko, Wilk and Nusair[27] which has resulted in the much used VWN correlation.

The local spin density approximation (LSDA) is the LDA but allows for a more general treatment since it includes spin polarization. It does however have a tendency to significantly over bind, i.e. produce shorter than expected bond distances and larger binding energies, due to failing to handle rapidly changing electronic densities. Despite the approximation being somewhat crude it is often sufficient for geometry optimisations and frequency calculations.

Generalized gradient approximation

The next step in the development of exchange-correlation functionals was the introduction of gradient dependent functionals. It was with the introduction of the generalised gradient approximation functionals (GGAs) in the 1980s that modern DFT really took off as the improvement they provided was not limited to geometries but also improved calculated binding energies, ionisation energies and atomisation energies. GGAs use more information on the behaviour of the density which is used to correct the over binding tendencies of LDA. The GGAs are a development of the LSDA; the LSDA approximates the electron exchange as if the local density is uniform throughout the entire system, i.e. at each point in space the density of the system is assumed to be the same uniform density as that of the point of reference. By taking into account the variation of the electron density in space, i.e. the gradient of the density, a better description of the electron exchange is obtained in, for example, bonding regions where the density changes significantly. The general form of GGA functionals, equation 1.56, shows the addition of the dimensionless gradient parameter, *x(r)*, of the electron density to the expression for exchange.

$$x(r) = \frac{\nabla\rho(r)}{\rho^{4/3}(r)} \tag{1.55}$$

$$E_X[\rho(r)] = \int \rho^{4/3}(r) f(x(r)) dx \tag{1.56}$$

GGA exchange-correlation functionals represent a significant improvement over LSDA functionals. The GGA exchange functionals include both the effects of exchange as well as non-dynamic electron correlation, while the GGA correlation functionals include effects of dynamic correlation. It is when adding these two elements together in an exchange-correlation functional that the real improvement over LSDA occurs.

Several GGA exchange and correlation functionals exist, perhaps the best known being the various Becke exchange functionals, with B86[28] using $f = \beta x^2$ and B88X[29] with $f = \beta x^2/(1+6\beta x \sinh^{-1} x)$. Equally well used are the P86[30] and LYP[31] correlation functionals.

A further, more recent, development has been functionals that take the second derivative of the electron density into account. These methods are generally called meta-GGA methods but the improvements in performance have so far been modest.

Two GGA functionals have been used in this thesis, the non-empirical PBE[32] and the OPBE[32, 33] functional. Actinides present unique challenges for DFT with the large number of electrons and relativistic effects. Many GGA functionals contain parameters which have been fit to test sets consisting of first row elements. Since PBE contains no empirically fit parameters it is not the functional which produces the results closest to experiment. It does however produce the right results for the right reasons and has been extensively used in computational investigations of actinides in the Kaltsoyannis research group. OPBE consists of the exchange functional proposed by Handy and Cohen and the correlation expression of Perdew, Burke and Ernzerhof. Since the functional is used to complete previous work where OPBE was used it was natural to continue using that functional.

Hybrid functionals

Hybrid functionals were developed in the early 90s and in many cases provided an improvement on the performance of DFT. The rationale for the hybrid methods is that Hartree-Fock theory includes exchange naturally in the HF equations, in a way that the Kohn-Sham equations do not. Using the adiabatic connection model the exchange-correlation energy in DFT can be written as a linear combination of HF exchange and some DFT exchange and correlation functional. This improves the accuracy of DFT and is the foundation of the hybrid functionals introduced by Becke. There are several hybrid functionals available that have excellent performance for a wide range of elements. By far the most commonly used is B3LYP[34], a hybrid functional which incorporates elements from classic HF exchange and the Becke exchange together with the LYP correlation functional. This has proven to be a very robust functional, even though there are functionals which are better at specific chemical problems.

Time dependent density functional theory

Naively, the electronic transition energies are the difference in energy between the donor and acceptor molecular orbitals. This is, however, not formally correct as non-classical interactions influence the transitions, thus other methods are needed to find the transition energies. DFT finds the ground state electronic density and unless the system is artificially forced to accept occupations of higher orbitals, the electronic structure will relax to the ground state electronic configuration in the SCF. There are ways, however, to find excitations from the ground state and the transition energies using time dependent DFT (TDDFT).[35]

TDDFT is a response method, a method which finds the response of a physical observable based on a perturbation. In the case of excitations, the focus is the response of the electronic density when exposed to an electric field with a constant frequency. There are two equivalent ways of formulating response theory for excitations, the first using an electric field as a perturbation to which the system responds and the second using Green's functions or propagators on the dipole operator. Both will be introduced briefly below.

In the Green's function approach propagators, mathematical functions which can be used to find the state of a system based on the initial state and a time interval, are formulated (equation 1.57) using time-dependent general operators *P* and *Q* as well as the Heaviside step function θ.

$$\left\langle\left\langle P(t);Q(t')\right\rangle\right\rangle = -i\theta(t-t')\left\langle\Psi_0\left|P(t)Q(t')\right|\Psi_0\right\rangle \pm i\theta(t'-t)\left\langle\Psi_0\left|Q(t)P(t')\right|\Psi_0\right\rangle \qquad (1.57)$$

This propagator can be Fourier transformed into an energy representation called the spectral representation or frequency representation. Inserting the position operator r into the Fourier transformed equation, the outcome is the response of the dipole expectation value to a field with constant frequency. Thus, equation 1.58 is a general equation for calculating excitation energies as used in this thesis.

$$\left\langle\left\langle r;r\right\rangle\right\rangle_{\omega} = \sum_{i\neq 0} \frac{\left|\left\langle \Psi_0 \left| r \right| \Psi_i \right\rangle\right|^2}{\omega - E_i + E_0} - \frac{\left|\left\langle \Psi_0 \left| r \right| \Psi_i \right\rangle\right|^2}{\omega + E_i - E_0} \tag{1.58}$$

ω is the frequency of the electronic field causing the perturbation, with Ψ_i and Ψ_0 being the wave function of the donor and acceptor systems. The poles, i.e. $\omega \pm E_i \pm E_0 = 0$, of this equation are the transition energies while the numerator residuals at the transition energies are the transition moments.

The response approach defines the unperturbed system, $H_0(t)$, and the small, time-dependent perturbation $V(t)$.

$$H(t) = H_0(t) + V(t) \tag{1.59}$$

V(t) is an oscillating electric field with constant frequency. To find the expectation value of the dipole operator for the perturbed system, an expansion of the dipole operator is carried out using V(t) as the perturbation. Keeping only the linear terms of the expansion produces the linear response of the system. The formulation of a time-dependent DFT is a relatively recent development and, as formulated by Gross and others[35, 36], based on the response approach.

$$\sum_q \left\{ H_{pq\sigma} P_{qr\sigma} - P_{pq\sigma} H_{qr\sigma} \right\} = i \frac{\partial P_{pr\sigma}}{\partial t} \tag{1.60}$$

The time-dependent KS equation (equation 1.60) is the starting point for TDDFT. In the equation, H and P are the Hamiltonian and the density matrices respectively; p, q and r are basis set indices and σ is a spin index. After a series of steps involving the response of the system to the perturbation, the resulting density response function is very similar to equation 1.58, but involves density operators instead of dipole operators. However, the basic principle is the same: finding poles to the density response function by finding $\omega = E_i + E_0$.

Two functionals have been used in the TDDFT calculations, SAOP[37] and LB94[38]. These functionals have been constructed to have the correct asymptotic behaviour of the exchange-correlation potential, which has been shown to be important to calculate electronic transitions accurately.

Atomic charge analysis schemes

There are many ways to partition the total net charge of a molecule into the charges of the atoms composing the molecule. The ones that have been used in this thesis are the Mulliken, Hirshfeld and Voronoi charge schemes, all of which are implemented in ADF.

Mulliken charge analysis scheme

The Mulliken charge analysis scheme[39-42] is one of the oldest and still most frequently cited charge decomposition schemes. In it the atoms in a molecule are assigned charge by using the product of the density and overlap matrices, P and S respectively, with the usual definitions, to assign the number of electrons belonging to a certain atom. Equation 1.61 shows how the total number of electrons is calculated using the MO coefficients, $c_{\alpha i}$ and $c_{\beta i}$, that are the result of the SCF as well as the occupation number n_i:

$$S = \int \chi_\alpha \chi_\beta dr$$

$$\sum_i^{N_{orb}} n_i \int \phi_i^2 dr = \sum_{\alpha\beta}^{M_{basis}} \left(\sum_i^{N_{orb}} n_i c_{\alpha i} c_{\beta i} \right) S_{\alpha\beta} = \sum_{\alpha\beta}^{M_{basis}} P_{\alpha\beta} S_{\alpha\beta} = N_{elec} \qquad (1.61)$$

The product PS contains the occupation of orbital α in the diagonal and the overlap population between orbitals α and β in the off-diagonal elements. The charge on each atom is then calculated using equation 1.62. The Mulliken charge of the atom, Q_A, is the difference between the nuclear charge, Z_A, and the charge, ρ_A, assigned to the atom.

$$\rho_A = \sum_{\alpha \in A}^{M_{basis}} \sum_{\beta}^{M_{basis}} P_{\alpha\beta} S_{\alpha\beta}$$

$$Q_A = Z_A - \rho_A \tag{1.62}$$

Voronoi charge analysis scheme

The Voronoi charge analysis scheme is quite dissimilar to the Mulliken charge decomposition. Instead of dividing the wave function into atomic contributions, the Voronoi scheme divides the electron density into volumes, Voronoi cells, belonging to a specific atom. The Voronoi cell for an atom is defined as the volume which is closest to the nucleus of that atom. The electron density in the Voronoi cell is then integrated and the charge of the volume is assigned to the atom.

Hirshfeld charge analysis scheme

In some ways the Hirshfeld scheme is similar to the Voronoi scheme in that it partitions the total density into atomic contributions. However, it uses a weighting factor, w_A, to assign different amounts of density to the atoms in the molecule. w_A is based on how large the atomic density contribution, $\rho_{atomicdensity}$, to the total density of the system is if the total density is defined as the sum of all atomic densities (equations 1.63 and 1.64). This density is called the $\rho_{promolecule}$ while the real density is called $\rho_{molecule}$.

$$\rho_{promolecule}(r) = \sum_{A}^{M_{Atoms}} \rho_A^{atomicdensity}(r) \tag{1.63}$$

$$w_A = \frac{\rho_A^{atomicdensity}(r)}{\rho_{promolecule}(r)} \tag{1.64}$$

The Hirshfeld charge of an atom is then calculated by taking the difference between the nuclear charge and the electron density, assigned using the total density multiplied by w_A, integrated over all space.

$$Q_A = Z_A - \int w_A(r)\rho_{molecule}(r)d(r) \tag{1.65}$$

Mayer bond order analysis

There are several ways to calculate how strong a bond between two atoms is. One particularly useful way is to use bond orders, which transforms the output of quantum mechanical calculations into the concept of single, double and triple bonds which chemists are familiar with. Bond orders can also say something about the covalency or ionicity of the bond. The Mayer bond order has proven useful in inorganic chemistry and will be used frequently throughout this thesis.[43]

$$B_{AB}^{Mayer} = \sum_{s}^{onA}\sum_{t}^{onB}(PS)_{st}(PS)_{ts} \tag{1.66}$$

The Mayer bond order is calculated using equation 1.66, where P is the density matrix and S is the atomic orbital overlap matrix. The product PS is the Mulliken overlap population, also seen in equation 1.61. The Mayer formulation of the bond order will produce the expected integer values for homonuclear diatomics and minimal basis sets. For larger basis sets and more complicated systems non-integer values will be calculated, showing the effects of ionicity and localization effects.

The advantage of the Mayer bond order formulation is that it accounts for all contributions from the molecule to the bond order. However, due to the Mayer bond order being close to the Mulliken formulation of atomic charges there is some basis set dependence of the bond orders. Comparisons between different sets of calculations can thus only be performed if the same basis sets have been used.

Codes

Two computational codes have been used in this thesis, the Amsterdam density functional theory suite of programs (ADF) and Gaussian03. ADF has been updated continuously

during this PhD. Calculations on the polyoxometallates in Chapter 3 were carried out using ADF2006 while the work in the remaining chapters was performed using ADF2007. The differences between the editions are minor in terms of computational algorithms meaning results obtained using the different versions are comparable provided all other variables remain the same. Some of the significant updates include algorithms for analytical frequencies. In the ADF suite, the visualisation program ADFview has been frequently used as a tool for visualising the molecular orbitals. Gaussian03 has been used in the investigations of the uranyl analogues presented in Chapter 5.

The most time consuming aspect of this thesis was the polyoxometallate work where ADF geometry optimizations in low symmetry, using two processors on the Xenon computer cluster, routinely took one week. The energy decomposition calculations were performed in a few days if the SCF was well behaved, a rare event considering the high anionicity of the systems. Calculations on the smaller actinide systems in the other chapters were relatively quick, on the order of an hour, even using all electron basis sets.

Gaussian03

One of the most commonly used codes in computational chemistry is the Gaussian set of codes, with the latest version being Gaussian03, the first version being written by Pople and co-workers in the 1970s.[44] The key feature of Gaussian is the use of GTO basis sets, something which significantly improves computational performance compared to STOs. Another advantage of the code is the inclusion of modules for most types of calculations, both wave function based methods such as HF, CI variants, MP calculations and coupled-cluster calculations, and DFT. In contrast to ADF, DFT hybrid functionals are readily calculated. Although implemented in ADF as well, the performance is not optimal due to the slower, numerical evaluation of the HF exchange matrix elements in ADF compared to Gaussian. The QM/MM implementation ONIOM is also implemented in the present code.

ADF

ADF is one of the few computational chemistry codes that uses Slater type orbitals.[45] The disadvantage is that all integrals have to be evaluated using numerical methods. The advantage is that fewer basis functions are needed for a particular orbital, in comparison with Gaussian basis functions which need to be contracted using, typically, three times as many basis functions for the same accuracy. The integral evaluation of GTOs is easier, however, as analytical solutions can be found.

In an ADF calculation the volume around an atomic fragment, the atomic cell, is divided into different regions depending on the character of the region; the core region contains the nuclear cusp in the electron density which is treated explicitly, while integrals in the remaining volume of the cell are evaluated using a Gaussian product formula. In the region outside the atomic cell the value of the integrals is set to decline exponentially.

To minimise the amount of integrals that need to be evaluated to calculate the Coulomb potential, the exact density, consisting of one and two centre products of basis functions, is fit to one-centre Slater type fit functions. In molecular calculations, the density is fit to one centre fit functions in a pair wise manner, where the fitting is performed between two atom centres at a time. The density is then approximated as the sum of all the pair fit functions and the Coulomb potential can be evaluated from this.

Frozen core approximation

ADF uses a frozen core approximation where the core orbitals are assumed to be unchanged on bonding. The presence of the core is approximated using the result of very accurate, large basis set atomic calculations. The frozen core orbitals are then combined with a set of valence orbitals that are allowed to vary on bonding to produce a full set of orbitals for the atom. What is lost in this approximation is the change in the core orbitals upon bonding with other atoms, which is assumed to very minor. ADF includes basis sets with varying core size, usually a “large” core, a “small core” basis set and an all-electron basis set for all elements of the periodic table. The nomenclature for the ADF frozen core

basis sets are *element.core*, so O.1s means that the 2 1s electrons in the oxygen atom are included in the frozen core.

Energy decomposition

The energy decomposition scheme in ADF is the Ziegler-Rauk approach.[46, 47] It divides the total bonding energy, E_B, into a sum of three components: the Pauli repulsion energy, E_P, the electrostatic interaction energy, E_E and the orbital interaction energy, E_O. E_B is a measure of the instantaneous interactions between the fragments in the molecule rather than the bond dissociation energy, which would require the inclusion of the preparation energy of the fragments to the geometries in the optimized molecule. Depending on the relative size of the energy terms conclusions on the interactions between the fragments can be drawn.

$$E_B = E_P + E_E + E_O \tag{1.67}$$

These terms can be considered the result of three steps in the interactions of the system. First, the optimized molecular system is divided into a number of user defined fragments, molecular or atomic. The fragments are initially imagined to be at infinite separation from each other in order to have no interaction, and each fragment has the wave function Ψ_1, Ψ_2, etc. They are then brought together to their optimized geometry. The only interactions at this stage are the classical electrostatic interaction between the charge densities of the fragments, E_E. This is usually an attractive interaction. The second step is to make the total wave function of the system, Ψ_{Tot}, consisting of the fragment wave functions, anti-symmetric in accordance with the Pauli principle and formulate a single Slater determinant for the molecular system. The result is a repulsive interaction as electron density shifts from the inter-atomic bonding regions, E_P. Commonly used terms for the sum of the Pauli repulsion and the electrostatic interaction are “steric” interaction and “pre-relaxation effects”. Lastly, the wave function of the total system is relaxed to self consistency. This produces an orbital interaction term in the energy decomposition, E_O. E_O includes effects of electron pair formation (covalency), charge transfer and

polarization (mixing between empty and occupied orbitals). In ADF it is possible to divide E_O into contributions from the irreducible representations of the point group of the molecule for a more in-depth analysis of which interactions contribute to the bonding.

The energy decomposition scheme contains some arbitrary elements. How the molecular system is divided into fragments is entirely decided by the user. Depending on what fragments are used the individual energy terms show different behaviour. For example, ionic fragments yield large electrostatic interaction energies that would not be visible in system where the fragments were neutral.

Research Projects

The work carried out for this thesis consists of four projects, all involving the coordination behaviour and bonding of actinides and lanthanides. The individual projects are introduced in this section.

Analysis of metal-metal bonding in $MUCl_6$, $MUCl_8^{2-}$, $NpReCl_8^{2-}$ and $PuOsCl_8^{2-}$ (M = Mo, W)

Much work, experimental and computational, has been carried out investigating d-block metal-metal bonds. Recently, computational studies of actinide metal-metal bonds have been carried out to determine if there exist some intrinsic reasons why no unsupported actinide-actinide bonds have been found. A systematic DFT study carried out by Cavigliasso *et al.*[48-50] featured an extensive analysis of the bond energies and electronic structure of M_2Cl_6 and $M_2Cl_8^{2-}$ (M = Mo, W, U) systems. The bond energy analysis showed that the M = U complexes had significantly higher Pauli repulsion energy terms compared to the d-block systems, not compensated by the stronger orbital interaction energy. Chapter 2 will include a natural extension of the Cavigliasso study with an investigation into the mixed transition metal – actinide systems, $MUCl_6$ and $MUCl_8^{2-}$, and compare with the previous results. An extension into $NpReCl_8^{2-}$ and $PuOsCl_8^{2-}$ complexes will also be carried out.

The coordination properties of plenary and lacunary Keggin phosphomolybdates to Hf, Zr, Ce and Th cations

Experimental work at the Centre for Radiochemistry Research at the University of Manchester has shown that the coordination of Keggin phosphomolybdates to Zr and Hf is different from what has been found for the corresponding phosphotungstenates, preferring a mixed lacunary-plenary Keggin coordination, $X[PMo_{11}O_{39}][PMo_{12}O_{40}]^{6-}$ (X = Zr, Hf), instead of a bis-lacunary coordination, $X(PMo_{11}O_{39})_2^{10-}$. Furthermore, the Hf cation has been found experimentally to coordinate to the lacunary Keggin moiety using the bridging oxygen atoms instead of the unsaturated oxygen atoms in the lacunary cavity. The coordination properties of the Ce and Th cations were also investigated. Experimentally the lanthanide and actinide phosphomolybdate coordination has been found to be similar to the phosphotungstenate systems, preferring a bis-lacunary Keggin coordination. The reason for this difference in coordination behaviour has not been completely investigated before and thus a systematic investigation into the coordination properties of polyoxometallates is carried out. The computational study presented in Chapter 3 investigates the coordination of different phosphomolybdate complexes, lacunary and plenary, using energy decomposition analysis, atomic charges and Mulliken population analysis to determine if there is a difference in the coordination behaviour of transition metals (Zr, Hf), actinides (Th) and lanthanides (La, Lu).

The electronic spectrum of NpO_2^{2+}, $NpO_2Cl_4^{2-}$ and $NpO_2(OH)_4^{2-}$ using time-dependent density functional theory

Many of the polyoxometallate complexes discussed in Chapter 3 have been characterised experimentally using UV/vis spectroscopy. It has been found experimentally that the f-f transition peak for the NpO_2^{2+} moiety in $Na_2(Ge_2W_9O_{34})_2(NpO_2)_2^{14-}$ shifts when it is coordinated in the polyoxometallate complex compared to when it is free in solution. Until quite recently time-dependent DFT (TDDFT) was not used to calculate the electronic spectrum of actinides but following the publication of computational results on

UO_2^{2+} and $UO_2Cl_4^{2-}$ demonstrating that TDDFT can get reasonably close to results obtained using multiconfigurational methods, it seemed appropriate to explore if TDDFT could be employed for the corresponding neptunium complexes.[51] Additionally, since DFT is significantly cheaper computationally than the multiconfigurational methods, larger systems can potentially be explored. The aim of the study in Chapter 4 is to investigate the electronic spectrum of small Np containing molecules, NpO_2^{2+}, $NpO_2Cl_4^{2-}$ and $NpO_2(OH)_4^{2-}$, in order to determine if TDDFT is applicable to open-shell actinides and to perform calculations on the real, experimental $Na_2(Ge_2W_9O_{34})_2(NpO_2)_2^{14-}$ system for comparison with experiment.[52]

Investigations on the bonding and bending in group 15 and group 16 uranyl analogues

UO_2^{2+} is one of the most investigated systems in computational chemistry and its electronic structure is well documented. Less work and no comprehensive study of the trends down group 15 have been performed on the =N-R and =P-R analogues of uranyl. Previous computational results on the =N-R systems indicate a shift in the electronic structure, with a π-bonding MO becoming the HOMO and the σ-bonding MOs being stabilized. The uranyl analogue, US_2, has also been investigated and found to be bent, unlike the linear UO_2 system but similar to ThO_2. There has been no further analysis of the heavier group 16, neutral uranyl analogues. Chapter 5 is a systematic DFT investigation of the geometry, electronic structure, frequencies, bond orders and bond energies of isoelectronic group 15 and group 16 analogues of UO_2^{2+} and UO_2. The aim is to investigate the reason for the difference in geometry between UO_2 and US_2 as well as to probe for trends down the group 15 and 16 uranyl analogues.

Chapter 2

Analysis of metal-metal bonding in $MUCl_6$, $MUCl_8^{2-}$, $NpReCl_8^{2-}$ and $PuOsCl_8^{2-}$ (M = Mo, W)

Introduction

One of the "holy grails" of actinide chemistry is to synthesize compounds with unsupported metal-metal bonds. In transition metal chemistry such bonds are well known and are the topic of much research.[53, 54] Much experimental work has gone into trying to find ways of binding two actinide nuclei together through clever use of ligands surrounding the two atoms. Systems have been synthesised which place two U atoms in close proximity to each other but this is often done by using bulky ligands which force the two atoms together for steric reasons or by using a bridging atom or atoms.[55, 56] Recently there has been an increasing interest in investigating the An-An bond computationally, to see if there are some inherent factors that makes it so difficult for this bond to form.

Figure 2.1. The optimized geometries of $MoUCl_6$ (left) and $WUCl_8^{2-}$ (right). The U atom is pictured in blue, the transition metal in pink and the Cl ligands in green.

Several studies on small actinide compounds such as U_2, Pu_2 and Th_2H_2 have been performed.[57-59] One of the more recent investigations of the U_2 molecule, along with

various uranium-chloride and uranium-carboxylate complexes, has been performed by Roos *et al.* using multiconfigurational methods.[60, 61] These systems were calculated to have bonding total energies and contain a multiply bonded U_2 unit; the nominal bond order of U_2 was found to exceed the traditionally assigned bond order of 3, and to have a bond order of 5 instead, one σ bond, two π bonds and two δ bonding interactions.

Previous work on the M_2X_6 and $M_2X_8^{2-}$ (M = U, W, Mo; X = Cl, F, OH, NH_2, CH_3) systems discussed in the present chapter has been carried out by Cavigliasso *et al.*[48-50] In those investigations the expected bond order of 3, one σ bond and two π bonds, was found and the rest of the valence AO set was used to form the ligand bonds. Geometry optimizations revealed that the calculated DFT bond distances were slightly shorter than the corresponding multireference geometries.

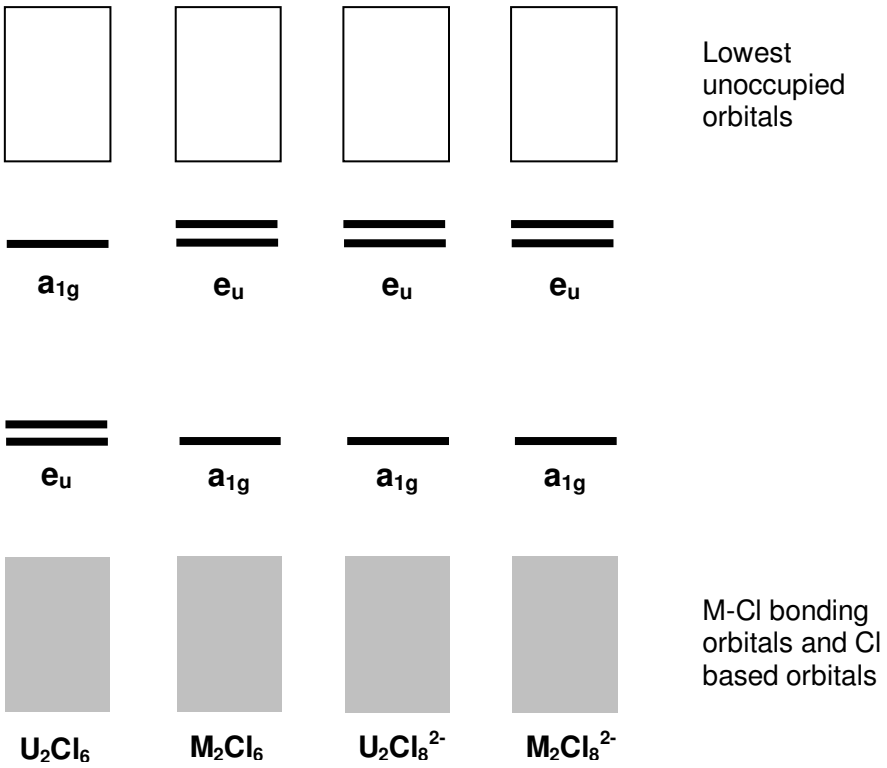

Figure 2.2. Qualitative MO diagram of U_2Cl_6 and M_2Cl_6 (M = Mo, W)

The electronic structure of the M_2X_6 and $M_2X_8^{2-}$ (M = U, W, Mo; X = Cl, F, OH, NH_2, CH_3) systems was also investigated (Figure 2.2). As the systems are all closed shell d^0 systems there is no participation of d based MOs in δ bond formation. The bonding in the U-U systems was the expected σ plus two π bonding and a nominal bond order of three. The same bond order was found for the transition metal systems. The electronic structure of the transition metals and the U-U systems varied, unsurprisingly, depending on the number of ligands. In all the M_2X_6 systems (M = Mo, W, U) there were only two main metal-metal bonding MOs, the $6e_u$ and $6a_{1g}$, the π and σ bonding MOs respectively. The main difference between the M = Mo, W and M = U is the ordering of the MOs; the transition metal HOMO is the $6e_u$ and HOMO-1 is $6a_{1g}$ while the opposite ordering is found for the ground state of the M = U system. The block of MOs lower in energy consists of M-X bonding orbitals and X based MOs. The virtual MOs are predominantly M-M based in character. The HOMO-LUMO energy gap varies with system; in the M = Mo, W compounds it was found that the separation is quite large while in the M = U systems the HOMO-LUMO gap is significantly smaller. Additional calculations, however, confirmed the initial calculated singlet ground state.[50]

In the $M_2X_8^{2-}$ systems Cavigliasso *et al.* found that, similar to M_2X_6, the DFT M-M distances are more or less independent of the type of ligand X or the conformation of the molecule. The study also found that the electronic structure is slightly different from the M_2X_6 systems. The expected type of bonding is found; σ + 2π bonds and the MOs involved span the a_{1g} and e_u irreps respectively. For the M = W, Mo systems the energetic ordering was the same as in the M_2X_6 system, i.e. $6e_u > 6a_{1g}$. For M = U, this was also found to be the ordering, in contrast to the ordering found in U_2X_6, where the order was the other way around, $6a_{1g} > 6e_u$. The reason for the reordering is anti-bonding contributions from the X ligands to the π-bonding MOs. Depending on the ligands X, the lower energy orbitals can become more significant in the bonding of the molecule but the main metal-metal bonding MOs will be the ones around the HOMO.

The energy decomposition analysis of Cavigliasso of the M_2X_6 and $M_2X_8^{2-}$ (M = U, W, Mo; X = Cl, F, OH, NH_2, CH_3) systems found that the U-U bond is different from the M-M (M = Mo, W) bond in that the pre-relaxation effects are larger in the U-U systems than in the M-M (M = Mo, W) systems. The pre-relaxation effects are the sum of the Coulomb electrostatic interaction energy and the Pauli repulsion energy. When analysing this difference it was found that it is the Pauli repulsion energy that is significantly higher for the U-U systems compared to the M-M (M = Mo, W) systems. The orbital interaction energy term was larger in the U-U systems, but this increase was not enough to balance out the increase in the Pauli repulsion and the total energy at the optimized geometry was positive, indicating that the molecule is unstable. In contrast, all of the investigated M-M (M = Mo, W) systems had negative total energies and were stable, confirming experimental results.[48]

Aim

The present investigation deals with mixed uranium-transition metal (U-M) systems (M = Mo, W) to determine the bonding behaviour of these molecules and compare with the calculations on M_2X_6 and $M_2X_8^{2-}$ (M = U, W, Mo; X = Cl). Studies have found that the impact of the X ligands is rather small, thus only Cl ligands will be used in the present investigation.[48-50] There will also be calculations on the effects of δ-bonding in the metal-metal bond moving across the 5f, 5d and 4d elements to $NpReCl_8^{2-}$ and $PuOsCl_8^{2-}$.

Computational details

All calculations have been performed using ADF.[46, 62, 63] The GGA OPBE functional, consisting of the exchange functional of Handy and Cohen[33] as well as the correlation expression of Perdew, Burke and Ernzerhof[32], has in previous computational studies proved to be the most suited functional for geometry optimizations and energy decomposition analysis. The full symmetry of the various systems have been employed; C_{3v} in the $UMCl_6$ and C_{4v} in the $UMCl_8^{2-}$ corresponding to the staggered formation for

$UMCl_6$ and the eclipsed for $UMCl_8^{2-}$. Two types of standard ADF frozen core STOs of triple-ζ quality and one polarization function (TZP) have been used for Cl, Mo, W, Re and Os; a small core basis set (Cl.2p, Mo.3d, W.4d, Re.4d, Os.4d) and a large core basis set (Mo.4p). There is no corresponding large core basis set for W. TZ2P basis sets were used for U, Np and Pu; U.5d, Np.5d and Pu.5d for the small core calculations and U.6p for the large core calculations. Relativistic effects were included in all calculations using the scalar relativistic zero order regular approximation (ZORA). The integration grid and convergence criteria were set to the ADF defaults.

Much of the analysis was based on the Ziegler-Rauk energy decomposition scheme and was performed using fragments that split the bonding electrons equally between the two $MCl_3(\uparrow\uparrow\uparrow)$ + $UCl_3(\downarrow\downarrow\downarrow)$ fragments and the corresponding division in the $MUCl_8^{2-}$ systems is $MCl_4^-(n\uparrow)$ + $MCl_4^-(n\downarrow)$ (M = Mo, W, Re, Os, U, Np, Pu), where n = 3, 4, 5 according to the number of unpaired electrons in the system.[62] Two same-spin electrons from the split π-bonding MOs are located on each fragment and the unpaired electrons of the σ-bond split in two, the spin of the σ-electrons being the same as the π-electrons of the fragment. Other tools used in this study were the Mayer bond[43, 64] order as well as molecular orbital decompositions and Mulliken atomic populations.

Results

$MUCl_6$ (M = Mo, W)

Geometry

The optimized geometries of the $MUCl_6$ molecules (Figure 2.1) are close to the average geometric parameters for the respective M_2Cl_6 and U_2Cl_6 molecules, slightly favouring M_2Cl_6 in the bond lengths. The U-U distance in U_2Cl_6 is 2.35 Å and 2.23 Å for Mo_2Cl_6 compared to the U-M distance of 2.27 Å. For M = W the M-U distance is almost exactly the average distance. The U-Cl bond distance remains the same regardless of system, 2.46 Å, while the M-Cl distance is increased in the mixed compounds, from 2.24 Å to

2.30 Å for $MoUCl_6$ and 2.25 Å to 2.27 Å for $WUCl_6$. The main change in going to the mixed U-M systems is in the U-M-Cl bond angles; for M = Mo the bond angle is reduced from 103° for Mo_2Cl_6 to 84° in the mixed system. In the M = W systems the bond angle is similarly reduced but from 103° to 90°. The M-U-Cl bond angle is only marginally increased from 119° to 123°, likely because of the proximity of the Cl atoms on the M atom.

M	M-U	M-Cl	U-Cl	M-U-Cl	U-M-Cl
Mo	2.27	2.30	2.46	123	84
W	2.32	2.27	2.46	123	90
Mo_2*	2.23	2.24		103	
W_2*	2.30	2.25		103	
U_2*	2.35	2.46		119	

Table 2.1. Optimized geometries of $MUCl_6$ (small cores, staggered) complexes using OPBE (Å and degrees respectively). *) Values taken from Cavigliasso *et al.*[48-50]

Electronic structure

The electronic structure of the $MUCl_6$ systems (Figure 2.3) shows the orbitals involved in the metal-metal bonding, a_1 (σ) and e (π). The a_1 is the HOMO and the e is the HOMO-1. Below these orbitals in energy is a block of orbitals based on the Cl ligands or involved in M-Cl bonding. The ordering of the metal-metal bonding MOs is identical to what has been found for U_2Cl_6, where the σ bonding MO is the HOMO.[50] For the Mo_2Cl_6 and W_2Cl_6 systems the ordering was reversed and the π-bonding e_u MO was the HOMO. The reason for this is the larger Cl contribution to e, which has been found to destabilize the π MO.[50]

The orbital composition of the metal-metal σ and π bonds (Table 2.2) reveals the contributions from the respective metals. In the $MoUCl_6$ molecule the ligand contribution to the a_1 MO remains the same as in the homonuclear dimer, 13%. Similarly, the ligand

contribution to the $WUCl_6$ a_1 MO is smaller than the Cl contribution in W_2Cl_6, 8% compared to 10%. The Mo s contribution to a_1 is lost, however, when going to the mixed system, while it still is seen in the W mixed system although decreased from 15% to 8 %.

Composition (%)										
	a_1 (σ)					e (π)				
M	*s*	*p*	*d*	*f*	*Cl p*	*s*	*p*	*d*	*f*	*Cl p*
Mo			35		13			38		24
U_{Mo}			5	36					25	
W	8		34		8			35		22
U_W			6	36				4	30	
Mo_2*	8	3	69		13		2	46		48
W_2*	15	3	68		10		4	54		40
U_2*	12	3	2	76	3		1	13	73	10

Table 2.2. Composition of metal-metal bonding orbitals of $MUCl_6$, M = Mo, W (staggered, small core) complexes. *) Values taken from Cavigliasso *et al.*[48-50]

The Cl p orbital contributions to the e MOs are halved going from Mo_2Cl_6 and W_2Cl_6 to the mixed systems. On the other hand, the Cl contribution to the U_2Cl_6 systems is quite low, only 10%, and the ligand contribution is small for both the a_1 and e MOs. Interestingly the U f contribution to e decreases more then expected, going from 73 % in U_2Cl_6 to 25% and 30 % for the $MoUCl_6$ and $WUCl_6$ systems, respectively. The metal d orbital contributions also decrease moving to the mixed systems.

The orbital compositions in Table 2.2, with the valence MOs consisting of the average of the AO contributions of the homonuclear complexes, indicate that the metal-metal bond is spread evenly between the two metal atoms in the heteronuclear complexes.

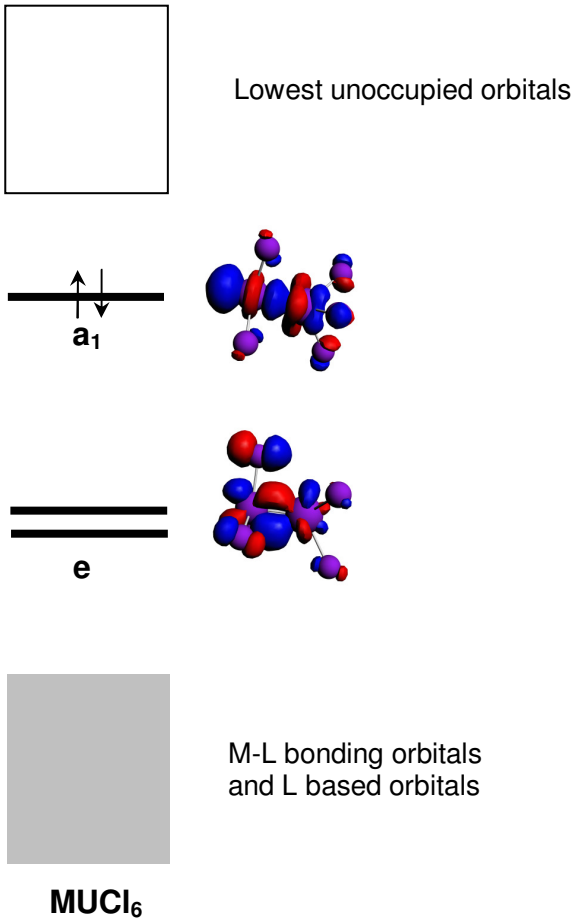

Figure 2.3. Qualitative molecular orbital diagram of the orbitals involved in metal-metal bonding in $MUCl_6$.

Energy decomposition analysis

The first thing to note in the energy decomposition is that the total bonding energy of the mixed $MUCl_6$ complexes is close to the average of the total bonding energy of the M_2Cl_6 and U_2Cl_6 complexes. For M = Mo E_B is -2.11 eV compared with -3.24 eV for Mo_2Cl_6 and -0.20 eV for U_2Cl_6 (average: -1.72 eV), meaning that energetically the bond is slightly closer to Mo_2Cl_6. For $WUCl_6$ the total bond energy is -1.85 eV compared to -4.34 eV for W_2Cl_6 and -0.20 eV (average: -2.27 eV) implying that $WUCl_6$ behaves slightly more like the U_2Cl_6 dimer.

M	E_B	E_P+E_E	E_P	E_E	E_O	$E_O(a_1)$	$E_O(e)$
Mo	-2.11	8.75	15.60	-6.85	-10.86	-3.76	-7.06
W	-1.85	8.09	15.67	-7.58	-9.94	-3.51	-6.41
Mo_2*	-3.24	4.73	12.51	-7.78	-7.97	-3.30	-4.67
W_2*	-4.34	4.02	15.45	-11.42	-8.37	-3.37	-5.00
U_2*	-0.20	10.44	11.39	-0.95	-10.64	-3.56	-6.98

Table 2.3. Energy decomposition analysis of $MUCl_6$ (small cores, staggered) complexes at OPBE optimized geometries (eV). *) Values taken from Cavigliasso *et al.* [48-50]

Looking at the individual energy terms it is noticeable that the Pauli repulsion is greater for $MoUCl_6$ than for either the Mo_2Cl_6 or U_2Cl_6 systems, 15.60 eV for $MoUCl_6$ and 12.51 eV and 11.39 eV for Mo_2Cl_6 and U_2Cl_6 respectively. The $WUCl_6$ Pauli repulsion is similar to the W_2Cl_6 Pauli term. The difference in the electrostatic interaction between the homonuclear dimers was investigated by Cavigliasso *et al.*, who found that the directionality of the a_1 metal fragment orbitals is important.[48-50] In the $MoCl_3$ and WCl_3 fragments the a_1 MO extends along the axis of the metal-metal bond while the corresponding a_1 MO in the UCl_3 fragment is more evenly spread around the axis. The larger radial extension of the transition metals results in a larger electrostatic interaction between the $MoCl_3$ and WCl_3 fragments than the UCl_3 fragments. The E_E terms for $MoUCl_6$ and $WUCl_6$, -6.85 eV and -7.58 eV, are smaller than for M_2Cl_6, -7.78 eV and -11.42 eV, but significantly higher than U_2Cl_6 at -0.95 eV. The electrostatic interactions of the heteronuclear molecules are thus close to being the average of the U_2Cl_6 and the transition metal systems, consistent with the behaviour of the a_1 radial extension.

The orbital interaction term, E_O, for $MoUCl_6$ is close to the U_2Cl_6 dimer, -10.86 eV compared to -10.64 eV. A similar behaviour is seen, but to a lesser extent in $WUCl_6$ -9.94 eV (closer to W_2Cl_6 (-8.37 eV) than $MoUCl_6$ is to Mo_2Cl_6 (-7.97 eV)) compared to -10.64 eV. In both mixed systems the E_O behaves very much like the U_2Cl_6 dimer and the main difference in bonding comes from differences in pre-relaxation effects.

The behaviour of the energy decomposition terms of the M_2Cl_6 and U_2Cl_6 and the mixed $MUCl_6$ molecules as a function of U-M bond length, 2.1 to 2.5 Å, is shown in Figure 2.4. The energy terms of the mixed systems show consistent behaviour; the E_E terms are close to E_E of the transition metal dimers. The exception is the E_P term, where for both the $MoUCl_6$ and $WUCl_6$ systems, the Pauli repulsion is higher in the mixed systems. The E_P and E_E terms are, similar to the energy decomposition at the optimized geometries, compensated by the relatively U_2-like E_O, resulting in a total bond energy that is close to the average total energy of the M_2Cl_6 and U_2Cl_6 systems.

M	E_B	E_P+E_E	E_P	E_E	E_O	$E_O(a_1)$	$E_O(e)$
Mo	-4.01	6.76	13.46	-6.70	-10.73	-3.78	-6.95
W	-1.62	8.58	16.20	-7.62	-10.19	-3.70	-6.47

Table 2.4. Energy decomposition analysis of $MUCl_6$ (large cores, staggered) complexes at OPBE optimized geometries (eV)

Energy decomposition analyses using large frozen cores for U, Mo and W (U.6p, Mo.4p and W.4f) were performed to investigate the basis set dependence of the results. The W basis set does not include the 5p MOs in the core and is thus not the corresponding basis set to the Mo and U basis sets. Table 2.4 shows that the differences in the large core energy terms are minor for the $WUCl_6$ system when comparing to the small core calculations; the total energy is 0.23 eV larger as a result of a slight increase in the Pauli repulsion. For the $MoUCl_6$ system the total bond energy is 1.90 eV more bonding in the large core calculations. The reason for this is a decrease in the E_P term, which accounts for almost the entire increase in bond strength.

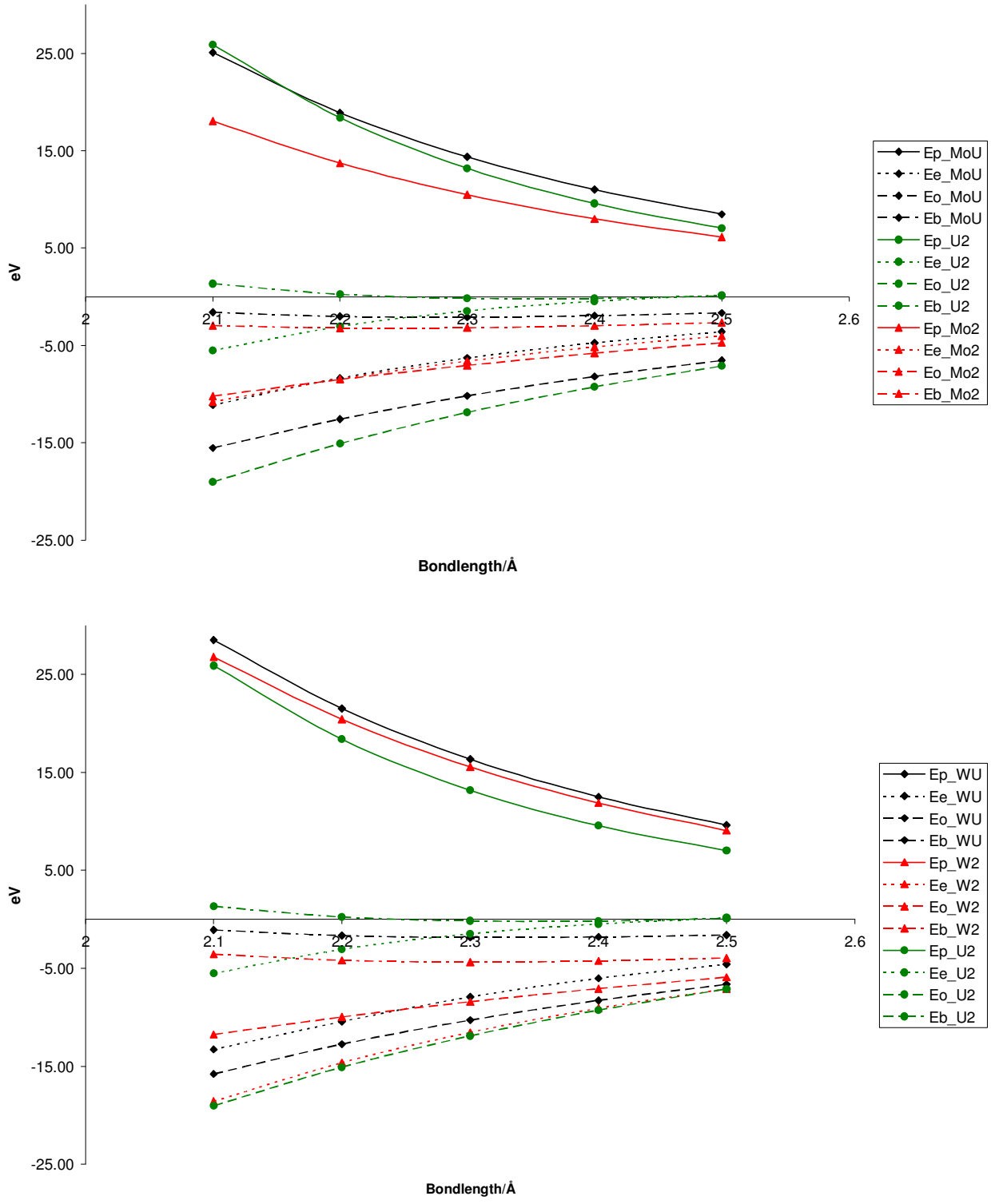

Figure 2.4. The terms of the energy decomposition analysis as a function of the U-M (M = Mo (top), W) bond length in $UMCl_6$.

In Table 2.5 a systematic investigation, at a fixed bond length, into the significance of the size of the frozen core is presented. Different combinations of core sizes are shown and the most important conclusion is that the total bonding energy only significantly changes for the $MoUCl_6$ systems, and then only when large cores are used on both the Mo and U atoms. With only one large core the total energy in $MoUCl_6$ change by *ca* 0.2 eV, but with two large cores the bond energy becomes almost 2 eV more stable, all through a decrease in the Pauli repulsion term.

M	E_B	E_P+E_E	E_P	E_E	E_O	$E_O(a_1)$	$E_O(e)$
Mo_s-U_s	-2.11	8.12	14.45	-6.32	-10.24	-3.57	-6.63
Mo_s-U_l	-1.93	8.58	14.88	-6.30	-10.51	-3.76	-6.72
Mo_l-U_s	-2.11	8.12	14.45	-6.32	-10.24	-3.57	-6.63
Mo_l-U_l	-3.82	6.52	12.85	-6.33	-10.33	-3.65	-6.65
W_s-U_s	-1.62	8.93	16.89	-7.96	-10.55	-3.82	-6.70
W_s-U_l	-1.71	8.94	16.87	-7.92	-10.49	-3.84	-6.78
W_l-U_s	-1.70	8.48	16.43	-7.95	-10.18	-3.59	-6.57
W_l-U_l	-1.62	8.93	16.89	-7.96	-10.55	-3.82	-6.70

Table 2.5. Energy decomposition analysis of $MUCl_6$ (staggered, large(l) and small(s) cores) complexes at 2.30 Å M-U distance (eV) NB: W basis set does not expand as Mo and U in the large cores. Calculations have been performed on available large core W basis sets.

Previous work on the Mo_2 and U_2 homonuclear dimer systems confirm that the Pauli repulsion energy term is dependent on the size of the atomic frozen core used in the calculations, with destabilizing contributions involving the outer-core orbitals of U.[48] The small core calculations, which include orbitals up to 3d in Mo, 4d for W and 5d for U in the frozen cores, have a higher E_P than calculations using a larger core, Mo 4p and U 6p. The reason for the difference in E_P is thought to be due to interactions between the filled 6p orbitals in U, occurring due to the large radial extension of the 6p orbitals. With the 6p included in the frozen core, these interactions disappear. The Mo 4p orbitals are more

core like and do not interact in the Mo_2 homonuclear dimer as much as the U 6p orbitals in U_2Cl_6. There is however some Mo 4p – U 6p interaction using small cores as E_B is higher than for the large core calculation. No equivalent 5p basis set exists for W hence the W containing combinations were excluded from Table 2.6 and the lack of noticeable change in the total bond energy in Table 2.5, where the W.4f basis set was used.

M	E_B	E_P	E_E	E_O
Mo	-1.90	-2.14	0.15	0.11
Mo_2*	-0.11	-0.53	0.24	0.13
U_2*	-5.04	-6.29	0.03	1.22

Table 2.6. Comparison of energy terms as a function of core size ("large core" – "small core") at OPBE optimized geometries. *) Values taken from Cavigliasso *et al.*[48-50]

It is also seen that the difference in Pauli repulsion interaction is the largest for the U_2 dimer, where there is a 6.29 eV destabilization. The mixed Mo-U system is clearly destabilized by the p orbital interaction, with a 2.14 eV difference between large and small cores, but not by as much as the U_2 system. The destabilization is significantly larger in the U_2Cl_6 system than in the Mo_2Cl_6 system, but the energy decomposition shows that change in E_P of the mixed system can not solely be attributed to the U 6p orbitals thus suggesting that the Mo 4p MOs also contribute.

Mayer bond orders

The Mayer bond order analysis (Table 2.7) finds that the U-M bond orders are close to the theoretical maximum of 3, 2.82 for Mo-U and 2.87 for W-U. These bond orders are in fact higher than what is found for the corresponding Mo_2Cl_6 and W_2Cl_6 compounds, where they were calculated to 2.47 and 2.43 for Mo_2Cl_6 and W_2Cl_6 respectively. A very low bond order, corresponding to what was found for U_2Cl_6, 1.63, was not found in any of the mixed systems.

M	M-U	M-Cl	U-Cl
Mo	2.82	1.34	0.80
Mo_2	2.47	0.98	-
W	2.87	1.33	1.04
W_2	2.43	1.08	-
U_2	1.63	-	1.21

Table 2.7. Mayer bond orders of $MUCl_6$ (small cores, staggered) complexes at OPBE optimized geometries.

The low bond order for the homonuclear U_2Cl_6 dimer corresponds well with the calculated total bond energy (Table 2.3) of the system; the U-U bond was found to be the least bonding of all the investigated systems. The bonds to the Cl ligands can all be characterized as single bonds but the calculated bond is slightly stronger between the transition metals and the Cl than the U-Cl bond. Also, the calculated M-Cl (M = Mo, W) bond order is higher in the mixed system, 1.34 and 1.33 for $MoUCl_6$ and $WUCl_6$, than in the M_2Cl_6 systems, where the bond orders are 0.98 and 1.08 for Mo_2Cl_6 and W_2Cl_6 respectively.

$MUCl_8^{2-}$ (M = Mo, W)

Geometry

M	M-U	M-Cl	U-Cl	M-U-Cl	U-M-Cl
Mo	2.31	2.40	2.59	115.90	99.14
W	2.39	2.38	2.60	115.08	98.86
Mo_2^*	2.28	2.37		104	
W_2^*	2.34	2.37		104	
U_2^*	2.35	2.60		112	

Table 2.8. Optimized geometries of $MUCl_8^{2-}$ (small cores, eclipsed) complexes using OPBE (Å and degrees respectively). *) Values taken from Cavigliasso *et al.*[48-50]

The optimized geometric parameters of $MUCl_8^{2-}$ can be seen in Table 2.8. The most prominent feature is the W-U distance, calculated to 2.39 Å, longer than both the $U_2Cl_8^{2-}$ and $W_2Cl_8^{2-}$ complexes. The Mo-U bond distance is 2.31 Å, close to the average bond distance of the $Mo_2Cl_8^{2-}$ and $U_2Cl_8^{2-}$ complexes. Similar to the $MUCl_6$ complexes the U-Cl bond distances are conserved from $U_2Cl_8^{2-}$ to the $MoUCl_8^{2-}$ and $WUCl_8^{2-}$ complexes, staying at 2.60 Å. The M-Cl bond distances in the mixed molecules are slightly longer than in the $M_2Cl_8^{2-}$ and $U_2Cl_8^{2-}$ complexes; 2.40 Å compared to 2.37 Å for $MoUCl_8^{2-}$ and 2.38 Å compared to 2.37 Å for $WUCl_8^{2-}$. The U-M-Cl angle is *ca.* 99°, not as close to a right angle as in the $MUCl_6$, a fact most likely due to the eclipsed formation which forces the ligands further apart compared to the staggered $MUCl_6$ formation. However, the trend is the same as in the $MUCl_6$ with the angle becoming more acute. The M-U-Cl angle is quite close to the U-U-Cl angle, 115° compared to 112°.

Electronic structure

The electronic structure around the HOMO in the $MUCl_8^{2-}$ systems is shown in Figure 2.5, with a selection of metal-metal bonding MOs lower in energy displayed below the line. The important metal-metal binding orbitals are the HOMO, a σ-bonding 11(12) a_1 MO (the labels of the $WUCl_8^{2-}$ system shown in parenthesis) and the HOMO-1, 11(13) e_1, a π-bonding MO. This valence electronic structure is similar to what was found in the $MUCl_6$ systems, where the ordering of the frontier orbitals was found to be the same as in the U_2Cl_6 system.[50] Previous calculations, however, found that the ordering of the frontier orbitals in $U_2Cl_8^{2-}$ has the π-bonding MO as the HOMO and the σ-bonding as the HOMO-1. Similarly, the HOMO and HOMO-1 in the $Mo_2Cl_8^{2-}$ and $W_2Cl_8^{2-}$ molecules are $6e_u$ and $6a_{1g}$ respectively, π bond higher in energy than a σ bond.

In the U_2Cl_6 system the ordering of the frontier orbitals is different from the ordering in W_2Cl_6 and Mo_2Cl_6; the HOMO is a σ-bonding orbital and HOMO-1 is a π-bonding orbital while the ordering is reversed for the transition metal systems. Previous studies found that the π bonding orbitals are destabilized in the transition metal systems due to

anti bonding interactions between the metal d orbitals and the chlorine orbitals.[50] In the uranium system, there was no corresponding anti bonding interactions between the f orbitals and the Cl orbitals and thus the σ-bond is higher in energy than the π-bond. As is seen in Figure 2.5, the electronic structure in the mixed $MUCl_8^{2-}$ systems is the same as in the $MUCl_6$ systems, indicating that there is limited anti bonding interactions from the Cl orbitals. This is in contrast to the $Mo_2Cl_8^{2-}$, $W_2Cl_8^{2-}$ and $U_2Cl_8^{2-}$ complexes which all have been found to have an electronic structure similar to the W_2Cl_6 and Mo_2Cl_6 systems.

M	$4a_{1g}$	$3e_u$	$5a_{1g}$	$6a_{1g}$	$6e_u$	$2b_{2g}$	$2b_{1u}$
Mo_2	7 d, 7 s	35 d	9 d, 4 p	73 d, 2 p, 7 s	52 d, 2 p	67 d	75 d
W_2	2 d, 16 s	24 d, 1 p	9 d, 4 p	72 d, 3 p, 15 s	60 d, 3 p	71 d	75 d

M	$5e_1$	$9a_1$	$11e_1$	$11a_1$	$3b_2$	$4b_2$	$13e_1$
Mo	13 Mo_d, 14 U_d	9 U_d, 4Mo_p, 2Mo_d	30 Mo_d, 28 U_f, 4 U_d	37 Mo_d, 33 U_f, 6 U_d	46 U_f, 34 Mo_d	49 U_f, 36 Mo_d, 2 U_d	59 U_f, 18 Mo_d, 8 U_d
	$8e_1$	$10a_1$	$13e_1$	$12a_1$	$4b_2$	$5b_2$	$15e_1$
W	11 U_d, 7 W_d, 3 W_p	6 U_d, 5 W_p, 3 W_d	33 U_f, 32 W_d, 5 U_d	40 W_d, 29 U_f, 9 U_d, 8 W_s	66 U_f, 22 W_d	51 W_d, 30 U_f, 2 U_d	55 U_f, 19 W_d, 10 U_d

Table 2.9. Molecular orbital decomposition (%) of the metal bonding orbitals of $M_2Cl_8^{2-}$ and $MUCl_8^{2-}$. MO labels are taken from Figures 2.5

The composition of the molecular orbitals involved in the metal-metal bonds is shown in Table 2.9. Since the point group of the mixed $MUCl_8^{2-}$ systems is different from that of the $M_2Cl_8^{2-}$ and $U_2Cl_8^{2-}$ systems, C_{4v} in the mixed eclipsed system compared to D_{4h} in the $M_2Cl_8^{2-}$ and $U_2Cl_8^{2-}$ eclipsed systems, the labelling of the irreps is different. The a_1 in C_{4v} corresponds to a_{1g} in D_{4h} and is the M-M σ-bonding level while δ and π bonds are in e_1/e_u symmetry. The d contributions from the Mo and W atoms in the HOMO ($11(12)a_1$) and HOMO-1 ($11(13)e_1$) in the mixed systems are roughly half of what was found for $Mo_2Cl_8^{2-}$ and $W_2Cl_8^{2-}$. The remainder of the two MOs are made up of contributions from

the U 5f orbitals, with some minor contributions from U 6d. This is in line with results from the orbital decomposition of the $MUCl_6$ systems.

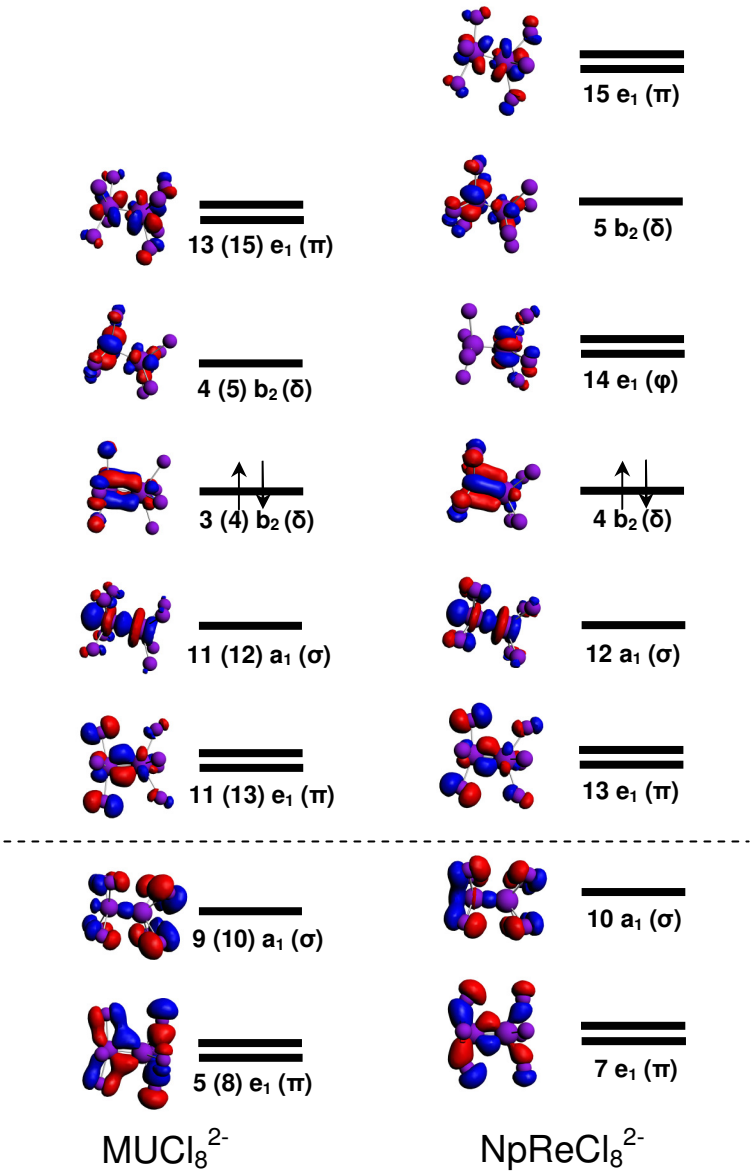

Figure 2.5. A qualitative diagram of the electronic structure of $MUCl_8^{2-}$ (M = Mo, W) and $NpReCl_8^{2-}$. The labelling of the $WUCl_8^{2-}$ and the type of bond is shown in parenthesis. Only a selection of metal-metal bonding MOs displayed below the line.

Energy decomposition analysis

The energy decomposition analysis of the $MUCl_8^{2-}$ compounds, shown in Table 2.10, resembles the $MUCl_6$ energy decompositions in that the energy terms are roughly the average of the $M_2Cl_8^{2-}$ complex energy terms. The total bonding energies of the $MoUCl_8^{2-}$ and $WUCl_8^{2-}$ molecules are -0.42 eV and -0.86 eV respectively compared to -0.82 eV, -1.83 eV and -0.05 eV for $Mo_2Cl_8^{2-}$, $W_2Cl_8^{2-}$ and $U_2Cl_8^{2-}$. The same trend is seen in the pre-relaxation energy where the mixed compounds again are the average of the three homonuclear dimers.

The Pauli repulsion energy term for the $MoUCl_8^{2-}$ complex is larger than the average of the two dimer terms, 15.58 eV for the $MoUCl_8^{2-}$ system compared to 13.08 eV for $Mo_2Cl_8^{2-}$ and 11.89 eV for $U_2Cl_8^{2-}$. It is also noticeably larger than E_P in $W_2Cl_8^{2-}$, where it is closer to the average of the two homonuclear dimers, while in the $MUCl_6$ systems the E_P term was almost identical. The difference in directionality of the a_1 MO in the UCl^{4-}, $MoCl^{4-}$ and WCl^{4-} fragments again determined the size of the electrostatic interaction. A larger E_E for the heteronuclear dimers than in the U_2 dimer was observed due to the radial extension of the a_1 in the M = Mo, W complexes along the metal-metal bond.

M	E_B	E_P+E_E	E_P	E_E	E_O	$E_O(a_1)$	$E_O(a_2)$	$E_O(b_1)$	$E_O(b_2)$	$E_O(e)$
Mo	-0.42	9.84	15.58	-5.75	-10.25	-3.56	0	-0.09	-0.03	-6.57
W	-0.86	8.62	14.88	-6.26	-9.48	-3.41	0	-0.06	-0.02	-5.98
Mo_2	-0.82	6.66	13.08	-6.42	-7.48	-2.94	0	-0.05	-0.03	-4.45
W_2	-1.83	6.07	16.12	-10.05	-7.90	-3.02	0	-0.05	-0.02	-4.80
U_2	-0.05	11.37	11.89	-0.52	-11.42	-3.41	0	-0.11	-0.01	-7.89

Table 2.10. Energy decomposition analysis of $MUCl_8^{2-}$ (small cores, eclipsed) complexes at OPBE optimized geometries (eV).

The difference in E_P is partly compensated by an orbital interaction term for $MoUCl_8^{2-}$ which is larger than for the $Mo_2Cl_8^{2-}$ complex, -7.48 eV for $Mo_2Cl_8^{2-}$ compared to -10.25 eV for $MoUCl_8^{2-}$, very close to the E_O of the $U_2Cl_8^{2-}$ (-11.42 eV). Again, this is not

observed for the $WUCl_8^{2-}$ system, where all terms are close to the average. In the breakdown of the E_O in terms of spanned irreps, all irreps in $MoUCl_8^{2-}$ are closer to $U_2Cl_8^{2-}$ than $Mo_2Cl_8^{2-}$, thus explaining the relatively high E_O term. This is not seen in the $WUCl_8^{2-}$ mixed system, something that can be partly attributed to the lower contribution from the e irrep in $WUCl_8^{2-}$ compared to the corresponding e in $MoUCl_8^{2-}$.

As in the $UMCl_6$ systems, energy decompositions were performed on the $UMCl_8^{2-}$ systems as a function of bond length, from 2.1 Å to 2.5 Å (Figure 2.6). The results are very similar to what was found for the hexachloride systems; the electronic interaction term for both the $WUCl_8^{2-}$ and the $MoUCl_8^{2-}$ systems is very close to E_E in $Mo_2Cl_8^{2-}$ and $W_2Cl_8^{2-}$.

M	E_B	E_P+E_E	E_P	E_E	E_O	$E_O(a_1)$	$E_O(a_2)$	$E_O(b_1)$	$E_O(b_2)$	$E_O(e)$
Mo	-2.19	8.07	13.86	-5.79	-10.27	-3.89	0	-0.08	0.03	-6.26
W	-0.74	9.05	15.69	-6.64	-9.79	-3.72	0	-0.06	-0.01	-6.00

Table 2.11. Energy decomposition analysis of $MUCl_8^{2-}$ (large cores, eclipsed) complexes at OPBE optimized geometries (eV)

In fact, the E_E for $MoUCl_8^{2-}$ is almost identical to the E_E in $Mo_2Cl_8^{2-}$. The Pauli repulsion energy is slightly larger in the mixed systems than in the $M_2Cl_8^{2-}$ systems but this, and the larger electrostatic interaction energy, is again compensated by a larger orbital interaction term. E_O in the $UMCl_6$ and U_2X_6 systems are very similar to each other, indicating similarity in the bonding of the two systems. The energy decomposition of $UMCl_8^{2-}$ shows the same trend, with the orbital interaction term being very similar to the $U_2Cl_8^{2-}$ calculations. Taking all of these effects into account, the total bond energy of the investigated $MUCl_8^{2-}$ systems are very close to being the average of the $U_2Cl_8^{2-}$ system and the $Mo_2Cl_8^{2-}$ and $W_2Cl_8^{2-}$ systems, as was found for the hexachloride complexes.

The effect of having large frozen cores was investigated for the $MUCl_8^{2-}$ systems. In calculations on $MUCl_6$ a significant effect was found when both metals had large cores, thus the data in Table 2.11 only show the energy decomposition of large core calculations. Again, the major change is observed in the Mo containing systems, where the U 6p and Mo 4p orbitals are included in core; the total bond energy changes from -0.42 eV to -2.19 eV, due almost entirely to the reduction in the Pauli repulsion. The large core W basis set includes all orbitals up to the 4f, thus it does not include the 5p orbitals in the core and the E_P is unaffected by the increase in size of the core in this calculation.

M	E_B	E_P	E_E	E_O
Mo	-1.77	-1.72	-0.04	-0.02
Mo_2	-0.17	-0.53	0.32	0.04
U_2	-4.98	-5.35	-1.00	1.37

Table 2.12. Comparison of energy terms as a function of core size (“large core” – “small core”) at OPBE optimized geometries. (eV)

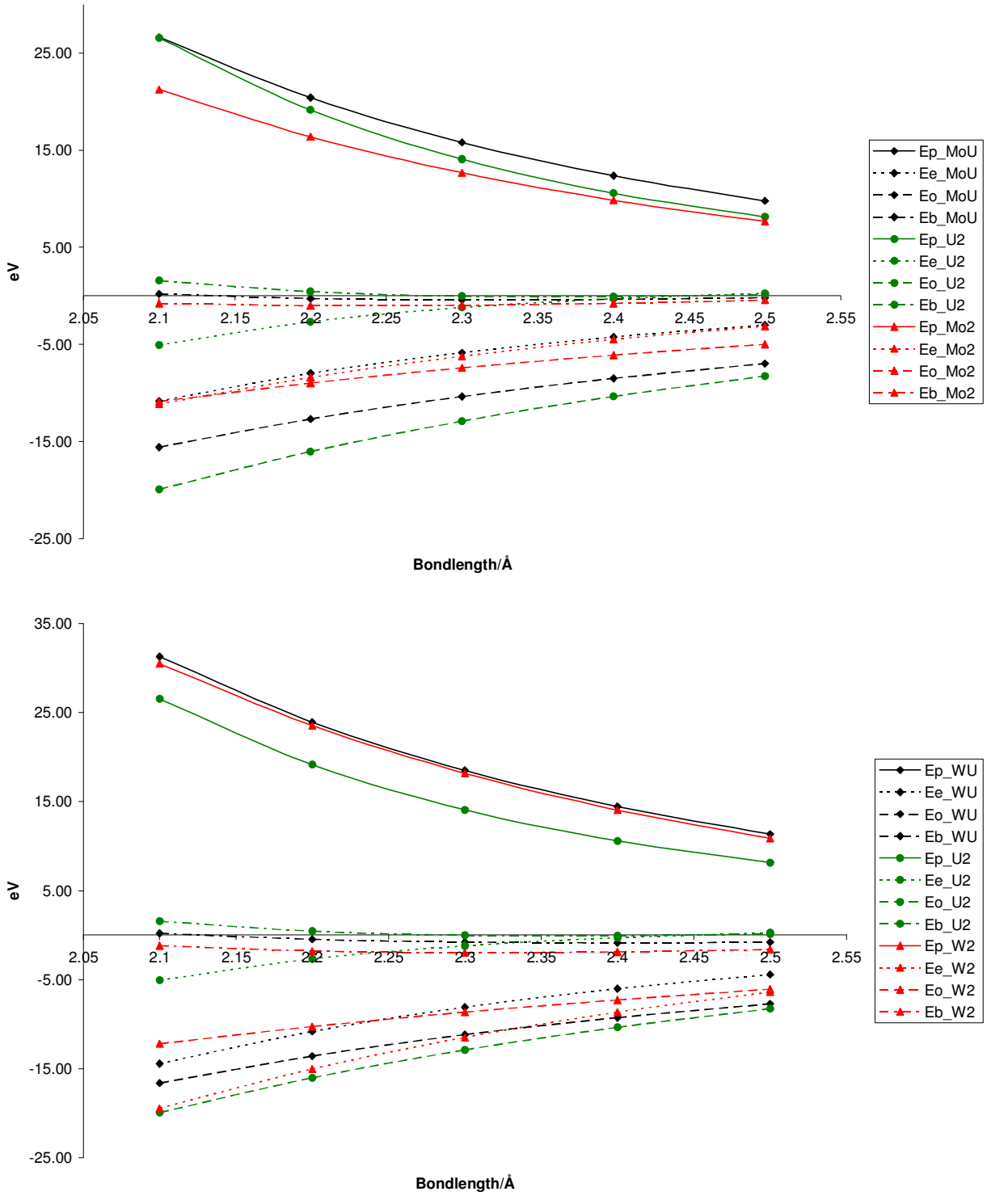

Figure 2.6. The terms of the energy decomposition analysis as a function of the U-M (M = Mo (top), W) bond length in $UMCl_8^{2-}$.

The impact of the large cores is quantified in Table 2.12, which confirms that there is a significant difference in the energy if the metal p orbitals are allowed to interact directly. The total bonding energy differs by 1.77 eV comparing the Mo and the Mo_2 systems. The effect is, as with the staggered $MUCl_6$ compounds, even more pronounced in the U_2 system, where the difference is almost 5 eV. The difference in the other energy terms is also more significant for the U_2 dimer, while they are small or almost non-existent in the Mo and Mo_2 systems.

Mayer bond orders

M	M-U	M-Cl	U-Cl
Mo	1.75	0.80	0.99
Mo_2	2.49	0.80	-
W	2.75	0.86	0.96
W_2	2.37	0.85	-
U_2	1.55	-	0.93

Table 2.13. Mayer bond orders of $MUCl_8^{2-}$ (small cores, eclipsed) complexes at OPBE optimized geometries.

The calculated Mayer bond orders are noteworthy because of the low value of the Mo-U bond, 1.75, which is quite close to the calculated $U_2Cl_8^{2-}$ (1.55) bond order but significantly lower than the bond order calculated for $MoUCl_6$, 2.82. The W-U bond order is close to 3, similar to the $WUCl_6$ bond order. The low bond orders in $MoUCl_8^{2-}$ and $U_2Cl_8^{2-}$ correspond to the results of the energy decomposition (Table 2.13) which found that these systems were the least stable. The ligand bonds are all single bonds, with the U-Cl bond stronger than the M-Cl bond, contradicting the trend from the $MUCl_6$ systems, where the M-Cl bond order was calculated to be about 1.3 compared to 0.8-0.9 in Mo and W. The U-Cl bond order remains about 1, similar to the $MUCl_6$ molecules and in line with the behaviour of the U-Cl bond distance, which remains conserved in all systems. In the mixed $MUCl_6$ systems the M-Cl bond orders were higher than the

corresponding M-Cl bond order in the M_2Cl_6 systems. This is not seen here, as the M-Cl bond orders are the same for both systems.

$NpReCl_8^{2-}$

Geometry

Moving to the right in the periodic table the Np-Re and Pu-Os eclipsed eight chlorine complexes were investigated. For clarity the optimized geometry of the Np-Re system will be discussed first, with all data being presented in Table 2.14. The reason for doing this is that to obtain a converged $PuOsCl_8^{2-}$ structure electron smearing needed to be employed, introducing some uncertainty into the final geometry.

Np-Re	Np-Cl	Re-Cl	Np-Re-Cl	Re-Np-Cl
2.20	2.58	2.36	101.3	116.4

Table 2.14. Optimized geometry of $NpReCl_8^{2-}$ (small cores, eclipsed) using OPBE (Å and degrees respectively)

The metal-metal bond in the converged geometry is quite short at 2.20 Å, significantly shorter than for the $U_2Cl_8^{2-}$, $Mo_2Cl_8^{2-}$ and $W_2Cl_8^{2-}$ systems, where the bond lengths averaged about 2.35 Å. This suggests that the δ-bonding MOs play a significant role in the geometry of this system. The Np-Cl distance though is the same as the calculated U-Cl distances in all compounds, similarly the Re-Cl distances are also in line with previous transition metal to ligand bond distances, 2.36 Å compared to 2.37 Å for Mo and W. The bond angles in this eclipsed system are those expected based on the behaviour of the $MUCl_8^{2-}$ systems; the Re-Cl bond angle is smaller than the Np-Cl bond angle, 101° (99° in $MUCl_8^{2-}$) compared to 116° (115°), but not as close to a right angle as in the $MUCl_6$ system. As in the Mo, W systems the reason is most likely the eclipsed chlorines preventing this.

Electronic structure

The electronic structure of $NpReCl_8^{2-}$ is similar to what was found for the $MUCl_8^{2-}$ systems. The doubly occupied HOMO is $4b_2$, a δ-bonding MO, due to having moved to the right in the periodic table and the $12a_1$ (HOMO-1) and $13e_1$ (HOMO-2) are a σ and π bond respectively. Again, there is no anti-bonding Cl contributions that destabilize the π MOs, thus the σ bonding MO is higher in energy than the π bonding MOs.

The orbital decomposition is shown in Table 2.15. The HOMO, $4b_2$, is a δ bonding orbital and the LUMO, $14e_1$, is a non-bonding φ orbital while the σ and π bonding MOs are $12a_1$ and $13e_1$ respectively. The LUMO, HOMO and HOMO-1 in $NpReCl_8^{2-}$ have similar compositions to the equivalent bonding MOs in $UMCl_8^{2-}$. There is slightly less actinide metal contribution and also less metal d character in the a_1 σ-bonding MO (HOMO), which consists of 37% Mo_d, 33% U_f and 6% U_d or 40% W_d, 29% U_f, 9% U_d and 8% W_s compared to 33 Np_f, 30 Re_d, 4% Np_d and 4% Re_s. A similar trend is found in the π-bonding MO, where the actinide contribution decreases from 33% to 28% to 26% in moving from $WUCl_8^{2-}$ to $MoUCl_8^{2-}$ and $NpReCl_8^{2-}$ respectively.

M	$7e_1$	$10a_1$	$13e_1$	$12a_1$	$4b_2$	$14e_1$	$5b_2$	$15e_1$
Np	7 Np_f	7 Np_d 7	26 Np_f 22	33 Np_f 30 Re_d	49 Np_f	86	46 Np_f	57 Np_f 19
	30 Re_d	Re_d 4 Re_p	Re_d 2 Np_d	4 Np_d 4Re_s	29 Re_d	Np_f	37 Re_d	Re_d 8 Np_d

Table 2.15. Molecular orbital decomposition analysis of $NpReCl_8^{2-}$ (small cores, eclipsed) at the OPBE optimized geometry.

The corresponding transition metal d orbital contribution decreases from 32%, 30% to 22% for the same systems. Looking at the δ-bonding MOs, $4b_2$ symmetry, it is a bit more difficult to make a direct comparison as the δ MOs are unoccupied in $WUCl_8^{2-}$ and $MoUCl_8^{2-}$ mixed systems. However, the contributions are quite similar, especially between the $MoUCl_8^{2-}$ and $NpReCl_8^{2-}$ systems where the actinide contribution is 46% and 49% respectively and the metal d contributions are 34% and 29%. The $4b_2$ virtual MO in

the $WUCl_8^{2-}$ system is slightly different than the other δ MOs, the U contribution of 66% is larger than in the other δ MOs and the metal d MOs contribute less, at 22%.

Energy decomposition analysis

The energy decomposition analysis (Table 2.16) shows that the total bonding energy is positive at both the optimized and at 2.25 Å, the reference Np-Re bond length, which was used to compare with previous computational work.[48] There was only a slight difference in E_B comparing the optimized geometry and the reference geometry. At both bond distances the system is unstable with positive total energies, similar to the $Np_2Cl_8^{2-}$ system but in contrast to the $Re_2Cl_8^{2-}$ system which has been shown to be stable. The orbital interaction energy in $NpReCl_8^{2-}$ decreases moving from the optimized to the standardized geometry, going from -7.54 eV to -6.69 eV, but still close to the average of the Re_2 and Np_2 system E_Os.

M	E_B	E_P+E_E	E_P	E_E	E_O	$E_O(a_1)$	$E_O(a_2)$	$E_O(b_1)$	$E_O(b_2)$	$E_O(e)$
Np	0.55	12.28	19.68	-7.40	-11.73	-3.94	0	-0.15	-0.11	-7.54
Np (2.25)	0.56	10.88	16.96	-6.08	-10.32	-3.59	0	-0.12	-0.08	-6.69
Np_2*	1.30	15.76	18.00	-2.24	-14.47	-4.15	0	-0.74	-0.83	-8.74
Re_2*	-1.42	7.32	15.75	-8.43	-8.74	-3.67	-0.01	-0.08	0.13	-5.11

Table 2.16. Energy decomposition analysis of $NpReCl_8^{2-}$, $Np_2Cl_8^{2-}$ and $Re_2Cl_8^{2-}$ (small cores, eclipsed) complexes at OPBE optimized geometry and at 2.25Å Np-Re distance (eV). *) Values taken from Cavigliasso *et al.*[48-50]

Looking at the pre-relaxation effects, E_P + E_E, there is a decrease from 12.28 eV to 10.88 eV moving to the standardized geometries, with the major difference in the Pauli repulsion energy term, which decreases from 19.68 eV to 16.96 eV. The fact that the total energy remains the same is due to the E_O and pre-relaxation energies cancelling each other out when the distance increases. E_P for the heteronuclear system is close to or larger than E_P for the Np_2 dimer; however, this is compensated by the E_E terms which are close to the Re_2 dimer electrostatic interaction terms.

There is evidence of δ-bonding in the $Np_2Cl_8^{2-}$ system in the orbital interaction term in the b_2 irrep; at -0.83 eV the term is significantly larger than what is found for the Re_2 dimer, where the interaction was positive. In the mixed $NpReCl_8^{2-}$ system some δ-bonding can be seen but it is weaker than in the Np_2 dimer.

Mayer bond orders

M	Np-Re	Np-Cl	Re-Cl
Np	2.91	0.99	0.81
Re_2	2.77	-	0.84
Np_2	1.84	0.91	-

Table 2.17. Mayer bond orders of $NpReCl_8^{2-}$ (small cores, eclipsed) at OPBE optimized geometry.

The calculated Mayer bond orders, displayed in Table 2.17, indicate that the Np-Re bond is a triple bond, with the remaining bonds being single bonds. The Np-Cl bond is slightly stronger than the Re-Cl bond, 0.99 compared to 0.81, but the difference is minor. The calculated bond orders are almost identical to the bond orders calculated for the mixed MoU complexes, with the Np-Re bond being slightly stronger, 2.91 compared to 2.75. The difference can be explained by the δ-bond participation in the Np-Re bond, seen in the slightly larger orbital interaction contribution in b_2 for $NpReCl_8^{2-}$ compared to the corresponding contribution in $MUCl_8^{2-}$. One notable feature is the increase in bond order in the mixed system compared to the Np_2 dimer, which is significantly lower at 1.84, an Np-Np double bond. The reason for this is seen in the calculated total bond energy where the Np_2 dimer had a large positive bond energy, thus the bond order is expected to be low. Re_2 on the other hand has a bonding total energy and it is expected that the heteronuclear complex would have a more bonding interaction. The Np_2 bond order is close to what was found in the U_2 system, where the calculated bond order is 1.55, indicating a similarity in bonding between the actinides.

$PuOsCl_8^{2-}$

Pu-Os	Pu-Cl	Os-Cl	Pu-Os-Cl	Os-Pu-Cl
2.29	2.58	2.34	101.3	115.4

Table 2.18. Optimized geometry of $PuOsCl_8^{2-}$ (small cores, eclipsed) using OPBE (Å and degrees respectively).

Geometry

The geometry of $PuOsCl_8^{2-}$ did not converge unless electronic smearing was employed; 0.001 Hartree in the presented calculations resulting in fractional occupations of the some of the valence MOs. In the calculated geometry (Table 2.18) the metal-metal bond is 2.29 Å, longer than what was found in the $NpReCl_8^{2-}$ system and slightly shorter than the mixed $MUCl_8^{2-}$ bond distances. The reason for this lengthening in the bond compared to the $NpReCl_8^{2-}$ system is probably the electronic smearing which places fractional occupation in anti-bonding MOs.

The Pu-Cl distance on the other hand is unaffected by the fractional valence occupations and is the same as the Np-Cl distance, 2.58 Å. The Os-Cl bond distance is slightly shorter than the Re-Cl distance and all the bond angles are very similar to the $NpReCl_8^{2-}$ angles; the Pu-Os-Cl angle is identical to the Np-Re-Cl angle and the Pu-Os-Cl and Os-Pu-Cl bond angles are different by only 1°.

Electronic structure

The electronic structure of $PuOsCl_8^{2-}$ is complicated by the fact that there are four MOs very close in energy above $4b_2$ (Table 2.19 and Figure 2.7); $8b_1$, $5b_2$, $14e_1$ and $13a_1$. This was not seen in $Pu_2Cl_8^{2-}$ where the electronic structure showed that DFT is well behaved but it has not been proven that it is single determinental. Using electronic smearing the two additional electrons in the system fractionally occupy all of these four orbitals, which

affects the metal-metal bond as some of these, dominantly f based, MOs are anti-bonding; the 0.05 electrons occupying $13a_1$ is not considered to have much effect on the bonding compared to the 0.52 electrons occupying $5b_2$, an anti-bonding MO.

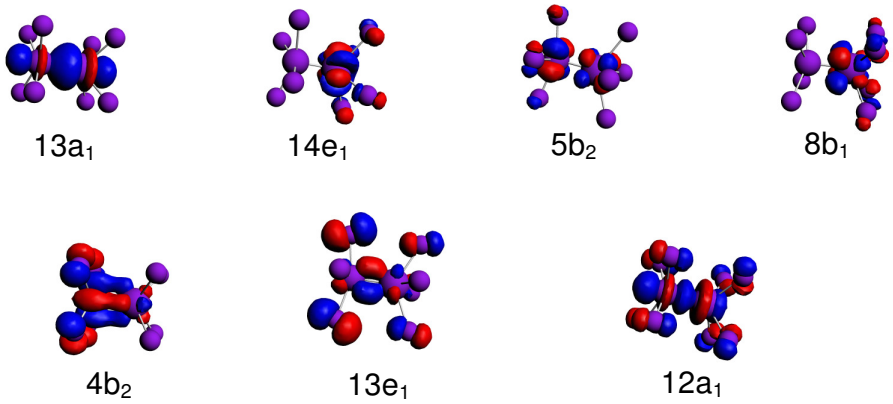

Figure 2.7 The occupied valence molecular orbitals in $PuOsCl_8^{2-}$. See Table 2.19 for their occupations.

MO	Occ.	E (eV)	Pu f	Pu d	Os d	Cl p	Type
$13a_1$	0.05	1.96	66	6	16		
$14e_1$	0.77	1.95	81			10	
$5b_2$	0.52	1.95	66		21	11	
$8b_1$	0.66	1.95	82			9	
$4b_2$	2	1.25	29		38	31	δ
$13e_1$	4	0.48	19		16	56	π
$12a_1$	2	0.11	19		30	35	σ

Table 2.19. Molecular orbital decomposition analysis of $PuOsCl_8^{2-}$ (small cores, eclipsed) at the OPBE optimized geometry.

Compared with the valence orbital compositions in the $MUCl_8^{2-}$ systems, the actinide contribution in $PuOsCl_8^{2-}$ is smaller; in the σ-bonding HOMO in both $MUCl_8^{2-}$ systems (M = Mo, W) the U contribution is *ca* 30% compared to 19% Pu contribution. Similarly,

the Pu contribution in the π-bonding MO is smaller. Compared to the valence electronic structure in $NpReCl_8^{2-}$ the actinide f contribution to the metal-metal bonds again has decreased, which is expected as the involvement of the 5f orbitals to bonding decrease moving along the actinide series, as they are increasingly stabilized.

The fractional occupations of the valence electronic structure makes an energy decomposition analysis on the mixed $PuOsCl_8^{2-}$ system less reliable than for the other systems investigated in this chapter, thus it will not be performed in the present investigation.

Mayer bond order

The Mayer bond order analysis (Table 2.20) confirms that there is a metal-metal triple bond; the calculated bond order is somewhat smaller than the bond order in $NpReCl_8^{2-}$, probably due to the electronic smearing of the bonding electrons required to obtain a converged electronic structure. The Pu-Cl and Os-Cl bonds are single bonds of approximately the same bond order as in the Np-Cl and Np-Re bonds.

M	Pu-Os	Pu-Cl	Os-Cl
Pu	2.53	0.87	0.82

Table 2.20. Mayer bond orders of $PuOsCl_8^{2-}$ (small cores, eclipsed) at the OPBE optimized geometry.

Periodic trends

The periodic trends in the energy decomposition analysis could not be investigated fully as a decomposition was not performed for $PuOsCl_8^{2-}$, thus the trends moving to the right from U to Pu are incomplete. However, some trends are seen for the $NpReCl_8^{2-}$ and the $WUCl_8^{2-}$ systems (Figure 2.8). Two energy decompositions were carried out, one with a fixed bond distance, 2.25 Å, and one at the optimized geometries.

In previous computational work on the $U_2Cl_8^{2-}$, $Np_2Cl_8^{2-}$, $W_2Cl_8^{2-}$ and $Re_2Cl_8^{2-}$ systems at 2.25 Å, the Pauli repulsion terms decreased moving to the right. The other energy terms showed different behaviour; the total bonding energy for the $M_2Cl_8^{2-}$ (M = W, Re) systems did not change significantly while for the actinide systems the total bonding energy increased moving to the right. The electrostatic interaction decreased significantly in the $M_2Cl_8^{2-}$ systems while for the actinides the electrostatic energy term did not change. Energy decompositions at the optimized geometries showed different trends; for the transition metal systems the Pauli repulsion stayed constant and the only term that changed was the electrostatic interaction. In the actinide systems the Pauli repulsion increased significantly, increasing the total bond energy even though the electrostatic and orbital interaction terms decrease.

The trend in the mixed actinide-transition metal systems at fixed geometry is the same as in the homonuclear systems; the Pauli repulsion decreases and the other energy terms increase slightly moving to the right. The reason for this could be the decrease in the radial extension of the f orbitals; the 5f orbital overlap decreases moving along the actinide series as they become more lanthanide-like in their bonding properties. The radii of the f orbitals decrease more rapidly compared to the d orbitals, which means that the change seen in the energy decomposition is mainly due to the actinide and not the transition metal. At the optimized geometry the observed trends in the mixed systems are similar to what was found in the bis-actinide systems; the Pauli repulsion increases more than the electrostatic and orbital interactions and thus the total bonding energy increases moving from $WUCl_8^{2-}$ to $NpReCl_8^{2-}$. To increase the orbital overlap and the f orbital involvement in $NpReCl_8^{2-}$ the optimized bond length is decreased compared to the $WUCl_8^{2-}$ system.

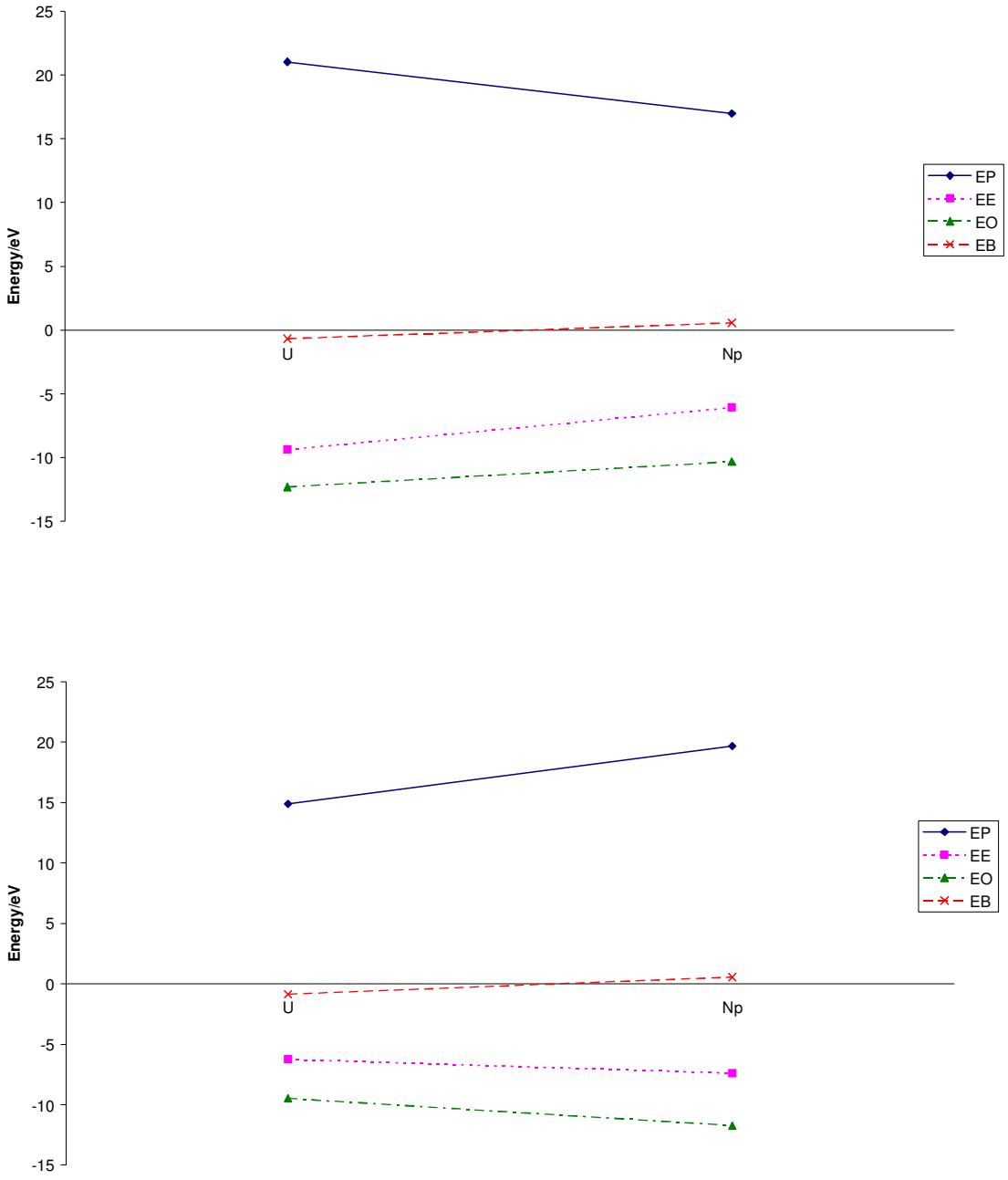

Figure 2.8. Periodic trends in the energy decomposition analysis of $WUCl_8^{2-}$ and $NpReCl_8^{2-}$ at 2.25 Å (top) and at optimized geometries

Conclusions

In this chapter different aspects of the bonding in $MUCl_6$ and $MUCl_8^{2-}$ (M = Mo, W) has been investigated. Using the Ziegler-Rauk bond decomposition analysis the total bond energy of these systems is very close to being the average of the respective M_2Cl_6 and $M_2Cl_8^{2-}$ dimer systems. This does not mean that all the energy decomposition terms behave similarly; the Pauli repulsion energy was found to be consistently higher for the mixed systems than what was found in the M_2 or U_2 homonuclear systems. This was compensated by orbital interaction terms which were more bonding in the mixed MU systems than in the pure transition metal systems, in fact being more like the U_2 systems in terms of the orbital interactions. The electrostatic interactions were found to be the average of the two homonuclear systems since the effect of the directionality of the valence a_1 MOs, so significant in the homonuclear complexes, was reduced due to the system consisting of one transition metal and one actinide fragment. It was also found that, similar to the dimer systems, it is vital to include the U 6p and the Mo 4p orbitals explicitly in the valence electronic structure as the effect of not doing so underestimates the Pauli repulsion energy significantly.

The ordering of the valence electronic structure of the mixed $MUCl_8^{2-}$ (M = Mo, W) systems is the same as what was seen in the U_2Cl_6 system, with a σ-bonding MO as the HOMO. The reason for this is that the Cl ligands do not form an anti-bonding interaction with the metal-metal bonding π MOs destabilizing the π-bonding MOs.

Moving across the actinide series to $NpReCl_8^{2-}$ the ordering in the valence electronic structure resemble what was found for the $MUCl_8^{2-}$ systems; the HOMO was a δ-bonding MO as the system contains additional valence electrons, but the ordering of the HOMO-1 and HOMO-2 is identical to the $MUCl_8^{2-}$ systems, and for the same reasons. The additional δ-bonding increases the bond strength, which was seen in the Mayer bond analysis, the energy decomposition and the relatively short metal-metal bond. The $PuOsCl_8^{2-}$ systems needed electronic smearing to obtain converged geometries and this

resulted in an electronic structure which weakened the metal-metal bonds compared to the $NpReCl_8^{2-}$ system, where the bond distances were significantly shorter than in the corresponding $U_2Cl_8^{2-}$ system. The fractional occupations in the electronic structure prevent an energy decomposition analysis being performed on $PuOsCl_8^{2-}$.

The energy decomposition and the Mayer bond order analysis trends moving from $WUCl_8^{2-}$ to $NpReCl_8^{2-}$ showed that the contracting f orbitals in the actinides decrease the orbital overlap, resulting in shorter metal-metal bond distances also for the mixed actinide-transition metal systems. Similar to the energy decomposition in the bis-actinide systems, the total bonding energy of these systems is increasing suggesting that the mixed transition metal – actinide systems are not stable.

Chapter 3

The coordination properties of plenary and lacunary Keggin phosphomolybdates to tri- and tetravalent cations

Introduction

Polyoxometallates

Polyoxometallate chemistry is a large and growing field of research, with applications in many areas of chemistry, for example oxidative catalysis, medical chemistry and separation chemistry.[65] The most general definition of polyoxometallates is that they are anionic transition metal-oxygen complexes. Polyoxometallates (POMs) were discovered by J. Berzelius in 1826 when a phosphovanadate, $[PV_{12}O_{40}]^{3-}$, was observed.[66] This discovery was followed by several other molecules belonging to the polyoxometallate family of compounds, also known today as polyoxoanions.

Polyoxometallates can be divided into two groups, heteropolyanions and isopolyanions; the general formula for heteropolyanions is $[XM_iO_j]^{n-}$ and isopolyanions have the formula $[M_iO_j]^{n-}$; X is the heteroatom, M is the transition metal addenda atom and n is the net charge of the structure. Polyoxometallate structures where M = Nb, Mo, V, W and Ta have been characterised.[67]

POMs are a diverse family of molecules and have been found in a large number of structures, some of the most common can be seen in Figure 3.1. The motif of the molecule Berzelius discovered is today called a Keggin structure, named for J.F. Keggin who characterised the molecule in 1933.[68] Similarly, there are the Anderson[69], Lindquist[70] and Wells-Dawson[71] structures just to mention a few. In addition to the

possible isomers of the mentioned structures, there are also the various POMs with substitutions in the addenda atoms and/or lacunary structures (structures missing one or more metal/oxygen units) making this a very diverse family of molecules.

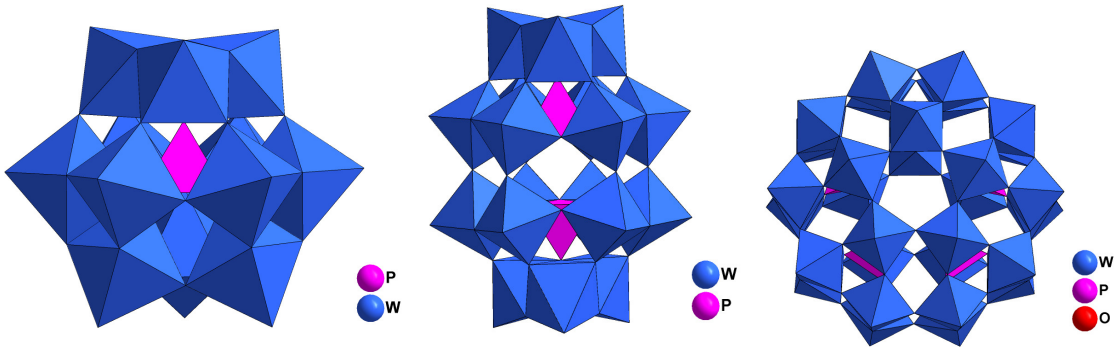

Figure 3.1. Polyhedral representation of common polyoxometallate structural motifs. The Keggin structure (left), the Dawson structure (middle) as well as the Preyssler structure (right).[72]

The principal building blocks of polyoxometallates are polyhedral [MO_n] units assembled in an edge-sharing or corner-sharing fashion. There are also a few known examples of polyoxometallate structures with face-sharing structures.[73]

Increasing computational power has allowed computational studies of polyoxometallates to appear. Much initial work was done by the group of Bénard.[74, 75] Later the groups of Bridgeman[76-82] and Poblet [72, 75, 83-98] continued to investigate the electronic structure, bonding and chemical properties of various POMs. These studies produced several papers, all investigating polyoxometallate systems of increasing size, from simple molybdate and tungstenate oxides to Dawson polyanions.

There exist several challenges in investigating polyoxometallates computationally: the total number of atoms in the systems, in particular the number of transition metal atoms, and the highly anionic nature of the complexes. This is the main reason much of the work

has been carried out on high symmetry structures, such as the Keggin structure (T_d). The early studies by Bénard[74, 75] used the Hartree-Fock formalism but subsequent investigations have used DFT. The advantage of DFT is the scaling of the computational cost, where DFT produces better results than HF methods at similar costs. This aspect is particularly important when it comes to heavier elements such as transition metals and large systems.

The most commonly investigated heteropolyanion is the Keggin structure, $XM_{12}O_{40}^{3-}$. It has been found that the DFT optimized geometry accurately matches the experimental geometry.[72] There are four different types of oxygen atoms in the Keggin structure, presented in Figure 3.2: the terminal oxygen atoms, O_t, double bonded to the transition metal addenda atoms; the tetrahedral oxygen atoms, O_P, inside the cage of the POM connecting the ionic core of the molecule with the clathrate cage; lastly, two types of bridging oxygen atoms, O_b and O_b' binding the addenda atoms together, distinguished by their bond angles, 125° and 152° for O_b and O_b' respectively.

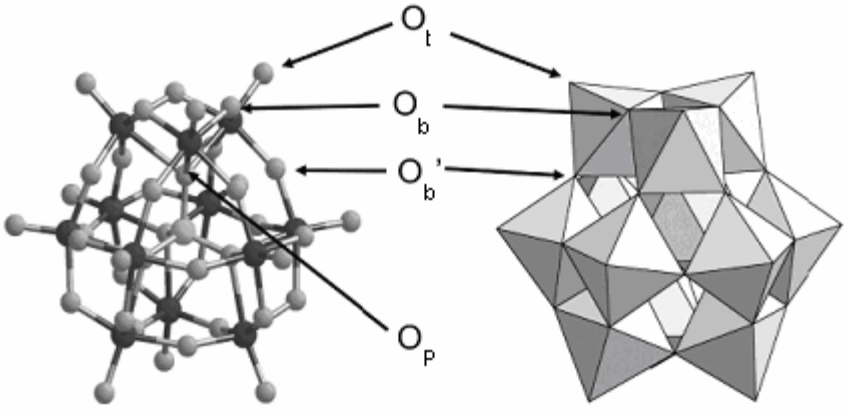

Figure 3.2. Labelling of the oxygen atoms in the Keggin structure, $XM_{12}O_{40}^{3-}$.[72]

The terminal oxygen-metal bond is consistently overestimated computationally compared to experimental data by, on average, 0.05 Å. This difference in theoretical geometry and

experimental results is due to the charge and size of the investigated complex, where large, highly charged complexes produce large discrepancies.[99]

The electronic structure of polyoxometallates is relatively simple; all bonds consist of M d – O p orbital admixtures. The computational investigations of Bridgeman *et al.* produced DFT calculations demonstrating that the occupied orbitals are delocalised over all oxo ligands and exhibit little or no interaction with the unoccupied metal d orbitals.[99, 100] It is often the case with heteropolyanions that the transition metal – oxygen structure surrounding the heteroatom can be viewed as a cage encapsulating a charged central heteroatom complex, the clathrate model, which has been confirmed in a study by Poblet *et al.* on the relative stability of α/β-Keggin isomers. Investigations have shown this to be a valid model for the Wells-Dawson structures as well.[89] Supporting the clathrate model is also the fact that the delocalised electrons form closed "loops", similar to conjugated interactions in aromatic systems, along the cage bridging bonds. The loops are clearly visible in orbital representations of polyoxometallates and it has been shown that they provide a stabilising influence on the POM structure.[72]

Polyoxometallate species are usually found in solution. Most computational studies however have been carried out in the gas phase. The Keggin anion has been studied using the continuum solvent model and results from these studies show that the molecular orbitals are significantly stabilized in solution, with the LUMO being the most stabilised.[90] For a proper understanding of the bonding between polyoxometallates and metals solvent effects would probably have to be included, however the computational cost prevents the use of a solvent model in the present study as the symmetry is greatly reduced compared to the tetrahedral point group of the Keggin structure.

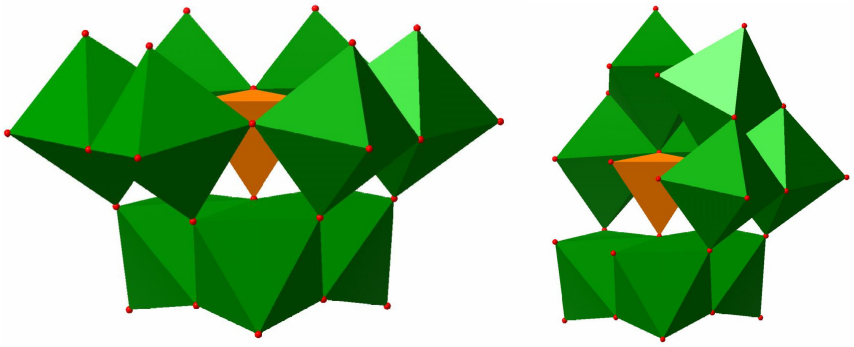

Figure 3.3. Polyhedral representation of two different tri-lacunary Keggin structures

One of the most interesting properties of polyoxometallates is the ability to remove metal and oxygen atoms to produce cavities in the structure, as seen in Figure 3.3, which has ramifications for the coordination behaviour of the resulting lacunary polyoxometallate.[101] Having available terminal oxygen atoms in a cavity enables the POM to coordinate to large atoms or molecules, such as actinides. It has been well established that uranyl preferentially coordinates additional ligands in the equatorial plane.[102] It is thought that the interactions between metals and polyoxometallates are almost purely ionic and that the behaviour of POMs is similar to hydroxides as far as the coordinating metal is concerned. This is why POMs have attracted much attention for use as potential separating agents for fission products, particularly for lanthanide and actinide separation.[103-105]

Much experimental work has been carried out investigating the coordination of polyoxometallates to actinides, lanthanides and transition metals. Gaunt *et al.* have synthesised and characterised several polyoxometallate systems with various metals coordinated to them. In particular, different phosphomolybdate systems have been investigated as analogues of the corresponding tungstenate systems, which are more stable. Among the complexes produced is a neptunyl-POM complex[106], and there have been investigations of the properties of trivalent lacunary phosphomolybdate across the lanthanide series,[107] and into the coordination of Zr and Hf to Keggin anions and lacunary Keggin anions[108].

Aim

Chapter 3 consists of three sub-projects; the first is an investigation of the mono-lacunary bis-phosphomolybdate $X[PMo_{11}O_{39}]_2^{10-}$ (X = Ce, Th) systems, both of which have been characterized experimentally.[109] The coordination in these systems is via the unsaturated oxygen atoms at the lacunary site. Th was used as it is a tetravalent actinide and Ce is the corresponding lanthanide. In both of these systems, but particularly in Th, the amount of metal d contributions were investigated in the computational studies, the reason being that the early actinides can resemble transition metals in their coordination behaviour.

The second project was to investigate the coordination of the Keggin phosphomolybdate anion, $[PMo_{12}O_{40}]^{3-}$, to Zr^{4+} and Hf^{4+}, two group 4 d^0 transition metal cations, and to La^{3+} and Lu^{3+}, two lanthanides at opposite ends of the lanthanide series. The transition metals were chosen because of the difference in structure observed experimentally between the Zr and Hf POM systems. Are there differences in the geometry or the electronic structure already on coordination to the mono Keggin phosphomolybdate structure? La and Lu were investigated to try to determine why the trivalent lanthanides prefer di-lacunary Keggin coordination while the Zr and Hf cations prefer mixed lacunary-plenary Keggin systems. After the initial investigation into the single Keggin complexes the corresponding di-Keggin systems were investigated.

The third project was an investigation of the coordination in the $X[PMo_{11}O_{39}][PMo_{12}O_{40}]^{6-}$ (X = Zr, Hf) mixed systems. These complexes are the main experimental result of the phosphomolybdate studies performed at the Centre for Radiochemistry Research at Manchester University. The experimental coordination behaviour of Zr and Hf is very different in these systems; the Zr cation coordinates in a mixed lacunary-plenary Keggin complex using the lacunary cavity oxygen atoms, while in the Hf cation the coordination does not occur through the lacunary site but instead uses four bridging oxygen atoms at each of the POM moieties.[108] The lacunary site was found

to coordinate a NH_4^+ counter ion. This was not an expected outcome and computational investigations of the reason for the Hf^{4+} behaviour compared to that of Zr^{4+} is one of the main areas of investigation in this chapter.

Computational details

The ADF2006.01b suite of programs was used with standard ADF frozen core basis sets (O.1s, N.1s, P.2p, Mo.3d, Hf.4d, W.4d, Ce.4d, Lu.4d, La.4d and Th.5d respectively) in all calculations.[110] The zero order regular approximation (ZORA)[18] accounted for scalar relativistic effects in all calculations. The Mulliken, Hirshfeld and Voronoi charge analysis schemes were used for analysis of the computational results. Mulliken populations were also investigated.

In the $X[PMo_{11}O_{39}]_2^{10-}$ (X = Ce, Th) calculations crystal structures were used as input structures for the geometry optimizations and the starting geometry was symmeterised to allow the calculations to be performed in C_2 symmetry. The basis sets were of TZP quality for O and P and TZ2P for Ce and Th. The local density approximation (LDA)[26] was used in the geometry optimization and the energy decomposition was performed using the PBE[32] exchange-correlation functional. The integration grid parameter was set to 4 and the default ADF convergence criteria for the SCF and geometry was used.

The $X[PMo_{12}O_{40}]^{3-}$ and $X[PMo_{12}O_{40}]_2^{6-}$ (X = Zr^{4+}, Hf^{4+}, La^{3+} and Lu^{3+}) systems were optimized and investigated in C_{2v} and D_{2h} symmetry respectively. The PBE exchange-correlation functional was employed for both the electronic structure calculations and the energy decomposition calculations. The grid parameter was again set to 4 and the ADF default convergence criteria employed.

In order to investigate the bonding in $NH_4[Hf(PMo_{11}O_{39})(PMo_{12}O_{40})]^{5-}$ more thoroughly, a similar complex, $X(PMo_{11}O_{39})(PMo_{12}O_{40})^{6-}$ (X = Zr, Hf), was used for comparison in which Hf and Zr were coordinated to the unsaturated oxygen atoms in the lacunary

cavities. Experimentally obtained crystal structures were used for the $X(PMo_{11}O_{39})(PMo_{12}O_{40})^{6-}$ structures and no additional geometry optimizations were performed.[108] The four hydrogen atoms in the $NH_4[X(PMo_{11}O_{39})(PMo_{12}O_{40})]^{5-}$ (X = Zr, Hf) complexes were optimized to chemically sensible positions around the nitrogen atom in the lacunary cavity. Frozen core, triple-ζ quality basis sets with one polarization function (TZP) were employed for Mo, Zr and P and DZP was used for H, O and N. In the $X(PMo_{11}O_{39})(PMo_{12}O_{40})^{6-}$ and $NH_4[X(PMo_{11}O_{39})(PMo_{12}O_{40})]^{5-}$ (X = Zr, Hf) systems the LDA was employed for the single point electronic structure calculations and the energy decomposition. The grid parameter was set to 3 with default ADF convergence criteria for the SCF and the geometry. Electronic smearing had to be introduced to converge the electronic structure. The electronic structures were considered converged if the smearing was less than 0.004 Hartree. Non-integer occupations can occur but the computational results do not change significantly on further reductions of the smearing.

The Ziegler-Rauk energy decomposition analysis scheme in ADF was used to study interactions between fragments.[62] The metal cations (Hf, Zr, Ce, Th, La, Lu) were used as one fragment and the POM as the other. For the mixed $X(PMo_{11}O_{39})(PMo_{12}O_{40})^{6-}$ (X = Zr, Hf) systems three fragments were used: X^{4+} + $PMo_{12}O_{40}^{3-}$ + $PMo_{11}O_{39}^{7-}$, splitting the POM ligands into two fragments.

Results

$X[PMo_{11}O_{39}]_2^{10-}$ (X = Ce, Th)

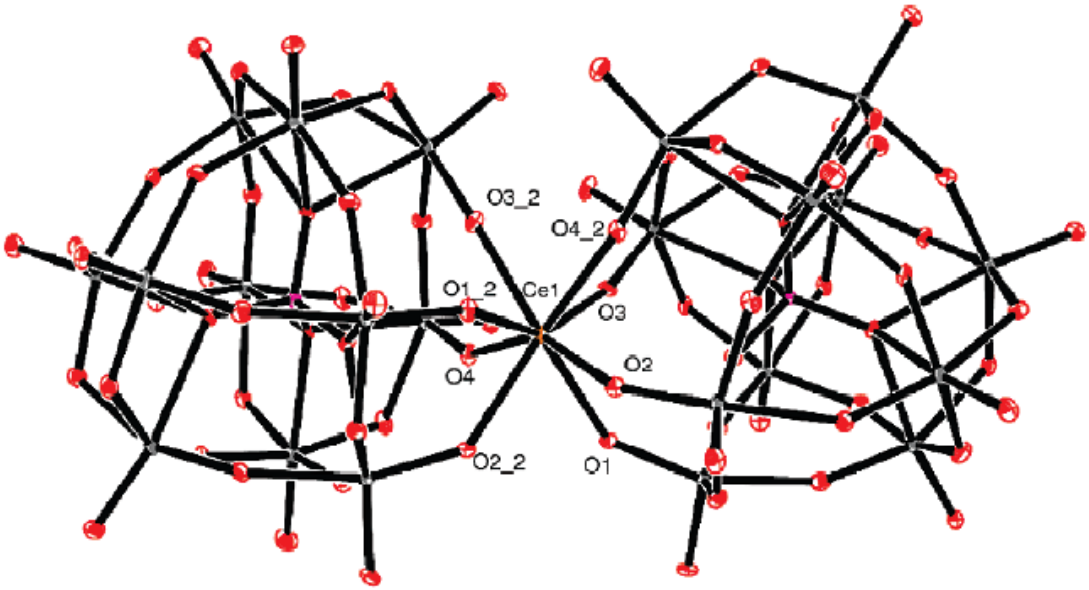

Figure 3.4. Ortep (50 % probability) representation of $Ce[PMo_{11}O_{39}]_2^{10-}$.[109] The labelling of the atoms has been used in the computational investigation.

Geometry

The dimer lacunary Keggin phosphomolybdate complexes, $X[PMo_{11}O_{39}]_2^{10-}$ (X = Ce, Th), have been characterised experimentally (Figure 3.4) and the crystal structure geometry is as expected; the metal cations in both the Ce and Th structures are coordinated to the unsaturated oxygen atoms in the lacunary defect of the polyanions.[109] This is in contrast to the mixed Hf lacunary-plenary Keggin complexes which will be discussed later in this chapter, where the coordination is mediated through the bridging oxygen atoms.[111]

The results of the geometry optimization of $X[PMo_{11}O_{39}]_2^{10-}$ ($X = Ce^{4+}$, Th^{4+}) are similar; the structure expands from what was found experimentally. The experimental coordination sphere, consisting of two long and two short O-X bonds, is preserved.[107, 112] The bond lengths increase for all Ce-O bonds (Table 3.1) compared to experiment, which is also seen for the Th-O bonds.

It is not surprising that the structures expand in the computational study. The input systems are highly charged anions, with a net charge of -10. The result of the high charge is an expansion of the structure to allow the electron density to fill a larger volume and minimize electron-electron repulsion effects.

The DFT geometry overestimates the average bond lengths by 0.06 Å in the Ce system and 0.04 Å in the Th system. The shorter Ce-O bond distances are the result of Ce^{4+} having a smaller ionic radius than Th^{4+}, 0.97 Å compared to 1.05 Å. Both the "long" and "short" bond distances show lengthening compared with experiment; the difference between the calculated "short" bond distance and the experimental one is 0.05 Å for Ce and 0.06 Å for the Th complex. For the long bond distance the differences are 0.07 Å and 0.04 Å for the Ce and Th complexes respectively.

	Distances (Å)	
Bond	$[Ce(PMo_{11}O_{39})_2]^{10-}$	$[Th(PMo_{11}O_{39})_2]^{10-}$
M^{4+}-O1	2.34 *2.44*	2.42 *2.44*
M^{4+}-O2	2.37 *2.41*	2.45 *2.48*
M^{4+}-O3	2.31 *2.37*	2.39 *2.44*
M^{4+}-O4	2.31 *2.33*	2.38 *2.46*
'Short' M^{4+}-O Average	2.31 *2.35*	2.39 *2.44*
'Long' M^{4+}-O Average	2.36 *2.42*	2.44 *2.47*
Average	2.33 *2.39*	2.41 *2.45*

Table 3.1. X^{4+}-O(terminal) bond length for $[Ce(PMo_{11}O_{39})_2]^{10-}$ and $[Th(PMo_{11}O_{39})_2]^{10-}$. Calculated values in italics.[109]

Atomic charge analysis

The atomic charges in the $X[PMo_{11}O_{39}]_2^{10-}$ (X = Ce, Th) systems were analysed using the Mulliken, Hirshfeld and Voronoi charge decomposition schemes (Table 3.2). Due to the nature of the charge schemes the atomic charges are unlikely to match the formal charges of the atoms.

The charge analysis shows that all four oxygen atoms involved in the coordination of the metal ions have approximately the same charge; the variation between O1-O4 is very small for each of the charge decomposition schemes. The Mulliken charges on the oxygen atoms in the Ce complex is *ca* -0.60 compared to -0.63 for the oxygen atoms in the Th system. The Th Mulliken charge is a slightly more positive, 1.67 compared to 1.56. Thus, the Mulliken charges show that the atomic charges are slightly larger for the Th system than the corresponding Ce system.

This trend is also seen for the Hirshfeld atomic charges; the difference in atomic charges on O1-O4 is very small, with -0.28 on average for both the Ce and Th systems. Again, the Th ion is more positive than the Ce ion, 0.67 compared to 0.54. The Voronoi oxygen atomic charges are also, as with the Mulliken and Hirshfeld scheme, very close to each other. However, in the Voronoi scheme the system with the highest atomic charges is $Ce[PMo_{11}O_{39}]_2^{10-}$, with oxygen charges of about -0.27 and a Ce charge of 0.32. In contrast the atomic charges on the Th complex oxygen atoms are about -0.26 and the Th charge is 0.27, indicating a larger outflow of charge from the Ce Voronoi cell than the Th cell, indicating a greater electron density contribution from the Ce in the Ce-O region.

All of the charge decomposition schemes show a significant difference in atomic charges on the oxygen atoms compared to the Ce and Th cations, indicating a highly ionic bonding in the system. The ionicity of the bond was probed using Mulliken orbital populations, which were investigated for any populated d or f metal orbitals.

	Mulliken		Voronoi		Hirshfeld	
	Ce	Th	Ce	Th	Ce	Th
O1	-0.59	-0.62	-0.27	-0.26	-0.27	-0.28
O2	-0.60	-0.62	-0.26	-0.25	-0.28	-0.28
O3	-0.59	-0.63	-0.27	-0.26	-0.28	-0.28
O4	-0.60	-0.63	-0.26	-0.25	-0.27	-0.28
M	1.56	1.67	0.32	0.27	0.54	0.67

Table 3.2. Partial atomic charges for $[Ce(PMo_{11}O_{39})_2]^{10-}$ and $[Th(PMo_{11}O_{39})_2]^{10-}$ at the LDA optimized geometries.

Mulliken population analysis

The Mulliken populations (Table 3.3) were investigated to gain further insights into the type of bonding which dominates the $X[PMo_{11}O_{39}]_2^{10-}$ (X = Ce, Th) complexes. Formally the occupations of the X tetravalent cations is $ns^0np^0(n\text{-}1)d^0(n\text{-}2)f^0$ with n = 6 for Ce and n = 7 for Th. There have been speculations on the involvement of the metal d contributions to the bonding in polyoxometallate systems. There is a higher than expected population of the metal d and f orbitals suggesting that these orbitals are involved in the bonding.

However, investigating the atomic orbital contributions to the 51 highest occupied MOs does not show any significant metal d or f contributions to the bonding. The oxygen p populations remain high for both systems, indicating relatively small participation from the oxygen p orbitals in any covalent interactions. These two results, taken together with the atomic charge analysis, indicate that there is little Ce or Th covalency in the two systems.

	Ce				Th			
	s	p	d	f	s	p	d	f
O1	1.91	4.65	0.03	0.0	1.90	4.69	0.03	0.0
O2	1.91	4.67	0.03	0.0	1.90	4.70	0.03	0.0
O3	1.91	4.65	0.03	0.0	1.90	4.70	0.03	0.0
O4	1.91	4.67	0.03	0.0	1.90	4.70	0.03	0.0
M	0.03	0.12	1.25	1.05	0.24	0.01	1.28	0.81

Table 3.3. PBE Mulliken population analysis of $[Ce(PMo_{11}O_{39})_2]^{10-}$ and $[Th(PMo_{11}O_{39})_2]^{10-}$ at their LDA optimized geometries.

Energy decomposition

The lacunary polyoxometallates, $[PMo_{11}O_{39}]_2^{14-}$, forms one fragment and the metal cation, Ce^{4+} or Th^{4+}, the second in the energy decomposition. Given the high charge of the systems it is expected that a large electrostatic interaction will dominate the energy decomposition (Table 3.4), which was confirmed in the calculations where it constituted the major part of the total bonding energy, -129.08 eV for $Ce[PMo_{11}O_{39}]_2^{10-}$ and -128.34 eV for $Th[PMo_{11}O_{39}]_2^{10-}$. In comparison the Pauli repulsion is very small, 9.51 eV for the Ce and 9.98 eV for the Th system. The pre-relaxation effects, E_{Pre}, are very similar for both complexes and are completely dominated by E_E.

The difference in E_B stems from the orbital interaction term, E_O, with the Ce complex having a larger E_O, -51.90 eV compared to -45.93 eV for the Th complex. The electrostatic interaction term, along with the results of the Mulliken populations and the atomic charge analysis, indicate that the bond is highly ionic. The larger orbital interaction term found for $Ce[PMo_{11}O_{39}]_2^{10-}$ than in the $Th[PMo_{11}O_{39}]_2^{10-}$ system can not be assigned unequivocally to a particular kind of interaction. However, the charge and

population analysis above indicates that the Ce/Th POM interactions are highly ionic in nature.

	$[Ce(PMo_{11}O_{39})_2]^{10-}$	$[Th(PMo_{11}O_{39})_2]^{10-}$
E_E	-129.08	-128.34
E_P	9.51	9.98
E_{Pre}	-119.57	-118.35
E_O	-51.90	-45.93
E_B	-171.47	-164.28

Table 3.4. PBE energy decomposition data (eV) for $[Ce(PMo_{11}O_{39})_2]^{10-}$ and $[Th(PMo_{11}O_{39})_2]^{10-}$ at their optimized (LDA) geometries.

Mayer bond order analysis

The Mayer bond orders were used as an indicator for the strength of the O-M^{4+} bonds. What is seen from Table 3.5 is the relatively low calculated bond orders with no bond order exceeding 0.5 for any of the O-M^{4+} bonds. The Ce-O bonds are calculated to be, on average, somewhat stronger than the Th-O bonds, with the O4-Ce bond being particularly strong. The calculated bond length for Ce-O4 is the shortest of all the calculated Ce-O bonds, 2.33 Å compared to the calculated average of 2.39 Å.

	Ce	Th
O1	0.37	0.39
O2	0.42	0.37
O3	0.39	0.39
O4	0.47	0.38
Average	0.41	0.38

Table 3.5. PBE Ce/Th–O Mayer Bond Orders of $X[PMo_{11}O_{39}]_2^{10-}$ (X = Ce, Th) at their LDA optimised geometries.

The Th-O4 calculated distance is 2.46 Å, higher than the calculated average of 2.45 Å. This implies that the relatively short Ce-O4 bond distance affects the resulting bond order. The distance effect is not seen looking at the atomic charges and the Mulliken populations of O4, where it has similar values as the other oxygen atoms. On average the Ce-O bond order is higher than for the corresponding Th-O bond, which was also seen in the energy decomposition analysis where the total bond energy was 7 eV larger for the Ce complex than in the Th complex.

$X[PMo_{12}O_{40}]^{3-}$ and $X[PMo_{12}O_{40}]_2^{6-}$ ($X = Zr^{4+}$, Hf^{4+}, La^{3+}, Lu^{3+})

Geometry

The structure of $X[PMo_{12}O_{40}]^{3-}$ ($X = Zr^{4+}$, Hf^{4+}, La^{3+}, Lu^{3+}) was investigated in C_{2v} symmetry and the $X([PMo_{12}O_{40}]^{3-})_2$ complexes were investigated in the staggered D_2 symmetry formation.[108] $X[PMo_{11}O_{39}]^{7-}$ ($X = Zr^{4+}$, Hf^{4+}, La^{3+}, Lu^{3+}) mono-lacunary structures were investigated but the geometries failed to converge.

Since both systems were constrained by symmetry restrictions, movement of the metal ion was only possible towards or away from the Keggin anion.

	Distances (Å)				
	Zr	Hf	La	Lu	Exp. Zr [108]
$X[PMo_{12}O_{40}]^{3-}$	1.93	1.96	2.24	2.06	N/A
$X([PMo_{12}O_{40}]^{3-})_2$	2.13	2.15	2.48	2.29	2.16

Table 3.6. Calculated bond lengths for O_b'-X in the $X(PMo_{12}O_{40}^{3-})_2$ and $XPMo_{12}O_{40}^{3-}$ (X = Zr^{4+}, Hf^{4+}, La^{3+}, Lu^{3+}) metal-Keggin systems. See Figure 3.2 for definition of O_b'.

The optimized M-O_b' bond lengths for Zr and Hf are very similar (Table 3.6) 1.93 Å and 1.96 Å respectively for the $X[PMo_{12}O_{40}]^{3-}$ (X = Zr^{4+}, Hf^{4+}) complexes. There are no experimental data available for the $X[PMo_{12}O_{40}]^{3-}$ (X = Zr^{4+}, Hf^{4+}) complexes so a comparison will be made using the bis-Keggin systems for which data exist, albeit for the mixed lacunary-plenary system.[108] The X-O_b' distance in the plenary moiety should still be a valid comparison for this calculation. Thus the optimized geometry produced slightly shorter X-O_b' bond distances for both the Zr and Hf complexes compared with experiment, 2.13 Å and 2.15 Å for the $X([PMo_{12}O_{40}]^{3-})_2$ (X = Zr^{4+}, Hf^{4+}) complexes respectively compared to 2.16 Å experimentally. The geometry of the optimized Zr-Keggin structures can be seen in Figure 3.5.

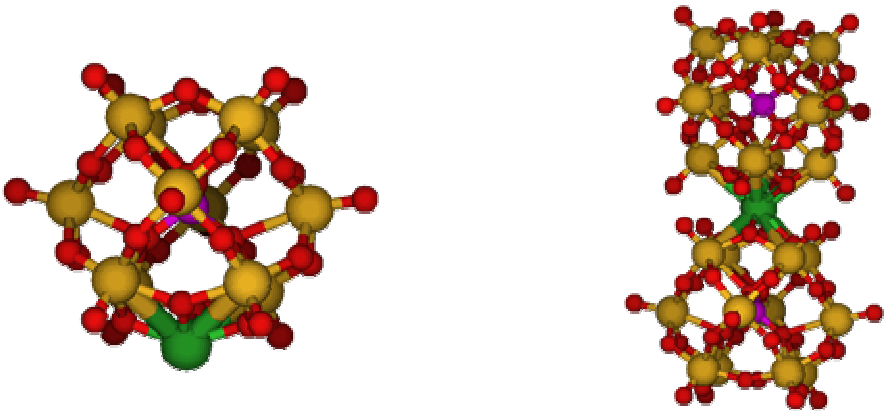

Figure 3.5. Optimized structure of $Zr^{4+}[PMo_{12}O_{40}]^{3-}$ (left) and $Zr^{4+}([PMo_{12}O_{40}]^{3-})_2$ (right)

The optimized $X[PMo_{12}O_{40}]^{3-}$ (X = La^{3+}, Lu^{3+}) bond distances are significantly longer than the corresponding X = Zr, Hf complexes, 2.24 Å and 2.06 Å for La and Lu respectively. The reason for this is the smaller charge of the lanthanide cations, +3 compared to +4, which makes for weaker bonds. The X-O_b' distance decreases moving across the lanthanides due to the lanthanide contraction; the bond distance decrease is 0.19 Å, close to the 0.17 Å decrease in ionic radius moving from La to Lu. The radial contraction increases the charge density of the lanthanide cations, thus increasing the

electrostatic interactions between the polyanion and the metal. In the optimized bis-Keggin structures the bond distance is the greatest for La, 2.48 Å, and then decreases to 2.29 Å for Lu.

The O_b'-X bond distances in $X[PMo_{12}O_{40}]^{3-}$ for X = Zr, Hf is shorter than for X = La, Lu. The proximity of the Zr and Hf cations forces the Mo atoms closest to the coordination site outwards, expanding the Keggin structure from its optimized Mo-Mo geometry of 3.70 Å to 3.94 Å and 3.95 Å when coordinated with Zr and Hf respectively (Table 3.7). The corresponding Lu and La systems also expand but not by the same amount, to 3.83 Å for La and 3.92 Å for Lu.

In the $X([PMo_{12}O_{40}]^{3-})_2$ structures there is less metal cation induced Mo-Mo expansion around the coordination site than in the single Keggin complexes, with the difference for the X = Zr, Hf systems being only *ca* 0.1 Å and about the same for X = Lu. For X = La there is a slightly smaller expansion of the Mo cage, only 0.05 Å. As in the $X[PMo_{12}O_{40}]^{3-}$ system this difference originates in the difference in geometry, with the X = Zr, Hf, Lu systems having similar X-O_b' bond distances and X = La having a longer bond distance. The $X[PMo_{12}O_{40}]^{3-}$ ($X = Zr^{4+}$, Hf^{4+}, La^{3+}, Lu^{3+}) structure is not something that would be seen experimentally due to the low coordination number that $[PMo_{12}O_{40}]^{3-}$ can provide and the structures have not been found experimentally.

	Distances (Å)				
	Zr	Hf	La	Lu	Keggin*
$X[PMo_{12}O_{40}]^{3-}$	3.94	3.95	3.83	3.92	3.70
$X([PMo_{12}O_{40}]^{3-})_2$	3.80	3.81	3.75	3.82	3.70

Table 3.7. Mo-Mo distances in the optimized $X(PMo_{12}O_{40}^{3-})_2$ and $XPMo_{12}O_{40}^{3-}$ ($X = Zr^{4+}$, Hf^{4+}, La^{3+}, Lu^{3+}) complexes. *) The Mo-Mo distance along the Mo-O_b'-Mo axis in uncoordinated $[PMo_{12}O_{40}]^{3-}$

The calculated Mo-Mo bond lengths (Table 3.7) again indicate that the +4 formal charge of the transition metals compared to the +3 of the lanthanides makes a difference as both Zr and Hf have the same behaviour. The differences in behaviour among the lanthanides are likely the results of the lanthanide contraction, making the charge density increase for the smaller Lu ion, further polarising the Mo atoms and the bridging oxygen atoms thus strengthening the X-POM bond. That this is the case should be seen also in the bond energy decomposition discussed below.

Atomic charge analysis

Hirshfeld and Voronoi atomic charge decomposition analysis were performed on all the complexes.[102] The bridging oxygen atoms, O_b and O_b', the metal cation, X, and the four Mo metal atoms closest to the coordination site were investigated. The charges for O_b and O_b' were very similar and are presented as one charge, O_b.

The result of the Hirshfeld charge analysis performed on the $X[PMo_{12}O_{40}]$ and $X([PMo_{12}O_{40}]^{3-})_2$ (X = Zr, Hf, La, Lu) systems is shown in Table 3.8 and the corresponding Voronoi charge decomposition in Table 3.9. The calculated atomic charges are contrasted with atomic charges in regions of the clathrate cage far removed from the coordination site in order to investigate the influence of the metal ion X. These values are presented in parenthesis.

Hirshfeld charge analysis

The Hirshfeld atomic charge analysis yields cation charges of 0.92 and 0.99 in $X[PMo_{12}O_{40}]^{3-}$ compared to 0.43 and 0.51 in $X([PMo_{12}O_{40}]^{3-})_2$ for X = Zr^{4+}, Hf^{4+}. The charges in the $X([PMo_{12}O_{40}]^{3-})_2$ complexes are roughly half of what is found in the $X[PMo_{12}O_{40}]^{3-}$ complexes. In the corresponding La and Lu complexes the charge drop in moving from $X[PMo_{12}O_{40}]^{3-}$ to $X([PMo_{12}O_{40}]^{3-})_2$ is 0.89 to 0.47 and 0.84 to 0.44. The

reason for this drop is the addition of a second Keggin ligand. The addition of a second $[PMo_{12}O_{40}]^{3-}$ anion allows more electron density to be transferred to the trivalent (or tetravalent) cation.

The charge of the bridging oxygen atoms coordinating the X cations is identical for the Zr and Hf systems, -0.32, and somewhat more negative for the lanthanide systems; -0.34 and -0.32 for $LaPMo_{12}O_{40}$ and $La([PMo_{12}O_{40}])_2^{3-}$ and -0.37 and -0.34 for the corresponding Lu complexes. The charges of the Mo atoms in closest proximity to the metal cations are very similar, *ca* 0.80 for all systems investigated. The Lu complex has slightly more positive Mo atoms, 0.83 and 0.82 for the $X[PMo_{12}O_{40}]^{3-}$ and $X([PMo_{12}O_{40}]^{3-})_2$ complexes respectively, corresponding to charge being transferred to the more negative O_b in that system. The Hirshfeld charge analysis also shows that there is relatively little difference in the charge of the atoms closest to the coordination site compared with the charge of atoms on other sites in the cage; the delocalised electronic structure in the clathrate cage effectively evens out the electronic charge between different parts of the structure.

	Zr	Hf	La	Lu	Δ_{Ln}
$PMo_{12}O_{40}$					
O_b	-0.32 (-0.28)	-0.32 (-0.28)	-0.34 (-0.28)	-0.37 (-0.30)	0.03
$Mo_{closest}$	0.81 (0.82)	0.80 (0.82)	0.79 (0.80)	0.83 (0.84)	-0.04
X	0.92	0.99	0.89	0.84	0.05
$(PMo_{12}O_{40})_2$					
O_b	-0.32 (-0.30)	-0.32 (-0.30)	-0.32 (-0.30)	-0.34 (0.32)	0.02
$Mo_{closest}$	0.79 (0.79)	0.78 (0.79)	0.78 (0.77)	0.82 (0.81)	-0.04
X	0.43	0.51	0.47	0.44	0.03

Table 3.8. Hirshfeld charge analysis of selected atoms in $X(PMo_{12}O_{40}^{3-})_2$ and $XPMo_{12}O_{40}^{3-}$ ($X = Zr^{4+}$, Hf^{4+}, La^{3+}, Lu^{3+}). Reference charges appear in parenthesis. Δ_{Ln} is calculated as the difference in charge between the La complex and the Lu complex: Q_{La}-Q_{Lu}

The Hirshfeld decomposition for $X(PMo_{12}O_{40}^{3-})_2$ and $XPMo_{12}O_{40}^{3-}$ (X = La, Lu) suggests that the Lu system is similarly charged to the La system and the calculated difference, Δ_{Ln}, is very small. However, some conclusions about the trends across the lanthanides can still be drawn; the La ion is more positively charged than Lu, which, as described earlier, is a result of the Lu having a higher charge density and thus inducing more charge polarization in the surrounding atoms in the coordination sphere.

Voronoi charge analysis

The Voronoi charge analysis (Table 3.9) shows that the $X[PMo_{12}O_{40}]^{3-}$ metal cation charges vary from 0.82 for Zr to 0.90, 0.65 and 0.73 for Hf, La and Lu respectively. The cation charges in the corresponding $X([PMo_{12}O_{40}]^{3-})_2$ complexes are 0.40, 0.48, 0.24 and 0.35. The metal charges can be divided into two groups, Zr and Hf in one group and the lanthanides a second. The transition metal charges are consistently *ca* 0.2 more positively

charged, reflecting the difference in formal charge of the metals, with the tetravalent transition metals being more positively charged than the trivalent lanthanides, as for the Hirshfeld charges. The charges change when the bis-Keggin complexes are formed, where the cation Voronoi charges are approximately halved same as was seen for the Hirshfeld charges. The reason for this drop is also the same; more electron density is available to be located on the metal cation with two Keggin ligands.

	Zr	Hf	La	Lu	Δ_{Ln}
$PMo_{12}O_{40}$					
O_b	-0.31 (-0.28)	-0.32 (-0.27)	-0.32 (-0.29)	-0.36 (-0.30)	0.04
$Mo_{closest}$	0.80 (0.80)	0.80 (0.80)	0.81 (0.80)	0.84 (0.83)	-0.03
X	0.82	0.90	0.65	0.73	-0.08
$(PMo_{12}O_{40})_2$					
O_b	-0.32 (-0.30)	-0.32 (-0.30)	-0.31 (-0.30)	-0.34 (-0.31)	0.03
$Mo_{closest}$	0.81 (0.80)	0.80 (0.80)	0.80 (0.80)	0.84 (0.83)	-0.04
X	0.40	0.48	0.24	0.35	-0.11

Table 3.9. Voronoi charge analysis of selected atoms in $X(PMo_{12}O_{40}^{3-})_2$ and $XPMo_{12}O_{40}^{3-}$ ($X = Zr^{4+}$, Hf^{4+}, La^{3+}, Lu^{3+}). Reference charges appear in parenthesis. Δ_{Ln} is calculated as the difference in charge in the La complex and the Lu complex: Q_{La}-Q_{Lu}

The Voronoi charges of the bridging oxygen atoms are, as with the Hirshfeld charges, similar for all the systems, at *ca* -0.32. The O_b coordinating to Lu has slightly more negative charges, -0.36 in $X[PMo_{12}O_{40}]^{3-}$ and -0.34 in $X([PMo_{12}O_{40}]^{3-})_2$. These larger charges affect the Mo charges for the Lu systems as well, where the most positively charged Mo atoms are found, 0.84 compared to 0.80-0.81 in the other systems. It is likely that the higher Voronoi charges in the Lu systems result from Lu having a higher charge density than La, leading to stronger electrostatic interactions and thus higher charges. The O_b charges are more negative compared with the clathrate reference charges which show

that additional electron density from the metal cations is transferred to the coordinating oxygen atoms.

Energy decomposition analysis

The complexes were divided into two fragments: $X + [PMo_{12}O_{40}]^{3-}$ or $X + ([PMo_{12}O_{40}]^{3-})_2$ ($X = Zr^{4+}$, Hf^{4+}, La^{3+}, Lu^{3+}) depending on the system investigated. There are potentially several ways of dividing the systems into fragments depending on what properties are investigated. In the present study the cation – polyanion interactions were the target for investigation and thus treating the systems as two fragments make analysing the interaction energies easier. However, as both fragments are highly charged the Coulombic interactions between the two fragments will be significant in these calculations.

$X[PMo_{12}O_{40}]^{3-}$ ($X = Zr^{4+}$, Hf^{4+}, La^{3+}, Lu^{3+})

The members of the two classes of cations show similar behaviour in the bond energy decomposition analysis (Table 3.10), both in the individual energy terms but also in the total bonding energy. The electrostatic and Pauli terms of the decomposition for Zr and Hf are very similar to each other, -43.24 eV and 17.15 eV in the $Zr^{4+}[PMo_{12}O_{40}]^{3-}$ system compared to -43.38 eV and 15.89 eV in the $Hf^{4+}[PMo_{12}O_{40}]^{3-}$. The Pauli repulsion energy of the $Hf^{4+}[PMo_{12}O_{40}]^{3-}$ system is 1.5 eV smaller than the equivalent energy in the Zr system and if the orbital interaction term, E_O, is included in the analysis of the two Keggin systems, then this accounts for the 4.61 eV difference in total energy, E_B. In the $La^{3+}[PMo_{12}O_{40}]^{3-}$ and $Lu^{3+}[PMo_{12}O_{40}]^{3-}$ systems E_E and E_P are also very similar, it is noticeable though that $Lu^{3+}[PMo_{12}O_{40}]^{3-}$ has a *ca* 1.3 eV higher E_E than $La^{3+}[PMo_{12}O_{40}]^{3-}$, which is expected because of the higher charge density of the Lu cation. A similar difference is not seen for the Zr and Hf systems, where the difference in E_E is only 0.1 eV. The pre-relaxation effects ($E_E + E_P$) are smaller for the Lu than the La system.

	$X^{n+}[PMo_{12}O_{40}]^{3-}$				$X^{n+}([PMo_{12}O_{40}]^{3-})_2$			
(eV)	Zr^{4+}	Hf^{4+}	La^{3+}	Lu^{3+}	Zr^{4+}	Hf^{4+}	La^{3+}	Lu^{3+}
E_E	-43.24	-43.38	-31.30	-32.63	-61.46	-62.01	-43.90	-44.59
E_P	17.15	15.89	11.40	10.57	13.48	12.80	8.86	7.68
E_O	-52.95	-57.43	-21.79	-24.56	-56.77	-54.73	-24.00	-24.12
E_B	-80.31	-84.92	-42.80	-46.63	-104.75	-103.94	-59.04	-61.03

Table 3.10. Energy decomposition at optimized geometries for the $X[PMo_{12}O_{40}]^{3-}$ and $X([PMo_{12}O_{40}]^{3-})_2$ ($X = Zr^{4+}$, Hf^{4+}, La^{3+}, Lu^{3+}) systems.

The difference in E_E between the transition metals and lanthanides, is significant, more than 10 eV. This is caused by the difference in formal charge, with the +4 charge of the Zr and Hf cations producing stronger electrostatic interactions than the +3 lanthanide cations. The significant difference in E_O of about 30 eV between the Zr, Hf and the La, Lu systems indicates that the electronic structure of the Hf/Zr $X^{4+}[PMo_{12}O_{40}]^{3-}$ systems changes more than for the La/Lu $X^{3+}[PMo_{12}O_{40}]^{3-}$ systems when the total wave function is allowed to relax. Higher ionicity in the lanthanide complexes than in the transition metal complexes produces this difference in E_O as the electronic structure of a highly ionic system changes relatively little. This is demonstrated by the fact that the metal atomic charges change more for the transition metals, from +4 in the uncoordinated metal fragment to the calculated Mulliken and Hirshfeld charges in Tables 3.8 and 3.9, than for the lanthanides. Thus the bonding interactions were found to be more covalent for the X = Zr^{4+}, Hf^{4+} systems than the X = La^{3+}, Lu^{3+} systems.

$X([PMo_{12}O_{40}]^{3-})_2$ ($X = Zr^{4+}$, Hf^{4+}, La^{3+}, Lu^{3+})

The $X([PMo_{12}O_{40}]^{3-})_2$ ($X = Zr^{4+}$, Hf^{4+}, La^{3+}, Lu^{3+}) systems follow the same energy decomposition trends as the $X[PMo_{12}O_{40}]^{3-}$ systems. E_E for the Zr and Hf bis-Keggin systems are very similar and E_P is also equally large for the two systems, 13.48 eV and

12.80 eV for Zr and Hf respectively. For the $X[PMo_{12}O_{40}]^{3-}$ systems Zr has the larger orbital interaction energy, -56.77 eV compared to -54.73 eV for the Hf system. In the E_B however, the small difference in E_O is compensated by the pre-relaxation energy, resulting in both $Zr^{4+}([PMo_{12}O_{40}]^{3-})_2$ and $Hf^{4+}([PMo_{12}O_{40}]^{3-})_2$ having almost the same total energy. Comparing these results with the $X[PMo_{12}O_{40}]^{3-}$ (X = Zr, Hf) energy decompositions the decrease in total energy of about 20 eV is almost exclusively the result of E_E, demonstrating that a second polyanion stabilises the complex considerably compared to a single Keggin ligand. It is interesting to note that E_P decreases for both transition metal systems when adding an extra $[PMo_{12}O_{40}]^{3-}$ unit as a result of the X-O_b bond distance increasing in $X[PMo_{12}O_{40}]^{3-}$ (X = Zr, Hf).

The pre-relaxation energy terms differ in the lanthanide $X([PMo_{12}O_{40}]^{3-})_2$ (X = La^{3+}, Lu^{3+}) complexes. This difference mirrors the result obtained for the $X([PMo_{12}O_{40}]^{3-})$ systems, both in the trends (Lu having a more binding pre-relaxation energy) and in terms of the absolute difference in energy. The E_O terms for the La and Lu systems are virtually identical, 24.00 eV compared to 24.12 eV, and rather similar to the single Keggin systems. Thus, as in the Zr and Hf $X[PMo_{12}O_{40}]^{3-}$ systems the character of the bonding interaction appears the same in moving from the single Keggin system to the bis-Keggin system. E_B for the $Lu^{3+}([PMo_{12}O_{40}]^{3-})_2$ system is slightly stronger than for the corresponding La system, -61.03 eV compared to -59.04 eV. The source of this difference is found in the pre-relaxation term, where the higher charge density of the Lu results in a stronger electrostatic interaction.

The electrostatic interactions are larger for the $X([PMo_{12}O_{40}]^{3-})_2$ (X = Zr^{4+}, Hf^{4+}) systems than for the $X([PMo_{12}O_{40}]^{3-})_2$ (X = La^{3+}, Lu^{3+}) systems, the difference being about 20 eV, twice as large as in the $X[PMo_{12}O_{40}]^{3-}$systems. This increased difference is explained by the increased charge of the fragments in the calculation, $[PMo_{12}O_{40}]_2^{6-}$ compared to $[PMo_{12}O_{40}]^{3-}$. There is no corresponding increase in the difference in the E_O for the $X([PMo_{12}O_{40}]^{3-})_2$ (X = La^{3+}, Lu^{3+}) systems. In fact the E_O terms are relatively unchanged

when moving from a $X[PMo_{12}O_{40}]^{3-}$ to a $X([PMo_{12}O_{40}]^{3-})_2$ system, indicating that the major changes in the bonding are electrostatic in origin.

The main difference between the lanthanide and transition metal systems continues to be the E_E and E_O terms, which together constitute the bulk of the difference in energy between the two families of complexes. The reason for the difference in E_E is the difference in formal charge of the X = Zr, Hf and X = La, Lu systems. Again the lanthanides display only relatively small differences in the electronic structure on bonding with the POM while there are larger changes in the transition metal-POM electronic structure, resulting in larger E_O interaction terms. Thus there are more covalent character in the interaction between the metal cation and the $[PMo_{12}O_{40}]^{3-}$ ligands for the transition metals than for the lanthanides.

The Lu complexes are shown to have a slightly stronger bond than the La complexes, indicating a stronger ionic interaction. The difference is relatively small, 3.83 eV for $X[PMo_{12}O_{40}]^{3-}$ ($X = La^{3+}$, Lu^{3+}) and 1.99 eV for $X([PMo_{12}O_{40}]^{3-})_2$ ($X = La^{3+}$, Lu^{3+}), and is a result of the lanthanide contraction with Lu having a higher charge density than La. The difference in energy between $Zr^{4+}[PMo_{12}O_{40}]^{3-}$ and $Hf^{4+}[PMo_{12}O_{40}]^{3-}$ is 4.61 eV, and is 0.81 eV in the corresponding bis-Keggin complexes. However, in relative terms these differences are not significant compared to the differences found for the lanthanide complexes.

Mulliken population analysis

The Mulliken net orbital populations are used in the present study as a measure of which orbitals are involved in the bonding. The size of the d population in the X cations is used to indicate how covalent the bonding in the system is. Formally the cations investigated, Zr^{4+}, Hf^{4+}, La^{3+} and Lu^{3+}, have no d orbital population, thus all electrons populating the d orbitals are donated by surrounding atoms (Table 3.11).

	Zr	Hf	La	Lu
$X[PMo_{12}O_{40}]^{3-}$	1.97	1.57	1.07	1.12
$X([PMo_{12}O_{40}]^{3-})_2$	1.80	2.31	1.55	1.87

Table 3.11. Net Mulliken populations of the X d orbitals ($X = Zr^{4+}$, Hf^{4+}, La^{3+}, Lu^{3+})

The electrons populating the d orbitals are donated from the O_b p and s orbitals. This indicates some degree of covalency in the interaction. In $X[PMo_{12}O_{40}]^{3-}$ ($X = Zr^{4+}$, Hf^{4+}) the d population is 1.97 and 1.57 for Zr and Hf respectively and for the corresponding $X([PMo_{12}O_{40}]^{3-})_2$ systems the population is 1.80 and 2.31. Based on these Mulliken populations it is clear that there is some overlap between O_b p orbitals and X d orbitals which would indicate some degree of covalency, similar to what was seen in the Ce and Th lacunary Keggin complexes above. The shift in which cation has the highest d orbital population is probably not too significant as this result is very qualitative. An inspection of the d orbital AO contributions to the individual X bonding MOs, however, could not find any significant contributions.

The lanthanide d orbital populations of the $X[PMo_{12}O_{40}]^{3-}$ and $X([PMo_{12}O_{40}]^{3-})_2$ complexes are all, with one exception, smaller than what is found for the transition metal d orbitals. The E_O was significantly larger for the Zr and Hf complexes and the population analysis supports the conclusion that there is a more covalent transition metal – polyanion bond compared to the lanthanide – polyanion bond.

It is difficult to draw any conclusions from the Mulliken populations on which of the lanthanides are more ionic in their interactions with the POM ligands. In the $X[PMo_{12}O_{40}]^{3-}$ complexes the d orbital populations are virtually identical while for the $X([PMo_{12}O_{40}]^{3-})_2$ complexes the Lu d population is very high, 1.87, comparable with the Zr and Hf d populations. This would appear to contradict the conclusion of higher

ionicity in the Lu-POM bond. It is possible, however, that the higher charge density of the Lu in the $Lu^{3+}([PMo_{12}O_{40}]^{3-})_2$ complex attracts extra charge which computationally is assigned to the d orbitals or that Lu, being the element just to the left of Hf, displays some transition metal like behaviour resulting in high d populations.

$X[PMo_{11}O_{39}][PMo_{12}O_{40}]^{6-}$ ($X = Zr^{4+}$, Hf^{4+})

Recent studies into the coordination of phosphomolybdate polyoxometallates with Zr and Hf cations have revealed differences in the preferential coordination of the two metal ions. The Zr complex coordinates in a mixed $Zr[PMo_{11}O_{39}][PMo_{12}O_{40}]^{6-}$ complex, with the coordinating oxygen atoms being bridging oxygen atoms and unsaturated oxygen atoms in the lacunary cavity. Both of these structures are different from previously discovered phosphotungstenate complexes where coordination to Hf and Zr cations preferentially occurs in the lacunary sites. The Hf mixed lacunary-plenary phosphomolybdate Keggin complex is particularly interesting due to the fact that coordination occurs completely through the O_b atoms instead of in the lacunary cavity.

The aim of this investigation into the $X[PMo_{11}O_{39}][PMo_{12}O_{40}]^{6-}$ (X = Zr, Hf) complexes (Figure 3.6) is to study these systems and try to find if there are any differences in the bonding characteristics compared to the $NH_4[X(PMo_{11}O_{39})(PMo_{12}O_{40})]^{5-}$ systems (Figure 3.7). These systems will be referred to as Zr, Hf for $X[PMo_{11}O_{39}][PMo_{12}O_{40}]^{6-}$ (X = Zr, Hf) and NH_4-Zr, NH_4-Hf for $NH_4[X(PMo_{11}O_{39})(PMo_{12}O_{40})]^{5-}$ ($X = Zr^{4+}$, Hf^{4+}) in all tables of this section. The main focus of this investigation will be on the energy decomposition analysis of the complexes, with additional information to be found in the various charge analysis schemes and the geometry optimizations carried out.

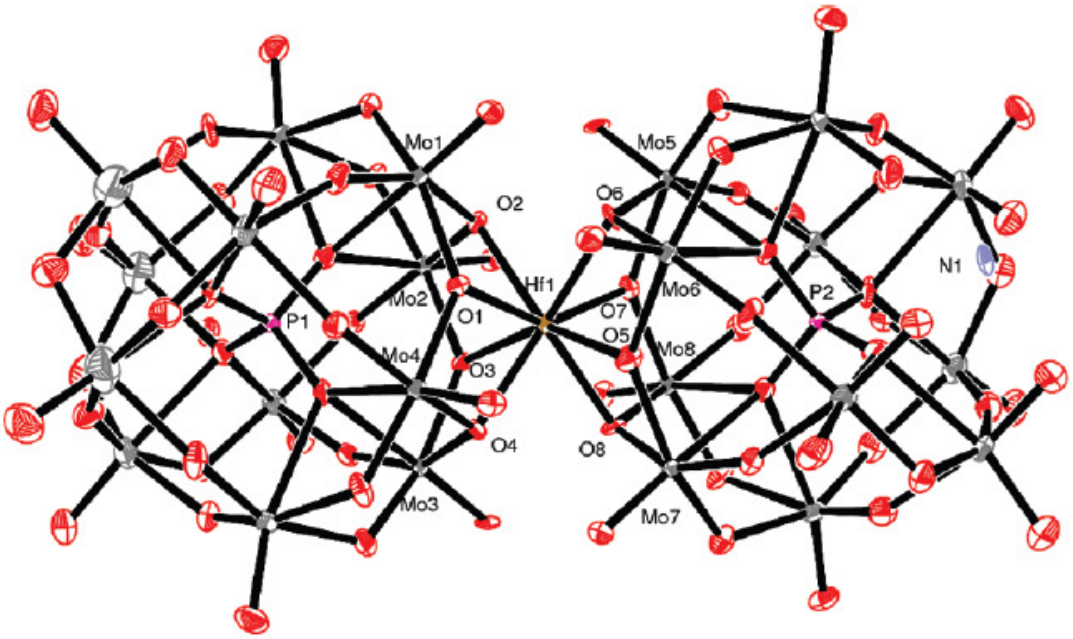

Figure 3.6. Ortep (50 % probability) representation of $Hf[PMo_{11}O_{39}][PMo_{12}O_{40}]^{6-}$, with the nitrogen atom of the ammonium cation seen in the lacunary cavity. For the corresponding Zr^{4+} complex the coordination takes place with four bridging oxygen atoms (O_b) and the lacunary cavity (Figure 3.7).[109]

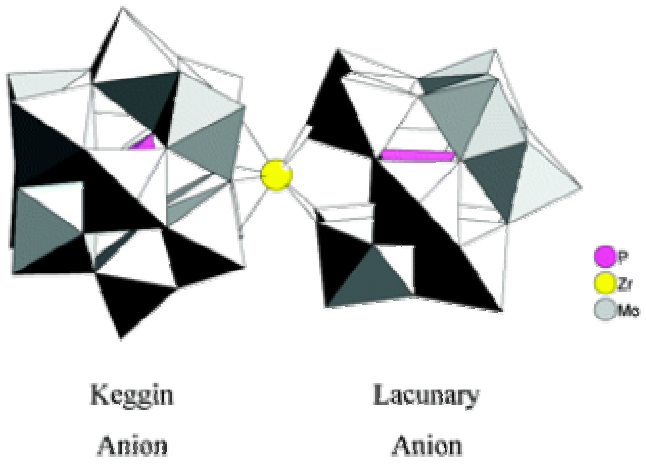

Figure 3.7. The experimental crystal structure of $Zr[PMo_{11}O_{39}][PMo_{12}O_{40}]^{6-}$ [108]

Energy decomposition

eV	$Zr^{@}$	Hf^{*}	NH_4-Zr	NH_4-Hf
E_E	-85.26	-86.25	-	-
E_P	15.32	15.36	-	-
E_{Pre}	-69.94	-70.89	-	-
E_O	-46.93	-46.43	-	-
E_B	-116.87	-117.32	-	-

Table 3.12. The energy decomposition analysis of Hf/Zr systems using a three fragment division of the molecule: $PMo_{12}O_{40}^{3-}$ + $PMo_{11}O_{39}^{7-}$ (and NH_4^+ where necessary) + $metal^{4+}$ $^{@}$) Smearing: 0.0006 *) Smearing: 0.0009

Energy decomposition calculations on the $NH_4[X(PMo_{11}O_{39})(PMo_{12}O_{40})]^{5-}$ (X = Zr, Hf) systems have been attempted but the calculations proved difficult to converge and were abandoned. However, calculations show that the $X[PMo_{11}O_{39}][PMo_{12}O_{40}]^{6-}$ systems are very similar when it comes to the bonding interactions with the X = Hf, Zr metal cations: in these systems the difference in bonding energy is less than 0.5 eV. Not unexpectedly the electrostatic interaction is the dominant term of the total energy, -85.26 eV for X = Zr and -86.25 eV for X = Hf. The orbital interaction terms for the two investigated complexes are virtually identical, -46.93 eV compared to -43.43 eV, but it is difficult to determine from the energy decomposition analysis if it is a covalent or ionic interaction and further investigations of the atomic charges and the Mulliken populations are presented.

Atomic charge analysis

The Mulliken atomic charge analysis of the $X[(PMo_{11}O_{39})(PMo_{12}O_{40})]$ test complexes show that the Zr cation is more charged than the Hf cation, 1.95 compared to 1.55 (Table 3.13). This is also true for $NH_4[Zr(PMo_{11}O_{39})(PMo_{12}O_{40})]^{5-}$ with a Zr charge of 1.77 compared to 0.60 in $NH_4[Hf(PMo_{11}O_{39})(PMo_{12}O_{40})]^{5-}$. In

$NH_4[Hf(PMo_{11}O_{39})(PMo_{12}O_{40})]^{5-}$ and $NH_4[Zr(PMo_{11}O_{39})(PMo_{12}O_{40})]^{5-}$ the coordinating oxygen atoms of the plenary Keggin fragment (O1-O4) are more charged than the corresponding lacunary fragments (O5-O8). Also, the atomic charges of the $X[(PMo_{11}O_{39})(PMo_{12}O_{40})]$ (X = Zr, Hf) test systems are consistently more negative by almost 0.1.

The Voronoi and Hirshfeld schemes provide different results compared with the Mulliken scheme on the charges for the metal cations, with the Hf atom being more charged than Zr; 0.47 and 0.52 for Zr and Hf respectively using the Voronoi scheme and 0.55 and 0.59 for the Hirshfeld scheme. For both $X[(PMo_{11}O_{39})(PMo_{12}O_{40})]$ systems the charges on all coordinating oxygen atoms on the same fragment are very similar regardless of the metal atom.

The main conclusion drawn from the atomic charge decompositions is that the very large differences in atomic charge found on the metal cations and the coordinating oxygen atoms show that the bonding is highly ionic, something that was already suggested in the energy decomposition analysis. Also, changing the coordination from a mixed $X[(PMo_{11}O_{39})(PMo_{12}O_{40})]$ system to a $NH_4[X(PMo_{11}O_{39})(PMo_{12}O_{40})]^{5-}$ system lowers the charge of the metal cations in all decomposition schemes.

	Mulliken				Voronoi				Hirshfeld			
	$Zr^{\#}$	$Hf^{?}$	NH_4-Zr^{x}	NH_4-Hf^{x}	$Zr^{\#}$	$Hf^{?}$	NH_4-Zr^{x}	NH_4-Hf^{x}	$Zr^{\#}$	$Hf^{?}$	NH_4-Zr^{x}	NH_4-Hf^{x}
O1	-0.92	-0.91	-0.84	-0.79	-0.35	-0.35	-0.33	-0.29	-0.35	-0.35	-0.33	-0.30
O2	-0.86	-0.85	-0.80	-0.75	-0.32	-0.32	-0.32	-0.29	-0.33	-0.33	-0.31	-0.28
O3	-0.92	-0.91	-0.84	-0.78	-0.35	-0.35	-0.33	-0.29	-0.31	-0.32	-0.33	-0.29
O4	-0.89	-0.88	-0.80	-0.75	-0.34	-0.34	-0.33	-0.30	-0.35	-0.35	-0.31	-0.29
O5	-0.82	-0.81	-0.84	-0.78	-0.27	-0.27	-0.33	-0.28	-0.27	-0.27	-0.33	-0.29
O6	-0.82	-0.82	-0.80	-0.74	-0.26	-0.27	-0.33	-0.29	-0.27	-0.27	-0.32	-0.28
O7	-0.82	-0.81	-0.84	-0.78	-0.27	-0.27	-0.34	-0.29	-0.27	-0.27	-0.34	-0.29
O8	-0.82	-0.82	-0.81	-0.75	-0.26	-0.27	-0.34	-0.29	-0.27	-0.27	-0.33	-0.28
M	1.95	1.55	1.77	0.60	0.47	0.52	0.40	0.24	0.55	0.59	0.43	0.27

Table 3.13. Atomic charges on atoms around the coordinated metal atom. $^{\#}$) Smearing: 0.003 $^{?}$) Smearing 0.004 ^{x}) Smearing: 0.001

Mulliken population analysis

	Zr[#]				Hf[?]			
	s	p	d	f	s	p	d	f
O1	2.00	4.89	0.03	0	2.00	4.89	0.03	0
O2	2.01	4.81	0.03	0	2.01	4.81	0.03	0
O3	2.00	4.89	0.03	0	2.00	4.89	0.03	0
O4	2.01	4.85	0.03	0	2.01	4.85	0.03	0
O5	2.05	4.73	0.03	0	2.05	4.73	0.03	0
O6	2.04	4.75	0.03	0	2.04	4.75	0.03	0
O7	2.05	4.73	0.03	0	2.05	4.73	0.03	0
O8	2.04	4.75	0.03	0	2.04	4.75	0.03	0
M	0.31	0.18	1.56	0	0.50	0.23	0.69	14.04

Table 3.14. $X[PMo_{11}O_{39}][PMo_{12}O_{40}]$ (X = Zr, Hf) Net Mulliken populations of atoms close to the M coordination site. [#]) Smearing: 0.003 [?]) Smearing 0.004

To further investigate the bonding interactions of the $NH_4[X(PMo_{11}O_{39})(PMo_{12}O_{40})]^{5-}$ and the $[X(PMo_{11}O_{39})(PMo_{12}O_{40})]^{5-}$ systems the Mulliken atomic orbital populations were investigated (Table 3.14). The formal orbital populations of the metal cations in these systems are $ns^0np^0(n\text{-}1)d^0$, n = 5 for Zr^{4+} and $ns^0np^0(n\text{-}1)d^0(n\text{-}2)f^{14}$, n = 6 for Hf. The Mulliken population analysis shows that the bonding interaction between the oxygen atoms and the metal cations occurs between O 2p and 4d/5d atomic orbitals for Zr/Hf systems respectively.

The Mulliken population analysis in Table 3.15 reveals a significantly higher s population in NH_4-Hf compared to NH_4-Zr, 1.6 and 0.8 respectively. The d and f orbitals are populated for both Zr and Hf. The increase in f orbital population above the formal value is small, only 0.20 for Zr and 0.32 for Hf.

	NH_4-Zr [x]				NH_4-Hf [x]			
	s	p	d	f	s	p	d	f
O1	2.01	4.80	0.03	0	2.01	4.74	0.03	0
O2	2.02	4.74	0.03	0	2.02	4.69	0.03	0
O3	2.02	4.79	0.03	0	2.02	4.73	0.03	0
O4	2.02	4.74	0.03	0	2.02	4.70	0.03	0
O5	2.01	4.79	0.03	0	2.02	4.73	0.04	0
O6	2.02	4.75	0.04	0	2.02	4.69	0.04	0
O7	2.01	4.80	0.03	0	2.02	4.73	0.03	0
O8	2.02	4.76	0.03	0	2.02	4.69	0.03	0
M	0.80	0.29	0.95	0.2	1.62	0.31	1.14	0.32

Table 3.15. $NH_4[X(PMo_{11}O_{39})(PMo_{12}O_{40})^{5-}]$ (X = Zr, Hf) Net Mulliken populations of atoms close to the M coordination site [x]) Smearing: 0.001

The d population of the metals are *ca* 1 for all the Zr and Hf systems, with the highest d population found in the $Zr[PMo_{11}O_{39}][PMo_{12}O_{40}]^{6-}$ complex, 1.56 (Table 2.14). The net d populations indicate that the bonding is covalent. As in the Ce and Th complexes, MOs contributing to these d populations were looked for but the AO d contributions were very small and spread over a large number of MOs, none of which contained d contributions of more than 2%. This, together with the results from the energy decomposition and the atomic charge analysis, all indicate that there are very ionic interactions in these systems.

Mayer bond order analysis

The calculated O-X Mayer bond orders (Table 3.16) are consistently higher for the lacunary ligand (O5-O8) than for the Keggin ligand (O1-O4), for the $X[PMo_{11}O_{39}][PMo_{12}O_{40}]^{6-}$ complexes more than in the $NH_4[X(PMo_{11}O_{39})(PMo_{12}O_{40})^{5-}]$ complexes. In all four systems investigated the Hf bond orders are higher than the

corresponding Zr complexes but the difference is quite small. Another major feature is that the calculated bond order drops significantly when a NH^{4+} cation is coordinated in the lacunary cavity.

	Zr	Hf	NH_4-Zr	NH_4-Hf
O1	0.36	0.41	0.24	0.19
O2	0.25	0.25	0.16	0.13
O3	0.24	0.23	0.15	0.13
O4	0.51	0.41	0.25	0.20
Avg.	0.34	0.33	0.20	0.16
O5	0.41	0.46	0.20	0.15
O6	0.38	0.45	0.31	0.23
O7	0.41	0.46	0.20	0.15
O8	0.51	0.45	0.28	0.20
Avg.	0.43	0.46	0.25	0.18

Table 3.16. The calculated O-X Mayer bond orders of $X(PMo_{11}O_{39})(PMo_{12}O_{40})$ and $NH_4[X(PMo_{11}O_{39})(PMo_{12}O_{40})^{5-}]$ (X = Zr, Hf)

The energy decomposition of the $X(PMo_{11}O_{39})_2^{10-}$ (X = Ce, Th) complexes supported the Mayer bond order calculations which suggested that the Ce-O interaction is stronger than the Th-O interaction. A similar comparison has not been performed for the $NH_4[X(PMo_{11}O_{39})(PMo_{12}O_{40})^{5-}]$ (X = Zr, Hf) as the energy decomposition calculations did not converge.

Conclusions

The polyoxometallate systems in this chapter proved difficult to investigate computationally, mainly because of the size and high anionicity of the systems which undermines the efficiency of available computational tools. The effects of the high charge of the systems are seen in all the calculated results; the optimized geometries of all systems consistently display longer bond lengths than seen experimentally. All energy decompositions were dominated by the electrostatic interaction terms making it difficult to analyse the bonding in detail. However, the calculated energy terms indicate that the coordination of lanthanides, transition metals and Th is mainly an ionic interaction. The Hf and Zr complexes were slightly more covalent but the interaction is still highly ionic.

The difference in bonding observed experimentally for Hf and Zr phosphomolybdate polyanions could not be traced to differences in the energy decompositions or any significant difference in the atomic charge analysis, where the behaviour of the two transition metals is almost identical. The $X(PMo_{12}O_{40})^{3-}$ and $X[(PMo_{12}O_{40})^{3-}]_2$ ($X = Zr^{4+}$, Hf^{4+}, La^{3+}, Lu^{3+}) complexes demonstrated that the lanthanide contraction is of great importance in determining the bond lengths and atomic charges of the trivalent lanthanides. The calculations also confirmed that the tetravalent transition metals are almost identical in behaviour. Since calculations could not successfully be completed for $NH_4[X(PMo_{11}O_{39})(PMo_{12}O_{40})^{5-}]$ (X = Zr, Hf) it was impossible to determine if there is any difference in the energy decomposition when an ammonium cation is introduced in the lacunary cavity. However, the two configurations had very different Mayer bond orders, with the complex using O_b' coordination having a significantly smaller bond order confirming that bonding using the lacunary cavity oxygen atoms is stronger. The difference between the Zr and Hf systems are again small and no difference was found between the two complexes.

The $[X(PMo_{11}O_{39})_2]^{10-}$ (X = Ce, Th) complexes were experimentally found to follow expected trends. Computationally, these complexes were very similar in almost all aspects. The most important difference was found in the energy decomposition analysis where the orbital interaction term for the Ce complex was larger, indicating a more covalent system.

Chapter 4

The electronic spectrum of NpO_2^{2+}, $NpO_2Cl_4^{2-}$ and $NpO_2(OH)_4^{2-}$ using time-dependent density functional theory

Introduction

The electronic structure of actinyls

Uranyl

Uranium is the heaviest naturally occurring element in the periodic table. It was only in the 1930s and 1940s that neutron bombardment of U isotopes produced transuranium elements. It was also at this time that it was recognized that the actinides were the 5f elements and needed their own series in the periodic table. The importance of uranium in both energy production and, initially, in weapons production, led to it being investigated continuously since the 1940s. Even today much actinide chemistry revolves around uranium chemistry, as it is by far the most common actinide and its radioactivity is relatively mild so it can be handled reasonably easy.

The most common structural motif in actinide chemistry, the uranyl cation UO_2^{2+} has been studied for a long time, both experimentally and computationally. It has been estimated that more than half of the known actinide structures feature the uranyl unit in some fashion. The ion is remarkably stable; the mean U-O bond enthalpy for dissociation to U + O atoms is 604 kJ/mol, in line with what is found for transition metal oxides.[113] Ligands coordinated in the equatorial plane, on the other hand, are much more weakly bound to the actinyl. It is also a linear ion; the O-U-O bond angle rarely deviates from 180° unless heavily strained by steric requirements.

Much of the information on the electronic structure of the actinyls comes from detailed experimental work on $Cs_2UO_2Cl_4$ or $Cs_2UO_2(NO_3)_3$ crystals.[114] A qualitative scheme of the electronic structure of UO_2^{2+} is displayed in Figure 4.1.

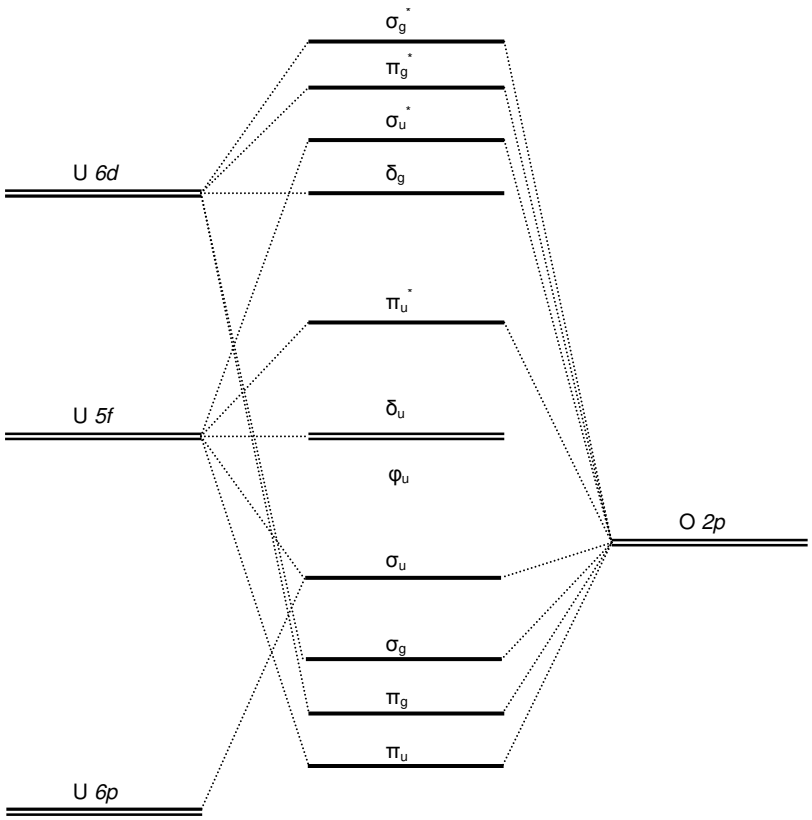

Figure 4.1. Qualitative molecular orbital energy level diagram of the electronic structure of UO_2^{2+}. σ_u is the HOMO in UO_2^{2+}.

The principal bonding orbitals are the doubly occupied σ_u, σ_g, π_g and π_u orbitals. σ_u and π_u consist of linear combinations of U 5f and O 2p orbitals and the even parity orbitals, σ_g and π_g, are formed by an admixture of U 6d and O 2p. Two U 5f orbitals can for reasons of symmetry not produce any linear combination with the O 2p AOs and as a result the corresponding δ_u and φ_u MOs are non-bonding. Even though the energetic ordering of the UO_2^{2+} MOs differ depending on the method used to investigate it, there are two constants; firstly, σ_u is always significantly destabilized compared to the other fully occupied MOs and second, the block of non-bonding orbitals is always higher in energy than the bonding orbitals. The destabilization of σ_u is an effect of anti-bonding covalent admixture from U 6p, an effect known as "pushing from below", the existence of which has been confirmed experimentally.[115, 116] This effect is also seen in the σ_u equivalent MOs also found in other actinyls and actinyl analogues.[117] The ordering of the remaining orbitals is more difficult to resolve experimentally. The U-O_{yl} has a notional bond

order of three. As was discussed in Chapter 1, relativistic effects play an important role in the electronic structure of all the actinides and need to be included in any computational investigation of these elements.[19, 118, 119]

There have been numerous computational and experimental studies investigating the electronic structure of UO_2^{2+} and $UO_2Cl_4^{2-}$.[120, 121] Recently, investigations into the lower energy electronic transitions of UO_2^{2+} and $UO_2Cl_4^{2-}$ using CASPT2 and TDDFT have been performed by Pierloot *et al.* in which all reported transitions were either f-f transitions or σ_u to f charge transfers.[51, 122] The CASPT2 results in particular were of very high quality and can be considered a benchmark for excitations in UO_2^{2+}. There was also good agreement with the CASPT2 $UO_2Cl_4^{2-}$ results and experiment.

Calculations of the higher energy transitions in UO_2^{2+} using TDDFT have recently been shown to be poor compared to wave function methods. The main drawback compared to other methods is the lack of a systematic error using TDDFT and different functionals. The study did show that CAM-B3LYP, a functional designed to correct the long-range behaviour of the functional, performed better than the usual B3LYP functional.[123] The asymptotically correct LB94 functional was not included in the study meaning no comparison with wave function methods has been done for that particular functional.[38]

Using TDDFT the same systems have been investigated and the agreement with experiment for $UO_2Cl_4^{2-}$ and with the CASPT2 results for UO_2^{2+} was very good, leading to the conclusion that time dependent DFT can perform well on closed-shell actinide systems.[51] One notable feature of the $UO_2Cl_4^{2-}$ results was that the orbital composition of the donor orbital, σ_u, showed a very high chlorine contribution, 73%, far more than what was seen in the CASPT2 study. This has previously been observed in DFT calculations of $UO_2Cl_4^{2-}$ and $CuCl_4^{2-}$,[124] and it was noted that such high Cl admixtures were at odds with CASPT2 calculations and experimental evidence.[51] This will be returned to later in this chapter.

Neptunyl

Neptunium was named for the Roman god of the sea and gets its name as Neptune is the next planet after Uranus, after which uranium is named. It was the first discovered transuranium element, produced by bombarding uranium nuclei with neutrons, and isolated in 1940.[125] There are only trace amounts of Np occurring naturally on Earth originating from decaying uranium isotopes. The electronic structure of NpO_2^{2+} is very similar to the electronic structure of UO_2^{2+} described above although moving from an f^0 to an f^1 electronic configuration means that there are some differences. The extra f electron occupies one of the non-bonding f_δ or f_φ MOs Figure 4.1). Due to the energetic proximity of these two f-orbitals, the density of states becomes quite high. The fully occupied orbitals are the same though, and the pushing from below effect destabilizing the σ_u MO is still found. There have been far fewer studies on NpO_2^{2+} than UO_2^{2+} because of the additional experimental hazards and, for computational investigations, because of the difficulty involved in open-shell calculations.

Early computational studies on NpO_2^{2+} to determine the electronic transition energies include an X_α investigation by Makhyoun[126] which found modest agreement with experiment. The geometry used in that study, however, is an estimate and relativistic effects were not explicitly included. Spin-orbit effects were included only as a perturbation. Several papers were published in the early nineties by Pershina *et al.*, where the electronic structure and spectra of all the actinyls, including NpO_2^{2+}, NpO^+ and $NpO_2Cl_4^{2-}$, were investigated using scattered wave X_α calculations.[127-133]

More recently Matsika and Pitzer have performed spin-orbit configuration interaction (SOCI) work on $UO_2Cl_4^{2-}$, NpO_2^+ and NpO_2^{2+}.[134, 135] The experimental ground state of NpO_2^{2+} is $^2\Phi_{5/2u}$, which was confirmed computationally.[136-141] It was found that only by introducing spin-orbit coupling could the correct ground state be evaluated, as without SO effects the ground state was found to be a $^2\Delta$ state. A further study by Matsika *et al.* on the spectrum of $NpO_2Cl_4^{2-}$ embedded in $Cs_2UO_2Cl_4$ showed that the effect of equatorial ligands is rather restricted, and no ligand-to-metal charge transfers were detected; the calculated transitions occurred within the NpO_2^{2+} moiety of the molecule.[142] This is consistent with what is found experimentally. The f-f and σ_u to

f charge transfers were lower in energy than the first Cl to Np f transitions. The calculated transition energies are in good agreement with the experimental transition energies.

Experimental electronic transitions from $Cs_2NpO_2Cl_4$ crystals have been used to measure the agreement between the calculated NpO_2^{2+} excitations and experiment.[134, 142] The rationale behind this is that calculated transitions out of the lower lying MOs, π_u, π_g and σ_g, have not been studied and at the transitions energies out of σ_u and the f orbitals no ligand based transitions have been observed. Thus a comparison with experiment can be made with Cl or other ligands present in the equatorial plane of the neptunyl moiety. This is not true for the higher energy transitions where ligand to metal energy transfer transitions start to appear. Studies which have calculated higher level excitations have refrained from making comparisons with results obtained from $Cs_2NpO_2Cl_4$ or other crystals as the impact of the ligands is not entirely established.

To date there has not been any time-dependent DFT investigation of NpO_2^{2+} published. There have however been DFT investigations of other actinyls. A comparative study by Vallet *et al.* investigating the performance of wave function based methods compared to density functional methods for a set of computational parameters on PuO_2^{2+}, showed that DFT was competitive for calculating the geometries and frequencies.[143] For the electronic transitions, however, TDDFT does not perform as well as the wave function methods. A recent comparison of different computational methods in calculating the electronic spectrum of UO_2^{2+} by the same group showed that the wave function based methods were more consistent than the TDDFT results.[144] The best methods were coupled cluster methods, which were shown to be superior to CASPT2.

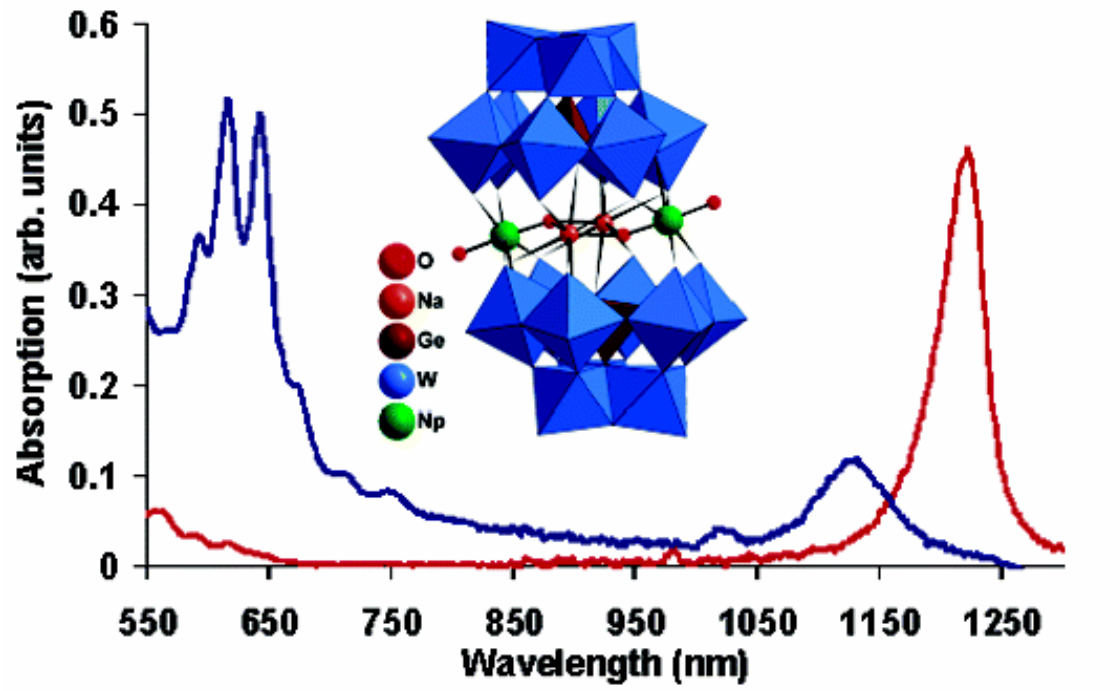

Figure 4.2. Vis/nIR spectrum of NpO_2^{2+} (red) and after the addition of two equivalents of $GeW_9O_{34}^{10-}$ (blue).[52]

Aim

This chapter will investigate the electronic spectrum of NpO_2^{2+}, $NpO_2Cl_4^{2-}$ and $NpO_2(OH)_4^{2-}$ using time dependent density functional theory. $NpO_2(H_2O)_5^{2+}$ will be discussed briefly in relation to experimental POM spectra. For completeness, the same calculations will be performed on two systems which have been thoroughly investigated in the past, UO_2^{2+} and $UO_2Cl_4^{2-}$.

In Chapter 3 various polyoxometallate systems were investigated. The experimental characterization of POMs are often performed using vis/nIR spectroscopy and it has been found that the f-f transitions in $Na_2(GeW_9O_{34})_2(NpO_2)_2^{14-}$ (Figure 4.2) change as free NpO_2^{2+} in solution is coordinated to the POM.[52] The transition energy is blue-shifted by about 0.1 eV as the NpO_2^{2+} unit is coordinated, and the intensity of the transition decreases. This chapter will investigate if this behaviour on coordination is found in small NpO_2^{2+} containing systems.

Absolute agreement between the experimental and computational change in transition energy is not likely as the experimental change is very small. Finding a qualitative trend, however, is more likely.

The final part of this chapter is a TDDFT investigation of the full $Na_2(GeW_9O_{34})_2(NpO_2)_2^{14-}$ system, partly to determine how accurate the result is in comparison to experiment, but also to see which of the small equatorial ligands (H_2O, Cl^- and OH^-) are the most similar to the full POM.[52]

Computational details

All calculations were performed using the Amsterdam Density Functional suite of programs (ADF2007).[110] Geometry optimizations were carried out using the PBE exchange-correlation functional[32] on NpO_2^{2+}, $NpO_2(OH)_4^{2-}$, $NpO_2(H_2O)_5^{2+}$ and $NpO_2Cl_4^{2-}$ while the crystal structure geometry was used for $Na_2(GeW_9O_{34})_2(NpO_2)_2^{14-}$.

In the geometry optimizations and subsequent TDDFT calculations on the NpO_2^{2+}, $NpO_2(OH)_4^{2-}$ and $NpO_2Cl_4^{2-}$ systems QZ4P all electron basis sets were used. CASPT2 geometries[51, 122] were used for the UO_2^{2+}, $UO_2Cl_4^{2-}$ TDDFT calculations; r(U-O) = 1.708 Å for $UO_2^{2+}$and r(U-O) = 1.783 Å and r(U-Cl) = 2.712 Å for $UO_2Cl_4^{2-}$. QZ4P all electron basis sets were used for the uranyl analogues as well. All electron basis sets were also used for $Na_2(GeW_9O_{34})_2(NpO_2)_2^{14-}$; TZ2P quality for Np, TZP for W and Ge and DZP for O and Na. For $NpO_2(H_2O)_5^{2+}$ a C_{2v} structure was used, similar to the $UO_2(H_2O)_5^{2+}$ used by Ingram *et al.*[102], with four water molecules perpendicular to the equatorial plane and one in the plane. Calculations using the QZ4P all-electron basis sets and the basis sets used for the polyoxometallate were also performed.

Since all of these systems are open shell f^1 systems unrestricted calculations were performed. It has been established that spin-orbit effects can be significant in calculations on transuranium elements. However, ADF is at present unable to take spin-orbit effects into account for open

shell systems, thus all results presented are the results of spin-orbit free (SOF) gas phase calculations.

To gain some insight into the spin-forbidden transitions in the absence of spin-orbit coupling spin-flip transitions have been calculated. The calculation of spin-flip transitions in ADF required the introduction of the Tamm-Dancoff approximation (TDA), which was also used on the spin-allowed transitions for consistency.[145] Comparing the transition energies of the spin-allowed transitions with and without TDA show a uniform upward shift in energy of a few hundred wavenumbers with TDA.

In all TDDFT calculations the asymptotically correct LB94 and SAOP (statistical average of orbital potentials) exchange-correlation functionals were applied to determine which functional would be most suitable.[146, 147] The 50 lowest energy transitions were calculated for NpO_2^{2+}, $NpO_2(OH)_4^{2-}$, $NpO_2(H_2O)_5^{2+}$ and $NpO_2Cl_4^{2-}$. Comparisons were made with previous high level calculations on NpO_2^{2+}. The first 10 excitations were calculated for $Na_2(GeW_9O_{34})_2(NpO_2)_2^{14-}$. The integration parameter was set to 6.0 and the convergence criteria set to 10^{-7} mHa/Å for the geometry optimizations. For the TDDFT calculations the integration parameter was set to 6.0 for the smaller systems, and to 3.0 for the $Na_2(GeW_9O_{34})_2(NpO_2)_2^{14-}$ calculations.

C_{2v} symmetry was enforced in the NpO_2^{2+} TDDFT calculations as ADF does not support the linear point groups for response calculations. The decent of symmetry in Table 4.1 shows that the δ and φ energy levels in $D_{\infty h}$ consist of combinations of a_1+a_2 and b_1+b_2 irreducible representations (irreps) in C_{2v}. For ease of comparison, the descent in symmetry is used to translate other MOs into the relevant $D_{\infty h}$ irreps.

$D_{\infty h}$	D_{4h}	D_{2d}	C_{2v}
π_g	e_g		a_2+b_2
π_u	e_u		a_1+b_1
σ_u	a_{2u}	b_2	a_1
σ_g	a_{1g}	a_1	a_1
δ_u	$b_{1u}+b_{2u}$	a_1+a_2	a_1+a_2
φ_u	e_u	e	b_1+b_2

Table 4.1. Descent of symmetry of $D_{\infty h}$.

The unpaired electron in the C_{2v} NpO_2^{2+} open-shell system will occupy one of the degenerate components of a non-bonding f orbital and thus lower the energy in comparison to the unoccupied one, thus splitting formally degenerate MOs. The resulting electronic structure is made more complicated due to this, with four non-bonding f orbitals (only one of which is occupied) where $D_{\infty h}$ neptunyl only has two. In the TDDFT calculations on NpO_2^{2+} this electronic ground state configuration results in transitions within the same f orbital, an unphysical result. These transitions have been removed from the reported results. For the $NpO_2Cl_4^{2-}$, $NpO_2(OH)_4^{2-}$, $NpO_2(H_2O)_5^{2+}$ and $Na_2(GeW_9O_{34})_2(NpO_2)_2^{14-}$ systems the true point groups could be used, D_{4h}, D_{2d}, C_{2v} and C_i respectively. Scalar relativistic effects were included in the calculations using the zero order regular approximation (ZORA).[18] Experimental data have been used to evaluate the calculated transitions for $NpO_2Cl_4^{2-}$. For gas phase NpO_2^{2+} and $NpO_2(OH)_4^{2-}$ systems no experimental data exist and comparisons will be made with previous computational studies.

The non-bonding f orbitals, f_δ and f_φ, are close in energy which makes it very likely that a proper description of the neptunyl systems will be multiconfigurational in nature. The rationale for using TDDFT is that the size of the POM systems makes it impossible to use other computational methods in the investigation of the electronic spectrum of the neptunyl complexes. This investigation is something of a benchmark on how viable TDDFT is in calculating open-shell electronic transitions in actinides.

Results

Geometry

The optimized geometry of NpO_2^{2+} results in r(Np-O) = 1.719 Å. The Makhyoun study estimated r(Np-O) = 1.75 Å based on r(An-O) trends along the actinide series while Pitzer *et al.* used a CI optimized geometry, with r(Np-O) = 1.66 Å. The result of this work ends up between these two numbers and can be considered reasonable.

Calculations on $NpO_2Cl_4^{2-}$ produced r(Np-O) = 1.789 Å and r(Np-Cl) = 2.717 Å. In contrast to the results on the bare NpO_2^{2+} system, there are experimental data available for the geometry of $NpO_2Cl_4^{2-}$. However, in all cases these are crystal geometries and not gas phase geometries. An early experimental structure of $NpO_2Cl_4^{2-}$ gave r(Np-O) = 1.66 Å. However, instead of finding equidistant equatorial ligands a rhombeous arrangement of the Cl ligands, with $r(Np\text{-}Cl)_1$ = 2.51 Å and $r(Np\text{-}Cl)_2$ = 2.85 Å was found. A recent X-ray diffraction study, however, only finds one r(Np-Cl) = 2.653 Å, with r(Np-O) = 1.775 Å.[148] Notable is that all the experimental studies were performed on $Cs_2NpO_2Cl_4$, while the computational investigation in the present work has been carried out on the anion, $NpO_2Cl_4^{2-}$, where the absence of counter ions will make the Columbic interactions expand the molecule. The difference compared to experiment is not very large though, r(Np-O) is overestimated by about 0.02 Å and r(Np-Cl) by 0.06 Å.

The geometry optimization of $NpO_2(OH)_4^{2-}$ resulted in r(Np-O) = 1.844 Å and $r(Np\text{-}O_{OH})$ = 2.297 Å. No experimental results on the geometry of $NpO_2(OH)_4^{2-}$ have been reported, but there have been computational studies performed on the system. The present result compares favourably with an investigation using B3LYP, which found r(Np-O) = 1.83 Å and $r(Np\text{-}O_{OH})$ = 2.29 Å.[149]

The calculated optimum geometry of $NpO_2(H_2O)_5^{2+}$ resulted in $r(Np\text{-}O_{yl})$ = 1.749 Å and three different $r(Np\text{-}O_{H2O})$: 2.503 Å for the H_2O molecule in the plane and 2.490 Å and 2.459 Å for the

water molecules perpendicular to the plane. The Np-O_{yl} bond distance is in good agreement with experimental data on neptunyl in water, r(Np-O_{yl}) = 1.742 Å, while the Np-O_{H2O} distance was overestimated compared to the experimental distance, r(Np-O_{H2O}) = 2.372 Å.[150, 151]

Electronic structure

A comprehensive MO diagram of the PBE electronic structures of NpO_2^{2+}, $NpO_2Cl_4^{2-}$ and $NpO_2(OH)_4^{2-}$ is given in Figure 4.3.

UO_2^{2+} and NpO_2^{2+}

The electronic structure is important in investigations of the electronic transitions of a system because, naively, the transition energy is the difference in energy between donor and acceptor orbital. The PBE and SAOP electronic structures of UO_2^{2+} (Table 4.2) show the energetic ordering of the doubly occupied orbitals: $\sigma_u > \sigma_g > \pi_u > \pi_g$. σ_u is significantly destabilized compared to σ_g. All of the occupied valence orbitals span an energy range of 1.52 eV for PBE and 1.57 eV for SAOP. The calculated LUMO is φ_u with δ_u 0.55 eV or 0.35 eV higher in energy for PBE and SAOP respectively. The calculated HOMO-LUMO gap is quite large for both functionals, 2.19 eV for PBE and 3.27 eV for SAOP.

			Composition (%)				
Orbital	Occupation	Energy (eV)	U 5f	U 6d	U 6p	U 7s	O 2p
δ_u	0	-19.17	99				
		-23.09	*99*				
φ_u	0	-19.72	99				
		-23.44	*99*				
σ_u	2	-21.91	55		9		34
		-26.71	*55*		*9*		*33*
σ_g	2	-22.67		8			91
		-27.60		*8*			*92*
π_u	4	-23.14	35				65
		-27.79	*29*				*70*
π_g	4	-23.43		14			83
		-28.28		*13*			*83*

Table 4.2. Valence molecular orbital energies, occupations and compositions for UO_2^{2+}. PBE data are given in upright text, while SAOP data are given in italics.

The orbital composition of the UO_2^{2+} valence MOs are as expected; φ_u and δ_u consist completely of U 5f for both functionals. σ_u are also similar comparing the two functionals, 55% U 5f, 9% U 6p and 34% O 2p (PBE) or 33% O 2p (SAOP). The pushing from below admixture from the U 6p MO is clearly seen and there is a significant U 5f contribution for both functionals. The composition of the σ_g, π_u and π_g are very similar for the two functionals; they all have large O 2p contributions compared to the U contributions, in the even parity MOs the U 6d contributions are only 8% (σ_g) and 13-14% (π_g). These results are in line with previous calculations which have found that the occupied valence MOs of UO_2^{2+} are primarily O based.[152]

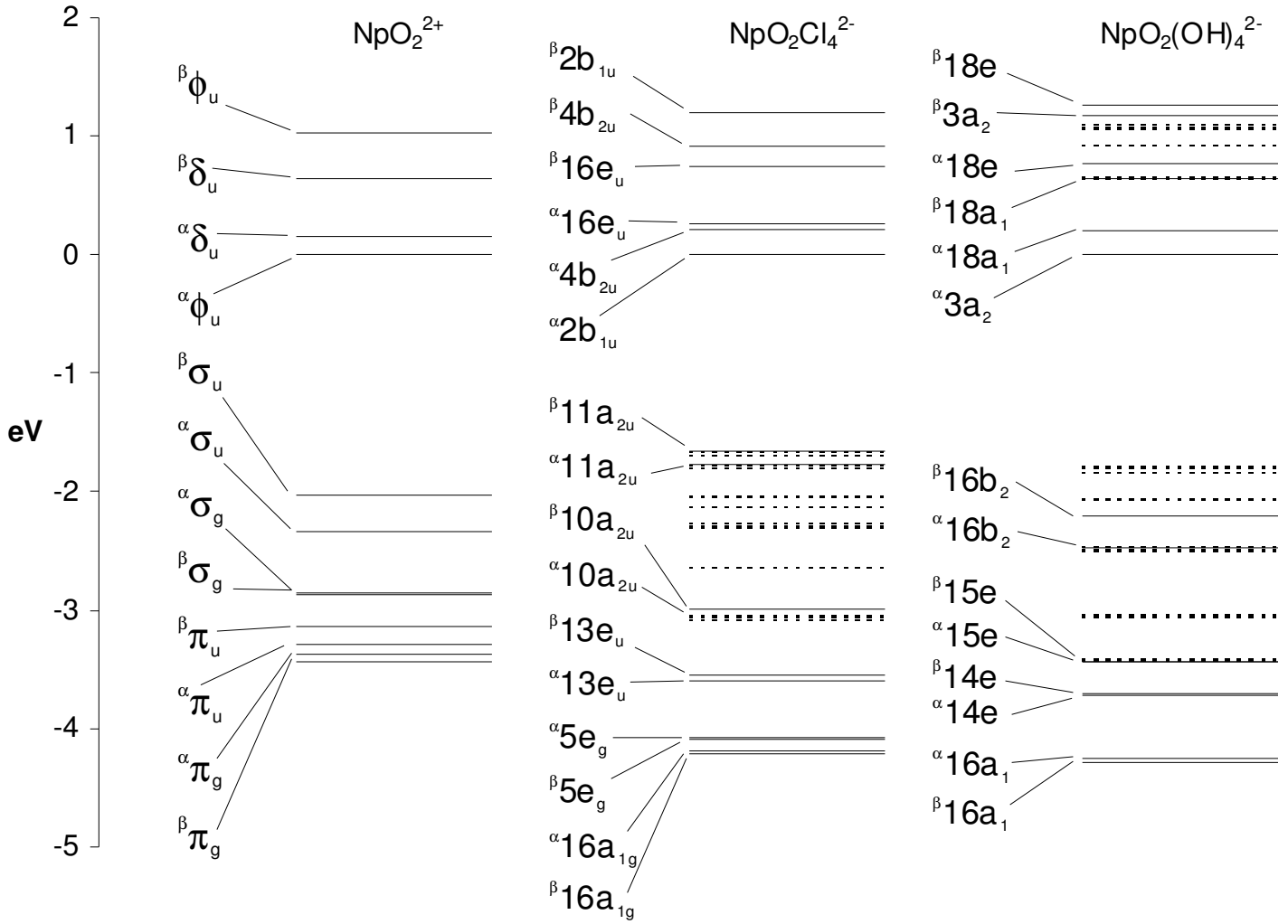

Figure 4.3: PBE molecular orbital energy level diagrams for NpO_2^{2+}, $NpO_2Cl_4^{2-}$ and $NpO_2(OH)_4^{2-}$. Solid lines indicate orbitals with significant neptunyl character, while dashed lines indicate orbitals which are largely localized on the equatorial ligands. The MO energies have been normalized at the HOMO.

			Composition (%)					
Orbital	Occupation	Energy (eV)	Np f	Np d	Np p	Np s	O p	NpO_2^{2+} component
$^{\beta}13b_2$	0	-19.19	99					ϕ_u
$^{\beta}13b_1$	0	-19.19	99					ϕ_u
$^{\beta}5a_2$	0	-19.58	99					δ_u
$^{\beta}26a_1$	0	-19.58	99					δ_u
$^{\alpha}5a_2$	0	-20.06	99					δ_u
$^{\alpha}26a_1$	0	-20.06	99					δ_u
$^{\alpha}13b_2$	0	-20.22	99					ϕ_u
$^{\alpha}13b_1$	1	-20.22	99					ϕ_u
$^{\beta}25a_1$	1	-22.24	57		9		34	σ_u
$^{\alpha}25a_1$	1	-22.56	58		8		32	σ_u
$^{\alpha}24a_1$	1	-23.08		5		6	87	σ_g
$^{\beta}24a_1$	1	-23.09		5		7	87	σ_g
$^{\beta}12b_1$	1	-23.36	35				65	π_u
$^{\beta}12b_2$	1	-23.36	35				65	π_u
$^{\alpha}12b_1$	1	-23.50	39				62	π_u
$^{\alpha}12b_2$	1	-23.50	39				62	π_u
$^{\alpha}11b_2$	1	-23.59		13			82	π_g
$^{\alpha}11b_1$	1	-23.59		13			82	π_g
$^{\beta}11b_1$	1	-23.65		12			84	π_g
$^{\beta}11b_2$	1	-23.65		12			84	π_g

Table 4.3. Valence molecular orbital energies, occupations and compositions of NpO_2^{2+} (PBE) in C_{2v} symmetry along with the $D_{\infty h}$ orbital symmetry to which it belongs.

The molecular orbitals of NpO_2^{2+} corresponding to π_g, π_u, σ_g, σ_u, δ_u and φ_u and their atomic orbital contributions are shown in Table 4.3 and Figure 4.3. The reduction in symmetry from $D_{\infty h}$ to C_{2v} results in the splitting of orbitals, for example ϕ_u splits into $13b_1$+$13b_2$. In the PBE electronic structure the split orbital pairs are degenerate making it easy to identify which orbitals belong to the $D_{\infty h}$ equivalent orbitals. A result of the splitting is that the unpaired electron potentially can occupy one of two orbitals making up a single MO in $D_{\infty h}$. The calculated HOMO is $13b_1$, ϕ_u, and the energy gap down to the fully occupied σ_u, $25a_1$, is 2.02 eV. This energy difference is quite close to the PBE HOMO-LUMO gap in UO_2^{2+}, 2.19 eV. The composition of δ_u ($26a_1$+$5a_2$) and ϕ_u ($13b_1$+$13b_2$) show that they consist entirely of Np 5f. Notable is the very small energy difference between δ_u and ϕ_u, 0.16 eV.

The energetic ordering of the fully occupied bonding MOs is the same as in UO_2^{2+} calculation: $\sigma_u > \sigma_g > \pi_u > \pi_g$. These MOs span a similar energy range as those in UO_2^{2+}, 1.41 eV in NpO_2^{2+} compared to 1.52 eV in UO_2^{2+} indicating that the bonding MOs in UO_2^{2+} and NpO_2^{2+} form a block of orbitals, spanning the same energy independent of metal. The trends of the MO composition remain the same as those in UO_2^{2+}; σ_u is the only MO with a majority Np 5f contribution, 57%, and a similar sized pushing from below effect, the Np 6p contribution is 9%, is seen. Again, the even parity MOs are O based MOs, the contributions from O 2p is 82% for π_g and 87% σ_g. One significant difference in the MO compositions of UO_2^{2+} and NpO_2^{2+} is that there are Np s contributions to σ_g, something not seen in σ_g in UO_2^{2+}.

The calculated HOMO in the SAOP electronic structure of NpO_2^{2+} has changed compared with the PBE calculation, from ϕ_u to δ_u (Table 4.4). Contrary to the PBE calculation, $5a_2$, the other MO of the pair constituting δ_u, is 1.90 eV higher in energy. The HOMO-LUMO gap is calculated to be 1.13 eV, significantly greater than the 0.16 eV found using PBE. The composition of the ϕ_u and δ_u is exclusively Np 5f. The energy gap from $26a_1$ to $25a_1$, i.e. from δ_u to the fully occupied valence orbitals is 0.89 eV, a much smaller gap than found in the PBE calculation. The compositions of the doubly occupied MOs are similar to the PBE calculations; σ_u is the only metal based MO, and has Np 5f contributions of about 56%. Again there are O 2p contributions of around 10%, 8% in the case of the HOMO. Contributions of Np s as well as high O 2p contributions to the even parity MOs are seen. The block of bonding MOs, σ_u to π_g, spans 1.4 eV, similar to the PBE result.

An important aspect of the SAOP electronic structure is the breakdown of degeneracy of formally degenerate MOs around the HOMO, something that was not observed for the PBE electronic structure. $5a_2$ is significantly higher in energy than $26a_1$, even though they span the same irrep in $D_{\infty h}$. In the doubly occupied π_u, $12b_1$ and $12b_2$ are degenerate, which is also seen for the virtual ϕ_u orbitals, $13b_1$ and $13b_2$.

			Composition (%)					
Orbital	Occupation	Energy (eV)	Np f	Np d	Np p	Np s	O p	NpO_2^{2+} component
$^{\beta}5a_2$	0	-23.33	99					δ_u
$^{\beta}26a_1$	0	-23.52	99					δ_u
$^{\beta}13b_2$	0	-24.00	99					ϕ_u
$^{\beta}13b_1$	0	-24.00	99					ϕ_u
$^{\alpha}5a_2$	0	-24.20	99					δ_u
$^{\alpha}13b_2$	0	-24.97	99					ϕ_u
$^{\alpha}13b_1$	0	-24.97	99					ϕ_u
$^{\alpha}26a_1$	1	-26.10	99					δ_u
$^{\beta}25a_1$	1	-26.99	56		8		32	σ_u
$^{\alpha}25a_1$	1	-27.59	59		5		32	σ_u
$^{\alpha}24a_1$	1	-27.67		5		8	87	σ_g
$^{\beta}24a_1$	1	-27.92		5		8	87	σ_g
$^{\beta}12b_2$	1	-27.95	27				72	π_u
$^{\beta}12b_1$	1	-27.95	27				72	π_u
$^{\alpha}12b_2$	1	-27.96	36				64	π_u
$^{\alpha}12b_1$	1	-27.96	36				64	π_u
$^{\alpha}11b_2$	1	-28.19		14			82	π_g
$^{\alpha}11b_1$	1	-28.19		14			82	π_g
$^{\beta}11b_2$	1	-28.39		12			85	π_g
$^{\beta}11b_1$	1	-28.39		12			85	π_g

Table 4.4. Valence molecular orbital energies, occupations and compositions of orbital decomposition of NpO_2^{2+} (TDA, SAOP) in C_{2v}

Finally, the electronic structure of NpO_2^{2+} has been calculated using LB94 (Table 4.5). As in the PBE and SAOP calculations the descent in symmetry splits MOs in an unphysical manner, which complicates things in the TDDFT calculations below. The LB94 ground state is the same as in the PBE calculations, Φ. As in the SAOP calculations the two MOs making up φ_u ($13b_1$ and $13b_2$) are separated by a large energy gap, 0.6 eV, less than what was found in the SAOP calculation but still significantly higher than in the PBE electronic structure. The first two, formally degenerate, virtual orbitals are separated by 0.02 eV. The splitting of orbitals decrease moving away from the HOMO and LUMO, for $^{\beta}\delta_u$ ($^{\beta}5a_2$ + $^{\beta}26a_1$) there is degeneracy and in the bonding π MOs there is degeneracy among the constituent MOs. The splitting of degenerate MOs is clearly only occurring close to the HOMO. The energy gap up to the LUMO ($26a_1$) though is significantly reduced in the LB94 electronic structure compared to the SAOP

structure; at 0.24 eV close to the gap of 0.16 eV found using PBE and significantly smaller than the 1.13 eV using SAOP. The difference in energy down to the first doubly occupied valence MO, $25a_1$, is 1.5 eV, larger than what was found using SAOP but still smaller than the 2.02 eV energy gap using PBE. All of the φ_u and δ_u MOs are exclusively Np 5f in character.

			Composition (%)					
Orbital	Occupation	Energy (eV)	Np f	Np d	Np p	Np s	O p	NpO_2^{2+} component
$^{\beta}13b_2$	0	-26.41	99					ϕ_u
$^{\beta}13b_1$	0	-26.50	99					ϕ_u
$^{\alpha}13b_2$	0	-26.79	99					ϕ_u
$^{\beta}26a_1$	0	-26.81	99					δ_u
$^{\beta}5a_2$	0	-26.81	99					δ_u
$^{\alpha}5a_2$	0	-27.13	99					δ_u
$^{\alpha}26a_1$	0	-27.15	99					δ_u
$^{\alpha}13b_1$	1	-27.39	99					ϕ_u
$^{\beta}25a_1$	1	-28.89	60		5		29	σ_u
$^{\alpha}25a_1$	1	-29.11	61		4		28	σ_u
$^{\alpha}24a_1$	1	-29.27		11			88	σ_g
$^{\beta}24a_1$	1	-29.27		9			90	σ_g
$^{\beta}12b_2$	1	-29.88	38				62	π_u
$^{\beta}12b_1$	1	-29.88	38				62	π_u
$^{\alpha}12b_2$	1	-29.95		13			84	π_u
$^{\alpha}12b_1$	1	-29.95		13			84	π_u
$^{\beta}11b_2$	1	-29.98		12			85	π_g
$^{\beta}11b_1$	1	-29.98		12			85	π_g
$^{\alpha}11b_1$	1	-30.00	41				59	π_g
$^{\alpha}11b_2$	1	-30.01	41				59	π_g

Table 4.5. Valence molecular orbital energies, occupations and compositions of NpO_2^{2+} (TDA, LB94) in C_{2v}

The energetic ordering of the fully occupied MOs is the same as was found for the other functionals: $\sigma_u > \sigma_g > \pi_u > \pi_g$. The spread of this block of orbitals is 1.12 eV, smaller than was found with the other functionals. One reason for this decrease in the spread is that there is less pushing from below of the σ_u MO, only 5% Np 6p compared to around 10% for PBE and SAOP. The atomic orbital contributions of the σ_g and π orbitals very closely mirror the results of the other functionals, with one exception. The Np s character of the σ_g seen in the SAOP and PBE calculations is no longer seen in the LB94 calculation.

$UO_2Cl_4^{2-}$ and $NpO_2Cl_4^{2-}$

Calculations of the electronic structure of the closed shell $UO_2Cl_4^{2-}$ system were performed to determine whether there were significant differences compared with the $NpO_2Cl_4^{2-}$ ground state electronic structure as well as investigate the impact of equatorial ligands. The resulting PBE electronic structure (Table 4.6) is different to the UO_2^{2+} structure in that it is not clear which MO is the σ_u bonding MO. Another major difference to the UO_2^{2+} calculation is the presence of a block of six Cl based MOs between the $11a_{2u}$ and $10a_{2u}$. Experimentally, the ligand to metal charge transfer transitions occur at significantly higher energies than f-f transitions or transitions out of σ_u. The PBE DFT ground state of $UO_2Cl_4^{2-}$ suggests that a large part of the TDDFT calculated excitations will be Cl to U excitations.

Both $11a_{2u}$ and $10a_{2u}$ are doubly occupied and have the correct symmetry to be the σ_u MO. Inspection of the composition of the two MOs reveal that $11a_{2u}$ has a high Cl contribution, 61% compared to 39% in $10a_{2u}$. The ligand contribution is even more pronounced in the SAOP composition, where $11a_{2u}$ has 74% Cl character. Also, the U 5f contribution of the $10a_{2u}$ is higher, 31% compared to 17% in $11a_{2u}$ and only 10% in SAOP. Performing a visual inspection of the two MOs (Figure 4.4) it is seen that the $11a_{2u}$ is out of phase with the Cl ligand and thus anti-bonding. The corresponding image of $10a_{2u}$ shows a bonding interaction with the Cl ligands. Finally, it was established in the NpO_2^{2+} and UO_2^{2+} that the fully occupied bonding MOs span about 1.5 eV in energy. If $11a_{2u}$ is the σ_u this span would be 2.60 eV compared to 1.38 eV with $10a_{2u}$. All of this taken together suggests that $10a_{2u}$ is the σ_u, and that previous calculations finding σ_u to contain very high levels of Cl contribution must have used $11a_{2u}$ as their σ_u. σ_g is stabilized compared to the π orbitals, and is in fact as stable as π_g. π_u is almost equidistant to both the σ_u and π_g, with 0.62 eV down to π_g and 0.76 eV up to σ_u.

(a)

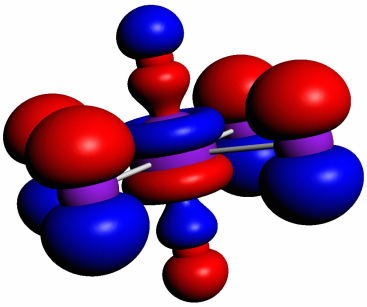

(b)

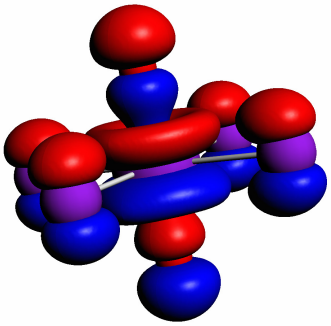

Figure 4.4. Three dimensional representations of the SAOP (a) $11a_{2u}$ and (b) $10a_{2u}$ orbitals of $UO_2Cl_4^{2-}$.

			Composition (%)					
Orbital	Occupation	Energy (eV)	U f	U d	U p	O	Cl	UO_2^{2+} component (Table 4.2)
$16e_u$	0	3.62	86				7	ϕ_u
		-0.09	*88*				*7*	
$4b_{2u}$	0	3.60	94				5	δ_u
		-0.14	*93*				*4*	
$2b_{1u}$	0	3.48	99					δ_u
		-0.30	*99*					
$11a_{2u}$	2	0.98	17		5	19	61	
		-3.24	*10*		*4*	*14*	*74*	
$2a_{2g}$	2	0.92					100	
$6e_g$	4	0.80				10	90	
$3b_{2u}$	2	0.55	5				95	
$15e_u$	4	0.46	6				94	
$14e_u$	4	0.36	4			5	88	
$5b_{2g}$	2	-0.09		4			95	
$10a_{2u}$	2	-0.24	31		10	24	39	σ_u
		-4.55	*36*		*9*	*30*	*27*	
$17a_{1g}$	2	-0.40				25	75	
$8b_{1g}$	2	-0.54		12		23	87	
$13e_u$	4	-1.00	26			71	3	π_u
		-5.35	*21*			*78*	*2*	
$5e_g$	4	-1.62		11		76	10	π_g
		-6.04		*9*		*80*	*7*	
$16a_{1g}$	2	-1.62		6		73	19	σ_g
		-6.04		*5*		*84*	*11*	

Table 4.6. Valence molecular orbital energies, occupations and compositions for $UO_2Cl_4^{2-}$. PBE data are given in upright text, while SAOP data for selected orbitals are given in italics.

The calculated PBE $NpO_2Cl_4^{2-}$ $^2B_{1u}$ ground state corresponds to a δ_u HOMO, and the molecular orbitals equivalent to π_g, σ_g, π_u, σ_u, δ_u and φ_u (Table 4.7 and Figure 4.3) were identified. The energetic ordering of the important valence MOs is, in terms of linear irreps: $\sigma_g < \pi_g < \pi_u < \sigma_u < \delta_u < \varphi_u$. The bonding σ_u orbitals are recognized by the admixture of anti-bonding O p AOs while the non-bonding δ_u and φ_u MOs are almost purely Np based f orbitals. As in $UO_2Cl_4^{2-}$ there was some difficulty in immediately identifying the σ_u, as both $11a_{2u}$ and $10a_{2u}$ have the correct symmetry and contain Np 6p contributions. The ligand contribution to $11a_{2u}$ is very high at 61% for $^{\beta}11a_{2u}$ and 74% for $^{\alpha}11a_{2u}$ but the characteristic admixture of anti-bonding O p is present. However, this is similar to what

was found in $UO_2Cl_4^{2-}$, where the calculated ligand contributions to $11a_{2u}$ were larger than shown with experimental and multireference methods.[51]

			Composition (%)					
Orbital	Occupation	Energy (eV)	Np f	Np d	Np p	O	Cl	NpO_2^{2+} component (Table 4.2)
$^{\beta}2b_{1u}$	0	3.78	99					$^{\beta}\delta_u$
$^{\beta}4b_{2u}$	0	3.49	94					$^{\beta}\delta_u$
$^{\beta}16e_u$	0	3.32	88				8	$^{\beta}\varphi_u$
$^{\alpha}16e_u$	0	2.84	84				11	$^{\alpha}\varphi_u$
$^{\alpha}4b_{2u}$	0	2.79	91				6	$^{\alpha}\delta_u$
$^{\alpha}2b_{1u}$	1	2.58	99					$^{\alpha}\delta_u$
$^{\beta}11a_{2u}$	1	0.92	18		5	18	61	σ_u/Cl
$^{\alpha}2a_{2g}$	1	0.92					100	
$^{\beta}2a_{2g}$	1	0.89					100	
$^{\alpha}11a_{2u}$	1	0.81	12			12	74	σ_u/Cl
$^{\alpha}6e_g$	2	0.81				10	90	
$^{\beta}6e_g$	2	0.78				10	90	
$^{\beta}3b_{2u}$	1	0.55					97	
$^{\alpha}3b_{2u}$	1	0.54	6				94	
$^{\beta}15e_u$	2	0.45	6				94	
$^{\alpha}15e_u$	2	0.44	5				93	
$^{\beta}14e_u$	2	0.32					90	
$^{\alpha}14e_u$	2	0.28	7				85	
$^{\alpha}5b_{2g}$	1	-0.06		4			93	
$^{\beta}5b_{2g}$	1	-0.06		3			94	
$^{\beta}10a_{2u}$	1	-0.20	32		9	24	39	$^{\beta}\sigma_u$
$^{\alpha}10a_{2u}$	1	-0.41	40		8	27	26	$^{\alpha}\sigma_u$
$^{\alpha}17a_{1g}$	1	-0.47				23	80	
$^{\beta}17a_{1g}$	1	-0.47				23	81	
$^{\alpha}8b_{1g}$	1	-0.48		11			87	
$^{\beta}8b_{1g}$	1	-0.50		11			88	
$^{\beta}13e_u$	2	-0.96	25			73		$^{\beta}\pi_u$
$^{\alpha}13e_u$	2	-1.01	29			69		$^{\alpha}\pi_u$
$^{\alpha}5e_g$	2	-1.49		11		75	10	$^{\alpha}\pi_g$
$^{\beta}5e_g$	2	-1.50		10		77	10	$^{\beta}\pi_g$
$^{\alpha}16a_{1g}$	1	-1.60		8		76	16	$^{\alpha}\sigma_g$
$^{\beta}16a_{1g}$	1	-1.63		9		78	16	$^{\beta}\sigma_g$

Table 4.7. Valence molecular orbital energies, occupations and compositions of $NpO_2Cl_4^{2-}$ (PBE).

Overall it is more plausible to label the $10a_{2u}$ as the σ_u, and to classify $11a_{2u}$ as a ligand based MO with out of phase σ_u character.

The two non-bonding f orbitals are split in three, $16e_u$, $2b_{1u}$ and $4b_{2u}$, spanning an energy range of *ca* 1.2 eV. $^{\alpha}4b_{2u}$ is a virtual orbital higher in energy than $^{\alpha}2b_{1u}$ while in $D_{\infty h}$ they both constitute δ_u. The gap between $^{\alpha}2b_{1u}$ and $^{\alpha}10a_{2u}$, the HOMO and HOMO-1, is substantial at 2.78 eV. As in $UO_2Cl_4^{2-}$ the gap is filled with a block of Cl based MOs. The HOMO-LUMO gap, between $^{\alpha}2b_{1u}$ and $^{\alpha}4b_{2u}$, is 0.21 eV and the energy gap to the first φ MO is only marginally higher at 0.26 eV. The unoccupied φ and δ orbitals contain significant amounts of Cl character, but transitions between the non-bonding MOs are still f-f transitions since Np, depending on the MO, contributes between 84 % and 99 % of the total.

The calculated SAOP and LB94 electronic ground state is $^2B_{1u}$ (Tables 4.8 and 4.9), i.e. a δ_u HOMO. The ordering of the MOs is very similar to the PBE electronic structure: $\pi_u < \sigma_u < \delta_u < \varphi_u$ for the highest energy orbitals. When it comes to the ordering of π_g and σ_g the result differ depending on the functional used; for LB94 $\sigma_g > \pi_g$, while in SAOP calculation $\sigma_g \approx \pi_g$. Again, both $11a_{2u}$ and $10a_{2u}$ could potentially be the highest fully occupied σ_u, but the arguments for $10a_{2u}$ remain strong here as well; there is a much larger Cl contribution, the energy gap down to the other Np-O_{yl} bonding MOs become too large and a visual inspection of the MO shows that there is an anti-bonding interaction with the Cl ligands destabilizing the $11a_{2u}$. There is a block of Cl orbitals between $10a_{2u}$ and the HOMO, $2b_{1u}$, similar to what was found in the PBE calculations on $NpO_2Cl_4^{2-}$ and $UO_2Cl_4^{2-}$.

The HOMO-LUMO gap shows significant functional dependence; the gap is 1.72 eV for SAOP and 0.38 eV for LB94, and this difference will be reflected in the calculated f-f transitions below. With SAOP $10a_{2u}$, σ_u, was about 3.2 eV lower in energy than the HOMO, $2b_{1u}$; the corresponding energy difference with LB94 is 2.5 eV. Both SAOP and LB94 produce very similar MO compositions for all Np-O_{yl} bonding orbitals. Thus, the difference between the two functionals in the $NpO_2Cl_4^{2-}$ calculations is the difference in the valence electronic structure; SAOP consistently produce larger HOMO-LUMO energy gaps than PBE or LB94.

			Composition (%)					
Orbital.	Occupation	Energy (eV)	Np f	Np d	Np p	O p	Cl	NpO_2^{2+} component (Table 4.2)
$^{\beta}4b_{2u}$	0	0.13	95					$^{\beta}\delta_u$
$^{\beta}16e_{1u}$	0	-0.03	90				6	$^{\beta}\varphi_u$
$^{\beta}2b_{1u}$	0	-0.19	99					$^{\beta}\delta_u$
$^{\alpha}4b_{2u}$	0	-1.03	93				5	$^{\alpha}\delta_u$
$^{\alpha}16e_{1u}$	0	-1.28	82				14	$^{\alpha}\varphi_u$
$^{\alpha}2b_{1u}$	1	-3.00	99					$^{\alpha}\delta_u$
$^{\alpha}2a_{2g}$	1	-3.16					100	
$^{\beta}2a_{2g}$	1	-3.24					100	
$^{\beta}11a_{2u}$	1	-3.29	15			13	72	σ_u/Cl
$^{\alpha}6e_{1g}$	2	-3.30				9	92	
$^{\beta}6e_{1g}$	2	-3.38				7	92	
$^{\alpha}11a_{2u}$	1	-3.40	3		1	5	91	σ_u/Cl
$^{\alpha}3b_{2u}$	1	-3.52					96	
$^{\beta}3b_{2u}$	1	-3.55					99	
$^{\alpha}15e_{1u}$	2	-3.62					96	
$^{\beta}15e_{1u}$	2	-3.64					96	
$^{\beta}14e_{1u}$	2	-3.78					94	
$^{\alpha}14e_{1u}$	2	-3.81	10				85	
$^{\alpha}5b_{2g}$	1	-4.11					96	
$^{\beta}5b_{2g}$	1	-4.16					95	
$^{\beta}10a_{2u}$	1	-4.47	35		7	30	29	σ_u
$^{\alpha}8b_{1g}$	1	-4.50		11			89	
$^{\alpha}17a_{1g}$	1	-4.52				15	88	
$^{\beta}8b_{1g}$	1	-4.56		10			90	
$^{\beta}17a_{1g}$	1	-4.58				17	89	
$^{\alpha}10a_{2u}$	1	-5.06	56			35	10	σ_u
$^{\beta}13e_{1u}$	2	-5.26	16			82		π_u
$^{\alpha}13e_{1u}$	2	-5.31	24			73		π_u
$^{\alpha}5e_{1g}$	2	-5.83		10		79	8	π_g
$^{\alpha}16a_{1g}$	1	-5.92		10		72	9	σ_g
$^{\beta}5e_{1g}$	2	-5.93		7		82	7	π_g
$^{\beta}16a_{1g}$	1	-6.06		5		82	8	σ_g

Table 4.8. Valence molecular orbital energies, occupations and compositions of $NpO_2Cl_4^{2-}$ (SAOP).

			Composition (%)					
Orbital.	Occupation	Energy (eV)	Np f	Np d	Np p	O p	Cl	NpO_2^{2+} component (Table 4.2)
$^{\beta}17e_{1u}$	0	-0.50	72			24		
$^{\alpha}17e_{1u}$	0	-0.76	69			26		
$^{\beta}2b_{1u}$	0	-1.92	99					$^{\beta}\delta_u$
$^{\beta}16e_{1u}$	0	-2.02	84				12	$^{\beta}\varphi_u$
$^{\beta}4b_{2u}$	0	-2.03	91				6	$^{\beta}\delta_u$
$^{\alpha}16e_{1u}$	0	-2.32	80				17	$^{\alpha}\varphi_u$
$^{\alpha}4b_{2u}$	0	-2.35	99					$^{\alpha}\delta_u$
$^{\alpha}2b_{1u}$	1	-2.73	99					$^{\alpha}\delta_u$
$^{\alpha}2a_{2g}$	1	-3.82					100	
$^{\beta}2a_{2g}$	1	-3.84					100	
$^{\alpha}6e_{1g}$	2	-3.95				8	92	
$^{\beta}11a_{2u}$	1	-3.96	8			9	81	σ_u/Cl
$^{\beta}6e_{1g}$	2	-3.97				8	92	
$^{\alpha}11a_{2u}$	1	-4.00	5			6	87	σ_u/Cl
$^{\beta}3b_{2u}$	1	-4.16	7				93	
$^{\alpha}3b_{2u}$	1	-4.17	9				92	
$^{\beta}15e_{1u}$	2	-4.27	10				90	
$^{\alpha}15e_{1u}$	2	-4.27	6				93	
$^{\beta}14e_{1u}$	2	-4.32					92	
$^{\alpha}14e_{1u}$	2	-4.36	12				84	
$^{\alpha}5b_{2g}$	1	-4.72		7			94	
$^{\beta}5b_{2g}$	1	-4.72		6			94	
$^{\alpha}8b_{1g}$	1	-4.98		10			89	
$^{\beta}8b_{1g}$	1	-4.99		10			90	
$^{\alpha}17a_{1g}$	1	-5.08				11	86	
$^{\beta}17a_{1g}$	1	-5.09				11	87	
$^{\beta}10a_{2u}$	1	-5.23	45			30	19	$^{\beta}\sigma_u$
$^{\alpha}10a_{2u}$	1	-5.46	49			32	13	$^{\alpha}\sigma_u$
$^{\beta}13e_{1u}$	2	-6.10	25			75		$^{\beta}\pi_u$
$^{\alpha}13e_{1u}$	2	-6.13	25			74		$^{\alpha}\pi_u$
$^{\alpha}16a_{1g}$	1	-6.43		5		88	7	$^{\alpha}\sigma_g$
$^{\beta}16a_{1g}$	1	-6.45		5		88	7	$^{\beta}\sigma_g$
$^{\beta}5e_{1g}$	2	-6.52		7		83	7	$^{\alpha}\pi_g$
$^{\alpha}5e_{1g}$	2	-6.52		9		82	7	$^{\beta}\pi_g$

Table 4.9. Valence molecular orbital energies, occupations and compositions of $NpO_2Cl_4^{2-}$ (LB94).

$NpO_2(OH)_4^{2-}$

One of the reasons for investigating the hydroxide complexes is that polyoxometallates are, by experimentalists, often characterised as large hydroxides when it comes to their coordination behaviour. The PBE electronic structure of $NpO_2(OH)_4^{2-}$ is similar to $NpO_2Cl_4^{2-}$ (Table 4.10 and Figure 4.3) albeit with some differences. The calculated ground state is $^2A_2$, (δ_u HOMO) and the energetic ordering of the MOs is $\sigma_g < \pi_g < \pi_u < \sigma_u < \delta_u < \varphi_u$. One of the differences to $NpO_2Cl_4^{2-}$ is that the δ_u to φ_u gap has increased from 0.26 eV to 0.77 eV. The main difference in the calculated electronic structure compared with $NpO_2Cl_4^{2-}$ is that there is no uncertainty in what orbital is the highest doubly occupied orbital. Both a visual inspection of the MOs and the atomic orbital contributions confirm that $16b_2$ is σ_u (38% Np 5f, 44% O_{yl} 2p). Unlike the $NpO_2Cl_4^{2-}$ electronic structure there is no splitting of the σ_u into orbitals in-phase or out-of-phase with the hydroxide ligands. In the tetrachloride the two σ_u orbitals bracketed a block of Cl based MOs. In $NpO_2(OH)_4^{2-}$ σ_u is in the middle of a block of ligand based MOs, with 2.20 eV up to the HOMO and 1.23 eV down to the π_u MO.

For the lower energy MOs the composition and relative energies are very similar to what was seen in the $NpO_2Cl_4^{2-}$ calculations. All of the Np-O_{yl} bonding MOs are centred on O_{yl}, with contributions up to 85% from the O_{yl}. The energy range over which the fully occupied bonding MOs are spread is 2.08 eV, a bit larger than expected but not unreasonable. In a few orbitals ($^{\alpha}17b_2$, $^{\beta}17b_2$, $^{\beta}18a_1$ and $^{\alpha}19a_1$) the breakdown of the MOs into AO contributions shows contributions from a large range of AOs, with only a few deemed significant enough to show in a table. Since all of the affected MOs are virtual orbitals it is not strange to find AO contributions that are out of place, as the virtual orbitals are what is left behind when trying to minimize the total energy of the system.

The SAOP and LB94 electronic structures have been calculated (see Tables 4.11 and 4.12) and the results agree remarkably well with the PBE electronic structures. The

ordering of the NpO_2^{2+}-based MOs remain the same $\sigma_g < \pi_g < \pi_u < \sigma_u < \delta_u < \varphi_u$ and the ground state is identical to that found in the PBE calculations: $^2A_2$. Differences can be found in the energy gaps between the various MOs. As with all the previously calculated electronic structures, the HOMO-LUMO gap is very different for the SAOP and LB94 systems; the gap is 2.08 eV using SAOP compared to only 0.34 eV using LB94. Similar to the PBE electronic structure $16b_2$, σ_u, can be found among a block of ligand based MOs and a visual inspection confirms that $16b_2$ is the σ_u for both functionals. The orbital decomposition shows that SAOP is much closer to PBE than to LB94. For example, the Np 5f composition of $^{\beta}16b_2$ is 49% in the LB94 calculation compared to 38% and 36% for PBE and SAOP respectively. As in the PBE calculation the O_{yl} contributions to the π and σ_g MOs are large, with contributions well over 80% in most MOs.

In the SAOP calculation σ_u is about 1 eV from both the HOMO and π_u while in the LB94 calculation the corresponding energy gap is 2 eV up to the HOMO and 1 eV down to π_u. The spread of the bonding MOs is 2.10 eV using SAOP and 1.69 eV using LB94. Unlike the PBE calculation there are no virtual MOs with unphysical AO contributions.

The calculated electronic structures of NpO_2^{2+}, $NpO_2Cl_4^{2-}$, $NpO_2(OH)_4^{2-}$ and corresponding U complexes showed significant differences depending on which functional was employed; the SAOP electronic structures all had relatively large HOMO-LUMO gaps while the LB94 energy gaps were smaller. There is also the fact that previous TDDFT calculations on $UO_2Cl_4^{2-}$ using LB94 underestimated the f-f transition energies compared to SAOP. The difference, as was explained above, was approximately the difference in MO energy between two MOs that could be the HOMO and LB94 is thus expected to perform better with a modified donor orbital. Thus, when using TDDFT to calculate the electronic transitions the choice was made to use LB94 as the experimental data on $NpO_2Cl_4^{2-}$ available indicated that the f-f transitions occur at quite low energies. For comparison, and to confirm that the choice of functional was correct, SAOP transitions were also calculated.

			Composition (%)					
Orbital	Occupation	Energy (eV)	Np f	Np d	Np p	O_{yl}	O_{OH}	NpO_2^{2+} component (Table 4.2)
$^{\beta}18e_1$	0	5.93	84				12	$^{\beta}\varphi_u$
$^{\beta}3a_2$	0	5.85	99					$^{\beta}\delta_u$
$^{\alpha}17b_2$	0	5.76						
$^{\beta}17b_2$	0	5.74						
$^{\beta}19a_1$	0	5.59	96					
$^{\alpha}18e_1$	0	5.45	76				15	$^{\alpha}\varphi_u$
$^{\beta}18a_1$	0	5.32						$^{\beta}\delta_u$
$^{\alpha}19a_1$	0	5.31						
$^{\alpha}18a_1$	0	4.88	95					$^{\alpha}\delta_u$
$^{\alpha}3a_2$	1	4.67	99					$^{\alpha}\delta_u$
$^{\alpha}2a_2$	1	2.88					99	
$^{\beta}2a_2$	1	2.84					99	
$^{\beta}17e_1$	2	2.62				8	80	
$^{\alpha}17e_1$	2	2.60				8	78	
$^{\beta}16b_2$	1	2.47	38			44	8	$^{\beta}\sigma_u$
$^{\beta}16e_1$	2	2.21	10		11		82	
$^{\alpha}16b_2$	1	2.20	38		8	41	9	$^{\alpha}\sigma_u$
$^{\alpha}16e_1$	2	2.18	14				76	
$^{\alpha}4b_1$	1	1.64		11			85	
$^{\alpha}17a_1$	1	1.64		0		15	79	
$^{\beta}4b_1$	1	1.64		10			86	
$^{\beta}17a_1$	1	1.62		0		15	80	
$^{\alpha}15b_2$	1	1.25	7	5		6	69	
$^{\beta}15b_2$	1	1.25	4	4			79	
$^{\beta}15e_1$	2	1.24	11			78	7	$^{\beta}\pi_u$
$^{\alpha}15e_1$	2	1.24	11			76	8	$^{\alpha}\pi_u$
$^{\beta}14e_1$	2	0.96	10	4		73		$^{\beta}\pi_g$
$^{\alpha}14e_1$	2	0.95	14			69	6	$^{\alpha}\pi_g$
$^{\alpha}16a_1$	1	0.42		4		84	7	$^{\alpha}\sigma_g$
$^{\beta}16a_1$	1	0.39		4		85	7	$^{\beta}\sigma_g$

Table 4.10. Valence molecular orbital energies, occupations and compositions of $NpO_2(OH)_4^{2-}$ (PBE)

			Composition (%)					
Orbital	Occupation	Energy (eV)	Np f	Np d	Np p	O_{yl}	O_{OH}	NpO_2^{2+} component (Table 4.2)
$^{\beta}18e_1$	0	2.27	89				9	$^{\beta}\varphi_u$
$^{\beta}18a_1$	0	2.06	96					$^{\beta}\delta_u$
$^{\beta}3a_2$	0	1.63	99					$^{\beta}\delta_u$
$^{\alpha}18e_1$	0	1.23	82				16	$^{\alpha}\varphi_u$
$^{\alpha}18a_1$	0	1.04	96					$^{\alpha}\delta_u$
$^{\alpha}3a_2$	1	-1.04	98					$^{\alpha}\delta_u$
$^{\alpha}2a_2$	1	-1.65					98	
$^{\beta}2a_2$	1	-1.83					99	
$^{\alpha}17e_1$	2	-1.88				10	83	
$^{\beta}17e_1$	2	-1.97				10	81	
$^{\beta}16b_2$	1	-2.05	36		9	46	8	$^{\beta}\sigma_u$
$^{\alpha}16e_1$	2	-2.27	12				77	
$^{\beta}16e_1$	2	-2.35	7				87	
$^{\alpha}16b_2$	1	-2.51	39			33	27	$^{\alpha}\sigma_u$
$^{\alpha}17a_1$	1	-2.75				17	82	
$^{\alpha}4b_1$	1	-2.78		8			87	
$^{\beta}17a_1$	1	-2.91				19	86	
$^{\beta}4b_1$	1	-2.92		7			88	
$^{\alpha}15e_1$	2	-3.12	11			78	7	$^{\alpha}\pi_u$
$^{\alpha}15b_2$	1	-3.20	14			11	65	
$^{\beta}15e_1$	2	-3.22	11			80	6	$^{\beta}\pi_u$
$^{\beta}15b_2$	1	-3.28		6			83	
$^{\alpha}14e_1$	2	-3.42	11			70	7	$^{\alpha}\pi_g$
$^{\beta}14e_1$	2	-3.53				78	5	$^{\beta}\pi_g$
$^{\alpha}16a_1$	1	-3.94		5		85	7	$^{\alpha}\sigma_g$
$^{\beta}16a_1$	1	-4.15		5		84	7	$^{\beta}\sigma_g$

Table 4.11. Valence molecular orbital energies, occupations and compositions of $NpO_2(OH)_4^{2-}$ (SAOP)

			Composition (%)					
Orbital	Occupation	Energy (eV)	Np f	Np d	Np p	O_{yl}	O_{OH}	NpO_2^{2+} component (Table 4.2)
$^{\beta}18e_1$	0	0.09	82				14	$^{\beta}\varphi_u$
$^{\alpha}18e_1$	0	-0.19	78				17	$^{\alpha}\varphi_u$
$^{\beta}3a_2$	0	-0.23	99					$^{\beta}\delta_u$
$^{\beta}18a_1$	0	-0.37	96					$^{\beta}\delta_u$
$^{\alpha}18a_1$	0	-0.70	95					$^{\alpha}\delta_u$
$^{\alpha}3a_2$	1	-1.04	99					$^{\alpha}\delta_u$
$^{\alpha}2a_2$	1	-2.57					98	
$^{\beta}2a_2$	1	-2.60					98	
$^{\beta}17e_1$	2	-2.74				7	80	
$^{\alpha}17e_1$	2	-2.76				8	78	
$^{\beta}16b_2$	1	-3.02	49			39		$^{\beta}\sigma_u$
$^{\beta}16e_1$	2	-3.17	12				82	
$^{\alpha}16e_1$	2	-3.19	15				77	
$^{\alpha}16b_2$	1	-3.25	44		6	34	14	$^{\alpha}\sigma_u$
$^{\alpha}17a_1$	1	-3.63				14	83	
$^{\alpha}4b_1$	1	-3.64		7			88	
$^{\beta}4b_1$	1	-3.64		6			89	
$^{\beta}17a_1$	1	-3.65				14	83	
$^{\beta}15b_2$	1	-3.95	6				80	
$^{\alpha}15b_2$	1	-3.96	11			8	68	
$^{\alpha}15e_1$	2	-4.09	8			79	7	$^{\alpha}\pi_u$
$^{\beta}15e_1$	2	-4.10	8			80	7	$^{\beta}\pi_u$
$^{\beta}14e_1$	2	-4.34	13			74	8	$^{\beta}\pi_g$
$^{\alpha}14e_1$	2	-4.36	16			71	9	$^{\alpha}\pi_g$
$^{\alpha}16a_1$	1	-4.68		5		86	7	$^{\alpha}\sigma_g$
$^{\beta}16a_1$	1	-4.71		5		86	10	$^{\beta}\sigma_g$

Table 4.12. Valence molecular orbital energies, occupations and compositions of $NpO_2(OH)_4^{2-}$ (LB94)

$NpO_2(H_2O)_5^{2+}$

The electronic structure of NpO_2^{2+} with five water molecules explicitly included in the equatorial plane has been investigated using LB94 and SAOP to determine the influence of the solvent compared to the electronic structure of the bare NpO_2^{2+} discussed above and the POM electronic structure.[52]

			Composition (%)					
Orbital	Occupation	Energy (eV)	Np f	Np d	Np p	O_{yl}	O_{H2O}	NpO_2^{2+} component (Table 4.2)
$^{\beta}18b_1$	0	-17.50	99					δ_u
$^{\beta}35a_1$	0	-17.64	94					φ_u
$^{\beta}21b_2$	0	-17.69	95					φ_u
$^{\beta}8a_2$	0	-17.69	99					δ_u
$^{\alpha}18b_1$	0	-18.36	98					δ_u
		-20.40	*97*					
$^{\alpha}35a_1$	0	-18.59	92					φ_u
		-20.51	*91*					
$^{\alpha}21b_2$	0	-18.65	93					φ_u
		-20.58	*90*					
$^{\alpha}8a_2$	1	-20.25	99					δ_u
		-20.67	*99*					
$^{\beta}17b_1$	1	-21.23	28		6	20	42	σ_u / H_2O
		-22.18	*13*			*12*	*68*	
$^{\alpha}17b_1$	1	-21.27	5			8	82	σ_u / H_2O
		-22.22	*8*			*8*	*79*	
$^{\alpha}20b_2$	1	-21.44					96	
$^{\beta}20b_2$	1	-21.57					96	
$^{\alpha}34a_1$	1	-21.72					95	
$^{\beta}16b_1$	1	-21.74	25		4	15	48	σ_u
		-22.74	*45*			*25*	*21*	
$^{\beta}34a_1$	1	-21.85					95	
$^{\alpha}19b_2$	1	-22.08					89	
$^{\alpha}16b_1$	1	-22.13	53		7	31	7	σ_u
		-22.97	*53*		*6*	*27*	*10*	
$^{\beta}19b_2$	1	-22.19					90	
$^{\alpha}33a_1$	1	-22.35	17			46	34	
$^{\alpha}18b_2$	1	-22.40	26			66		
$^{\beta}33a_1$	1	-22.41	18			67	9	
$^{\alpha}32a_1$	1	-22.42	12			23	61	
$^{\beta}18b_2$	1	-22.46	19			72		
$^{\beta}32a_1$	1	-22.52					83	

Table 4.13. Valence molecular orbital energies, occupations and compositions for $NpO_2(H_2O)_5^{2+}$. SAOP data are given in upright text, while LB94 data for selected orbitals are given in italics. POM basis set.

The calculated HOMO for $NpO_2(H_2O)_5^{2+}$ was δ_u for both SAOP and LB94. The calculated electronic structure (Table 4.13) shows the same functional dependence as was seen in $NpO_2Cl_4^{2-}$, with two MOs of the correct symmetry to be the σ_u, $17b_1$ and $16b_1$. Using the same arguments as in the tetrachloride, it was determined that the "correct" σ_u is $16b_1$, due to a higher contribution from Np f and O_{yl} as well as a visual inspection showing out of phase ligand interactions in $17b_1$. The main difference between the SAOP and LB94 electronic structure is that the HOMO-LUMO gap is very small using LB94, 0.09 eV, compared to 1.61 eV using SAOP. This difference in gap size is in agreement with what was found for the other small Np complexes, for example the HOMO-LUMO gap in $NpO_2(OH)_4^{2-}$ was found to be 0.34 eV and 2.08 eV for LB94 and SAOP respectively. For NpO_2^{2+} the HOMO-LUMO gap was 0.24 eV and 1.13 eV, smaller than in the hydroxide systems but the overall electronic structures are very similar. The difference in MO energies between the hydroxide and water complexes should be reflected in higher calculated transition energies for the hydroxide complex compared to the water complex, which will be discussed in the TDDFT section below.

$Na_2(GeW_9O_{34})_2(NpO_2)_2^{14-}$

It was established above that LB94 produces the best electronic structure of the small neptunyl systems, thus the electronic structure of $Na_2(GeW_9O_{34})_2(NpO_2)_2^{14-}$ was investigated using that functional. The SAOP electronic structure is included in Appendix 1. The neptunyl based MOs in the valence electronic structure (Table 4.14) are flanked by blocks of MOs located on the oxygen atoms of the polyoxometallate, illustrated by $548a_u$ and $548a_g$ where all O_{POM} contributions have been added to one value. The HOMO is δ_u and the HOMO-LUMO gap is 0.24 eV using LB94 and 1.70 eV using SAOP. The presence of two NpO_2^{2+} units in the complex is the reason for the two f-based δ-levels in the electronic structure. Although the HOMO-LUMO gap is identical to the calculated gap in NpO_2^{2+} the HOMO is different, φ_u compared to δ_u in the POM complex.

The AO composition of the σ-bonding MOs are different than in the NpO_2^{2+} calculation due to the presence of the POM and the Np f and O_{yl} contributions are relatively small. Thus the doubly occupied valence MOs, σ_u and σ_g were identified using both the AO compositions and visual inspection. Comparing the MO compositions of σ_u and σ_g in NpO_2^{2+} coordinated to the POM with the compositions of the same MOs in $NpO_2Cl_4^{2-}$ and $NpO_2(OH)_4^{2-}$, shows significant mixing in of O p AOs from the POM, substantially larger than what was seen with Cl^- or OH^- equatorial ligands; in $NpO_2Cl_4^{2-}$ the Cl contribution was 19% and 7% for σ_u and σ_g respectively while in $NpO_2(OH)_4^{2-}$ the contribution was *ca* 10% in each MO. Thus, using the MO composition to characterise polyoxometallates as large hydroxides is difficult using $Na_2(GeW_9O_{34})_2(NpO_2)_2^{14-}$. The energy gap between σ_u and the HOMO is *ca* 2 eV compared to *ca* 1.5 eV in NpO_2^{2+}. The span between σ_u and σ_g was found to be *ca* 0.4 eV in the present calculation, again close to the span found in NpO_2^{2+}. The present results indicate that the electronic structure of NpO_2^{2+} is reasonably conserved on complexation with the polyoxometallates, in line with results on $NpO_2Cl_4^{2-}$ and $NpO_2(OH)_4^{2-}$.

			Composition (%)					
Orbital	Occupation	Energy (eV)	Np f	Np d	Np p	O_{yl}	O_{POM}	NpO_2^{2+} component (Table 4.2)
$^{\alpha}552a_g$	0	19.36	76					$^{\alpha}\varphi$
$^{\alpha}552a_u$	0	19.34	75					$^{\alpha}\varphi$
$^{\beta}549a_u$	0	19.32	86					$^{\alpha}\varphi$
$^{\beta}549a_g$	0	19.32	85					$^{\alpha}\varphi$
$^{\alpha}551a_g$	0	19.18	88					$^{\alpha}\varphi$
$^{\alpha}551a_u$	0	19.18	89					$^{\alpha}\varphi$
$^{\alpha}550a_u$	0	19.05	82					$^{\alpha}\varphi_u$
$^{\alpha}550a_g$	0	19.04	82					$^{\alpha}\varphi$
$^{\alpha}549a_u$	1	18.80	91					$^{\alpha}\delta_u$
$^{\alpha}549a_g$	1	18.80	91					$^{\alpha}\delta$
$^{\beta}548a_g$	1	17.82					84	POM-based
$^{\alpha}548a_g$	1	17.82					83	POM-based
$^{\beta}548a_u$	1	17.81					85	POM-based
$^{\alpha}548a_u$	1	17.80					85	POM-based
$^{\beta}526a_u$	1	16.79	6			5	64	σ_u
$^{\alpha}518a_g$	1	16.44	6			4	57	σ_g

Table 4.14. Valence molecular orbital energies, occupations and compositions of $Na_2(GeW_9O_{34})_2(NpO_2)_2^{14-}$ (LB94, TDA)

Electronic transitions

UO_2^{2+} and NpO_2^{2+}

TDDFT calculations of the electronic spectrum of UO_2^{2+} have recently been performed and published.[51] In the present investigation the published SAOP UO_2^{2+} transition energies were reproduced and, due to uranyl having a well defined electronic structure, unambiguously assigned to donor and acceptor orbitals. Thus the focus of this section will be on the neptunyl TDDFT calculations, and the UO_2^{2+} data will not be given as they are in reference [51].

The calculated LB94 and SAOP transition energies in NpO_2^{2+} are presented in Tables 4.15 and 4.16. The calculated transitions include only transitions out of the Np based f orbitals as well from the σ_u and σ_g MOs, the highest doubly occupied MOs. Transitions out of the π MOs have not been included in this investigation.

The result of the LB94 calculation on NpO_2^{2+} is displayed in Table 4.15. The spin-flip δ_u to φ_u f-f transitions occur at 0.26 eV and 0.28 eV to $26a_1$ and $5a_2$ respectively. The decrease in symmetry to C_{2v} is the reason for this split in MOs. The corresponding spin-allowed transitions are calculated to 0.31 eV and 0.35 eV. These transition energies are close to the naive view of transition energies, that they equal the difference in MO energies; the difference in LB94 MO energy between the $^{\alpha}13b_1$ and $26a_1$ and $5a_2$ are 0.24 eV and 0.26 eV respectively, close to the calculated transition energies. Transitions out of the fully occupied σ_u orbital, $25a_1$, are significantly higher in energy, starting at 1.40 eV with the spin-flip transitions slightly lower in energy than the corresponding spin-allowed transitions, which start at 1.64 eV, close to the 1.74 eV difference in MO energy. Most calculated transitions have close to zero oscillator strengths, e.g. the oscillator strength of the $^{\alpha}13b_1 \rightarrow {}^{\alpha}26a_1$ transition is 3.39×10^{-20}.

The calculated SAOP transitions (Table 4.16) in NpO_2^{2+} are different to the LB94 transitions; the f-f transition energies are significantly higher in energy than in the LB94 calculations, 1.18 eV in the SAOP calculation compared to 0.26 eV for LB94. Again, the reason for this is the difference in the valence electronic structure; the SAOP HOMO is δ_u compared to the φ_u LB94 HOMO but the main difference is the energy gap between the HOMO and the LUMO, which at 1.13 eV is close to the first calculated f-f transition.

Energy/eV	Energy/cm^{-1}	*f*	Transition symmetry	Principal orbital contribution (Table 4.2)
0.26	2112	0	B_1	$^{\alpha}13b_1 \rightarrow {}^{\beta}26a_1$ ($\varphi \rightarrow \delta$)
0.28	2294	0	B_2	$^{\alpha}13b_1 \rightarrow {}^{\beta}5a_2$ ($\varphi \rightarrow \delta$)
0.31	2467	3.39×10^{-20}	B_1	$^{\alpha}13b_1 \rightarrow {}^{\alpha}26a_1$ ($\varphi \rightarrow \delta$)
0.35	2799	2.91×10^{-21}	B_2	$^{\alpha}13b_1 \rightarrow {}^{\alpha}5a_2$ ($\varphi \rightarrow \delta$)
1.40	11274	0	A_1	$^{\beta}25a_1 \rightarrow {}^{\alpha}26a_1$ ($\sigma_u \rightarrow \delta$)
1.43	11541	0	A_2	$^{\beta}25a_1 \rightarrow {}^{\alpha}5a_2$ ($\sigma_u \rightarrow \delta$)
1.64	13264	4.63×10^{-23}	A_1	$^{\alpha}25a_1 \rightarrow {}^{\alpha}26a_1$ ($\sigma_u \rightarrow \delta$)
1.66	13361	0	A_2	$^{\alpha}25a_1 \rightarrow {}^{\alpha}5a_2$ ($\sigma_u \rightarrow \delta$)
1.84	14870	0	B_2	$^{\beta}25a_1 \rightarrow {}^{\alpha}13b_2$ ($\sigma_u \rightarrow \varphi$)
1.97	15862	0	A_1	$^{\alpha}25a_1 \rightarrow {}^{\beta}26a_1$ ($\sigma_u \rightarrow \delta$)
1.97	15867	0	A_2	$^{\alpha}25a_1 \rightarrow {}^{\beta}5a_2$ ($\sigma_u \rightarrow \delta$)
2.08	16804	0	A_1	$^{\beta}24a_1 \rightarrow {}^{\alpha}26a_1$ ($\sigma_g \rightarrow \delta$)
2.11	17026	0	A_2	$^{\beta}24a_1 \rightarrow {}^{\alpha}5a_2$ ($\sigma_g \rightarrow \delta$)
2.11	17054	1.04×10^{-21}	B_2	$^{\beta}25a_1 \rightarrow {}^{\beta}13b_2$ ($\sigma_u \rightarrow \varphi$)
2.12	17108	0	A_2	$^{\alpha}24a_1 \rightarrow {}^{\alpha}5a_2$ ($\sigma_g \rightarrow \delta$)
2.33	18831	8.90×10^{-20}	B_1	$^{\beta}25a_1 \rightarrow {}^{\beta}13b_2$ ($\sigma_u \rightarrow \varphi$)
2.39	19262	0	B_1	$^{\alpha}25a_1 \rightarrow {}^{\beta}13b_1$ ($\sigma_u \rightarrow \varphi$)
2.42	19548	0	A_2	$^{\alpha}24a_1 \rightarrow {}^{\beta}5a_2$ ($\sigma_g \rightarrow \delta$)
2.43	19581	0	B_2	$^{\beta}24a_1 \rightarrow {}^{\alpha}13b_2$ ($\sigma_g \rightarrow \varphi$)
2.43	19593	0	A_1	$^{\alpha}24a_1 \rightarrow {}^{\beta}26a_1$ ($\sigma_g \rightarrow \delta$)
2.43	19634	0	A_2	$^{\beta}24a_1 \rightarrow {}^{\beta}5a_2$ ($\sigma_g \rightarrow \delta$)
2.44	19683	7.57×10^{-9}	A_1	$^{\beta}24a_1 \rightarrow {}^{\beta}26a_1$ ($\sigma_g \rightarrow \delta$)

Table 4.15: Calculated TDA LB94 transition energies and characters in NpO_2^{2+} in C_{2v} *(δ: a_1+a_2, φ: b_1+b_2)*

Also the calculated transitions out of σ_u occur at higher energies than the σ_u transitions using LB94, 2.46 eV compared to 1.64 eV in LB94. The difference in MO energy is 2.02 eV, reasonably close to the calculated transition. The SAOP oscillator strengths for the f-f transition are similar to the LB94 oscillator strengths, i.e. almost zero. Transitions out of σ_g though have higher oscillator strengths, e.g. the $^{\beta}24a_1 \rightarrow {}^{\beta}13b_1$ transition has an oscillator strength of 3.12×10^{-5}, far higher than what was seen for the other transitions.

Energy/eV	Energy/cm^{-1}	*f*	Transition symmetry	Principal orbital contribution
1.18	9505	5.35 x 10^{-21}	B_1	$^{\alpha}26a_1 \rightarrow {}^{\alpha}13b_1$ ($\delta \rightarrow \varphi$)
1.18	9505	4.81 x 10^{-21}	B_2	$^{\alpha}26a_1 \rightarrow {}^{\alpha}13b_2$ ($\delta \rightarrow \varphi$)
1.64	13253	0	A_2	$^{\alpha}26a_1 \rightarrow {}^{\alpha}5a_2$ ($\delta \rightarrow \delta$)
2.46	19868	8.32 x 10^{-20}	B_1	$^{\alpha}25a_1 \rightarrow {}^{\alpha}13b_1$ ($\sigma_u \rightarrow \varphi$)
2.46	19868	3.99 x 10^{-20}	B_2	$^{\alpha}25a_1 \rightarrow {}^{\alpha}13b_2$ ($\sigma_u \rightarrow \varphi$)
2.70	21736	1.39 x 10^{-5}	B_1	$^{\alpha}24a_1 \rightarrow {}^{\alpha}13b_1$ ($\sigma_g \rightarrow \varphi$)
2.70	21736	1.39 x 10^{-5}	B_2	$^{\alpha}24a_1 \rightarrow {}^{\alpha}13b_2$ ($\sigma_g \rightarrow \varphi$)
2.93	23598	2.99 x 10^{-21}	A_1	$^{\alpha}12b_2 \rightarrow {}^{\alpha}13b_2$ ($\pi_u \rightarrow \varphi$)
2.93	23606	0	A_2	$^{\alpha}12b_1 \rightarrow {}^{\alpha}13b2$ ($\pi_u \rightarrow \varphi$)
2.96	23866	0	A_2	$^{\alpha}12b_2 \rightarrow {}^{\alpha}13b_1$ ($\pi_u \rightarrow \varphi$)
2.96	23869	4.01 x 10^{-19}	A_1	$^{\alpha}12b1 \rightarrow {}^{\alpha}13b_1$ ($\pi_u \rightarrow \varphi$)
3.02	24347	2.51 x 10^{-20}	B_1	$^{\beta}25a_1 \rightarrow {}^{\beta}13b_1$ ($\sigma_u \rightarrow \varphi$)
3.02	24347	7.91 x 10^{-20}	B_2	$^{\beta}25a_1 \rightarrow {}^{\beta}13b_2$ ($\sigma_u \rightarrow \varphi$)
3.11	25072	0	A_2	$^{\alpha}25a_1 \rightarrow {}^{\alpha}5a_2$ ($\sigma_u \rightarrow \delta$)
3.19	25689	0	A_2	$^{\alpha}11b_1 \rightarrow {}^{\alpha}13b_2$ ($\pi_g \rightarrow \varphi$)
3.19	25764	5.87 x 10^{-4}	A_1	$^{\alpha}11b_2 \rightarrow {}^{\alpha}13b_2$ ($\pi_g \rightarrow \varphi$)
3.21	25902	3.20 x 10-^{16}	A_1	$^{\alpha}11b_1 \rightarrow {}^{\alpha}13b_1$ ($\pi_g \rightarrow \varphi$)
3.21	25910	0	A_2	$^{\alpha}11b_2 \rightarrow {}^{\alpha}13b_1$ ($\pi_g \rightarrow \varphi$)
3.45	27841	0	A_2	$^{\alpha}24a_1 \rightarrow {}^{\alpha}5a_2$ ($\sigma_g \rightarrow \delta$)
3.53	28448	2.57 x 10^{-18}	A_1	$^{\beta}25a_1 \rightarrow {}^{\beta}26a_1$ ($\sigma_u \rightarrow \delta$)
3.70	29801	1.63 x 10^{-19}	B_1	$^{\alpha}12b_2 \rightarrow {}^{\alpha}5a_2$ ($\pi_u \rightarrow \delta$)
3.70	29801	1.12 x 10^{-18}	B_2	$^{\alpha}12b_1 \rightarrow {}^{\alpha}5a_2$ ($\pi_u \rightarrow \delta$)
3.79	30530	0	A_2	-
3.90	31460	3.12 x 10^{-5}	B_1	$^{\beta}24a_1 \rightarrow {}^{\beta}13b_1$ ($\sigma_g \rightarrow \varphi$)
3.90	31460	3.12 x 10^{-5}	B_2	$^{\beta}24a_1 \rightarrow {}^{\beta}13b_2$ ($\sigma_g \rightarrow \varphi$)

Table 4.16. Calculated SAOP transitions for NpO_2^{2+} in C_{2v} *(δ: a_1+a_2, φ: b_1+b_2)* (No spin-flip transitions. No TDA)

The NpO_2^{2+} transitions calculated by Pitzer *et al.* are shown in Table 4.17. The calculation was performed using SOCI, which means that the calculation takes spin-orbit effects into consideration which, at present, can not be investigated using TDDFT in ADF. However, the comparison with experimental data is still interesting as it gives an indication of whether the calculated f-f transitions should occur at *ca* 10000 cm^{-1} as in the SAOP calculation or at *ca* 2500 cm^{-1} as in the LB94 calculation. The experimental results on $Cs_2NpO_2Cl_4$ show that the first proper f-f transition, i.e. a transition from a state with majority φ to a majority δ state occurs at 1000 cm^{-1} and the second φ to δ at 6880 cm^{-1}. The first σ_u to f transition is found experimentally at 13265 cm^{-1}.

In Pitzer *et al.*'s results on NpO_2^{2+} the lower energy f-f transitions occur at 447 cm^{-1} and 5515 cm^{-1} depending on the excited state. For the present TDDFT calculations the first

LB94 f-f transition is at around 2500 cm^{-1} and the first charge transfer transition at 11274 cm^{-1}. The corresponding SAOP transitions are at 9505 cm^{-1} and 19868 cm^{-1}. The difference between the TDDFT and the SOCI results are smaller for LB94 than for SAOP, particularly looking at the transitions out of the σ_u, where the difference between the calculated SOCI transition and the first LB94 transition is 1348 cm^{-1} compared to 7246 cm^{-1} for SAOP. Thus, it appears that LB94 is the functional that produces the best TDDFT results on NpO_2^{2+}, but the agreement with previous calculations is adequate at best.

Experimental NpO_2^{2+} spectra can not be obtained as the isolated ion has not been made. However, NpO_2^{2+} in solution has been characterised by Talbot-Eeckelaers *et al.* for the study of polyoxometallates and an f-f transition was found at 1223 nm (1.01 eV or 8177 cm^{-1}).[52] This transition energy is close to what was found in the SAOP calculations and significantly higher than the f-f transitions from crystallographic investigations. It suggests that SAOP might be a better functional for reproducing the experimental results. However, as see in Table 4.17, there exist more than one f-f transition and it is thus not possible to say which one is found experimentally.

State	Configuration	cm^{-1}	$Cs_2NpO_2Cl_4$ [137, 138]
$5/2_u$	68% $^2\Phi_{5/2u}$ + 17% $^2\Delta_{3/2u}$	0	0
$3/2_u$	85 % $^2\Delta_{3/2u}$	447	1000
$5/2_u$	85 % $^2\Phi_{7/2u}$	5515	6880.4
$7/2_u$	69% $^2\Delta_{3/2u}$ + 17% $^2\Phi_{5/2u}$	6565	7990
$7/2_u$	85% $^4H_{7/2u}$ ($\sigma_u\delta_u\varphi_u$)	12622	13264.9
$9/2_u$	83% $^4H_{9/2u}$ ($\sigma_u\delta_u\varphi_u$)	15418	15683
$1/2_u$	60% $^4\Sigma_{1/2u}$ ($\sigma_u\delta_u^2$)	15668	15406.4
$3/2_u$	65% $^4\Sigma_{3/2u}$ ($\sigma_u\delta_u^2$)	16664	16799.8
$1/2_u$	52% $^4\Pi_{1/2u}$ + 24% $^4\Pi_{-1/2u}$ ($\sigma_u\delta_u\varphi_u$)	21580	19375

Table 4.17. The calculated SOCI and the experimental electronic transitions in NpO_2^{2+}. The assignment of the different electronic states is part of the SOCI calculation.

$UO_2Cl_4^{2-}$ and $NpO_2Cl_4^{2-}$

There have been several studies carried out on $UO_2Cl_4^{2-}$ to determine the influence equatorial ligands have on the electronic excitations. Recently Pierloot *et al.*[51],

investigating the system using TDDFT and a set of various functionals, and found that SAOP produced better results than LB94 and various GGA functionals for the low energy excitations. The published SAOP results on $UO_2Cl_4^{2-}$ showed good agreement with CASPT2 results and with experimental data while the LB94 results were consistently about 8000 cm^{-1}, *ca* 1 eV, too low. As has been mentioned above, the study by Vallet *et al.*[144] on the excitations in UO_2^{2+} showed TDDFT to be inadequate for the higher energy excitations out of the π MOs.

The present PBE and SAOP calculations on $UO_2Cl_4^{2-}$ produced very different ground state structures in terms of energy separations of the MOs. However, in both of the calculated electronic structures there was a split of the σ_u in a bonding and an anti-bonding MO with respect to the Cl ligands. The anti-bonding MO was in the present work characterised as a ligand based MO with some σ_u character, which was confirmed by the MO decompositions. The Pierloot study found the donor σ_u to have a significant amount of Cl character, around 73%. This would match the decomposition of the anti-bonding $11a_{2u}$ MO in our calculation. In work by Green *et al.*[120] the $10a_{2u}$ MO has been characterized as the σ_u, the same characterisation as used in the present work.

In the LB94 and SAOP transitions out of the $UO_2Cl_4^{2-}$ $10a_{2u}$ MO (Table 4.18) an increase in transition energy moving from LB94 to SAOP is seen compared to results from references 51 and 122, corresponding roughly to the difference in MO energy between the $11a_{2u}$ and the $10a_{2u}$, 1.2 eV (*ca* 10000 cm^{-1}). This shift changes the conclusion on which functional is the best suited for the $UO_2Cl_4^{2-}$ electronic transitions, as the calculated LB94 transitions now show much better agreement with the CASPT2 results than the SAOP transitions, which are now about 10000 cm^{-1} too high in energy. However, the ordering of the singlet states are different in the LB94 calculation from what was found using CASPT2; the CASPT2 ordering is $^1E_{1g} \approx {}^1B_{1g} < {}^1B_{2g}$ while the corresponding LB94 ordering is $^1B_{1g} < {}^1B_{2g} \approx {}^1E_{1g}$. The SAOP ordering in the present work is $^1B_{1g} \approx {}^1E_{1g} < {}^1B_{2g}$, almost the same as the CASPT2 ordering except for the minor differences in energy of the $^1B_{1g}$ and $^1E_{1g}$ transitions. Since the difference in transition

energy is so much greater using SAOP compared to LB94 the conclusion is that LB94 produces a better electronic structure for $UO_2Cl_4^{2-}$.

The first calculated SAOP transition for $NpO_2Cl_4^{2-}$ is $^{\alpha}2b_{1u}$ to $^{\alpha}16e_u$ (δ_u to φ_u) at 13642 cm^{-1}, a δ_u to φ_u transition (Table 4.19). The second calculated transition ($^{\alpha}2b_{1u}$ to $^{\alpha}4b_{2u}$) at 14058 cm^{-1} is a δ_u to δ_u transition. In D_{4h} δ_u corresponds to b_{1u} + b_{2u}, and since the two b_u irreps are separated in energy due to the b_{1u} being an occupied MO, a b_{1u}-b_{2u} transition is possible. The calculated f-f transition is much higher in energy than seen experimentally (Table 4.17), where the f-f transitions start at 1000 cm^{-1} and continue up to *ca* 8000 cm^{-1}. Clearly SAOP does a poor job in reproducing these low energy transitions.

	LB94		SAOP		CASPT2
State	Reference 51	This work	Reference 51	This work	Reference 122
$^3B_{1g}$	13408	23174	22601	32528	22862
$^3B_{2g}$	14670	24500	23825	33807	23711
^3E_g	16556	26799	24715	34800	27175
$^1B_{1g}$	15041	27695	24600	36643	30736
^1E_g	17102	28995	25837	36853	30624
$^1B_{2g}$	16925	28924	26153	37848	31578

Table 4.18. Calculated spin-orbit free σ_u transition energies in $UO_2Cl_4^{2-}$. The transitions given as "This work" may all be characterized as being between the occupied $10a_{2u}$ (σ_u) level and the unoccupied $2b_{1u}$, $4b_{2u}$ and $16e_u$ 5f-based orbitals.

Makhyoun also found a b_1 to b_2 transition, but at lower energy, 1052 cm^{-1} compared to 13642 cm^{-1} for SAOP TDDFT.[126] The difference in calculated energy for this transition may be due to failings in SAOP as the difference in energy between the $2b_{1u}$ and $4b_{2u}$ MOs is large for formally degenerate MOs. Interestingly, the transition energy for the δ_u to φ_u ($2b_{1u}$ to $16e_u$) transition is lower than the transition to $4b_{2u}$, while the reverse is true for the experimental results. However, the difference is only 416 cm^{-1}. Experimentally the difference between these two transitions is around 6000 cm^{-1}.

The first SAOP charge transfer excitation out of the anti-bonding σ_u/Cl MO ($^{\alpha}11a_{2u} \rightarrow 16e_u$ or $\sigma_u \rightarrow \varphi_u$) corresponds roughly, in terms of transition energies, with the experimental charge transfer transitions. Transitions out of the "real" σ_u, $10a_{2u}$, on the other hand are about 1 eV (8000 cm^{-1}) higher in energy, again the difference in MO energy between the $11a_{2u}$ and $10a_{2u}$.

Energy/eV	Energy/cm^{-1}	*f*	Transition symmetry	Principal orbital contribution (Table 4.2)
1.69	13642	0	E_g	$^{\alpha}2b_{1u} \rightarrow {}^{\alpha}16e_u$ ($\delta \rightarrow \varphi$)
1.74	14058	0	A_{2g}	$^{\alpha}2b_{1u} \rightarrow {}^{\alpha}4b_{2u}$ ($\delta \rightarrow \delta$)
1.93	15539	6.27 x 10^{-3}	E_u	$^{\alpha}2a_{2g} \rightarrow {}^{\alpha}16e_u$ (Cl $\rightarrow$ Np)
2.02	16311	0	A_{1u}	$^{\alpha}6e_g \rightarrow {}^{\alpha}16e_u$ (Cl $\rightarrow$ Np)
2.02	16312	0	B_{1u}	$^{\alpha}6e_g \rightarrow {}^{\alpha}16e_u$ (Cl $\rightarrow$ Np)
2.02	16330	0	B_{2u}	$^{\alpha}6e_g \rightarrow {}^{\alpha}16e_u$ (Cl $\rightarrow$ Np)
2.02	16332	4.54 x 10^{-5}	A_{2u}	$^{\alpha}6e_g \rightarrow {}^{\alpha}16e_u$ (Cl $\rightarrow$ Np)
2.12	17069	0	E_g	$^{\alpha}11a_{2u} \rightarrow {}^{\alpha}16e_u$ (σ_u/Cl $\rightarrow \varphi$)
2.13	17160	0	B_{1u}	$^{\alpha}2a_{2g} \rightarrow {}^{\alpha}4b_{2u}$ (Cl $\rightarrow$ Np)
2.25	18165	0	E_g	$^{\alpha}3b_{2u} \rightarrow {}^{\alpha}16e_u$ (Cl $\rightarrow$ Np)
2.30	18554	0	B_{2g}	$^{\alpha}15e_u \rightarrow {}^{\alpha}16e_u$ (Cl $\rightarrow$ Np)
2.31	18609	0	B_{1g}	$^{\alpha}15e_u \rightarrow {}^{\alpha}16e_u$ (Cl $\rightarrow \varphi$)
2.31	18646	1.13 x 10^{-2}	E_u	$^{\alpha}6e_g \rightarrow {}^{\alpha}4b_{2u}$ (Cl $\rightarrow$ Np)
2.35	18923	0	A_{2g}	$^{\alpha}15e_u \rightarrow {}^{\alpha}16e_u$ (Cl $\rightarrow$ Np)
2.38	19160	0	B_{1g}	$^{\alpha}11a_{2u} \rightarrow {}^{\alpha}4b_{2u}$ (σ_u/Cl $\rightarrow \delta$)
2.39	19268	0	A_{1g}	$^{\alpha}15e_u \rightarrow {}^{\alpha}16e_u$ (Cl $\rightarrow$ Np)
2.48	19998	0	B_{2g}	$^{\alpha}14e_u \rightarrow {}^{\alpha}16e_u$ (Cl $\rightarrow \varphi$)
2.50	20163	0	A_{1g}	$^{\alpha}3b_{2u} \rightarrow {}^{\alpha}4b_{2u}$ (Cl $\rightarrow$ Np)
2.53	20388	0	A_{2g}	$^{\alpha}14e_u \rightarrow {}^{\alpha}16e_u$ (Cl $\rightarrow \varphi$)
2.59	20915	0	E_g	$^{\alpha}15e_u \rightarrow {}^{\alpha}4b_{2u}$ (Cl $\rightarrow$ Np)
2.65	21353	0	B_{1g}	$^{\alpha}14e_u \rightarrow {}^{\alpha}16e_u$ (Cl $\rightarrow$ Np)
2.76	22301	0	E_g	$^{\alpha}14e_u \rightarrow {}^{\alpha}4b_{2u}$ (Cl $\rightarrow \delta$)
2.85	22974	0	A_{1g}	-
2.86	23052	5.41 x 10^{-3}	E_u	$^{\alpha}5b_{2g} \rightarrow {}^{\alpha}16e_u$ (Cl $\rightarrow$ Np)
3.06	24665	0	B_{2u}	$^{\alpha}2a_{2g} \rightarrow {}^{\alpha}2b_{1u}$ (Cl $\rightarrow$ Np)

Table 4.19. Calculated spin-orbit free transition energies in $NpO_2Cl_4^{2-}$ (SAOP, no TDA, no spin flip transitions)

Experimental spectra indicate that equatorial ligand-to-metal charge transfers do not take place at the energies at which transitions f-f or σ-f transitions occur. The results of the SAOP TDDFT calculations show that the first Cl to Np transfer transition is at 15539 cm^{-1}. Unlike the formally forbidden f-f transitions, which have oscillator strength zero, this calculated charge transfer transition has oscillator strength 6.27 x 10^{-3}. All of the calculated transitions with oscillator strength above zero are in fact ligand-to-metal charge transfers. Since experimental data in this energy region, below 30000 cm^{-1}, does

not find any ligand-to-metal transitions, only comparisons of theoretical and non charge transfer transitions experimental data will be done. However, it is certainly worth noting that the block of ligand based MOs between the $11a_{2u}$ and $10a_{2u}$ bonding orbitals play a significant role in the calculated spectrum, which is not found experimentally.

As the most interesting transitions are the low energy transitions, the SAOP results for the f-f transitions are discouraging. The first calculated LB94 f-f transition (see Appendix 1) is a δ-δ transition at 1452 cm^{-1} with the remaining f-f transitions at 3187 cm^{-1}, 3510 cm^{-1} and 3714 cm^{-1}. The higher energy transitions among this group, the 3187 cm^{-1} and the 3714 cm^{-1} transitions, are both proper δ to φ transitions, with the 3714 cm^{-1} transition being the spin-forbidden $^{\alpha}2b_{1u} \rightarrow {}^{\beta}16e_u$ transition. All of these energies are significantly lower than what was found in the SAOP calculations, where the first f-f transition was at 13642 cm^{-1}. Going back to experiment, the f-f transitions were relatively low in energy, between 1000 cm^{-1} and 8000 cm^{-1}. All the LB94 f-f transitions are calculated to be around 3500 cm^{-1}. The deviation from experiment is less than what was found for SAOP but the agreement with experimental data is qualitative at best.

Below the block of f-f transitions a large block of Cl based transitions was found, stretching from 11909 cm^{-1} down to the first transition out of $10a_{2u}$ at 21617 cm^{-1}. The first transition out of $11a_{2u}$ occurs at 12255 cm^{-1}, but as has been established previously, this is not the true σ_u MO even though the agreement with experiment would be good at this energy. All the TDDFT results confirm that LB94 does better than SAOP in calculating the low energy spectrum, with the f-f transition energies being close to the average of the experimental values.

$NpO_2(OH)_4^{2-}$

The first calculated SAOP transition (Appendix 1) at 14860 cm^{-1} is $^{\alpha}3a_2 \rightarrow 18a_1$, a δ to δ transition. The second transition is $^{\alpha}3a_2 \rightarrow 18e_1$, a δ to φ transition at 17805 cm^{-1}, 3000 cm^{-1} higher in energy. As with $NpO_2Cl_4^{2-}$ the ligand based transitions feature prominently

among the calculated transitions. Throughout a span of about 10000 cm^{-1} higher in energy than the f-f transitions only ligand-to-metal charge transfer transitions were found. The first SAOP transition out of σ_u, $16b_2 \rightarrow 18a_1$, is calculated at 27763 cm^{-1} (3.44 eV), where the difference in energy for this donor-acceptor orbital pair is 3.09 eV.

The difference in these calculations compared to the $NpO_2Cl_4^{2-}$ calculations are the absence of an anti-bonding ligand based MO with σ_u character, $11a_{2u}$ in $NpO_2Cl_4^{2-}$. This split makes the SAOP charge transfer transition results, at 27763 cm^{-1} in $NpO_2(OH)_4^{2-}$, appear at higher energies than where the $11a_{2u}$ MO is used as the donor orbital in $NpO_2Cl_4^{2-}$.

The first calculated LB94 electronic transition (Table 4.20), the spin allowed δ - δ transition at 1043 cm^{-1}, is significantly lower in energy compared to the first SAOP transition. The corresponding spin-forbidden transition is at 3146 cm^{-1}. The δ – φ transitions are higher in energy than the δ - δ transition, the spin-allowed at 6432 cm^{-1} and the spin-forbidden at 7152 cm^{-1}. Both of these transitions, the δ – δ and the δ – φ transitions, are lower in energy than the calculated SAOP transitions, where the δ – δ transition was at 14860 cm^{-1} and the δ –φ transition at 17805 cm^{-1}. Looking at the LB94 transitions out of σ_u, the first charge transfer transition is at 16426 cm^{-1}, about 10000 cm^{-1} lower in energy than the calculated SAOP transition. Again, the explanation is the difference in the calculated electronic ground state structure, which has large energy gaps between the valance molecular orbitals. LB94 produces smaller gaps in energy between the valence MOs resulting in smaller TDDFT transition energies. There is a lack of experimental data to compare these calculated transitions with, which makes it difficult to assess which of the two functionals produce the best results. However, based on the performances of LB94 and SAOP on NpO_2^{2+}, $NpO_2Cl_4^{2-}$ and $UO_2Cl_4^{2-}$ it is reasonable to assume that LB94 performs better than SAOP on the $NpO_2(OH)_4^{2-}$ system as well.

One of the main reasons for performing this TDDFT investigation on small Np containing systems was to see what the impact of equatorial ligands are on the calculated

transition energies. Experimentally it has been found that the f-f transitions in $NpO_2(H_2O)_5^{2+}$ blue-shifts as it is coordinated to polyoxometallates. Part of the reason for the present investigation is to see which type of ligand the large POM system resembles, an OH-type ligand or a Cl-type ligand. The experimental blue shift is very small, about 0.1 eV (1000 cm^{-1}), and the calculations will only yield qualitative results.

Comparing the LB94 calculated transition energies for all systems in this study, the lowest f-f transition energies can be found in the NpO_2^{2+} system, where the transitions were calculated to start at about 2500 cm^{-1}. Moving to the $NpO_2Cl_4^{2-}$ system a blue shift in the f-f transitions is found, moving up to about 3500 cm^{-1}. Hydroxide groups in the equatorial plane of the NpO_2^{2+} moiety blue shifts the first calculated transition energy by about 1500 cm^{-1} compared to $NpO_2Cl_4^{2-}$ and about 3000 cm^{-1} for the second transition. It is clear that the f-f transitions are significantly blue-shifted for the two systems with equatorial ligands.

Energy/eV	Energy/cm^{-1}	*f*	Transition symmetry	Principal orbital contribution (Table 4.2)
0.13	1043	0	A_2	$^{\alpha}3a_2 \rightarrow {}^{\alpha}18a_1$ ($\delta \rightarrow \delta$)
0.39	3146	0	A_2	$^{\alpha}3a_2 \rightarrow {}^{\beta}18a_1$ ($\delta \rightarrow \delta$)
0.80	6432	2.56×10^{-5}	E	$^{\alpha}3a_2 \rightarrow {}^{\alpha}18e$ ($\delta \rightarrow \varphi$)
0.89	7152	0	E	$^{\alpha}3a_2 \rightarrow {}^{\beta}18e$ ($\delta \rightarrow \varphi$)
1.70	13679	1.26×10^{-5}	E	$^{\alpha}3a_2 \rightarrow {}^{\alpha}19e$
1.75	14114	0	E	$^{\alpha}3a_2 \rightarrow {}^{\beta}19e$
1.87	15090	0	A_2	$^{\alpha}2a_2 \rightarrow {}^{\alpha}18a_1$ (OH $\rightarrow \delta$)
1.89	15280	0	A_2	$^{\beta}2a_2 \rightarrow {}^{\alpha}18a_1$ (OH $\rightarrow \delta$)
2.01	16250	0	E	$^{\beta}17e \rightarrow {}^{\alpha}18a_1$ (OH $\rightarrow \delta$)
2.04	16426	0	B_2	$^{\beta}16b_2 \rightarrow {}^{\alpha}18a_1$ ($\sigma_u \rightarrow \delta$)
2.05	16549	4.29×10^{-4}	E	$^{\alpha}17e \rightarrow {}^{\alpha}18a_1$ (OH $\rightarrow \delta$)
2.19	17690	0	A_2	$^{\alpha}2a_2 \rightarrow {}^{\beta}18a_1$ (OH $\rightarrow \delta$)
2.22	17933	0	A_2	$^{\beta}2a_2 \rightarrow {}^{\beta}18a_1$ (OH $\rightarrow \delta$)
2.29	18482	1.98×10^{-7}	B_2	$^{\alpha}16b_2 \rightarrow {}^{\alpha}18a_1$ ($\sigma_u \rightarrow \delta$)
2.34	18845	0	A_1	$^{\alpha}2a_2 \rightarrow {}^{\beta}3a_2$ (OH $\rightarrow \delta$)
2.35	18949	0	E	$^{\beta}2a_2 \rightarrow {}^{\beta}18e$ (OH $\rightarrow \varphi$)
2.36	19008	1.43×10^{-5}	E	$^{\beta}17e \rightarrow {}^{\beta}18a_1$ (OH $\rightarrow \delta$)
2.36	19031	0	E	$^{\alpha}17e \rightarrow {}^{\beta}18a_1$ (OH $\rightarrow \delta$)
2.36	19062	0	A_1	$^{\beta}2a_2 \rightarrow {}^{\beta}3a_2$ (OH $\rightarrow \delta$)
2.41	19472	2.94×10^{-3}	E	$^{\alpha}2a_2 \rightarrow {}^{\alpha}18e$ (OH $\rightarrow \varphi$)
2.43	19586	0	B_2	$^{\beta}17e \rightarrow {}^{\alpha}18e$ (OH $\rightarrow \varphi$)
2.44	19647	0	A_1	$^{\beta}17e \rightarrow {}^{\alpha}18e$ (OH $\rightarrow \varphi$)
2.44	19707	0	E	$^{\beta}16e \rightarrow {}^{\alpha}18a_1$ (OH $\rightarrow \delta$)
2.45	19798	5.36×10^{-4}	E	$^{\alpha}16e \rightarrow {}^{\alpha}18a_1$ (OH $\rightarrow \delta$)
2.48	20005	0	E	$^{\alpha}17e \rightarrow {}^{\beta}3a_2$ (OH $\rightarrow \delta$)
2.49	20063	0	A_2	$^{\beta}17e \rightarrow {}^{\alpha}18e$ (OH $\rightarrow \varphi$)
2.52	20302	0	B_1	$^{\beta}17e \rightarrow {}^{\alpha}18e$ (OH $\rightarrow \varphi$)
2.52	20321	0	A_1	$^{\alpha}17e \rightarrow {}^{\alpha}18e$ (OH $\rightarrow \varphi$)
2.54	20456	0	B_1	$^{\alpha}17e \rightarrow {}^{\alpha}18e$ (OH $\rightarrow \varphi$)
2.55	20552	1.05×10^{-5}	B_2	$^{\alpha}17e \rightarrow {}^{\alpha}18e$ (OH $\rightarrow \varphi$)
2.55	20578	0	A_2	$^{\alpha}17e \rightarrow {}^{\alpha}18e$ (OH $\rightarrow \varphi$)
2.58	20787	7.43×10^{-7}	E	$^{\beta}17e \rightarrow {}^{\beta}3a_2$ (OH $\rightarrow \delta$)
2.59	20873	0	B_2	$^{\alpha}16b_2 \rightarrow {}^{\beta}18a_1$ ($\sigma_u \rightarrow \delta$)
2.61	21055	0	E	$^{\alpha}2a2 \rightarrow {}^{\beta}18e$ (OH $\rightarrow \varphi$)
2.67	21570	0	E	$^{\beta}16b_2 \rightarrow {}^{\alpha}18e$ ($\sigma_u \rightarrow \varphi$)
2.75	22164	0	A_1	$^{\alpha}17e \rightarrow {}^{\beta}18e$ (OH $\rightarrow \varphi$)
2.75	22175	0	B_1	$^{\alpha}16b_2 \rightarrow {}^{\beta}3a_2$ ($\sigma_u \rightarrow \delta$)

Table 4.20. Calculated spin-orbit free transition energies in $NpO_2(OH)_4^{2-}$ (LB94, TDA, spin flip transitions)

$Na_2(GeW_9O_{34})_2(NpO_2)_2^{14-}$

The experimental UV/nIR spectrum of the f-f transitions in $Na_2(GeW_9O_{34})_2(NpO_2)_2^{14-}$ showed an increase in transition energy, from 1223 nm (1.01 eV) to 1130 nm (1.10 eV), and decrease in intensity of the Np f-f transitions when NpO_2^{2+} in aqueous solution coordinates to two equivalents of $GeW_9O_{34}^{10-}$.[52] (Figure 4.2) While the change in energy is too small to be calculated accurately, it is possible to investigate if the same trends are detected in the polyoxometallate complex and if it is possible to get transition energies in rough agreement with experiment. The change in intensity noted experimentally was attributed to a change in the local symmetry at the metal centre on complexation.

Under experimental conditions NpO_2^{2+} will be coordinated to five water molecules in the equatorial plane. Thus the polyoxometallate f-f transition energies were compared to calculated $NpO_2(H_2O)_5^{2+}$ transition energies. The ten lowest energy LB94 f-f transitions in $Na_2(GeW_9O_{34})_2(NpO_2)_2^{14-}$ (Table 4.21) are all δ to φ transitions with the first transition at 0.12 eV. This is higher in energy than what was found in the corresponding $NpO_2(H_2O)_5^{2+}$ transitions, where the lowest energy transition occurred at 0.05 eV, but significantly lower than what was found experimentally for the polyoxometallate complex.

The oscillator strength in the POM f-f transitions is similar in the POM complex compared to the NpO_2^{2+} - water complex transitions. The increase in transition energy qualitatively reproduces the trend in the experimental results but all the LB94 transition energies are very low. The reason for the low LB94 transition energies is that the calculated valence electronic structure has a very small HOMO-LUMO gap.

$Na_2(GeW_9O_{34})_2(NpO_2)_2^{14-}$

Energy/eV	Energy/cm^{-1}	*f*	Transition symmetry	Principal orbital contribution (Table 4.14)
0.12	957	0	A_g	$^{\alpha}549a_g \rightarrow {}^{\alpha}550a_g$ ($\delta \rightarrow \varphi$)
0.12	958	2.25 x 10^{-5}	A_u	$^{\alpha}549a_u \rightarrow {}^{\alpha}550a_g$ ($\delta \rightarrow \varphi$)
0.25	2004	0	A_g	$^{\alpha}549a_u \rightarrow {}^{\alpha}550a_u$ ($\delta \rightarrow \varphi$)
0.25	2006	6.73 x 10^{-6}	A_u	$^{\alpha}549a_g \rightarrow {}^{\alpha}550a_u$ ($\delta \rightarrow \varphi$)
0.34	2721	0	A_g	$^{\alpha}549a_u \rightarrow {}^{\alpha}551a_u$ ($\delta \rightarrow \varphi$)
0.34	2722	1.78 x 10^{-5}	A_u	$^{\alpha}549a_g \rightarrow {}^{\alpha}551a_u$ ($\delta \rightarrow \varphi$)
0.38	3088	9.63 x 10^{-7}	A_u	$^{\alpha}549a_u \rightarrow {}^{\alpha}551a_g$ ($\delta \rightarrow \varphi$)
0.38	3089	0	A_g	$^{\alpha}549a_g \rightarrow {}^{\alpha}551a_g$ ($\delta \rightarrow \varphi$)
0.55	4454	0	A_g	$^{\alpha}549a_u \rightarrow {}^{\alpha}552a_u$ ($\delta \rightarrow \varphi$)
0.55	4463	8.90 x 10^{-6}	A_u	$^{\alpha}549a_g \rightarrow {}^{\alpha}552a_u$ ($\delta \rightarrow \varphi$)

$NpO_2(H_2O)_5^{2+}$

Energy/eV	Energy/cm^{-1}	*f*	Transition symmetry	Principal orbital contribution (Table 4.13)
0.05	438	7.44 x 10^{-8}	B_2	$^{\alpha}8a_2 \rightarrow {}^{\alpha}18b_1$ ($\delta \rightarrow \delta$)
0.16	1326	1.10 x 10^{-6}	B_1	$^{\alpha}8a_2 \rightarrow {}^{\alpha}21b_2$ ($\delta \rightarrow \varphi$)
0.23	1888	0	A_2	$^{\alpha}8a_2 \rightarrow {}^{\alpha}35a_1$ ($\delta \rightarrow \varphi$)
1.62	13048	0	A_2	$^{\alpha}17b_1 \rightarrow {}^{\alpha}21b_2$ ($\sigma_u \rightarrow \varphi$)
1.69	13615	6.44 x 10^{-6}	B_1	$^{\alpha}17b_1 \rightarrow {}^{\alpha}35a_1$ ($\sigma_u \rightarrow \varphi$)
1.80	14486	9.16 x 10^{-4}	A_1	$^{\alpha}17b_1 \rightarrow \alpha 18b_1$ ($\sigma_u \rightarrow \delta$)
1.86	15032	2.43 x 10^{-3}	A_1	$^{\alpha}20b_2 \rightarrow {}^{\alpha}21b_2$ ($H_2O \rightarrow \varphi$)
1.88	15198	0	A_2	$^{\beta}17b_1 \rightarrow {}^{\beta}21b_2$ ($\sigma_u \rightarrow \varphi$)
1.94	15677	2.13 x 10^{-3}	B_2	$^{\alpha}20b_2 \rightarrow {}^{\alpha}35a_1$ ($H_2O \rightarrow \varphi$)
1.95	15758	9.65 x 10^{-6}	B_1	$^{\beta}17b_1 \rightarrow {}^{\beta}35a_1$ ($\sigma_u \rightarrow \varphi$)

Table 4.21. Calculated spin-orbit free transition energies in $Na_2(GeW_9O_{34})_2(NpO_2)_2^{14-}$ and $NpO_2(H_2O)_5^{2+}$ (LB94, TDA, no spin flip transitions).

To be able to reproduce the experimental results in $Na_2(GeW_9O_{34})_2(NpO_2)_2^{14-}$ and $NpO_2(H_2O)_5^{2+}$ (C_{2v}), TDDFT calculations using SAOP were performed and the result can be seen in Table 4.22. The SAOP electronic structures in the NpO_2^{2+}, $NpO_2Cl_4^{2-}$, $NpO_2(H_2O)_5^{2+}$ and $NpO_2(OH)_4^{2-}$ all had significantly larger HOMO-LUMO gaps than what was found in the corresponding LB94 complexes, resulting in larger transition energies.

$Na_2(GeW_9O_{34})_2(NpO_2)_2^{14-}$

Energy/eV	Energy/cm^{-1}	*f*	Transition symmetry	Principal orbital contribution (Table 4.13)
1.64	13198	2.12 x 10^{-4}	A_u	$^{\alpha}549a_u \rightarrow {}^{\alpha}550a_g$ ($\delta \rightarrow \varphi$)
1.70	13749	8.48 x 10^{-6}	A_u	$^{\alpha}549a_g \rightarrow {}^{\alpha}550a_u$ ($\delta \rightarrow \varphi$)
1.79	14464	2.34 x 10^{-4}	A_u	$^{\alpha}549a_u \rightarrow {}^{\alpha}552a_g$ ($\delta \rightarrow \varphi$)
1.89	15281	5.04 x 10^{-5}	A_u	$^{\alpha}549a_g \rightarrow {}^{\alpha}551a_u$ ($\delta \rightarrow \varphi$)
1.91	15398	6.53 x 10^{-5}	A_u	$^{\alpha}549a_u \rightarrow {}^{\alpha}551a_g$ ($\delta \rightarrow \varphi$)
1.92	15515	2.25 x 10^{-6}	A_u	$^{\alpha}549a_g \rightarrow {}^{\alpha}552a_u$ ($\delta \rightarrow \varphi$)
2.09	16830	3.57 x 10^{-4}	A_u	$^{\alpha}548a_u \rightarrow {}^{\alpha}550a_g$
2.10	16907	6.78 x 10^{-4}	A_u	$^{\alpha}548a_g \rightarrow {}^{\alpha}550a_u$
2.11	17004	5.37 x 10^{-5}	A_u	$^{\alpha}547a_u \rightarrow {}^{\alpha}550a_g$
2.12	17062	3.58 x 10^{-4}	A_u	$^{\alpha}547a_g \rightarrow {}^{\alpha}550a_u$

$NpO_2(H_2O)_5^{2+}$

Energy/eV	Energy/cm^{-1}	*f*	Transition symmetry	Principal orbital contribution (Table 4.14)
1.65	13305	5.60 x 10^{-6}	B_1	$^{\alpha}8a_2 \rightarrow {}^{\alpha}21b_2$ ($\delta \rightarrow \varphi$)
1.65	13340	6.11 x 10^{-6}	B_2	$^{\alpha}8a_2 \rightarrow {}^{\alpha}18b_1$ ($\delta \rightarrow \delta$)
1.71	13804	0	A_2	$^{\alpha}8a_2 \rightarrow {}^{\alpha}35a_1$ ($\delta \rightarrow \varphi$)
2.61	21032	0	A_2	$^{\alpha}17b_1 \rightarrow {}^{\alpha}21b_2$ ($\sigma_u \rightarrow \varphi$)
2.67	21546	1.46 x 10^{-5}	B_1	$^{\alpha}17b_1 \rightarrow {}^{\alpha}35a_1$ ($\sigma_u \rightarrow \varphi$)
2.82	22723	3.69 x 10^{-3}	A_1	$^{\alpha}20b_2 \rightarrow {}^{\alpha}21b_2$ ($H_2O \rightarrow \varphi$)
2.89	23322	3.93 x 10^{-3}	B_2	$^{\alpha}20b_2 \rightarrow {}^{\alpha}35a_1$ ($H_2O \rightarrow \varphi$)
2.94	23745	5.75 x 10^{-3}	A_1	$^{\alpha}17b_1 \rightarrow {}^{\alpha}18b_1$ ($\sigma_u \rightarrow \varphi$)
3.08	24808	0	A_2	$^{\alpha}20b_2 \rightarrow {}^{\alpha}18b_1$ ($H_2O \rightarrow \delta$)
3.11	25108	7.03 x 10^{-3}	B_2	$^{\alpha}34a_1 \rightarrow {}^{\alpha}21b_2$ ($H_2O \rightarrow \varphi$)

Table 4.22. Calculated spin-orbit free transition energies in $Na_2(GeW_9O_{34})_2(NpO_2)_2^{14-}$ and $NpO_2(H_2O)_5^{2+}$ (SAOP, no spin flip transitions).

The SAOP transition energy of the lowest f-f transition increased by *ca* 1.6 eV compared to the LB94 results and is similar to the first SAOP transitions in $NpO_2Cl_4^{2-}$ and somewhat lower than what was found for $NpO_2(OH)_4^{2-}$. (Appendix 1) Again, the energy of the first transition reflects the larger HOMO-LUMO gaps in the electronic structure using SAOP compared to LB94. The first calculated transitions are slightly lower in energy for the POM system than in the $NpO_2(H_2O)_5^{2+}$ and in experiment, and are thus in qualitative disagreement with experimental data.

However, all transitions out of $549a_u$ and $549a_g$ to the corresponding 550, 551 and 552 MOs are f-f transitions which means that the f-f transition energies span energies from 13198 cm^{-1} to 15515 cm^{-1}. For LB94 the energy range spans all the calculated transitions

in Table 4.21, 957 cm^{-1} to 4463 cm^{-1}. Thus, SAOP performs adequately in being able to get the transition energies qualitatively correct, with energies closer to the experimental results than LB94, even though none of the functionals can be said to produce high quality results. The trend, higher transition energies in the POM than in aqueous solution, is not seen using SAOP.

Comparing the SAOP calculated polyoxometallate and $NpO_2(H_2O)_5^{2+}$ transitions with the $NpO_2(OH)_4^{2-}$ transitions (Table 4.20 and Appendix 1), it is clear that the $NpO_2(OH)_4^{2-}$ f-f transitions, the first occurring at 14860 cm^{-1}, are higher in energy than both the first corresponding $NpO_2(H_2O)_5^{2+}$ (13305 cm^{-1}) and $Na_2(GeW_9O_{34})_2(NpO_2)_2^{14-}$ (13198 cm^{-1}) transition. The first LB94 f-f transitions occur at 6432 cm^{-1}, 438 cm^{-1} and 957 cm^{-1} for $NpO_2(OH)_4^{2-}$, $NpO_2(H_2O)_5^{2+}$ and $Na_2(GeW_9O_{34})_2(NpO_2)_2^{14-}$ respectively. Based on these transition energies it could be argued that the ligand effect of the polyoxometallate is more water-like than hydroxide-like.

As was mentioned above, the range of the f-f transitions was quite broad and, from the experimental data it is not clear which of the calculated transitions were observed. The oscillator strengths of two calculated SAOP f-f transitions in the POM, $^{\alpha}549a_u \rightarrow {}^{\alpha}550a_g$ and $^{\alpha}549a_u \rightarrow {}^{\alpha}552a_g$ at 13198 cm^{-1} and 14464 cm^{-1}, are on the order of 10^{-4}, significantly larger than the other f-f transitions and are thus the transitions most likely to be seen. The LB94 transitions, in addition to being lower in energy, have oscillator strengths around 10^{-6} and 10^{-8}. This means that even though the calculated LB94 transitions have the right qualitative behaviour SAOP produces transition energies closer to experiment and that the SAOP span of f-f transition energies includes the experimentally determined energies.

Conclusions

The purpose of the investigations presented in this chapter has been to investigate the possibility of using TDDFT to calculate the electronic transitions in NpO_2^{2+}, $NpO_2Cl_4^{2-}$, $NpO_2(OH)_4^{2-}$ and $Na_2(GeW_9O_{34})_2(NpO_2)_2^{14-}$. $NpO_2(H_2O)_5^{2+}$ was included to model the effect on the TDDFT transition energies of the aqueous environment on NpO_2^{2+} prior to complexation to the POM. For completeness the corresponding calculations have been performed on UO_2^{2+} and $UO_2Cl_4^{2-}$, for which there exist experimental data and high level theory data. The two functionals SAOP and LB94 have been tested but results show that the calculated LB94 electronic transitions provide better agreement with experiment than SAOP for all systems. The exception is in the $Na_2(GeW_9O_{34})_2(NpO_2)_2^{14-}$ system where SAOP qualitatively reproduces the experimental f-f transitions better than LB94 for both the $NpO_2(H_2O)_5^{2+}$ molecule and the NpO_2^{2+} - POM complex. Comparing the calculated transition energies of $Na_2(GeW_9O_{34})_2(NpO_2)_2^{14-}$ with those of $NpO_2(OH)_4^{2-}$ and $NpO_2(H_2O)_5^{2+}$ illustrates one of the main issues with the present study; SAOP, which proved inadequate for the smaller systems, performs significantly better than LB94 on the polyoxometallate, the difference between experiment and calculation is *ca* 1000 cm^{-1}. This is likely due to the same reasons LB94 performs well on the smaller systems, i.e. the electronic structure for the particular system is best described by SAOP rather than LB94.

Comparisons to previously performed SOCI calculations on NpO_2^{2+} are difficult due to the present calculations being single reference spin-orbit free calculations. Overall though, the agreement of the f-f transition energies is quite poor. The reason for LB94 performing better than SAOP is that LB94 generates significantly smaller HOMO-LUMO gaps than SAOP. It is also noticeable that formally degenerate valence MOs are split quite significantly, by SAOP more than LB94.

Calculations of the charge transfer transitions performed on UO_2^{2+} and $UO_2Cl_4^{2-}$ show better agreement with experimental results (or CASPT2 results in the case of UO_2^{2+}) than

the corresponding Np containing systems, provided the correct functional is used. SAOP show better agreement in the case of UO_2^{2+} while LB94 performs better for $UO_2Cl_4^{2-}$, NpO_2^{2+} and $NpO_2Cl_4^{2-}$, provided the correct donor MO is used.

It was found that the Cl^-, H_2O and OH^- equatorial ligands, in $NpO_2Cl_4^{2-}$, $NpO_2(H_2O)_5^{2+}$ and $NpO_2(OH)_4^{2-}$ respectively, shift the transition energies upwards in agreement with experimental data on NpO_2^{2+} in aqueous solution but to different extents depending on the ligand. The blue shift in the Cl^- ligands is smaller than what was seen for the OH^- ligands system. One of the main rationales for carrying out this investigation was to characterize the polyoxometallate coordination in terms of smaller ligands. In the end the behaviour of the POMs appear to be, like the other neptunyl results, dependent on the functional employed; SAOP gets energies in closer agreement to experiment and close to both the OH^- and H_2O coordinated systems, albeit the H_2O coordinated complex has transition energies closest to the experimental data of the Np – POM complex. LB94 on the other hand reproduces the correct trend, with higher transition energies with NpO_2^{2+} coordinated to $Na_2(GeW_9O_{34})_2(NpO_2)_2^{14-}$ compared to in aqueous solution.

Chapter 5

Investigations of the bonding and bending in group 15 and group 16 uranyl analogues

Introduction

The most studied system in computational actinide chemistry is the uranyl dication, UO_2^{2+}, due to it being a small, closed shell system that can be accurately described by a single determinant, and also because the uranyl unit features in roughly half of all known uranium molecules.[153] Uranyl is also an interesting case study for the participation of 5f electrons in covalent bonding, which has also been investigated in e.g. uranocenes.[154, 155] The uranyl dication is never found as a stand alone species but the fact that it is common and relatively easy to study computationally has made it very popular for use in studies of the electronic structure of the actinides.

Uranyl analogues

Exotic uranyl-like species such as CUO[156, 157], UON[158], UON^+ [158], UN_2 [159], UO_2^- and US_2[160] have been produced using laser ablation in inert atmospheres. These have been investigated using both computational and experimental methods. All of these systems, with the exception of US_2, are linear.

Group 16 uranyl analogues

One of the purposes of this chapter is to investigate the bonding in the uranyl group 16 analogues. The bonding and electronic structure of UO_2^{2+} (Chapter 4) is well known but the corresponding properties of the group 16 analogues are not known. Multiple studies have been performed on U(VI) uranyl in order to investigate why the molecule is linear when thoranyl, ThO_2, has a bond angle of 120.4° in its ground state geometry.[161-164] This

is due to the greater Th 6d overlap with the O 2p orbitals, which favour the bent geometry, compared to the Th 5f overlap with O 2p. Continuing research has focused on the impact of different ligands in the equatorial plane and the effect those have on the U-O_{yl} bond.[102, 165-167]

The bent geometry found experimentally for US_2 and ThS_2 indicate that there are differences among the actinyl analogues worth exploring with regards to the electronic structure and its trends in descending group 16.[168]

A systematic computational study of closed shell group 16 analogues of UO_2^{2+} and the neutral group 15 systems is not present in the literature. Uranium-chalcogen bonding has been investigated though, using Mulliken population analysis and atomic charge analysis schemes, in $[M(N(EPH_2)_2)_3]$ (M = La, U, Pu; E = O, S, Se, Te). The calculations found that the U-E bond becomes longer, from 2.39 Å in (U-O) to 2.96 Å (U-Te) with the largest increase in bond distance occurring between O and S. Also, the bond grows increasingly covalent descending group 16.[169]

Bulk crystal properties such as phase shift, magnetic and thermodynamic properties of US_2, USe_2 and UTe_2 have been studied using various experimental techniques.[170] For US_2, the crystal structure features U bonded to eight sulfur atoms in a distorted anti-prismatic coordination polyhedron; the U-S bond average distance is 2.84 Å.[171] The crystal structure geometry of USe_2 is similar to US_2, a distorted anti-prismatic coordination polyhedron with the uranium atom coordinated to eight Se atoms; the average U-Se crystal structure bond distance is 2.97 Å. Both the U-S and U-Se bond distances are in good agreement with previously reported U-E (E = S, Se) mean distances for eight-coordinated U(IV), 2.82 Å and 2.97 Å for S and Se respectively.[172]

The geometry of UTe_2 has also been investigated and the U-Te distance is reported to be about 3.1 Å. Hence there is an almost linear increase in bond distance going down the group. As with the other solid-state uranium-chalcogen systems, the coordination number

in UTe_2 is eight.[173] However, these bulk crystal investigations do not provide much insight into the geometry or the bonding and electronic structure of the isolated molecular systems, which is the focus of the present study.

US_2 is the only group 16 uranyl analogue which has been investigated both experimentally, using IR spectroscopy, and computationally using DFT by Andrews *et al.*[160] The result was a $^3B_2$ ground state, a bond angle of 121.4° (experimentally 118±5°); close to the bond angle of ThO_2, and a U-S bond distance of 2.38 Å. The experimental bond angle is in contrast to the corresponding, linear, UO_2 system. The calculated bond angle of US_2 indicates that the U 6d influence is the dominating interaction in this system. The rationale for this is that U 6d, with a mean orbital radius of 1.7 Å, has a greater overlap with the S 3p (mean radius 1.03 Å) orbitals compared to the U 5f (mean radius 0.76 Å).[160] The U 5f and the more contracted O 2p (radius 0.66 Å) on the other hand produces a larger 5f-2p overlap and UO_2 is thus linear. The electronic structure of the system was not investigated in depth, but is explored in the present study.

Group 15 uranyl analogues

Over the last 10-15 years, experimentalists have successfully produced UO_2^{2+} analogues where O_{yl} has been substituted by isoelectronic groups, such as imido, -N-R, and phosphorane-iminato, -N-PR_3. This type of substitution was first proposed by Denning based on the similarity between d block oxo (M-O), imido (M-NR) and iminato (M-NPR_3) groups.[174, 175] The main experimental difficulty in producing these analogues has been to prevent the imido and iminato systems from hydrolyzing back to the very stable dioxo systems. Also, the lower electronegativity of the N containing substituents has made it difficult to prevent a spontaneous reduction from U(VI) to U(IV). These difficulties have now been largely overcome, facilitating further investigations into the nature of uranyl analogues.

There has been more computational work on group 15 uranyl analogues than on the group 16 analogues; work has been performed on $U(NR)_2$, but investigations of the group 15 P-R and As-R analogues have not been found.[176, 177] Previous N-R analogue investigations have not been part of a systematic study into the R-X=U=X-R (X = N, P, As) uranyl analogues, which will be carried out in this study. As with the group 16 analogues the electronic structure, charges and the trends down group 15 will be investigated here.

U(VI) imido complexes have been found experimentally but the discovered structures were not diimido complexes and required stabilization from bulky ligands.[178-180] Recently however, $U(N^tBu)_2I_2(THF)_2$ and $U(NPh)_2I_2(THF)_3$ (^{t}Bu = *tert*-butyl, THF = tetrahydrofuran) have been synthesized and the U-N bond distances are 1.844 Å and 1.862 Å for the two complexes respectively. Notable is also the N-U-N bond angle in the crystal structures, 175.4° and 177.7° for the two systems respectively, close to linear.[176, 177] DFT calculations on the corresponding $U(NMe)_2I_2(THF)_2$ system agree well with the experimental results for both bond distances and bond angles. The experimental U-N bond distances for these diimido complexes are short compared to other known U-N interactions, where bond distances are typically 1.90-1.95 Å. The main difference between the above studies and the present work is the presence of equatorial ligands in the experimental systems.

Thorough DFT investigations of the R_3P-N=U=N-PR_3 system have been carried out by Kaltsoyannis[181], including $UO(NPH_3)^{3+}$, $U(NPH_3)_2^{4+}$, $[UCl_4(NPR_3)_2]$ (R = H, Me) and $[UOCl_4(NP(C_6H_5)_3)^-]$. One conclusion from this study was that the U-N-P unit is linear for the centrosymmetric molecules. The U-N bond distance was found to change moving from UNO^+ and UN_2 to the $UO(NPH_3)^{3+}$ and $U(NPH_3)_2^{4+}$ systems, the U-N bond distance increasing by 0.2 and 0.1 Å respectively compared with UNO^+ and UN_2 for both systems. The U-N bond distances in $UO(NPH_3)^{3+}$ and $U(NPH_3)_2^{4+}$ are similar, 1.824 and 1.823 Å respectively.

DFT work on R_3P-N=U=N-PR_3 and R–N=U=N-R systems has shown some common features, particularly in the electronic structure.[182, 183] The most noticeable effect of replacing O_{yl} with imido and iminato groups is that the U-N π MOs increase in energy compared to the σ MOs. Comparing with the electronic structure of the UO_2^{2+} cation, $\sigma_u > \sigma_g > \pi_u > \pi_g$ (discussed in detail in Chapter 3), the N-based systems were found to have a $\pi_u > \pi_g > \sigma_u > \sigma_g$ configuration. The reason for this MO reordering is that in the linear imido substituted system, R-N=U=N-R, the presence of the R in the N-R group stabilizes the N $2p_\sigma$. This is due to its ability to σ-bond with the R group, forming a σ backbone along the entire structure stabilizing the $2p_\sigma$ and lowering the $2p_\sigma$ MO energy, leaving the $2p_\pi$ as the HOMO. Further investigations demonstrated that the effect is dependent on the N-H bond angle, as the inversion of the MO ordering did not occur in bent geometries where the σ backbone bond cannot form.

The pushing from below effect[116], which significantly destabilizes the σ_u HOMO in UO_2^{2+}, is also observed for the R_3P-N=U=N-PR_3 systems. Other important conclusions from the imido systems is that the systems are more covalent than the dioxide systems, seen in orbital population analysis of the metal, and lastly, that the total energy of the =N-PR_3 systems is almost independent of the U-N-P bond angle.[181]

Aim

In this chapter investigations into the electronic structure of the group 16 analogues to UO_2^{2+} will be reported. Calculations on the corresponding U(IV) systems, UO_2, US_2, USe_2 and UTe_2, have also been carried out to investigate if these molecules are linear, like UO_2, or bent like US_2. Based on the experimental and computational result of the US_2 study the heavier elements of group 16 are expected to produce bent molecules. ADF allows spin-orbit coupled (SOC) calculations, which were also performed for the closed-shell UE_2^{2+} systems.[160] The remaining calculations were spin-orbit free (SOF).

To complete the study, investigations were carried out into the uranyl -N-R, -P-R and -As-R (R = H, CH_3) analogues. The starting geometries were linear, $D_{\infty h}$, for the X-H systems and D_{3d} (staggered) for the X-CH_3 systems. Lastly, calculations were performed on the neutral species of the group 15 to see if, as in US_2 compared with US_2^{2+}, the neutral species produces bent configurations.

Computational details

All calculations have used the Amsterdam Density Functional (ADF) code and uncontracted, all-electron QZ4P STO basis sets. The local density parameterization of Vosko, Wilk and Nusair[27] was employed together with the PBE exchange-correlation functional.[32] Scalar relativistic effects were included using the zero order relativistic approximation (ZORA).[18] The integration parameter was set to 6.0 for all calculations and the SCF convergence criterion was 10^{-7} and the geometry convergence criterion 10^{-7} mHa/Å. In the ADF calculations on USe_2^{2+} and UTe_2^{2+} the occupation number of the HOMO and the LUMO was adjusted to converge the electronic structure. This will be discussed in the relevant sections. Energy decomposition analyses have been performed using ADF default atomic fragments.

Due to difficulties in obtaining convergence in the geometry and SCF in the $U(XR)_2^{2+}$ (X = P, As; R = H, CH_3) calculations, electronic smearing was employed. The maximum smearing employed in the X = P, As systems was 9 x 10^{-4} Hartree leading to fractional occupations in the valence orbitals, the consequences of which will be discussed below in the relevant sections. No electron smearing was employed in the X = N calculations.

Gaussian03[44] has been employed for DFT geometry and frequency calculations on UE_2^{2+}, US^+, UO_2^+ and UE_2 (E = O, S, Se, Te). All Gaussian calculations used the B3LYP[184, 185] functional and Stuttgart/ Dresden (SDD) ECP[186-188] basis sets.

Results

Geometry of UE_2^{2+} (E = O, S, Se, Te)

Gaussian03 SOF geometry optimizations of UE_2^{2+} (E = O, S, Se, Te) using C_{2v} symmetry and a bent (bond angle 150°) initial structure produced linear molecules (Table 5.1). Frequency calculations were also performed; all systems have only positive Hessian eigenvalues showing that the linear structures are true energy minima, and all molecules have $^1A_1$ states. For completeness, calculations were performed on UO_2^+ and US_2^+. The results confirm that the two monocations are linear and that the bending of US_2 only occurs for the neutral system.

	U-E (Å)	E-U-E (°)	ν_1 (cm^{-1})	ν_2 (cm^{-1})	ν_3 (cm^{-1})	ν_4 (cm^{-1})
UO_2^+	1.76	179.99	158.27	158.27	929.54	1003.57
UO_2^{2+}	1.71	179.97	106.67	106.67	1036.36	1135.14
US_2^+	2.29	179.95	47.54	47.54	462.76	512.06
US_2^{2+}	2.25	180.00	54.92	54.92	483.23	552.55
USe_2^{2+}	2.38	179.99	40.55	40.55	285.15	372.17
UTe_2^{2+}	2.61	180.00	22.04	22.04	173.98	283.21

Table 5.1. Optimized Gaussian03 (B3LYP/SDD) SOF geometries using C_{2v} symmetry.

To simplify the MO analysis of the dication systems the calculations were redone in ADF starting at a linear geometry and using full point group symmetry, $D_{\infty h}$, instead of C_{2v}. The ADF geometries for UO_2^{2+} and US_2^{2+} are very similar to the G03 results (Table 5.2) and show an almost linear increase in the U-E bond distance, from 1.713 Å in UO_2^{2+} to 2.662 Å in UTe_2^{2+}. The major increase in bond distance occurs moving from UO_2^{2+} to US_2^{2+}, with an increase of 0.512 Å, from 1.713 Å to 2.225 Å. Continuing down group 16 the increase in bond length is about 0.2 Å for each element down the group. However, to obtain converged electronic structures of USe_2^{2+} and UTe_2^{2+} it was necessary to modify the electronic configuration of the molecules by exciting 0.5 electrons from σ_u to the non-bonding φ_u orbital. The removal of half an electron from the bonding σ_u might weaken

the bond strength compared to the systems with doubly occupied MOs, and hence the bond lengths should be treated with caution.

	UO_2^{2+}	US_2^{2+}	USe_2^{2+}*	UTe_2^{2+}*
SOF	1.713	2.225	2.413	2.662
SOC	1.716	2.257	2.424	2.747

Table 5.2. Bond lengths in the ADF SOF and SOC optimized geometries ($D_{\infty h}$) of group 16 closed-shell uranyl analogues. *) Indicates where electrons have been excited out of σ_u. See text for explanation.

Since the geometries of the closed-shell systems were found to be linear for the SOF calculations, the SOC geometries were calculated in $D_{\infty h}$. In Table 5.2 the inclusion of spin-orbit effects is seen to increase the bond distance in all the molecules investigated. The SOC U-O bond in UO_2^{2+} is only marginally longer, with an increase of just 0.003 Å in comparison to the SOF calculations. The impact of spin-orbit effects increases going down group 16 and for USe_2^{2+} the difference is larger, *ca* 0.01 Å, and for the UTe_2^{2+} the difference is *ca* 0.1 Å. In US_2^{2+}, the difference is larger than expected on the basis of the effect of SOC on UO_2^{2+} and USe_2^{2+}.

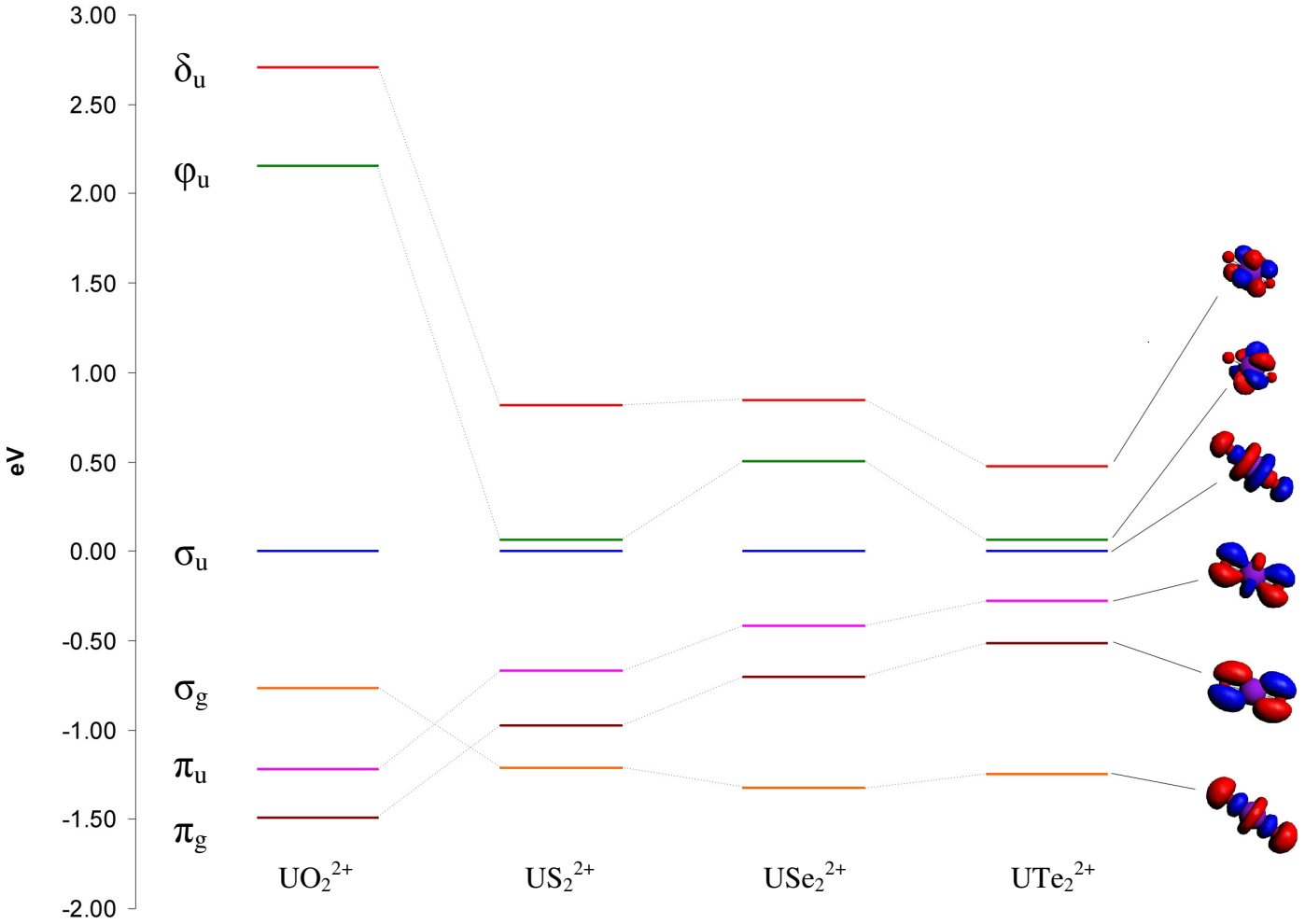

Figure 5.1. The PBE electronic structure of UE_2^{2+} (E = O, S, Se, Te). The HOMO has been normalized to have zero energy. The pictured MOs are from UO_2^{2+} but the general form of the orbitals is the same for all E.

Electronic structure - UE_2^{2+} (E = O, S, Se, Te)

SOF electronic structure

The SOF valence electronic structures of the group 16 uranyl analogues are shown in Figure 5.1. The ground state configuration of all the molecules studied involves similar bonding orbitals as in uranyl: σ_u, σ_g, π_u and π_g, all of which are doubly occupied for E = O, S (the occupation number of σ_u is 1.5 for E = Se, Te) and composed of U-E admixtures. In particular, the pushing from below of the anti-bonding 6p admixture significantly destabilizes the σ_u orbital, something which is well known from UO_2^{2+}, but also seen in the group 16 analogues. In addition the non-bonding, uranium 5f based δ_u and φ_u MOs are the first virtual orbitals. For E = Se, Te the occupation number of φ_u is 0.5.

The energetic ordering of the four highest occupied valence orbitals and the two non-bonding orbitals change moving down group 16. In UO_2^{2+} the familiar ordering of MOs: $\sigma_u > \sigma_g > \pi_u > \pi_g$ is observed. The HOMO-LUMO (σ_u to φ_u) gap is substantial, here calculated to be 2.15 eV. The difference in energy between σ_u and σ_g is 0.77 eV, the π MO levels are 0.28 eV apart and that π_u, the highest energy π MO, is 0.45 eV lower in energy than σ_g. Moving to US_2^{2+} two things are noticed; firstly, the HOMO-LUMO gap is drastically reduced, from 2.15 eV in UO_2^{2+} to 0.06 eV. Secondly, the σ_g orbital is stabilized by 0.5 eV at the same time as the π MOs (of both parities) are destabilized by *ca* 0.7 eV compared to their UO_2^{2+} equivalents. This alters the ordering of the MOs, leaving σ_g lower in energy than the π MOs. The gap between the π MOs remains approximately the same, 0.28 eV for UO_2^{2+} and 0.31 eV for US_2^{2+}. Also, the energy difference between σ_u and the HOMO-1 is slightly smaller for US_2^{2+} than for UO_2^{2+}, 0.67 eV compared to 0.77 eV.

Going further down the group to USe_2^{2+} the same general trends as between UO_2^{2+} and US_2^{2+} are found. The stabilization of σ_g continues, as does the destabilization of the π MOs. The gap between π_u and σ_u decreases, going from 0.67 eV in US_2^{2+} to 0.42 eV in

USe_2^{2+}. The difference in energy between π_g and σ_g continues to increase, from 0.23 eV in US_2^{2+} to 0.62 eV in USe_2^{2+}. Finally, moving to UTe_2^{2+} π_u continues to destabilize and is very close to the energy of the σ_u HOMO, only 0.28 eV more stable. In contrast, the stabilizing trend of σ_g is broken and a small destabilization of 0.11 eV compared to USe_2^{2+} is observed. However, the energy gap between σ_g and π_g is larger than for any of the other analogues, 0.75 eV. The HOMO-LUMO gap is very small for UTe_2^{2+}, 0.07 eV, similar to what is found in US_2^{2+}.

The behaviour of the non-bonding virtual orbitals for all the systems studied does not display the same clear trends as the occupied orbitals. One noticeable trend however is the relative stabilization of the non-bonding f orbitals compared with the occupied bonding orbitals as moving down group 16 from UO_2^{2+} to the heavier elements.

The absolute MO energies (Figure 5.2) show that the occupied valence orbitals are destabilized moving down group 16, reflecting the decreasing electronegativity from O to Te and the increasing radius of the ligand p orbitals. The largest change in the electronic structure occurs when moving from O to S, moving to heavier ligands the changes become relatively small. σ_g is stabilized relative to the other MOs as discussed above and the π MOs are destabilized. σ_u is the HOMO throughout the investigation, but the HOMO-LUMO gap decreases relative to UO_2^{2+} for the heavier substituents.

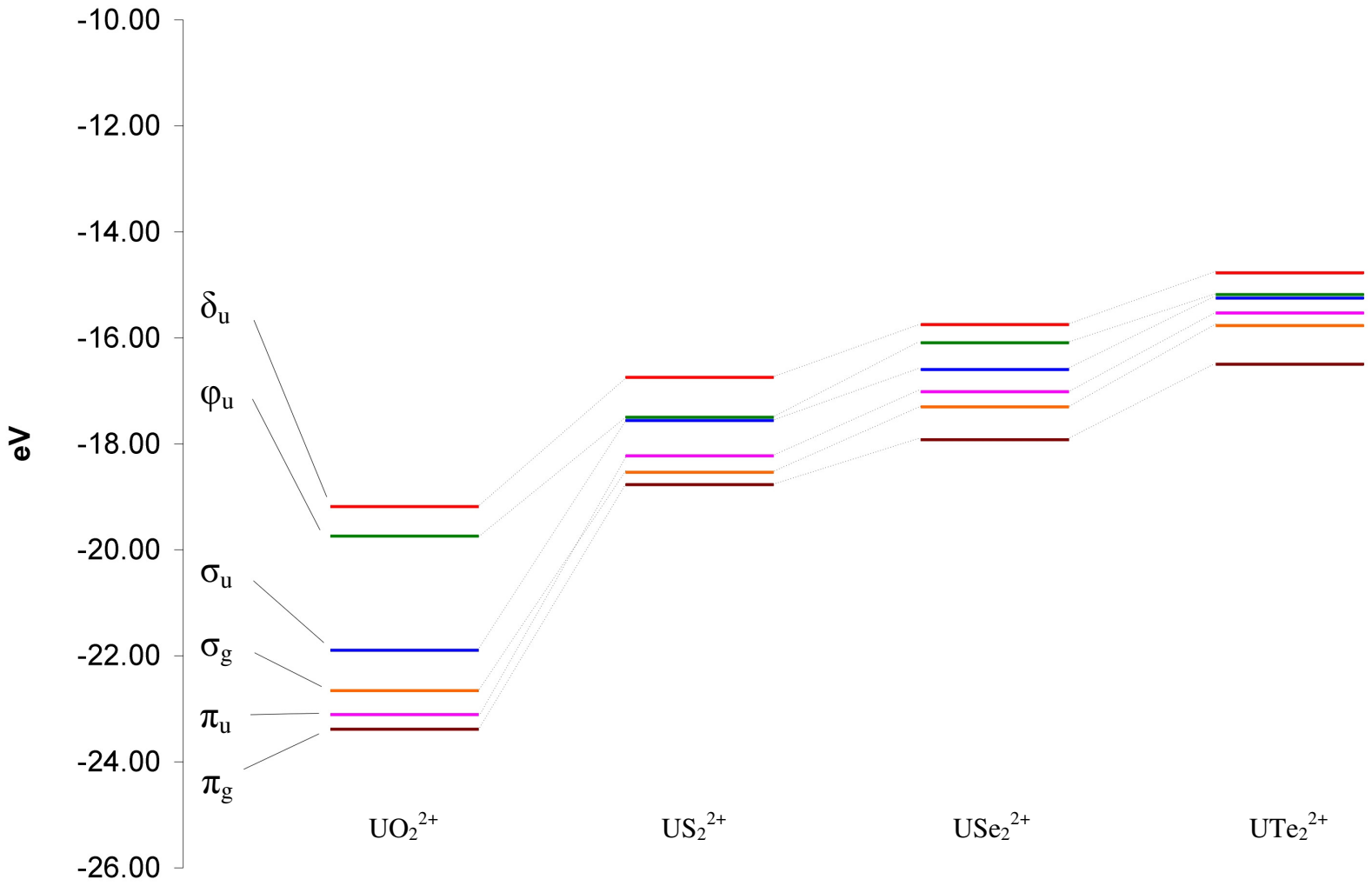

Figure 5.2. The electronic structure of UE_2^{2+} (E = O, S, Se, Te). Absolute energies.

SOC electronic structure

Calculations have been performed to investigate the spin-orbit electronic structure of the group 16 uranyl analogues. The resulting electronic structure is shown in Table 5.3. Only UO_2^{2+} has doubly occupied MOs, the analogues all have fractional occupations, a result of having adjusted the occupations to allow the calculation to converge. In UTe_2^{2+} this produces a non-aufbau configuration with a "hole" in the 29 $J_{1/2u}$ and 5 $J_{5/2u}$, with occupation number 0.5, is lower in energy than 16 $J_{3/2u}$. This is not the valence ordering seen in US_2^{2+} and USe_2^{2+}, where the MOs with occupation number 0.5 are the HOMO. The HOMO-LUMO gap decreases moving down group 16, from 1.66 eV in UO_2^{2+} to 0.15 eV in USe_2^{2+} while in UTe_2^{2+} the gap is not well defined.

Translating the double symmetry group labels to the $D_{\infty h}$ labels, the MO ordering of the UE_2^{2+} analogues is similar to what was found in the SOF calculations: σ_g is stabilized in relation to the π MOs while σ_u remains the HOMO in all systems except in UTe_2^{2+}, where σ_u is unoccupied. As in the SOF calculations the energy gap between σ_u to the HOMO-1 decreases from 0.84 eV to 0.31 eV, showing that the "pushing from below" effect lessens moving down the group. The LUMO is consistently φ_u for the UO_2^{2+}, US_2^{2+} and USe_2^{2+} systems.

UO_2^{2+}

$D_{\infty h}$ equivalent	$D_{\infty h}^*$	Occupation	Energy [eV]
δ_u	4 $E_{5/2u}$	0	-18.71
φ_u	2 $E_{7/2u}$	0	-19.21
δ_u	9 $E_{3/2u}$	0	-19.34
φ_u	3 $E_{5/2u}$	0	-20.08
σ_u	16 $E_{1/2u}$	2	-21.74
σ_g	16 $E_{1/2g}$	2	-22.58
π_u	8 $E_{3/2u}$	2	-22.91
π_u	15 $E_{1/2u}$	2	-23.21
π_g	7 $E_{3/2g}$	2	-23.27
π_g	15 $E_{1/2g}$	2	-23.37

US_2^{2+}

$D_{\infty h}$ equivalent	$D_{\infty h}^*$	Occupation	Energy [eV]
δ_u	4 $E_{5/2u}$	0	-15.89
φ_u	2 $E_{7/2u}$	0	-16.16
δ_u	10 $E_{3/2u}$	0	-16.52
φ_u	3 $E_{5/2u}$	0.5	-17.01
σ_u	19 $E_{1/2u}$	1.5	-17.44
π_u	9 $E_{3/2u}$	2	-18.02
π_u	18 $E_{1/2u}$	2	-18.26
π_g	8 $E_{3/2g}$	2	-18.40
π_g	19 $E_{1/2g}$	2	-18.49
σ_g	18 $E_{1/2g}$	2	-18.90

USe_2^{2+}

$D_{\infty h}$ equivalent	$D_{\infty h}^*$	Occupation	Energy [eV]
δ_u	5 $E_{5/2u}$	0	-15.21
φ_u	2 $E_{7/2u}$	0	-15.53
δ_u	13 $E_{3/2u}$	0	-15.82
φ_u	4 $E_{5/2u}$	0.5	-16.37
σ_u	24 $E_{1/2u}$	1.5	-16.52
π_u	12 $E_{3/2u}$	2	-16.83
π_u	23 $E_{1/2u}$	2	-17.12
π_g	11 $E_{3/2g}$	2	-17.14
π_g	24 $E_{1/2g}$	2	-17.37
σ_g	23 $E_{1/2g}$	2	-17.91

UTe_2^{2+}

$D_{\infty h}$ equivalent	$D_{\infty h}^*$	Occupation	Energy [eV]
σ_u^*	30 $E_{1/2u}$	0	-13.69
φ_u	2 $E_{7/2u}$	0	-13.75
δ_u	16 $E_{3/2u}$	1.5	-14.17
φ_u	5 $E_{5/2u}$	0.5	-14.57
π_u	15 $E_{3/2u}$	2	-15.13
σ_u	29 $E_{1/2u}$	0	-15.35
π_g	14 $E_{3/2g}$	2	-15.43
π_u	28 $E_{1/2u}$	2	-15.64
π_g	29 $E_{1/2g}$	2	-15.82
σ_g	28 $E_{1/2g}$	2	-16.86

Table 5.3. The spin-orbit coupled electronic structure of UE_2^{2+} (E = O, S, Se, Te)

SOF molecular orbital Mulliken decomposition

UO_2^{2+}

	Occ.	E	Uf	Ud	Up	Us	O
δ_u	0	-19.19	99				
φ_u	0	-19.74	99				
σ_u	2	-21.89	55		8		34
σ_g	2	-22.66		5		7	86
π_u	4	-23.11	35				65
π_g	4	-23.39		14			83

US_2^{2+}

	Occ.	E	Uf	Ud	Up	Us	S
δ_u	0	-16.74	99				
φ_u	0	-17.50	99				
σ_u	2	-17.56	62		2		29
π_u	4	-18.23	40				59
π_g	4	-18.54		20			78
σ_g	2	-18.77		13			85

USe_2^{2+}

	Occ.	E	Uf	Ud	Up	Us	Se
δ_u	0	-15.75	99				
φ_u	0.5	-16.09	100				
σ_u	1.5	-16.60	58		3		32
π_u	4	-17.02	39				60
π_g	4	-17.30		21			78
σ_g	2	-17.92		15		3	79

UTe_2^{2+}

	Occ.	E	Uf	Ud	Up	Us	Te
δ_u	0	-14.78	99				
φ_u	0.5	-15.18	100				
σ_u	1.5	-15.25	56		4		37
π_u	4	-15.53	41				56
π_g	4	-15.77		29			71
σ_g	2	-16.50		16		5	71

Table 5.4. The SOF molecular orbital composition of UE_2^{2+} (E = O, S, Se, Te). To ensure SCF convergence for E = Se, Te 0.5 electrons were excited from σ_u to φ_u.

σ_u	Uf	Ud	Up	Us	L
UO_2^{2+}	55		8		34
US_2^{2+}	62		2		29
USe_2^{2+}	58		3		32
UTe_2^{2+}	56		4		37

σ_g	Uf	Ud	Up	Us	L
UO_2^{2+}		5		7	86
US_2^{2+}		13		5	85
USe_2^{2+}		15		3	79
UTe_2^{2+}		16		5	71

π_u	Uf	Ud	Up	Us	L
UO_2^{2+}	35				65
US_2^{2+}	40				59
USe_2^{2+}	39				60
UTe_2^{2+}	41				56

π_g	Uf	Ud	Up	Us	L
UO_2^{2+}		14			83
US_2^{2+}		20			78
USe_2^{2+}		21			78
UTe_2^{2+}		29			71

Table 5.5. A comparison of the compositions of the bonding valence orbitals and the non-bonding f orbitals for all the investigated group 16 uranyl analogues. L is the chalcogen p contributions

The molecular orbital composition analysis on the uranyl analogues is shown in two different ways. First, in Table 5.4 the energy of the MOs and the AO contributions to the valence MOs for the different systems are shown and second, in Table 5.5, the composition of the MOs are compared depending on which irreducible representation they belong to. Table 5.5 offers an easier comparison between the AO contributions to MOs in the different systems. In $D_{\infty h}$ symmetry the virtual orbitals, δ_u and φ_u, can not mix with ligand p orbitals and are thus completely centered on the uranium atom, with AO contributions of *ca* 100% from the U 5f orbital in both MOs.

In all σ_u MOs the ligand contribution is between 30-35% and the U 5f contribution is around 55-60%. The σ_u in UO_2^{2+} has an 8% U 6p contribution, 55% U 5f contribution and 34% O 2p contribution; in US_2^{2+} the U 5f contribution and the ligand p contribution is more or less the same as in the UO_2^{2+} system, with 62% U 5f and 29% S 3p contribution. The main change is that the U 6p contribution decreases significantly, from 8% to 2%. For the heavier group 16 elements the U 6p contribution increases from 2% in

US_2^{2+} to 3% in USe_2^{2+} and finally 4% in UTe_2^{2+}. This reduction in U 6p character compared to UO_2^{2+} reduces the pushing from below effect and means a stabilization of σ_u compared with the other MOs. Indeed, the gap between the σ_u and the HOMO-1 decreases from 0.7 eV to 0.3 eV on going from US_2^{2+} to UTe_2^{2+}.

σ_g shows a clear trend down group 16 with increasing U 6d character and decreasing ligand p character. For all the investigated molecules there are small, around 5%, U 7s contributions. In investigations of US_2 [160] it was shown that similarity in the mean orbital radius increased the overlap between different AOs. The contracted O 2p orbital has more overlap with the contracted U 5f than with the more diffuse 6d orbital. Descending the group the larger ligand p orbitals will have a better overlap with the U 6d orbitals, increasing the d character of the orbital and explains the relative stabilization of the σ_g MO (Figure 5.2) compared to the other valence MOs, giving it a more bonding role in the heavier analogues.

In terms of relative energy the π MOs shift dramatically down group 16; in terms of the AO compositions the shift is not as dramatic. In π_u there is the least amount of change to the composition; moving from UO_2^{2+} to US_2^{2+} the U 5f contribution increases from 35% to 40% and the ligand contribution decreases from 65% to 60%. Descending further down the group these proportions remain unchanged. In contrast, the composition of π_g changes more significantly; UO_2^{2+} has 14% U 6d contributions and 83% ligand p, in US_2^{2+} the U 6d contribution increases to 20% and the p contribution decreases to 78%.

The relative destabilization of the π orbitals observed on moving down group 16 is the result of two different factors; the first is the reduction of anti-bonding U 6p admixture to σ_u, reducing the pushing from below effect on σ_u. This results in a reduction in the energy gap between the lower energy valence MOs and σ_u, seen in a normalised diagram (Figure 5.1). The second factor is the stabilization of the σ_g orbital due to increased orbital overlap with the U 6d orbital, leading to a lowering of the MO energy compared to other

MOs. Thus, the apparent destabilization of the π orbitals is in fact the result of a stabilization of the σ_g and the σ_u molecular orbitals.

Mulliken atomic orbital population analysis

The net Mulliken orbital populations have been investigated for the group 16 uranyl analogues to further probe for differences in bonding. For U(VI) the formal s, p, d and f populations are 12, 30, 30 and 14, which have been subtracted from the relevant gross populations to yield the net Mulliken populations. The same procedure has been carried out for the ligand populations. In UO_2^{2+} (Table 5.6) the oxygen atoms have some added population in the s orbital but the main feature is the strong donation from the O 2p orbital, clearly seen in the -1.48 net population of O^{2-}. The negative net U p population of -0.61 is smaller than the expected zero population. This U p-hole has been seen in previous investigations of UO_2^{2+}.[189, 190] The p-hole indicates a donation of U 6p electrons due to charge being transferred to the bonding σ_u orbital. This is confirmed by noting the increased population of the U d and U f levels, 0.76 in d and 2.54 in f, as well as the MO composition analysis.

The O p population is smaller than expected considering the large difference in electronegativity for O and U, 3.44 compared to 1.38 on the Pauling electronegativity scale.[191] Based on previous computational work and the involvement of the O 2p and U 5f in the Mulliken population analysis, this confirms that the U-O_{yl} bond is largely covalent as this would explain the high Mulliken U f populations in the present study. The orbital compositions presented above support this as well, with all bonding orbitals having large O 2p contributions.

Moving to US_2^{2+}, the behaviour of the S Mulliken atomic populations is similar to previous U-chalcogen studies[169]; the magnitude of the S p donation increases compared to UO_2^{2+} to -1.92, a sign of a more covalent bond in US_2^{2+}. Correspondingly, the U d and U f populations increase by 0.22 and 0.34 respectively compared to the UO_2^{2+} system, demonstrating an increased participation in the U-S bond. In USe_2^{2+} the calculations

show that the trend observed for the UO_2^{2+} and US_2^{2+} populations continue; the net chalcogen p donation increases to -2.18, demonstrating that the bond is increasingly covalent down the group. The populations of the U d and f orbitals again increase compared to the populations in previous UO_2^{2+} and US_2^{2+} systems. The trends that began in US_2^{2+} are more developed in USe_2^{2+}; the U-chalcogen covalency increases as seen in the Se p donation to the U f and d orbitals.

		s	p	d	f
UO_2^{2+}	U	-0.34	-0.61	0.76	2.54
	O	0.20	-1.48	0.09	0.01
US_2^{2+}	U	-0.34	-0.06	0.98	2.88
	S	0.03	-1.92	0.14	0.02
USe_2^{2+}	U	0.03	0.06	1.16	2.92
	Se	-0.03	-2.18	0.10	0.01
UTe_2^{2+}	U	0.15	-0.02	1.31	3.10
	Te	-0.02	-2.34	0.07	0.01

Table 5.6. Net Mulliken atomic populations of UE_2^{2+} (E = O, S, Se, Te)

In UTe_2^{2+} the trends from USe_2^{2+} are even clearer; the Te p donation is the largest calculated in the present study, -2.34, with the donated population ending up in the U d and f populations as seen in the U d and f orbitals, which have the highest calculated net population of all the group 16 analogues, 1.31 and 3.10 for d and f respectively. The increased p donation from all the ligand chalcogen atoms in the study strongly suggests that the covalency of the bond increases going down group 16.

In all analogues heavier than UO_2^{2+} the U p-hole decreases, from a net population of -0.61 in UO_2^{2+} to *ca* 0 in US_2^{2+}, USe_2^{2+} and UTe_2^{2+}. This is confirmed in the relative

energies of the valence MOs, where σ_u is stabilized relative to the other MOs, thus displaying a lessening of the pushing from below effect.

Atomic charge analysis

The Mulliken, Hirshfeld and Voronoi charge analysis data (Table 5.7) agree with the conclusions from the Mulliken population analysis; the Mulliken charge of U is the most positive for UO_2^{2+} at 3.65, where the charge is the most negative for O, -0.83. This corresponds to the high electronegativity of the oxygen atom attracting electron density from the U centre to the O centre. Moving down group 16 the difference in Mulliken charges for the ligand and the metal decreases as less charge is moved from U to E. In US_2^{2+} the U charge has become noticeable less positive while the S Mulliken charge is 0.56 more positive compared to UO_2^{2+} and in USe_2^{2+} this trend continues. For UTe_2^{2+} the difference between the E and U charges is only 1.19 compared to 4.48 for UO_2^{2+}. The Hirshfeld atomic charges follow the same pattern; moving down group 16 the charge on U decreases while at the same time the ligand charges increase.

Even though the Voronoi charge decomposition scheme is based on partitioning the electron density, it produces the same result as the other, wave function based schemes; the U charge decreases moving down group 16, from 1.56 for UO_2^{2+} to 1.14 for UTe_2^{2+}, and the ligand charges become more positive moving down group 16, from 0.22 for O to 0.43 for Te. Again, this trend is an effect of the electronegativity of the chalcogen ligand decreasing down the group. In all the charge analysis schemes the difference in charge between U and the E ligand decreases going down group indicating a less ionic bond. This supports the result of the population analysis, which showed an increase in covalency moving down group 16.

		Mulliken	Hirshfeld	Voronoi
UO_2^{2+}	U	3.65	2.13	1.56
	O	-0.83	-0.07	0.22
	Δ	*4.48*	*2.20*	*1.34*
US_2^{2+}	U	2.54	1.56	1.44
	S	-0.27	0.22	0.28
	Δ	*2.81*	*1.34*	*1.16*
USe_2^{2+}	U	1.82	1.42	1.35
	Se	0.09	0.29	0.33
	Δ	*1.73*	*1.13*	*1.02*
UTe_2^{2+}	U	1.46	1.17	1.14
	Te	0.27	0.41	0.43
	Δ	*1.19*	*0.76*	*0.71*

Table 5.7. The Mulliken, Hirshfeld and Voronoi atomic charges of the UE_2^{2+} (E = O, S, Se, Te). Δ is the difference charge between the chalcogen and the uranium atom.

Energy decomposition - UE_2^{2+} (E = O, S, Se, Te)

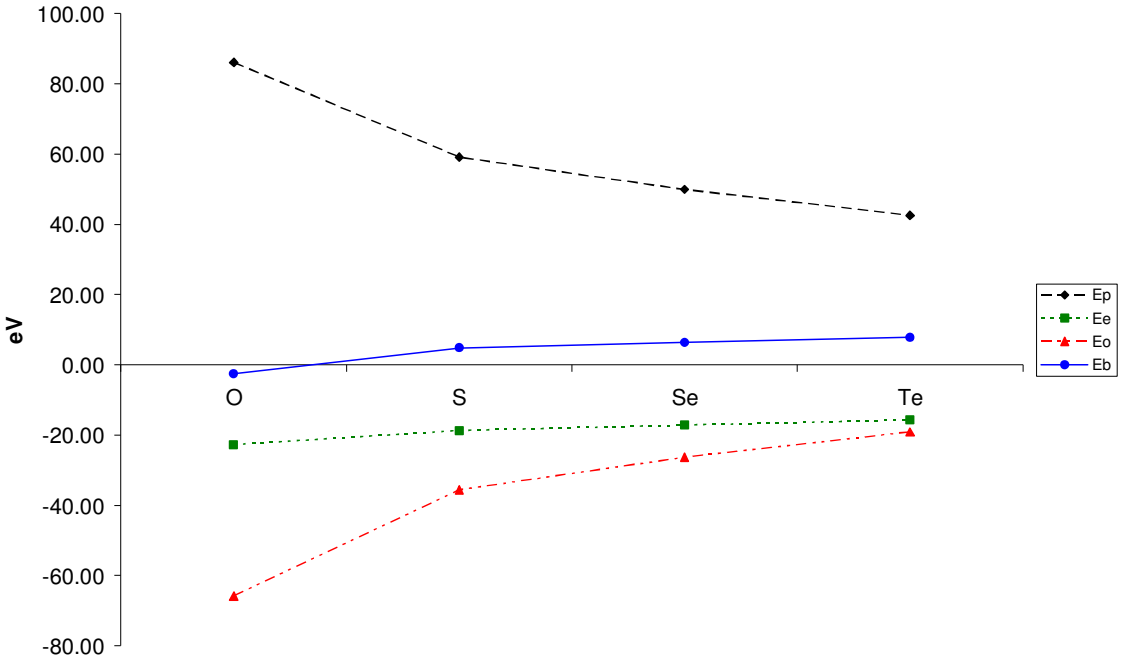

Figure 5.3. The energy decomposition analysis of the group 16 uranyl analogues, using atomic fragments. SOF optimized geometries.

Spin-orbit free energy decompositions of all the group 16 uranyl analogues are presented in Figure 5.3 and Table 5.8. The Ziegler-Rauk energy decomposition analysis in ADF is heavily dependent on how the molecule is divided into fragments. It is not straight forward to divide the uranyl analogues into relevant fragments. If the molecule is divided into fragments according to the oxidation number of the atoms, i.e. U^{6+} and 2 E^{2-} (E = O, S, Se, Te) fragments, the decomposition will inevitably be dominated by the electrostatic interaction term, as the fragments are highly charged. Thus in the present calculations the fragments used are the ADF basic atom fragments of U and E.[62] The basic atom fragments are neutral, spin-restricted and spherically symmetric. The problem with using basic atomic fragments is that comparisons of the calculated bonding energy to experimental bonding energies needs to be corrected, as the basic fragment does not

include the correct spin multiplet state making it a poor representative of the real atom. However, when only comparing to other computational results calculated in exactly the same way, the conclusions are still valid and discrepancies with experimental results are not important.[192]

	Optimized geometry			
	UO_2^{2+}	US_2^{2+}	USe_2^{2+}*	UTe_2^{2+}*
E_p	86.06	59.11	49.89	42.54
E_e	-22.73	-18.72	-17.17	-15.68
E_{pre}	63.33	40.39	32.72	26.86
E_o	-65.85	-35.57	-26.33	-19.07
σ_g	*-17.03*	*-12.39*	*-9.57*	*-7.28*
σ_u	*-21.63*	*-9.44*	*-1.43*	*-0.16*
π_g	*-30.44*	*-23.23*	*-20.47*	*-17.68*
π_u	*-20.08*	*-12.10*	*-10.23*	*-8.43*
δ_g	*3.60*	*3.43*	*3.28*	*3.13*
δ_u	*9.88*	*9.02*	*8.53*	*8.00*
φ_g	*0.00*	*0.00*	*0.00*	*0.00*
φ_u	*9.91*	*9.18*	*3.58**	*3.38**
E_b	-2.53	4.81	6.39	7.79

Table 5.8. The SOF PBE ADF energy decomposition analysis of the group 16 uranyl analogues, using atomic fragments. *) Occupation number of σ_u 1.5, φ_u 0.5.

The first thing of note is that the total bond energy, E_B, is bonding only for UO_2^{2+}: -2.53 eV; the other analogues have increasingly positive bonding energies from 4.81 eV for US_2^{2+} to 7.79 eV for UTe_2^{2+}. The Pauli repulsion energy term, E_P, is highest in UO_2^{2+} with 86.06 eV and decreasing moving down group 16. The major decrease occurs moving from UO_2^{2+} to US_2^{2+}, the systems where the bond distance increases the most (1.713 to 2.225 Å). The decrease in E_P for the heavier chalcogens is linear, corresponding to the almost linear increase in U-E bond distance. The electrostatic energy term, E_E, does

not change much down the group, the difference is only 7 eV. As a result E_{Pre} (E_E + E_P) decreases significantly, from 63.33 eV in UO_2^{2+} to 26.86 eV in UTe_2^{2+}.

The orbital interaction term, E_O, decreases significantly moving down group 16. In UO_2^{2+} the E_O is -65.85 eV which drops to -35.57 eV in US_2^{2+}, a drop of almost 30 eV exclusively located in the bonding irreps, π_u, π_g, σ_g and σ_u. The most significant drop is in the odd parity MOs, σ_u and π_u, while the non-bonding φ_u and δ_u MOs are mostly unaffected. This indicates that there is significantly less orbital interaction between the S 3p and the U 5f due to the difference in orbital radii.[160] Moving from US_2^{2+} to USe_2^{2+} and UTe_2^{2+} the σ_u E_O drops from -9.44 to -0.16 eV and the corresponding decrease in φ_u is from 9.18 to 3.38 eV. The reason for this is computational, as in order to achieve SCF convergence 0.5 electrons have been excited into the φ_u orbital in USe_2^{2+} and UTe_2^{2+}, which impacts E_B. However, the σ_u and φ_u terms have different sign, largely canceling out each other in US_2^{2+} and to a lesser degree in USe_2^{2+} and UTe_2^{2+}. The maximum impact of these two terms is in UTe_2^{2+}, where E_O will be decreased by 3.2 eV if they were removed. This will not significantly change the total bonding energy, which already is very positive at 7.79 eV.

The reason for increased E_B going down group 16 is that the 45 eV decrease in E_O is not compensated by a corresponding decrease in the Pauli repulsion energy term. However, the fact that non-aufbau occupations were used in the analysis of the USe_2^{2+} and UTe_2^{2+} analogues makes those results slightly more uncertain. The fact that UO_2^{2+} is calculated to be the only stable compound agrees with experimental results; there are numerous known UO_2^{2+} containing systems while there are very few known examples of group 16 analogues.

Geometry of UE_2 (E = O, S, Se Te)

	State	U-E (Å)	E-U-E (°)	ν_1 (cm^{-1})	ν_2 (cm^{-1})	ν_3 (cm^{-1})	ν_4 (cm^{-1})
UO_2							
$D_{\infty h}$	-	1.80	180.00	152	152	868	925
C_{2v}	$^3B_2$	1.80	178.81	-	145	683	891
US_2							
$D_{\infty h}$	-	2.33	180.00	91*i*	91*i*	439	480
C_{2v}	$^3A_1$	2.36	116.72	-	89	445	447
USe_2							
$D_{\infty h}$	-	2.48	180.00	654*i*	658*i*	249	318
C_{2v}	$^3B_1$	2.51	116.50	-	56	275	292
UTe_2							
$D_{\infty h}$	-	2.79	180.00	42*i*	60*i*	163	221
C_{2v}	$^3B_1$	2.75	114.44	-	34	161	210

Table 5.9. Gaussian03 (B3LYP/SDD) geometry optimization and frequency results on the group 16 analogues of UO_2.

Two sets of geometry optimizations were carried out; one optimization of the linear molecules using $D_{\infty h}$ symmetry and a second in C_{2v}. Additionally, frequency calculations were performed on the optimized geometries in both symmetries. Where possible, the electronic ground state of the system was determined.

The optimized bond distances display the same trends as the closed shell dications; an increase moving down group 16, from 1.80 Å in UO_2 to 2.75 Å in UTe_2. As in the cations, the largest increase is in moving from UO_2 to US_2, where the bond distance increases by 0.56 Å, while in the cation the increase was 0.51 Å. Moving from US_2 to

USe_2 and UTe_2 the increase in bond length is almost linear. The C_{2v} bond distances are almost the same as the linear bond distances.

In the bond distance analysis above, the U-O bond distance have been given for the linear system, and with a C_{2v} O-U-O angle of 178.81° and no imaginary frequencies in either $D_{\infty h}$ or C_{2v}, this is a reasonable value to quote. For all other optimized $D_{\infty h}$ geometries imaginary frequencies are found indicating that the structure is optimized to a transition state geometry. The calculated imaginary frequencies in USe_2 are quite large at around $655i$ cm^{-1} compared to the imaginary frequencies of USe_2 and UTe_2 which are around $90i$, $60i$ and $43i$ cm^{-1}. The calculated imaginary modes in Table 5.9 should be degenerate and the fact that they are not suggests that G03 might have difficulties working in the $D_{\infty h}$ point group.

In the C_{2v} calculations the bond angle of UO_2 is close to 180°, for US_2 the calculated bond angle is 116.7°, for USe_2 116.5° and for UTe_2 114.4°. There is thus a decreasing bond angle descending group 16, the change however is only 0.22° moving from US_2 to USe_2. When moving to UTe_2 the bond angle decreases *ca* 2° compared to the lighter group 16 elements. The US_2 bond angle is more acute than previous studies have found, 116.7° compared to 121.4° however this is not too worrying; the basis sets for the previous work and the present study were not the same. More importantly, both sets of calculations confirm the bent geometry of the US_2 system.

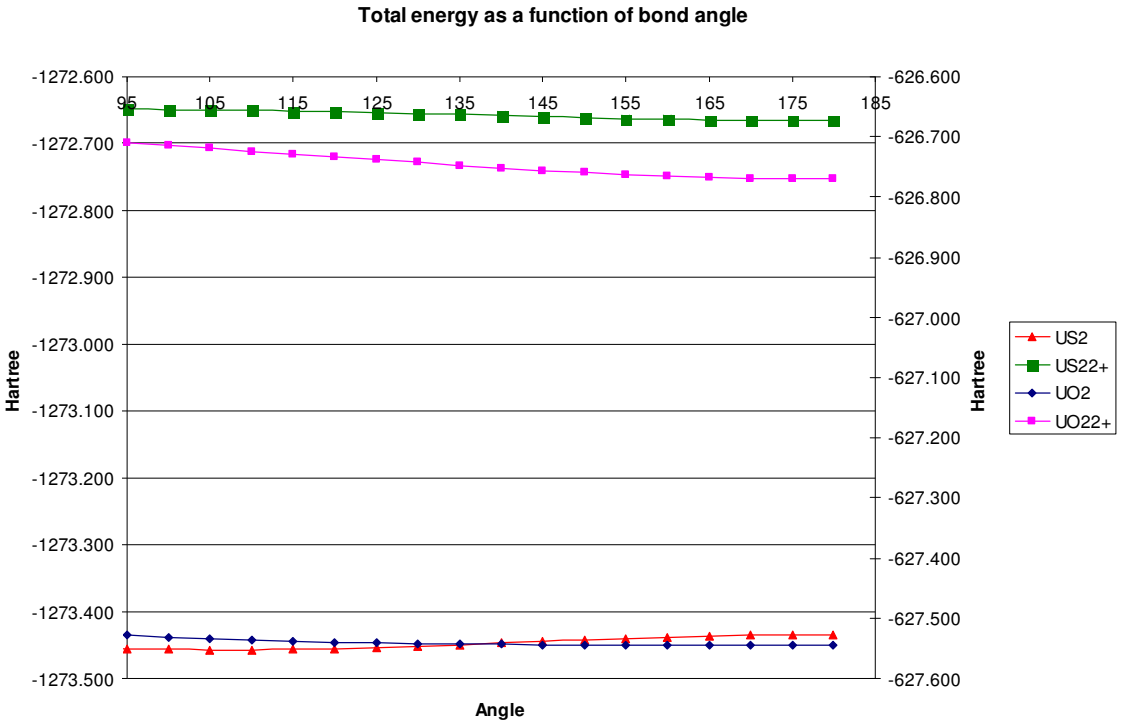

Figure 5.4. Total energy of UE_2 and UE_2^{2+} (E = O, S) as a function of bond angle. G03 using B3LYP/SDD.

To determine if the bent geometry of US_2 is the result of a "floppy" structure having a shallow minimum on the potential energy surface compared to UO_2, the energy barrier to bending the E-U-E molecule from linear was calculated keeping the bond distances fixed throughout the energy scan (Figure 5.4). All systems have an energy minimum at 180.0° except US_2, which has a calculated energy minimum at 105°. The difference between the linear geometry and the 90° for UO_2^{2+} and UO_2 is calculated as 170.7 kJ/mol and 61.4 kJ/mol respectively. The corresponding energy difference in US_2^{2+} is 47.2 kJ/mol. The energy barrier calculation was also performed on US_2, but here the bent geometry was calculated to be 59.8 kJ/mol more stable than the linear system. All geometries are thus shown to lie within well defined minima. The calculated S-U-S bond angle in US_2 is smaller than in the optimized structure due to the geometry not being able to relax at each point of the scan.

Electronic structure

This section compares the electronic structures at the linear and bent (E-U-E = 120°) geometries of UO_2 and US_2 to determine if there is any difference in the electronic structure which might explain the differences between the two molecules.

E-U-E = 180°

The ground state is $^3B_1$ for both UO_2 and US_2. In the electronic structure of both complexes (Table 5.10 and Figure 5.5) the unpaired electrons are purely U based and the HOMO is an f_φ MO for both systems. The HOMO-1, $^\alpha 24a_1$ in UO_2 and $^\alpha 27a_1$ in US_2, is of undetermined symmetry and the composition of $^\alpha 24a_1$ consists of large U s and U p core MOs, larger than what is found in the US_2 system. It is likely this is an effect of the QZ4P basis sets employed in the calculation and those results have been removed. The ordering of the doubly occupied MOs below the U based MOs is, using $D_{\infty h}$ symmetry labels, σ_u, π_u, σ_g, π_g for UO_2 and σ_u, π_u, π_g, σ_g for US_2. There are two main differences between the UO_2 and US_2 occupied MOs. The first is the amount of U p contribution of the σ_u, 9% in UO_2 and 4% in US_2. Also, there is a smaller energy gap between the σ_u and the π_u MOs, *ca* 1 eV for UO_2 compared to ca 0.5 eV for US_2.

The second difference is the smaller energy gap between the non-bonding f based MOs and the doubly occupied valence MOs in US_2, the gap is only 1.27 eV compared to 2.93 eV in UO_2. This is the same trend as was observed for the UE_2^{2+} dication, where the electronic structure is increasingly compact moving down group 16. The doubly occupied MOs span the same range of energy, 1.99 eV for UO_2 and 1.87 eV for US_2.

UO_2								US_2							
MO	E	Occ.	Uf	Ud	Up	Us	Op	MO	E	Occ.	Uf	Ud	Up	Us	Sp
$^{\alpha}15b_2$	-4.17	0	100					$^{\alpha}28a_1$	-3.94	0	47	14		39	
$^{\alpha}6a_2$	-4.17	0	100					$^{\alpha}18b_2$	-4.06	0.19	99				
$^{\alpha}25a_1$	-4.17	0	100					$^{\alpha}7a_2$	-4.06	0.18	99				
$^{\alpha}12b_1$	-4.19	1	100					$^{\alpha}13b_1$	-4.07	0.63	100				
$^{\alpha}24a_1$	-4.31	1						$^{\alpha}27a_1$	-4.16	1	53	10		32	
$^{\beta}14b_2$	-7.24	1	45		9		45	$^{\beta}17b_2$	-5.43	1	34		4		59
$^{\alpha}14b_2$	-7.55	1	48		9		43	$^{\alpha}17b_2$	-5.74	1	48		3		45
$^{\beta}11b_1$	-8.58	1	19				79	$^{\beta}12b_1$	-6.23	1	13				85
$^{\beta}23a_1$	-8.58	1	21				79	$^{\beta}26a_1$	-6.23	1	14				85
$^{\alpha}11b_1$	-8.67	1	24				75	$^{\alpha}12b_1$	-6.28	1	22				75
$^{\alpha}23a_1$	-8.67	1	24				75	$^{\alpha}26a_1$	-6.28	1	24				75
$^{\beta}22a_1$	-9.10	1		5			95	$^{\alpha}16b_2$	-6.72	1		22			78
$^{\alpha}22a_1$	-9.13	1		5			93	$^{\alpha}6a_2$	-6.72	1		22			78
$^{\alpha}5a_2$	-9.23	1		17			81	$^{\beta}16b_2$	-6.73	1		17			82
$^{\alpha}13b_2$	-9.23	1		17			81	$^{\beta}6a_2$	-6.73	1		17			82
$^{\beta}5a_2$	-9.23	1		14			84	$^{\alpha}25a_1$	-7.27	1		6			90
$^{\beta}13b_2$	-9.23	1		14			84	$^{\beta}25a_1$	-7.30	1		5			94

Table 5.10. The MO compositions of UO_2 and US_2 (bond angle 180°) in C_{2v} symmetry. 0.00008 Hartree electronic smearing used in US_2

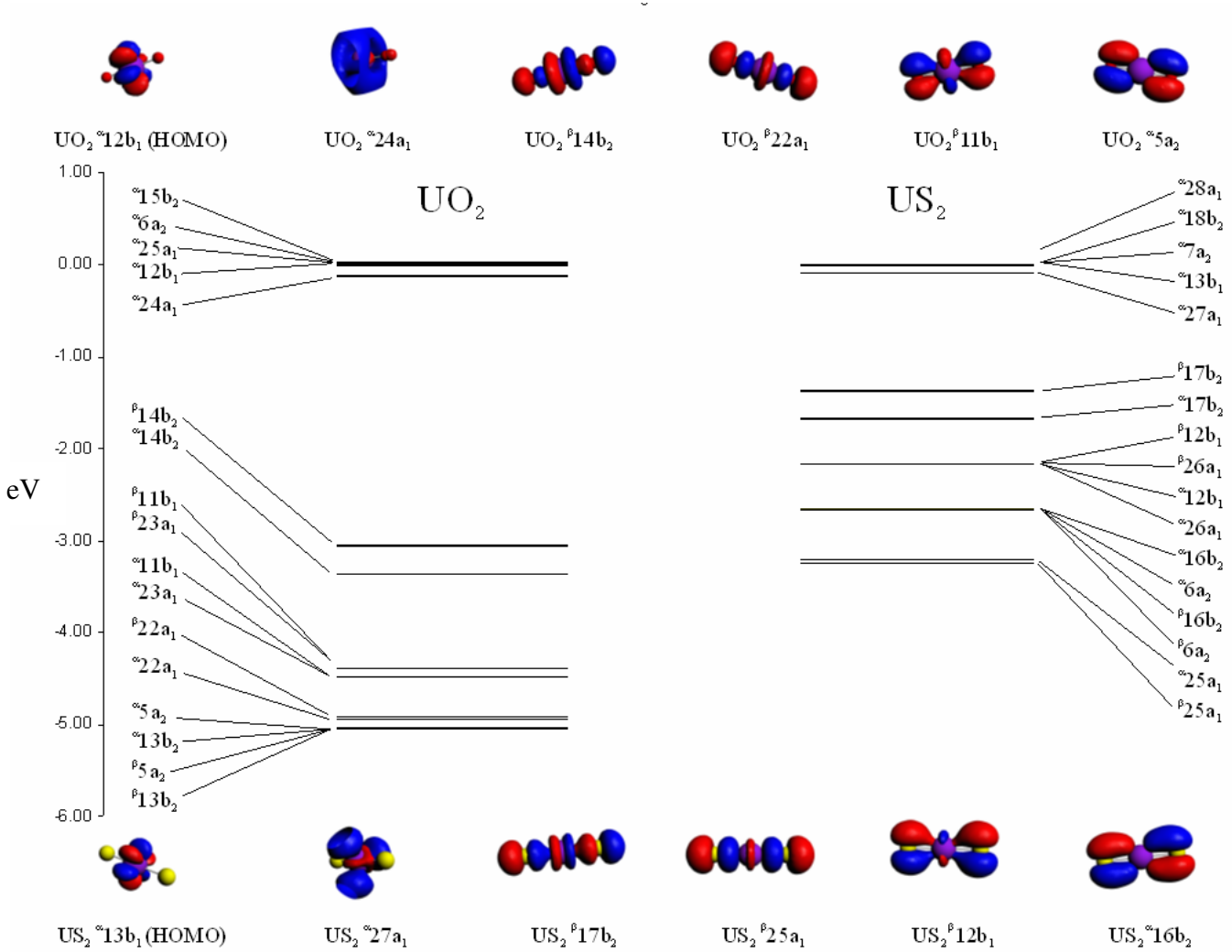

Figure 5.5. ADF single point electronic structure of UO_2 and US_2 at E-U-E = 180°, using Gaussian03 optimized bond distances

E-U-E = 120°

The ground state is $^3B_1$ for both UO_2 and US_2 at the bent geometry. Previous work has assigned US_2 a $^3B_2$ ground state based on an analysis of the calculated frequencies. The present result might be different due to the use of a different definition of the principle axis thus switching the b_1 and b_2 labels. UO_2 and US_2 (Figure 5.6) have a slightly different MO ordering; first, there is a notable difference in the overall electronic structure of UO_2 compared to US_2. The energy gap between the σ_u ($14b_2$ in UO_2 and $17b_2$ in US_2) and the f-based MOs ($24a_1$, $12b_1$ and $27a_1$ and $13b_1$ for UO_2 and US_2 respectively) is much larger for UO_2 than US_2, 3.0 eV compared to 1.5 eV. The bonding MOs of UO_2 are well separated and span a greater range than the US_2 MOs, with the UO_2 MOs being spread over *ca* 3 eV compared to *ca* 2 eV for US_2. The bonding MOs in UO_2 span a greater energy range in the bent system compared to the linear system (Figure 5.5), with the π bonding MOs being about 1 eV lower in energy. In contrast, the valence MOs in US_2 span the same energy range regardless of whether the system is linear or bent. The f based orbitals are very close together in energy for both systems, UO_2 more so than US_2.

Second, the stabilizing trend for σ_g that was seen for the UE_2^{2+} cations is confirmed for US_2; the $25a_1$ MO is the bonding valence MO lowest in energy. $22a_1$, the corresponding MO in UO_2, is also stabilized compared to what was found for the linear system, albeit not as much as σ_g in US_2; in UO_2 the lowest energy valence MO is still π-bonding. One interesting feature is the hint of ligand-ligand interactions seen in the $26a_1$ and $22a_1$ orbitals of both the US_2 and UO_2 systems respectively. This feature would stabilize the bent geometry over the linear geometry and explain the stabilization of $22a_1$ in UO_2 compared to the corresponding MO is the linear structure. However, $26a_1$ in US_2 also display the same ligand interaction yet show no stabilization compared to the electronic structure in the linear system. Thus the effect is likely due to the cut-off setting in the displayed MOs.

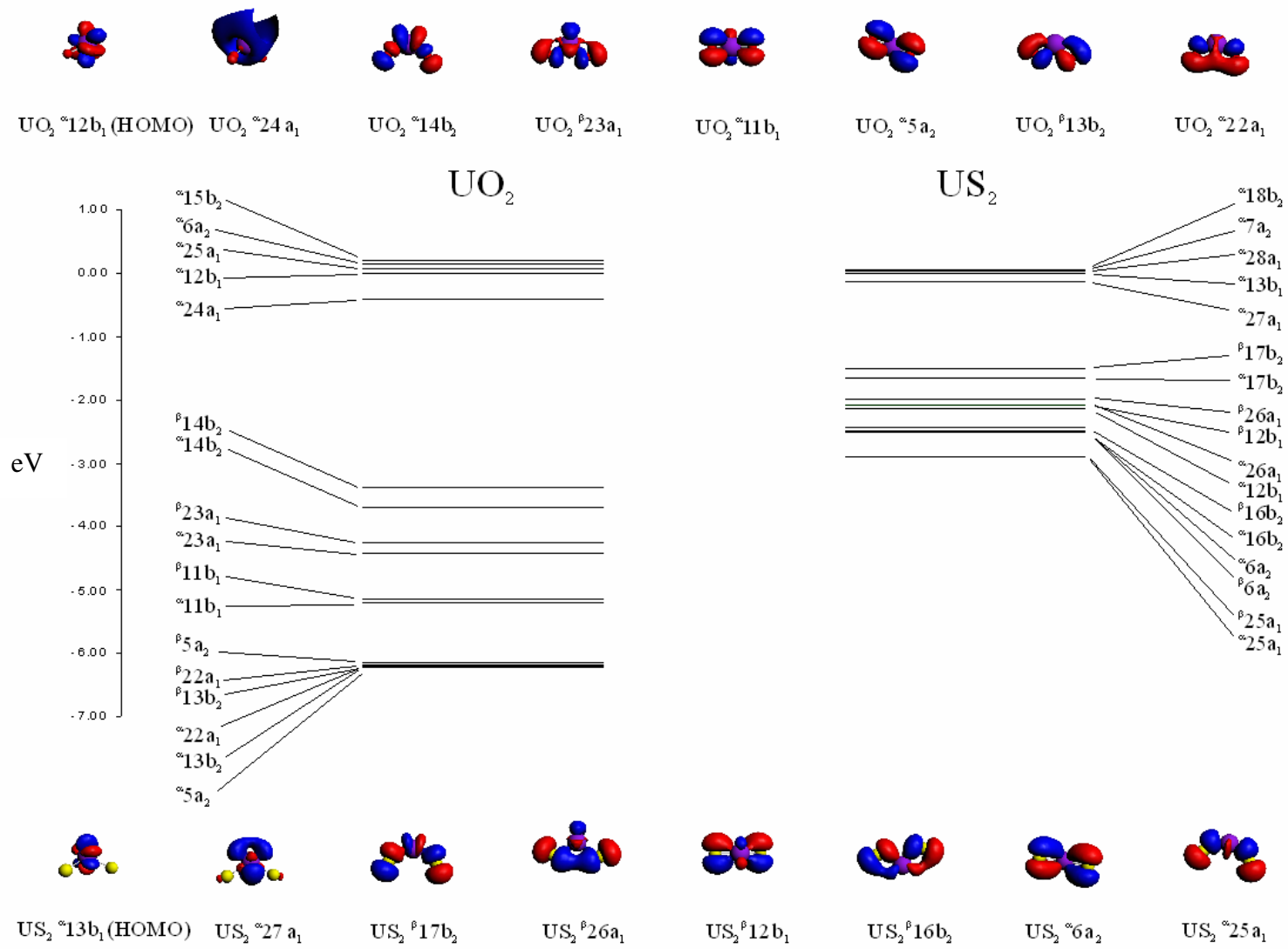

Figure 5.6. Single point electronic structure of UO_2 and US_2 at E-U-E = 120°, using the Gaussian03 optimized bond distances.

This is confirmed by looking at Table 5.11 which presents the AO decomposition of the valence MOs of UO_2 and US_2. The U 6d contributions to the US_2 MOs are larger than in UO_2, 6-16 % compared to 5-6 % in the three lowest lying bonding valence MOs. The opposite trend is seen for the U 5f contributions where the contributions to the bonding orbitals are larger in the UO_2 system, even though the calculations have been performed on the bent system. The largest 5f contribution is in the $14b_2$ MO (σ_u) in UO_2 and the corresponding MO in US_2, $17b_2$. The other 5f contributions in US_2 are smaller, below 10%, with an exception for the $^{\alpha}12\ b_1\ \pi$ MO. In UO_2 the 5f contributions are consistently above 13 %, and for $^{\alpha}23a_1$ the contribution is 20 %. Thus, US_2 is bent because of the enhanced U 6d contributions.

Calculations were also performed on UO_2 in which the 5f orbital basis functions were removed from the basis set. These calculations confirm that the d AOs are the reason for bent neutral actinyls; with no 5f orbitals the PBE optimized O-U-O angle was 98.35°, more bent than the preferred angles of *ca* 120° found for US_2 and ThO_2.[160]

			UO_2									US_2					
MO	E	Occ.	Uf	Ud	Up	Us	Op	MO	E	Occ.	Uf	Ud	Up	Us	Sp
$^{\alpha}15b_2$	-4.10	0	81	14				$^{\alpha}18b_2$	-4.12	0	90	6			
$^{\alpha}6a_2$	-4.18	0	82	15				$^{\alpha}7a_2$	-4.12	0	89	8			
$^{\alpha}25a_1$	-4.24	0	98					$^{\alpha}28a_1$	-4.13	0	94				
$^{\alpha}12b_1$	-4.31	1	96					$^{\alpha}13b_1$	-4.17	1	97				
$^{\alpha}24a_1$	-4.73	1	-	-	-	-	-	$^{\alpha}27a_1$	-4.30	1	64			23	8
$^{\beta}14b_2$	-7.70	1	21		15		58	$^{\beta}17b_2$	-5.66	1	17		3		81
$^{\alpha}14b_2$	-8.01	1	28	6	12		55	$^{\alpha}17b_2$	-5.82	1	33				64
$^{\beta}23a_1$	-8.56	1	15		9		77	$^{\beta}26a_1$	-6.15	1	4	7			89
$^{\alpha}23a_1$	-8.74	1	20		6		71	$^{\beta}12b_1$	-6.24	1	9	6			85
$^{\beta}11b_1$	-9.46	1	13				83	$^{\alpha}26a_1$	-6.24	1	8	11			78
$^{\alpha}11b_1$	-9.52	1	15	5			79	$^{\alpha}12b_1$	-6.31	1	16	8			76
$^{\beta}5a_2$	-10.46	1	8				87	$^{\beta}16b_2$	-6.60	1	7	13			77
$^{\beta}22a_1$	-10.49	1		6			84	$^{\alpha}16b_2$	-6.66	1	10	16			71
$^{\beta}13b_2$	-10.50	1	12				85	$^{\alpha}6a_2$	-6.67	1	8	16			75

Table 5.11. PBE molecular orbital decomposition of UO_2 and US_2 at E-U-E = 120°

Why is UE_2^{2+} linear and UE_2 (E = O, S, Se, Te) bent?

Why are the neutral US_2, USe_2 and UTe_2 systems (but not UO_2) bent when the corresponding dications are linear? Previous investigations of the bonding in actinyls have shown that the 5f and 6d orbitals prefer different bond angles, with a bond dominated by the 5f MOs being linear and 6d dominated bonds preferring bond angles of *ca* 120°. Investigations of UO_2^+ and US_2^+ [193] have shown that they are also linear, thus reducing the question to the difference in the bonding of neutral species. It has been demonstrated that this bending is not the result of a false minimum on a shallow potential surface, as all systems have significant energy barriers to deformation from their optimized geometries.

The Mulliken populations in the neutral UO_2 and US_2 systems as a function of bond angle (Figure 5.7) show that the major differences are in the U f and d populations, with the f population being larger in the linear UO_2 system and then sharply dropping in the bent systems, while for US_2 the decrease with smaller bond angles is more gradual. At the same time the d population in the US_2 system is consistently higher (and increasing) than in UO_2 for both the bent and linear geometries, suggesting a higher d participation in US_2. The s and p populations in both UO_2 and US_2 do not vary significantly as the bond angle decreases. Thus, the fact that US_2 is bent reflects the increased d participation and the smaller f participation. This reason for the bending has been suggested in previous work[160]: the mean orbital radius of the 2p in oxygen corresponds more closely to the U 5f than the U 6d while the more diffuse higher p AOs have radii closer to the U 6d. All evidence presented in this work support an increased d participation in the heavier group 16 uranyl analogues.

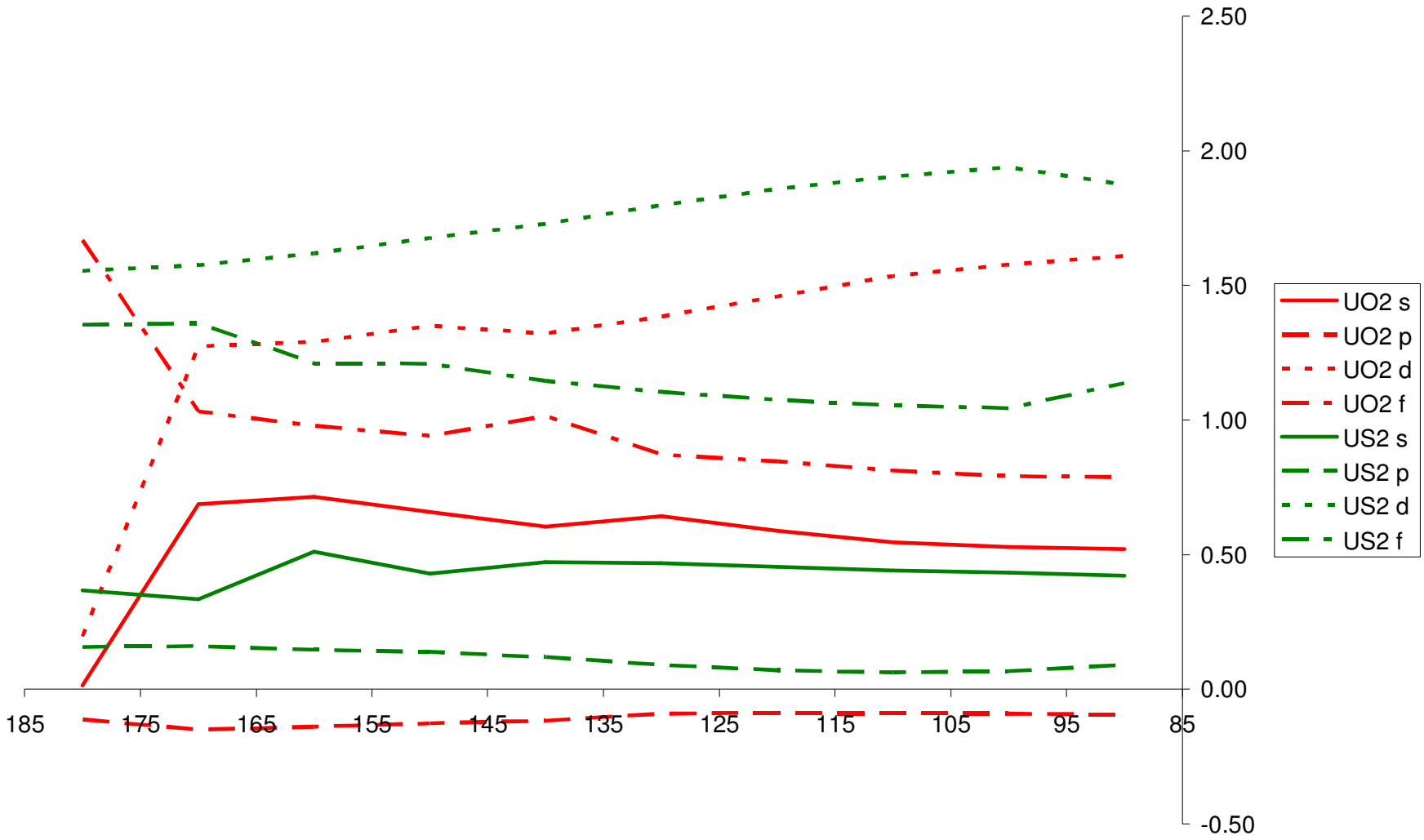

Figure 5.7. The net Mulliken atomic populations in U as a function of bond angle in UO_2 and US_2.

Geometry of $U(XR)_2^{2+}$ (X = N, P, As; R = H, CH_3)

The second part of this chapter is the investigation into the $U(XR)_2^{2+}$ (X = N, P, As; R = H, CH_3) uranyl analogues.

The initial calculations were performed using no symmetry constraints to allow for maximum flexibility in the calculation, where the starting geometries were assumed to be linear for R = H and staggered for R = CH_3. The eclipsed formation was investigated for R = CH_3, but the SCF did not converge unless large electronic smearing was used, resulting in unphysical electronic structures with many MOs fractionally occupied. The calculated geometries using no symmetry, were all very close to the highest symmetry structures, $D_{\infty h}$, for $U(XH)_2^{2+}$ and D_{3d} (staggered formation) for $U(XCH_3)_2^{2+}$.

	U-X	X-C	X-H	C-H	X-C-H (°)	X-U-X (°)
X=N						
H	1.77	-	1.04	-	-	180.0
CH_3 (s)	1.79	1.47	-	1.10	108.6	180.0
X=P						
H	2.42	-	1.44	-	-	180.0
CH_3 (s)	2.37	1.81	-	1.10	108.7	180.0
X=As						
H	2.55	-	1.52	-	-	180.0
CH_3 (s)	2.54	1.94	-	1.10	107.6	180.0

Table 5.12. The ADF optimized geometries of $U(XR)_2^{2+}$ (X = N, P, As; R = H, CH_3). Distances in Å.

Metric parameters from the optimized geometries are shown in Table 5.12. The U-X distances increase in the R = H complexes moving down group 15. 1.77 Å for X = N is shorter than the U-N distance found in $U(NPH_3)_2^{4+}$ (1.823 Å) and the 1.90-1.95 Å found in other imido complexes, most likely as a result of the absence of competing equatorial

interactions.[176, 177] The U-X distance increases to 2.42 Å and 2.55 Å for X = P and As respectively, with the largest increase seen when moving from N to P, where the increase is *ca* 0.65 Å. There is only a minor increase in bond length moving from P to As, reminiscent of the bond length variations in the group 16 analogues. The increase in atomic radius descending group 15 is the principal reason for the increase in bond distance, however, the electron smearing employed in the X = P and As calculations are also partially responsible. The partial excitation results in orbitals having fractional occupation numbers, making interpretation difficult unless very little smearing is employed. Albeit a small effect, the removal of bonding electrons to non-bonding MOs will have an effect on the bond distances. However, since the smearing is very small in the present calculations, its effect on the calculated geometries can be considered minor.

The U-X distances are largely conserved on exchanging R = H for R = CH_3; the bond length increases from 1.79 Å to 2.37 Å and 2.54 Å for X = N, P and As. The X-C bond is similarly lengthened, increasing from 1.47 Å to 1.81 Å and 1.94 Å for X = N, P and As, due to the increase in atomic radius of X. The fractional occupations discussed above only effect the U-X bonding MOs and not the MOs responsible for X-C bonding. The C-H calculated bond distances, as well as the X-C-H bond angles, are conserved for all systems, being very close to 1.10 Å and 108.6° respectively. A slight exception is the As-C-H angle, which is 107.6°.

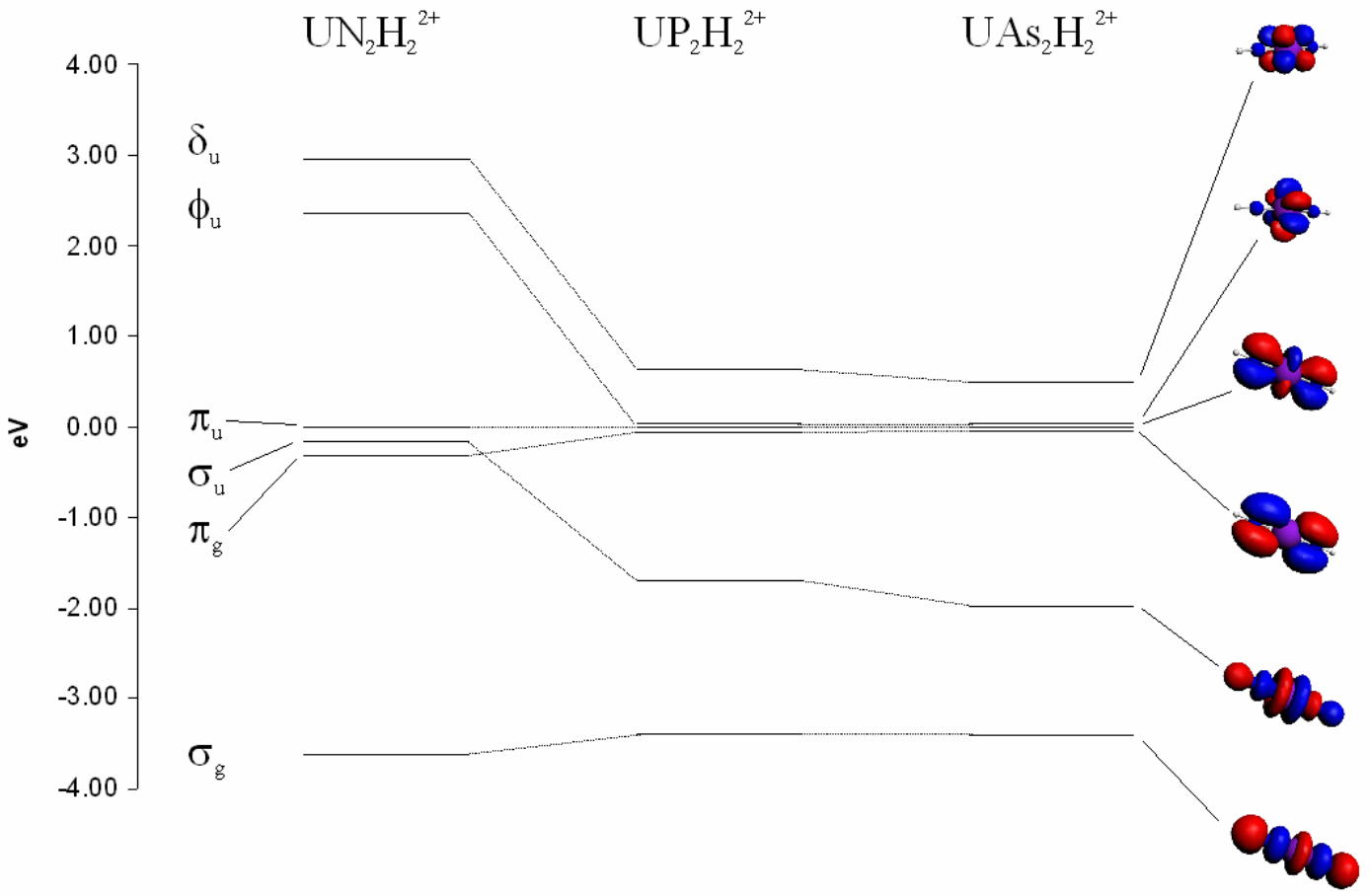

Figure 5.8. Valence MO energy level diagram of $U(XR)_2^{2+}$ (X = N, P, As; R = H). The HOMO has been normalized to 0 eV in all systems. Displayed MOs from $U(NH)_2^{2+}$

Electronic structure - $U(XR)_2^{2+}$ (X = N, P, As; R = H, CH_3)

$U(XR)_2^{2+}$ (X = N, P, As; R = H)

The calculated electronic structure of the R = H systems is shown in Figure 5.8. With X = N the energetic ordering of the occupied MOs is, using $D_{\infty h}$ symmetry labels: $\pi_u > \sigma_u > \pi_g >> \sigma_g$, with all MOs well separated energetically. The ordering changes for X = P, As where the two π MOs are the highest occupied orbitals, π_u being the HOMO, and some of the MOs are very close in energy, not dissimilar to the group 16 molecules. As has been seen in previous work on R-N=U=N-R systems[176], σ_u is stabilized, here by *ca* 1.6 eV (X = P) and *ca* 2 eV (X = As) compared to X = N. The reason for this is the formation of a σ bond "backbone" along the axis of the molecule, causing stabilization of the σ_u. The most noticeable feature, however, is the decrease of the HOMO-LUMO gap descending group 15. For X = N, the gap is 2.4 eV, which decreases to 0.03 eV for both X = P, As. The gap between the two non-bonding 5f orbitals δ_u and φ_u is kept almost constant for all the systems at *ca* 0.6 eV; the energy gap to σ_g is also relatively stable.

The very small HOMO-LUMO gap is due to having to use smearing, thus fractionally occupying the HOMO+1, φ_u. Looking at the φ_u levels of the X = P and As systems (Table 5.13) there is an occupation of 0.3 or higher. The small HOMO-LUMO gap in the heavier systems indicates that they are multiconfigurational in nature, meaning DFT by definition will struggle. The applied electronic smearing is one way around the problem which hopefully will not significantly affect trends in the bonding MOs.

			Composition (%)				
MO	**Occupation**	**Energy [eV]**	**U f**	**U d**	**U p**	**X p**	**H s**
$U(NH)_2^{2+}$							
small U core							
2 δ_u	0	-16.49	99				
2 φ_u	0	-17.09	99				
7 π_u	4	-19.44	41			59	
9 σ_u	2	-19.61	57		11	21	5
4 π_g	4	-19.76		19		80	
12 σ_g	2	-23.05		10		67	20
large U core							
1 δ_u	0	-16.68	99				
1 φ_u	0	-17.67	99				
1 π_u	4	-19.51	40			59	
1 π_g	4	-19.84		22		77	
3 σ_u	2	-20.42	50			27	7
3 σ_g	2	-23.10		11		48	26
$U(PH)_2^{2+}$							
2 δ_u	0	-15.26	99				
2 φ_u	0.3	-15.84	100				
8 π_u	3.7	-15.88	56			42	
5 π_g	4	-15.93		28		71	
11 σ_u	2	-17.57	20		4	35	20
14 σ_g	2	-19.27		9		59	26
$U(AsH)_2^{2+}$							
3 δ_u	0	-14.76	99				
2 φ_u	0.48	-15.22	100				
10 π_u	3.52	-15.25	60			38	
7 π_g	4	-15.29		21		77	
14 σ_u	2	-17.23	14		6	41	27
17 σ_g	2	-18.65		10		55	30

Table 5.13. Valence molecular orbital compositions of $U(XH)_2^{2+}$ (X = N, P, As) ($D_{\infty h}$).

Table 5.13 reveals that the composition of the π_u orbital changes down the group, with decreasing participation of the ligand p orbitals. In σ_u the reverse trend is found, with 5f contributions decreasing down the group, 57% in X = N decreasing to 14% for As, similar to the group 16 analogues. The stabilization of the σ_u orbital is due to a decrease in the U 6p anti-bonding admixture, which drops from 11% to 4% and 6% for X = N, P, As respectively. Calculations on X = N where the U 6p orbitals are included in the frozen core show that it is indeed the pushing from below effect that destabilizes σ_u. σ_g, has a slightly higher N 2p contribution compared to the other ligand p contributions, 67% compared to 59% and 55% for X = P and X = As, but the metal contribution remains the same, *ca* 10%. To summarize: the σ_u orbital is stabilized compared to the π orbitals partly due to a decrease in the pushing from below and, same as in UE_2^{2+} (E = O, S, Se, Te), and a formation of a σ backbone.

$U(XR)_2^{2+}$ (X = N, P, As; R = CH_3)

For the electronic structure of the R = CH_3 systems, as in the R = H calculations, electronic smearing had to be employed for X = P, As. Despite the relatively small smearing the calculated electronic structure had fractional occupations, in X = As 0.6 electrons occupy the formally unoccupied φ_u orbital ($18a_{2u}$ + $2a_{1u}$) and there are 0.2 electrons in virtual orbitals in X = P (Table 5.14).

The MO diagram (Figure 5.9) is very similar to the $U(XR)_2^{2+}$ (X = N, P, As; R = H) MO diagram. The major difference is the MO ordering in X = N, where in R = H the ordering was $\pi_u > \sigma_u > \pi_g > \sigma_g$. Descending group 15 σ_u is stabilized more than π_g and the energetic ordering changes to $\pi_u > \pi_g > \sigma_u > \sigma_g$, the ordering found for all R = CH_3 systems. The π_u and π_g MOs are very close in energy, within 0.1 eV for all X. The relative ordering of the virtual orbitals, the formally unoccupied φ_u and δ_u, remains constant. The energetic difference between them decreases from 0.67 eV in X = N to 0.64 eV and 0.35 eV for X = P, As. The virtual orbitals also come down in energy relative to the HOMO, the HOMO-LUMO gap drops from 1.45 eV (X = N) to 0.03 eV for X = P

and 0.23eV for X = As. This may be explained by the partial occupations of the LUMO, lowering the energy of the formally unoccupied orbitals.

The σ_u and σ_g MOs show opposite trends; descending group 15 σ_u is gradually stabilized and σ_g is destabilized, the energy gap between σ_u and σ_g decreases from 2.28 eV to 1.52 eV and 1.21 eV for X = N, P and As respectively. These trends can be explained investigating the composition of the molecular orbitals (Table 5.14).

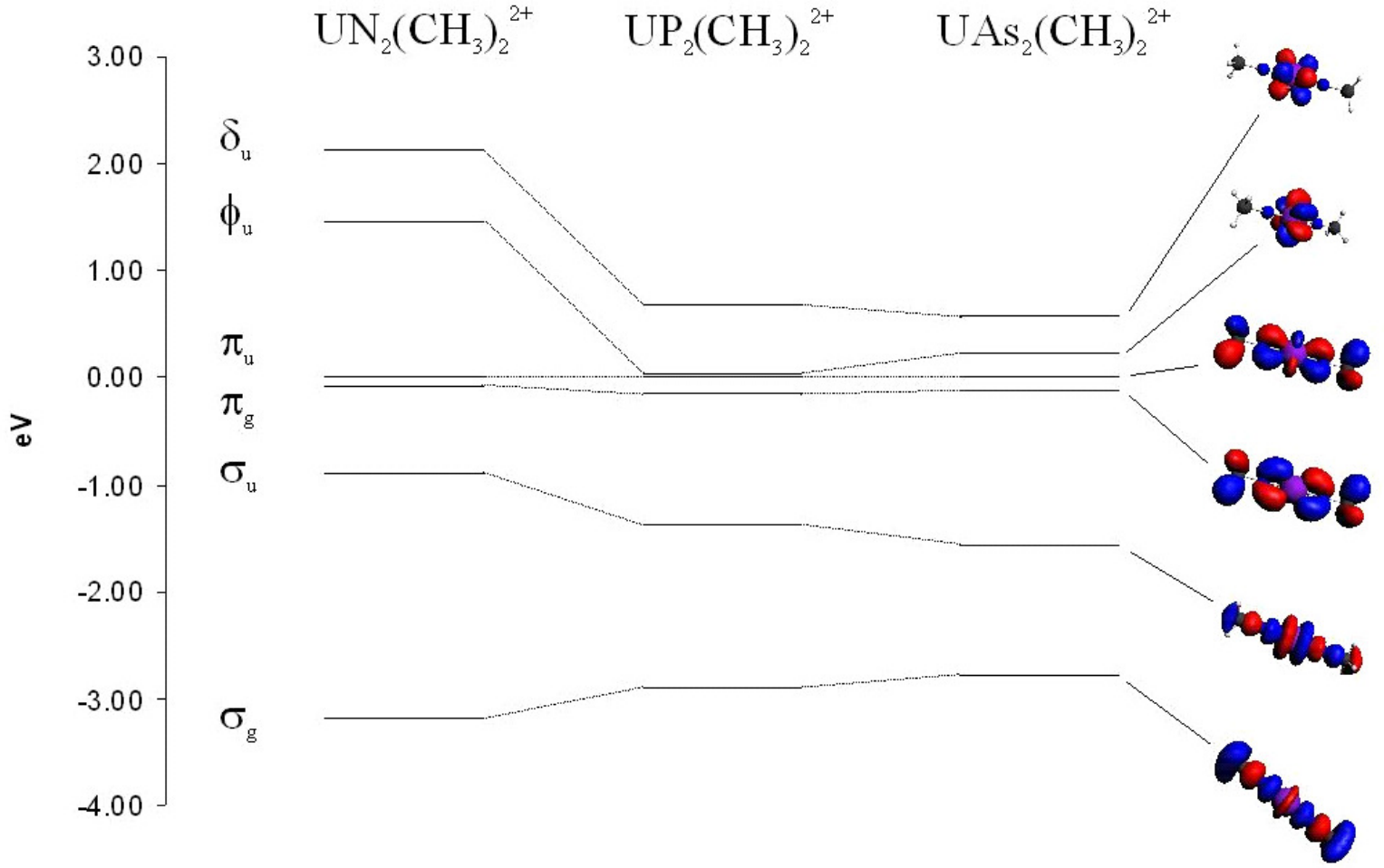

Figure 5.9. Valence MO energy level diagram of $U(XR)_2^{2+}$ (X = N, P, As; R = CH_3). The HOMO has been normalized to 0 eV in all systems. Displayed MOs from $U(NCH_3)_2^{2+}$

The U 5f contribution to the HOMO, π_u, increases down group 15; in X = N it is 36% compared to 53% and 57% in X = P, As respectively and accordingly, the ligand contribution is the greatest in X = N, 26% N 2p, but also 18% C 2p and 14% H 1s. The same is seen in π_g, where the ligand contributions are 33% N 2p, 25% C 2p and 18% H 1s. The two MOs designated L, $8e_{1u}$ and $7e_{1g}$, are orbitals with very high ligand contributions, around 85% are contributions from N 2p, C 2p or H 1s. These contributions from $-CH_3$ suggest that a π bond extends along the entire axis of the molecule. Indeed, visual inspection of these orbitals (Figure 5.10) confirms the existence of such a back bone. This π back bone is not seen for the X = P, As, where the C 2p contributions disappear.

Figure 5.10. The π "back-bone" in $U(NCH_3)_2^{2+}$, consisting of $7e_{1g}$ (left) and $8e_{1u}$ (right)

There are contributions to both the σ_u and σ_g MOs from the methyl group, indicating participation in the bonding. The contributions to σ_g remains more or less constant for all the systems, a small U 6d contribution, a ligand p contribution of *ca* 40% and a *ca* 30% contribution from C 2p. There is also a small H 1s contribution in all systems, smaller than the corresponding contributions in the R = H systems. The composition of σ_u changes more descending group 15, as the contribution from U 5f decreases from 53% in X = N to 22% and 16% for P and As respectively. In turn, the ligand contribution has increased for σ_u, from 20% N to 33% moving down the group. A more dramatic increase can be seen for C 2p, which increases from 9% to 33%. As in the case for R = H, the U 6p admixture in σ_u decreases as moving down the group, which is the main reason for the relative stabilization of the σ_u compared to the π_g and π_u orbitals. However, the AO

compositions for the other valence orbitals in the R = H and R = CH_3 systems is very similar.

				Composition (%)					
MO type ($D_{\infty h}$)	**Irrep (D_{3d})**	**Occupation**	**Energy [eV]**	**U f**	**U d**	**U p**	**X p**	**C p**	**H s**
$UN_2(CH_3)_2^{2+}$									
δ	$10e_{1u}$	0	-14.78	99					
φ	$2a_{1u}$	0	-15.45	100					
φ	$13a_{2u}$	0	-15.45	100					
π_u	$9e_{1u}$	4	-16.90	36			26	18	14
π_g	$8e_{1g}$	4	-16.98		14		33	25	18
σ_u	$12a_{2u}$	2	-17.80	53		10	20	9	
L	$8e_{1u}$	4	-19.57	8			33	41	10
L	$7e_{1g}$	4	-19.80		7		43	36	8
σ_g	$14a_{1g}$	2	-20.08		5		41	31	13
$UP_2(CH_3)_2^{2+}$									
δ	$11e_{1u}$	0	-13.86	99					
φ	$2a_{1u}$	0.11	-14.50	100					
φ	$15a_{2u}$	0.11	-14.50	100					
π_u	$10e_{1u}$	3.78	-14.53	57			38		
π_g	$9e_{1g}$	4	-14.67		29		60		
σ_u	$14a_{2u}$	2	-15.90	22		4	30	27	6
σ_g	$16a_{1g}$	2	-17.42		9		40	36	7
$UAs_2(CH_3)_2^{2+}$									
δ	$14e_{1u}$	0	-13.42	99					
φ	$18a_{2u}$	0.30	-13.77	100					
φ	$2a_{1u}$	0.31	-13.77	100					
π_u	$13e_{1u}$	3.39	-14.00	58			36		
π_g	$12e_{1g}$	4	-14.11		25		69		
σ_u	$17a_{2u}$	2	-15.56	16		5	33	33	5
σ_g	$19a_{1g}$	2	-16.77		8		44	30	6

Table 5.14. Valence MO compositions of $UX_2(CH_3)_2^{2+}$ (X = N, P, As) in D_{3d} (staggered).

Mulliken population analysis

The major change in Mulliken populations moving down group 15 is in the p populations, where the p hole is significantly reduced for P and As. The d and f populations are relatively stable for the methyl ligand complexes and the hydride complexes with no trend observed going down the group. It is noteworthy that the net s population in the -N-H system increases dramatically moving from N to P, from -1.47 to -0.04. The reason for the large changes in the Mulliken population when moving down the group is likely the fractional occupations in the valence MOs observed for the P and As complexes.

		s	p	d	f
-H	N	-1.47	-0.84	0.74	2.82
	P	-0.04	-0.04	1.36	2.78
	As	0.05	0.00	1.00	2.87
$-CH_3$	N	-0.05	-0.37	1.30	2.90
	P	-0.07	-0.06	1.45	2.82
	As	0.07	-0.04	1.13	2.90

Table 5.15. The net Mulliken atomic populations of U in $U(XR)_2^{2+}$ (X = N, P, As; R = H, CH_3)

Mayer bond order analysis

The Mayer bond orders (MBOs) (Table 5.16) for all group 15 analogues suggest that the U-N bond is the strongest, with a gradual decrease in bond order descending the group for both R ligands. The calculated U-X bond orders are lower than the formal bond order in UO_2^{2+} which is due to the X atoms forming single bonds with the R groups. This is evidenced by the bond orders of the X-H bonds, which increase as the U-X bond order decreases. Using the same argument as in the group 16 analogues, the reason for the weakening bond is the decrease in f orbital overlap with the X p orbitals moving down

the group. For the X-CH_3 MBOs the trend is not as clear, the MBO of the P-CH_3 is *ca* 0.3 higher than the other X-CH_3 MBOs, which are almost the same. The trend for the U-X bond in the R = CH_3 complexes, however, is similar to the trend in the R = H with a decrease in the MBOs descending the group, for the same reasons as in the hydride.

	U-X	X-R
R = H		
N	2.38	0.64
P	2.24	0.95
As	1.82	1.03
R = CH_3		
N	2.40	0.94
P	2.17	1.21
As	1.78	0.95

Table 5.16. The Mayer bond orders (MBOs) of $U(XR)_2^{2+}$ (X = N, P, As; R = H, CH_3)

Atomic charge analysis

The Mulliken, Hirshfeld and Voronoi atomic charges have been analyzed for all of the isoelectronic systems. Looking at the U Mulliken atomic charges for the $U(XH)_2^{2+}$ (X = N, P, As) systems there is a decrease moving down group 15, from 2.60 down to 2.02 and 2.08 for X = N, P and As respectively. This is the same trend as in the UE_2^{2+} (E = O, S, Se, Te) systems and is due a decrease in the difference in electronegativity between the ligand and metal atoms. The electronegativity of U is 1.38, while the electronegativity of N is 3.04 decreasing to 2.19 and 2.18 for P and As respectively with the electronegativity of H 2.20. The charge of the X atoms increases from -0.79 for X = N to -0.12 and -0.07 for P and As. The Mulliken atomic charge of H decreases descending down the group, a result of the electronegativity of H and X being almost equal.

The same electronegativity effects are seen in $U(XCH_3)_2^{2+}$ (X = N, P, As); the atomic charge of U decreases moving down group 15 and correspondingly, the Mulliken charges of the X ligands decrease, from -0.59 to -0.19. The electronegativity of C is 2.55, close to the electronegativity of the X ligand, which results in the Mulliken charge of C being almost constant down the group, -0.40, -0.41 and -0.32 for X = N, P, As.

	$U(XH)_2^{2+}$			$U(XCH_3)_2^{2+}$		
	Mulliken	Hirshfeld	Voronoi	Mulliken	Hirshfeld	Voronoi
U	2.60	1.84	1.43	2.22	1.67	1.37
N	-0.79	-0.18	-0.09	-0.59	-0.19	-0.14
C	-	-	-	-0.40	0.02	-0.02
H	0.49	0.27	0.37	-0.29	0.11	0.16
U	2.02	1.35	1.32	1.97	1.23	1.24
P	-0.12	0.19	0.12	-0.20	0.12	0.03
C	-	-	-	-0.41	-0.07	-0.13
H	0.11	0.13	0.22	0.21	0.11	0.16
U	2.08	1.27	1.24	1.94	1.14	1.16
As	-0.07	0.25	0.17	-0.19	0.19	0.09
C	-	-	-	-0.32	-0.08	-0.11
H	0.03	0.12	0.21	0.18	0.10	0.15

Table 5.17. Atomic charges of $U(XH)_2^{2+}$ and $U(XCH_3)_2^{2+}$ (X = N, P, As)

In the R = CH_3 systems the Voronoi charges are almost constant. The smaller -0.02 charge in X = N is a result of the very high electronegativity of N redistributing the density over the entire system. Accordingly the Voronoi charge is -0.14 on N. For P and As this increases to 0.03 and 0.09, indicating a net outflow of charge. The U Voronoi charges decrease, from 1.37 to 1.16 for X = N, P, As, still positive numbers but a substantial reduction of the charge flow out of the U Voronoi cell.

Conclusions

The group 16 UE_2^{2+} and UE_2 (E = O, S, Se, Te) uranyl analogues have been investigated with a view to probing systematic trends. The closed-shell dicationic systems are found to be linear, and the U-E bond distances increase almost linearly down the group. UO_2 was found to be linear while the heavier, neutral analogues were bent with bond angles of *ca* 116°.

UE_2^{2+}, both in the spin-orbit free and the spin-orbit coupled calculations, display a systematic stabilization of the σ_g MO and a destabilization of the π MOs on descending group 16. The HOMO-LUMO gap did not follow any trend, but was smaller for the heavier elements of group 16, which required electronic smearing for the E = Se, Te systems. This indicates that DFT struggles as the systems become increasingly multiconfigurational for the heavier ligands and that methods capable of handling such systems are needed to investigate the E = Se, Te systems in the future. The "pushing from below" contribution to σ_u was clearly visible with significant ligand p orbital contributions in all analogues with the effect being the largest in UO_2^{2+}. The Mulliken population analysis of the analogues show a decrease in the U 6p hole descending group 16 while the U f and d populations increase systematically.

The electronic structure of UO_2 and US_2 was compared at two bond angles, 120° and 180°. This investigation revealed that there are differences in the electronic structure at the two geometries; in bent UO_2 there is a stabilization of valence σ_g, similar to that found in the dications. The π MOs are also stabilized, while the electronic structure of US_2 does not display any major changes on bending. A Mulliken population analysis was carried out as a function of bond angle on UO_2 and US_2. This revealed that the f contributions decrease E-U-E is reduced for both systems, while the d population in US_2 peaks at 115°, close to the optimized geometry. This suggests that the bending is the result of a similarity in atomic orbital radii of ligand p MOs and U 6d MO compared to ligand p and U 5f for the heavier systems. The exception is O 2p which has a mean

orbital radius close to that of U 5f. When linear, UO_2 has a very large f Mulliken population.

The energy decomposition analysis of the group 16 dication analogues showed that only UO_2^{2+} was stable with respect to the basic atomic fragments employed in ADF. The other investigated complexes have bond energies which become increasingly positive moving down the group. Atomic charge analyses were carried out on both the neutral and the dication systems and showed that the charges of the atoms are not unexpected on the basis of their electronegativity, with O the most negatively charged atom.

The isoelectronic group 15 uranyl analogues, $U(XR)_2^{2+}$ (X = N, P, As; R = H, CH_3), were investigated and the optimized geometries, in contrast to the group 16 analogues, remained unbent in all complexes, remaining at the highest symmetry geometries. The U-X bond lengths were found to increase down the group with the distance being largely independent of R. As in the group 16 analogues the largest increase in bond distance occurs when moving from the 2p to the 3p ligand.

The electronic structure of the group 15 complexes is such that, unlike in the group 16 analogues, π_u is the HOMO. Descending group 15 the π MOs are destabilized compared to the σ-bonding MOs but the two π MOs are very close in energy. An interesting feature in the electronic structure is the formation of back bone π orbitals in $U(NCH_3)_2^{2+}$, similar to what has been observed in previous studies on N substituted uranyl complexes.

The Mayer bond orders suggest that the U-X bond weakens moving down group 15, with concomitantly stronger X-R bonds. The Mulliken population analysis shows that the U 6p hole disappears, as indicated by a decrease in the p participation in the bonding. Evidence for this is seen in the MO decomposition analysis as well where the p contribution to the σ_u lessens moving down the group. The atomic charge analysis of the group 15 analogues follow the same pattern as the group 16 analogues, i.e. the charges are largely as expected on the basis of the electronegativity of the atoms.

Chapter 6

Summary

The various research projects included in this thesis were quite varied in nature, from small actinide systems consisting of three atoms all the way to large polyoxometallate complexes. Each project also presented different computational challenges. For example, in the polyoxometallate work in Chapter 3 it was the size of the systems and in the TDDFT work in Chapter 4 it was the difficulty in working with open-shell actinides. All of these challenges were more or less overcome and some general conclusions on the whole thesis can be drawn, tying everything together. Thus, the purpose of this chapter is to summarize the main findings of this thesis as well as present areas which future researchers can build on and which could not be included due to technical constraints or time constraints.

The work done on the mixed transition metal – actinide complexes in Chapter 2 showed that the mixed $MUCl_6/MUCl_8^{2-}$ (M = Mo, W) systems are more stable than the corresponding homonuclear systems and that they should be stable enough to detect experimentally. However, environmental effects such as pH or solvent effects have not been included in this study. This is something that would have to be included in future studies in order to provide experimentalists with information on where the mixed systems are the most stable. It might even be that the energetics of the system changes on inclusion of solvents, changing the result completely. This is definitely an area for future research.

The polyoxometallate studies in Chapter 3 confirmed that the bonding in the investigated complexes is highly ionic. More extensive work on the bonding in POMs will most likely find that this conclusion does not change dramatically. Some of the very large systems that were the focus of the study, for example the Hf/Zr lacunary-plenary phosphomolybdates with NH_4^+ coordinated in the lacunary cavity, could not be investigated to the same extent as smaller systems. Since the chemistry of POMs involves

very large structures, more work should be carried out on finding suitable model systems in order to decrease the computational cost. Modern force fields, fitted using high level QM calculations, might prove more suited for geometry optimizations in transition metal containing complexes than older ones such as the Universal Force Field (UFF).

The high anionicity of the complexes also made calculations difficulty. Any future work on polyoxometallate systems should also try to reduce the net charge of the systems perhaps by including counter ions in the calculations or, if possible, try to incorporate solvent effects, as this stabilizes the electronic structure greatly.

Much of the experimental work on POMs involves spectroscopic characterisations of large complexes. In Chapter 4 the electronic transitions of both uranium and neptunium complexes were investigated to see if TDDFT can be used as a tool in finding out information about the actinide complexation to POMs. TDDFT was adequate for small uranyl systems but did not do a good job on the open-shell Np systems.

If a model system for larger POMs can be found, future investigations into the electronic transitions should be done using multireference methods, such as CASPT2. This would produce improved results compared to known experimental data as well as provide better tools for predicting the behaviour of new POM - actinide complexes. Unfortunately, the present TDDFT investigation into small Np systems could not determine if hydroxides are adequate models for POMs. Doing a similar investigation with CAS methods would allow a better comparison with experimental results and is something that should be done in any future work. There has been much more experimental and theoretical work done on Pu containing systems than on the Np equivalents. Thus, a natural next step would be to investigate Pu – POM complexes as well.

In Chapter 5 the bonding and bending of uranyl analogues was investigated. This project was interesting, since even though there have been some theoretical work done on uranyl analogues, it is only quite recently that proper uranyl analogues have been produced experimentally. For the heavier group 15 and 16 analogues actual experimental data for

molecular systems might still be some way off, meaning trends down the groups are of more theoretical interest than actually experimental interest.

The results of this project showed that the U-N analogues are linear and that their electronic structure changes from that which is well known in U-O. The formation of a back-bone along the axis of the molecule, stabilising the linear geometry is something not seen in the U-O analogues. The computational results also predicted that the U-P analogues will behave similarly.

There is less experimental information on the uranyl chalcogen analogues. Thus, the fact that UE_2 (E = S, Se, Te) are bent, as opposed to the linear UO_2 molecule proved an interesting, if not completely unexpected, result. The increased overlap between the U 6d and the ligand p orbitals was confirmed as being the reason the systems bent. What was more interesting was the fact that all the dications of the same systems were linear, even though the same argument should have been applicable.

For the heaviest group 15 and 16 electron smearing was necessary to be able to carry out the calculations. It is possible, in future work, that this smearing could be reduced to obtain more reliable results for these complexes.

Looking back at the work done over the past three years, it is always possible to find things that could have been done differently or things that were left incomplete. That is just in the nature of research. The different research projects have investigated a selection of areas of actinide chemistry and, hopefully, some future researcher will find the results interesting and continue from the foundation laid here.

Appendix 1

Electronic structure of $Na_2(Ge_2W_9O_{34})_2(NpO_2)_2^{14-}$ and electronic transitions in $NpO_2Cl_4^{2-}$ and $NpO_2(OH)_4^{2-}$

			Composition (%)					
Orbital	Occupation	Energy (eV)	Np f	Np d	Np p	O_{yl}	O_{POM}	NpO_2^{2+} component
$^{\alpha}552a_g$	0	20.73	92					$^{\alpha}\varphi$
$^{\alpha}552a_u$	0	20.73	92					$^{\alpha}\varphi$
$^{\alpha}551a_g$	0	20.71	81					$^{\alpha}\varphi$
$^{\alpha}551a_u$	0	20.70	80					$^{\alpha}\varphi$
$^{\alpha}550a_u$	0	20.51	84					$^{\alpha}\varphi$
$^{\alpha}550a_g$	0	20.51	84					$^{\alpha}\varphi$
$^{\alpha}549a_u$	1	18.81	79					$^{\alpha}\varphi_u$
$^{\alpha}549a_g$	1	18.81	79					$^{\alpha}\varphi$
$^{\alpha}548a_u$	1	18.43					80	POM-based
$^{\alpha}548a_g$	1	18.42					85	POM-based
$^{\alpha}547a_u$	1	18.41					86	POM-based
$^{\alpha}547a_g$	1	18.41					84	POM-based

Table A.1. Valence molecular orbital energies, occupations and compositions of $Na_2(GeW_9O_{34})_2(NpO_2)_2^{14-}$ (SAOP)

Energy/eV	Energy/cm^{-1}	*f*	Transition symmetry	Principal orbital contribution
0.18	1452	0	A_{2g}	$^{\alpha}2b_{1u} \rightarrow {}^{\alpha}4b_{2u}$ ($\delta \rightarrow \delta$)
0.40	3187	0	E_g	$^{\alpha}2b_{1u} \rightarrow {}^{\alpha}16e_u$ ($\delta \rightarrow \varphi$)
0.44	3510	0	A_{2g}	$^{\alpha}2b_{1u} \rightarrow {}^{\beta}4b_{2u}$ ($\delta \rightarrow \delta$)
0.46	3714	0	E_g	$^{\alpha}2b_{1u} \rightarrow {}^{\beta}16e_u$ ($\delta \rightarrow \varphi$)
1.48	11909	0	B_{1u}	$^{\alpha}2a_{2g} \rightarrow {}^{\alpha}4b_{2u}$ (Cl $\rightarrow \delta$)
1.48	11967	0	B_{1u}	$^{\beta}2a_{2g} \rightarrow {}^{\alpha}4b_{2u}$ (Cl $\rightarrow \delta$)
1.50	12089	0	E_u	$^{\beta}2a_{2g} \rightarrow {}^{\alpha}16e_u$ (Cl $\rightarrow \varphi$)
1.52	12255	0	B_{1g}	$^{\beta}11a_{2u} \rightarrow {}^{\alpha}4b_{2u}$ (Cl/$\sigma_u \rightarrow \delta$)
1.53	12373	1.15×10^{-3}	E_u	$^{\alpha}2a_{2g} \rightarrow {}^{\alpha}16e_u$ (Cl $\rightarrow \varphi$)
1.59	12800	0	E_g	$^{\beta}11a_{2u} \rightarrow {}^{\alpha}16e_u$ (Cl/$\sigma_u \rightarrow \varphi$)
1.61	12958	0	E_u	$^{\beta}6e_g \rightarrow {}^{\alpha}4b_{2u}$ (Cl $\rightarrow \delta$)
1.64	13217	0	B_{2u}	$^{\beta}6e_g \rightarrow {}^{\alpha}16e_u$ (Cl $\rightarrow \varphi$)
1.64	13218	0	A_{2u}	$^{\beta}6e_g \rightarrow {}^{\alpha}16e_u$ (Cl $\rightarrow \varphi$)
1.64	13223	0	B_{1u}	$^{\alpha}6e_g \rightarrow {}^{\alpha}4b_{2u}$ (Cl $\rightarrow \delta$)
1.64	13230	0	A_{1u}	$^{\alpha}6e_g \rightarrow {}^{\alpha}16e_u$ (Cl $\rightarrow \varphi$)
1.64	13245	0	B_{2u}	$^{\alpha}6e_g \rightarrow {}^{\alpha}16e_u$ (Cl $\rightarrow \varphi$)
1.64	13247	3.96×10^{-5}	A_{2u}	$^{\alpha}6e_g \rightarrow {}^{\alpha}16e_u$ (Cl $\rightarrow \varphi$)
1.64	13262	0	B_{1g}	$^{\alpha}11a_{2u} \rightarrow {}^{\alpha}4b_{2u}$ (Cl/$\sigma_u \rightarrow \delta$)

Appendix 1 - *Electronic structure of $Na_2(Ge_2W_9O_{34})_2(NpO_2)_2^{14-}$ and electronic transitions in $NpO_2Cl_4^{2-}$ and $NpO_2(OH)_4^{2-}$*

Energy/eV	Energy/cm^{-1}	f	Transition symmetry	Principal orbital contribution
1.64	13264	0	A_{1u}	$^{\beta}6e_g \rightarrow {}^{\alpha}16e_u$ (Cl $\rightarrow \varphi$)
1.65	13268	0	B_{1u}	$^{\beta}6e_g \rightarrow {}^{\alpha}16e_u$ (Cl $\rightarrow \varphi$)
1.65	13345	4.69 x 10^{-3}	E_u	$^{\alpha}6e_g \rightarrow {}^{\alpha}4b_{2u}$ (Cl $\rightarrow \delta$)
1.67	13493	0	E_g	$^{\alpha}11a_{2u} \rightarrow {}^{\alpha}16e_u$ (Cl/$\sigma_u \rightarrow \varphi$)
1.74	14058	0	A_{1g}	$^{\beta}3b_{2u} \rightarrow {}^{\beta}4b_{2u}$ (Cl $\rightarrow \delta$)
1.78	14364	0	B_{1u}	$^{\alpha}2a_{2g} \rightarrow {}^{\beta}4b_{2u}$ (Cl $\rightarrow \delta$)
1.79	14400	0	E_u	$^{\alpha}2a_{2g} \rightarrow {}^{\beta}16e_u$ (Cl $\rightarrow \varphi$)
1.79	14409	0	A_{1g}	$^{\alpha}3b_{2u} \rightarrow {}^{\alpha}4b_{2u}$ (Cl $\rightarrow \delta$)
1.81	14570	0	B_{1u}	$^{\beta}2a_{2g} \rightarrow {}^{\beta}4b_{2u}$ (Cl $\rightarrow \delta$)
1.81	14616	0	E_g	$^{\alpha}2b_{1u} \rightarrow {}^{\alpha}17e_u$
1.81	14631	0	E_g	$^{\beta}3b_{2u} \rightarrow {}^{\alpha}16e_u$ (Cl $\rightarrow \varphi$)
1.83	14750	0	A_{1g}	$^{\beta}15e_u \rightarrow {}^{\beta}16e_u$ (Cl $\rightarrow \varphi$)
1.86	14999	0	E_g	$^{\alpha}3b_{2u} \rightarrow {}^{\alpha}16e_u$ (Cl $\rightarrow \varphi$)
1.87	15042	2.68 x 10^{-3}	E_u	$^{\beta}2a_{2g} \rightarrow {}^{\beta}16e_u$ (Cl $\rightarrow \varphi$)
1.87	15056	0	A_{1g}	$^{\alpha}3b_{2u} \rightarrow {}^{\alpha}4b_{2u}$ (Cl $\rightarrow \delta$)
1.89	15207	0	B_{2g}	$^{\beta}15e_u \rightarrow {}^{\alpha}16e_u$ (Cl $\rightarrow \varphi$)
1.89	15249	0	B_{1g}	$^{\beta}15e_u \rightarrow {}^{\alpha}16e_u$ (Cl $\rightarrow \varphi$)
1.89	15226	0	B_{1g}	$^{\alpha}15e_u \rightarrow {}^{\alpha}16e_u$ (Cl $\rightarrow \varphi$)
1.89	15228	0	B_{2g}	$^{\alpha}15e_u \rightarrow {}^{\alpha}16e_u$ (Cl $\rightarrow \varphi$)
1.90	15292	0	B_{2u}	$^{\alpha}2a_{2g} \rightarrow {}^{\beta}2b_u$ (Cl $\rightarrow \delta$)
1.90	15341	0	B_{1g}	$^{\alpha}11a_{2u} \rightarrow {}^{\beta}4b_{2u}$ (Cl/$\sigma_u \rightarrow \delta$)
1.90	15348	0	E_g	$^{\beta}15e_u \rightarrow {}^{\alpha}4b_{2u}$ (Cl $\rightarrow \delta$)
1.91	15425	0	B_{2u}	$^{\beta}2a_{2g} \rightarrow {}^{\beta}2b_u$ (Cl $\rightarrow \delta$)
1.91	15372	0	E_u	$^{\alpha}6e_g \rightarrow {}^{\beta}4b_{2u}$ (Cl $\rightarrow \delta$)
1.92	15496	0	B_{1g}	$^{\beta}11a_{2u} \rightarrow {}^{\beta}4b_{2u}$ (Cl/$\sigma_u \rightarrow \delta$)
1.92	15508	0	B_{2u}	$^{\alpha}6e_g \rightarrow {}^{\beta}16e_u$ (Cl $\rightarrow \varphi$)
1.92	15509	0	A_{2u}	$^{\alpha}6e_g \rightarrow {}^{\beta}16e_u$ (Cl $\rightarrow \varphi$)
1.93	15539	0	A_{1u}	$^{\alpha}6e_g \rightarrow {}^{\beta}16e_u$ (Cl $\rightarrow \varphi$)
1.93	15541	0	B_{1u}	$^{\alpha}6e_g \rightarrow {}^{\beta}16e_u$ (Cl $\rightarrow \varphi$)
1.93	15549	0	E_g	$^{\alpha}15e_u \rightarrow {}^{\alpha}4b_{2u}$ (Cl $\rightarrow \delta$)
1.94	15639	0	B_{1g}	$^{\beta}14e_u \rightarrow {}^{\alpha}16e_u$ (Cl $\rightarrow \varphi$)
1.94	15659	0	E_g	$^{\alpha}11a_{2u} \rightarrow {}^{\beta}16e_u$ (Cl/$\sigma_u \rightarrow \varphi$)
1.94	15661	0	A_{2g}	$^{\beta}15e_u \rightarrow {}^{\alpha}16e_u$ (Cl $\rightarrow \varphi$)
1.95	15702	0	E_g	$^{\beta}11a_{2u} \rightarrow {}^{\beta}16e_u$ (Cl/$\sigma_u \rightarrow \varphi$)
1.95	15762	0	A_{1u}	$^{\beta}6e_g \rightarrow {}^{\beta}16e_u$ (Cl $\rightarrow \varphi$)
1.96	15772	0	B_{1u}	$^{\beta}6e_g \rightarrow {}^{\beta}16e_u$ (Cl $\rightarrow \varphi$)
1.96	15780	0	B_{2u}	$^{\beta}6e_g \rightarrow {}^{\beta}16e_u$ (Cl $\rightarrow \varphi$)
1.96	15781	4.85 x 10^{-5}	A_{2u}	$^{\beta}6e_g \rightarrow {}^{\beta}16e_u$ (Cl $\rightarrow \varphi$)
1.96	15789	0	E_g	$^{\beta}14e_u \rightarrow {}^{\alpha}4b_{2u}$ (Cl $\rightarrow \delta$)
1.97	15869	0	A_{1g}	$^{\beta}14e_u \rightarrow {}^{\alpha}16e_u$ (Cl $\rightarrow \varphi$)
1.99	16020	0	A_{2g}	$^{\beta}14e_u \rightarrow {}^{\alpha}16e_u$ (Cl $\rightarrow \varphi$)
1.99	16027	0	A_{1g}	$^{\alpha}15e_u \rightarrow {}^{\alpha}16e_u$ (Cl $\rightarrow \varphi$)
1.99	16036	0	E_g	$^{\alpha}2b_{1u} \rightarrow {}^{\beta}17e_u$
1.99	16057	0	B_{2g}	$^{\alpha}14e_u \rightarrow {}^{\alpha}16e_u$ (Cl $\rightarrow \varphi$)
2.00	16101	0	B_{2g}	$^{\beta}14e_u \rightarrow {}^{\alpha}16e_u$ (Cl $\rightarrow \varphi$)
2.00	16158	0	E_g	$^{\alpha}14e_u \rightarrow {}^{\alpha}4b_{2u}$ (Cl $\rightarrow \delta$)
2.02	16301	1.69 x 10^{-2}	E_u	$^{\beta}6e_g \rightarrow {}^{\beta}4b_{2u}$ (Cl $\rightarrow \delta$)
2.02	16307	0	B_{2g}	$^{\alpha}11a_{2u} \rightarrow {}^{\beta}2b_{1u}$ (Cl/$\sigma_u \rightarrow \delta$)

Appendix 1 - *Electronic structure of $Na_2(Ge_2W_9O_{34})_2(NpO_2)_2^{14-}$ and electronic transitions in $NpO_2Cl_4^{2-}$ and $NpO_2(OH)_4^{2-}$*

Energy/eV	Energy/cm^{-1}	f	Transition symmetry	Principal orbital contribution
2.02	16325	0	E_u	$^{\alpha}6e_g \rightarrow {}^{\beta}2b_{1u}$ (Cl → δ)
2.04	16490	4.48 x 10^{-5}	E_u	$^{\beta}6e_g \rightarrow {}^{\beta}2b_{1u}$ (Cl → δ)
2.05	16563	0	A_{1g}	$^{\alpha}3b_{2u} \rightarrow {}^{\beta}4b_{2u}$ (Cl → δ)
2.05	16571	0	B_{2g}	$^{\beta}11a_{2u} \rightarrow {}^{\beta}2b_{1u}$ (Cl/σ$_u$ → δ)
2.09	16830	0	B_{1g}	$^{\beta}11a_{2u} \rightarrow {}^{\beta}4b_{2u}$ (Cl/σ$_u$ → δ)
2.12	17070	0	E_g	$^{\alpha}3b_{2u} \rightarrow {}^{\beta}16e_u$ (Cl → φ)
2.15	17314	0	A_{1g}	$^{\alpha}3b_{2u} \rightarrow {}^{\beta}4b_{2u}$ (Cl → δ)
2.15	17376	0	E_g	$^{\beta}3b_{2u} \rightarrow {}^{\beta}16e_u$ (Cl → φ)
2.18	17546	0	A_{1g}	$^{\beta}3b_{2u} \rightarrow {}^{\beta}4b_{2u}$ (Cl → δ)
2.18	17546	0	B_{1g}	$^{\beta}15e_u \rightarrow {}^{\beta}16e_u$ (Cl → φ)
2.18	17559	0	B_{2g}	$^{\beta}15e_u \rightarrow {}^{\beta}16e_u$ (Cl → φ)
2.20	17757	0	B_{2g}	$^{\alpha}15e_u \rightarrow {}^{\beta}16e_u$ (Cl → φ)
2.20	17763	0	B_{1g}	$^{\alpha}15e_u \rightarrow {}^{\beta}16e_u$ (Cl → φ)
2.22	17907	0	E_g	$^{\alpha}15e_u \rightarrow {}^{\beta}4b_{2u}$ (Cl → δ)
2.22	17917	0	E_g	$^{\beta}15e_u \rightarrow {}^{\beta}4b_{2u}$ (Cl → δ)
2.23	17961	0	A_{2g}	$^{\alpha}3b_{2u} \rightarrow {}^{\beta}2b_{1u}$ (Cl → δ)
2.24	18084	0	A_{2g}	$^{\alpha}15e_u \rightarrow {}^{\beta}16e_u$ (Cl → φ)
2.26	18251	0	B_{1g}	$^{\alpha}14e_u \rightarrow {}^{\beta}16e_u$ (Cl → φ)
2.27	18338	0	A_{1g}	$^{\alpha}14e_u \rightarrow {}^{\beta}16e_u$ (Cl → φ)
2.28	18398	0	E_g	$^{\beta}14e_u \rightarrow {}^{\beta}4b_{2u}$ (Cl → δ)
2.30	18516	0	B_{2g}	$^{\beta}14e_u \rightarrow {}^{\beta}16e_u$ (Cl → φ)
2.30	18534	0	A_{1g}	$^{\beta}14e_u \rightarrow {}^{\beta}16e_u$ (Cl → φ)
2.30	18578	0	E_g	$^{\alpha}14e_u \rightarrow {}^{\beta}4b_{2u}$ (Cl → δ)
2.31	18599	0	B_{2g}	$^{\alpha}14e_u \rightarrow {}^{\beta}16e_u$ (Cl → φ)
2.34	18887	0	A_{2g}	$^{\alpha}14e_u \rightarrow {}^{\beta}16e_u$ (Cl → φ)
2.36	19006	0	E_g	$^{\beta}15e_u \rightarrow {}^{\beta}2b_{1u}$ (Cl → δ)
2.68	21617	0	B_{1g}	$^{\beta}10a_{2u} \rightarrow {}^{\alpha}4b_{2u}$ (σ$_u$/Cl → δ)
2.78	22408	0	E_g	$^{\beta}10a_{2u} \rightarrow {}^{\alpha}16e_u$ (σ$_u$/Cl → ϕ)
2.88	23213	0	B_{1g}	$^{\alpha}10a_{2u} \rightarrow {}^{\alpha}4b_{2u}$ (σ$_u$/Cl → δ)
2.93	23592	0	B_{1g}	$^{\beta}10a_{2u} \rightarrow {}^{\beta}4b_{2u}$ (σ$_u$/Cl → δ)
3.00	24212	0	E_g	$^{\alpha}10a_{2u} \rightarrow {}^{\alpha}16e_u$ (σ$_u$/Cl → ϕ)
3.20	25825	0	B_{1g}	$^{\alpha}10a_{2u} \rightarrow {}^{\beta}4b_{2u}$ (σ$_u$/Cl → δ)
3.29	26507	0	E_g	$^{\alpha}10a_{2u} \rightarrow {}^{\beta}16e_u$ (σ$_u$/Cl → ϕ)
3.31	26673	0	B_{2g}	$^{\alpha}10a_{2u} \rightarrow {}^{\beta}2b_{1u}$ (σ$_u$/Cl → δ)
3.32	26801	0	E_g	$^{\beta}10a_{2u} \rightarrow {}^{\beta}16e_u$ (σ$_u$/Cl → ϕ)
3.45	27853	0	B_{1g}	$^{\beta}10a_{2u} \rightarrow {}^{\beta}4b_{2u}$ (σ$_u$/Cl → δ)
3.53	28436	0	B_{2g}	$^{\beta}10a_{2u} \rightarrow {}^{\beta}2b_{1u}$ (σ$_u$/Cl → δ)

Table A.2. Calculated spin-orbit free transition energies in $NpO_2Cl_4^{2-}$ (LB94, TDA, spin flip transitions)

Appendix 1 - *Electronic structure of $Na_2(Ge_2W_9O_{34})_2(NpO_2)_2^{14-}$ and electronic transitions in $NpO_2Cl_4^{2-}$ and $NpO_2(OH)_4^{2-}$*

Energy/eV	Energy/cm^{-1}	*f*	Transition symmetry	Principal orbital contribution
1.84	14860	0	A_2	$^{\alpha}3a_2 \rightarrow 18a_1$ ($\delta \rightarrow \delta$)
2.21	17805	1.47 x 10^{-4}	E	$^{\alpha}3a_2 \rightarrow 18e_1$ ($\delta \rightarrow \varphi$)
2.68	21651	0	A_2	$^{\alpha}2a_2 \rightarrow 18a_1$ ($O_{OH} \rightarrow Np$)
2.9	23396	8.32 x 10^{-4}	E	$^{\alpha}17e_1 \rightarrow 18a_1$ ($O_{OH} \rightarrow Np$)
2.93	23651	6.69 x 10^{-3}	E	$^{\alpha}2a_2 \rightarrow 18e_1$ ($O_{OH} \rightarrow Np$)
3.08	24879	0	B_1	$^{\alpha}17e_1 \rightarrow 18e_1$ ($O_{OH} \rightarrow Np$)
3.1	24993	0	A_2	$^{\alpha}17e_1 \rightarrow 18e_1$ ($O_{OH} \rightarrow Np$)
3.12	25175	0	A_1	$^{\alpha}17e_1 \rightarrow 18e_1$ ($O_{OH} \rightarrow Np$)
3.16	25520	5.36 x 10^{-5}	E	$^{\alpha}3a_2 \rightarrow 19e_1$ ($O_{OH} \rightarrow Np$)
3.22	25986	1.27 x 10^{-4}	B_2	$^{\alpha}17e_1 \rightarrow 18e_1$ ($O_{OH} \rightarrow Np$)
3.33	26866	3.98 x 10^{-4}	E	$^{\alpha}16e_1 \rightarrow 18a_1$ ($O_{OH} \rightarrow \delta$)
3.43	27626	0	B_1	$^{\alpha}16e_1 \rightarrow 18e_1$ ($O_{OH} \rightarrow \varphi$)
3.43	27673	5.57 x 10^{-5}	B_2	$^{\alpha}16e_1 \rightarrow 18e_1$ ($O_{OH} \rightarrow Np$)
3.44	27763	7.00 x 10^{-5}	B_2	$^{\alpha}16b_2 \rightarrow 18a_1$ ($\sigma \rightarrow \delta$)
3.46	27881	0	A_1	$^{\beta}2a_2 \rightarrow 3a_2$ ($O_{OH} \rightarrow Np$)
3.51	28283	0	A_2	$^{\alpha}16e_1 \rightarrow 18e_1$ ($O_{OH} \rightarrow \varphi$)
3.63	29260	2.51 x 10^{-4}	E	$^{\alpha}17e_1 \rightarrow 3a_2$ ($O_{OH} \rightarrow Np$)
3.67	29628	0	A_1	$^{\alpha}16e_1 \rightarrow 18e_1$ ($O_{OH} \rightarrow \varphi$)
3.71	29892	6.90 x 10^{-4}	E	$^{\alpha}16b_2 \rightarrow 18e_1$ ($\sigma \rightarrow \varphi$)
3.71	29953	0	B_1	$^{\alpha}16b_2 \rightarrow 3a_2$ ($\sigma \rightarrow \delta$)
3.8	30612	0	A_1	$^{\alpha}17a_1 \rightarrow 18a_1$ ($O_{OH} \rightarrow \delta$)
3.82	30779	0	B_1	$^{\alpha}4b_1 \rightarrow 18a_1$ ($O_{OH} \rightarrow Np$)
3.86	31129	0	A_2	$^{\alpha}3a_2 \rightarrow 19a_1$ ($O_{OH} \rightarrow Np$)
3.89	31354	0	A_2	$^{\beta}2a_2 \rightarrow 18a_1$ ($O_{OH} \rightarrow Np$)
3.89	31364	4.02 x 10^{-4}	E	$^{\alpha}2a_2 \rightarrow 19e_1$ ($O_{OH} \rightarrow Np$)

Table A.3. Calculated spin-orbit free transition energies in $NpO_2(OH)_4^{2-}$ (SAOP, no TDA, no spin flip transitions)

References

1. N. Kaltsoyannis and P. Scott, *The f elements*, 1 edn., Oxford University Press, Oxford, 1999.
2. F. A. Cotton and G. Wilkinson, *Advanced Inorganic Chemistry*, John Wiley and Sons, New York, 1988.
3. R. D. Shannon, *Acta Crystallographica Section A*, 1976, **32**, 751-767.
4. F. Jensen, *Introduction to Computational Chemistry*, Wiley, Chichester, 1999.
5. A. Szabo and N. S. Ostlund, *Modern Quantum Chemistry: Introduction to Advanced Electronic Structure Theory*, McGraw-Hill, New York, 1989.
6. C. J. Cramer, *Essentials of Computational Chemistry -Theories and Models*, 2 edn., John Wiley & Sons Ltd, London, 2005.
7. E. Schrödinger, *Annalen der Physik*, 1926.
8. M. Born and R. Oppenheimer, *Annalen der Physik*, 1927.
9. W. J. Hehre, R. F. Stewart and J. A. Pople, *J. Chem. Phys.*, 1969, **59**, 2657.
10. P. A. M. Dirac, *Proceedings of the Royal Society*, 1928, **A117**.
11. J. C. Slater, *Physical Review*, 1951, **81**, 385-390.
12. D. R. Hartree, *Proceedings of the Cambridge Philosophical Society*, 1928, **24**.
13. C. C. J. Roothaan, *Reviews of Modern Physics*, 1951, **23**, 69-89.
14. B. O. Roos and P. R. Taylor, *Chemical Physics*, 1980, **48**, 157-173.
15. M. S. Plesset and C. Moller, *Physical Review*, 1934, **46**.
16. J. Cizek, *Journal of Chemical Physics*, 1966, **45**, 4256-&.
17. P. A. M. Dirac, *Proc. Roy. Soc. Ser. A*, 1929, **123**, 714.
18. E. Vanlenthe, E. J. Baerends and J. G. Snijders, *Journal of Chemical Physics*, 1993, **99**, 4597-4610.
19. P. Pyykko, *Chemical Reviews*, 1988, **88**, 563-594.
20. D. L. Clark, *Los Alamos Science*, 2000, **26**, 367.
21. E. Fermi, *Rend. Accad. Lincei*, 1927, 602-607.
22. L. H. Thomas, *Proceedings of the Cambridge Philosophical Society*, 1927, **23**, 542-548.
23. J. C. Slater, *Adv. Quantum Chem.*, 1972, **6**, 1.
24. J. S. Slater, *Phys. Rev.*, 1951, **81**, 385.
25. P. Hohenberg and W. Kohn, *Physical Review B*, 1964, **136**, B864-&.
26. W. Kohn and L. J. Sham, *Physical Review*, 1965, **140**, 1133-&.
27. S. H. Vosko, L. Wilk and M. Nusair, *Canadian Journal of Physics*, 1980, **58**, 1200-1211.
28. A. D. Becke, *Journal of Chemical Physics*, 1986, **84**, 4524-4529.
29. A. Becke, *Phys. Rev. A.*, 1988, **38**, 3098.
30. J. P. Perdew, *Phys. Rev.*, 1986, **B33**, 8822.
31. C. Lee, W. Yang and R. G. Parr, *Phys. Rev. B*, 1988, **37**, 785.
32. J. P. Perdew, K. Burke and M. Ernzerhof, *Physical Review Letters*, 1996, **77**, 3865-3868.
33. N. C. Handy and A. J. Cohen, *Molecular Physics*, 2001, **99**, 403-412.
34. A. D. Becke, *Physical Review A*, 1988, **38**, 3098-3100.

35. M. A. L. Marques and E. K. U. Gross, *Annual Review of Physical Chemistry*, 2004, **55**, 427-455.
36. E. Runge and E. K. U. Gross, *Phys. Rev. Lett.*, 1984, **52**, 997.
37. P. R. T. Schipper, O. V. Gritsenko, S. J. A. van Gisbergen and E. J. Baerends, *J. Chem. Phys.*, 2000, **112**, 1344.
38. R. van Leeuwen and E. J. Baerends, *Phys. Rev. A*, 1994, **49**, 2421.
39. R. S. Mulliken, *Journal of Chemical Physics*, 1955, **23**, 1833-1840.
40. R. S. Mulliken, *Journal of Chemical Physics*, 1955, **23**, 1841-1846.
41. R. S. Mulliken, *Journal of Chemical Physics*, 1955, **23**, 2338-2342.
42. R. S. Mulliken, *Journal of Chemical Physics*, 1955, **23**, 2343-2346.
43. I. Mayer, *Chemical Physics Letters*, 1983, **97**, 270-274.
44. M. J. Frisch, G. W. Trucks, H. B. Schlegel, G. E. Scuseria, M. A. Robb, J. R. Cheeseman, J. A. Montgomery Jr., T. Vreven, K. N. Kudin, J. C. Burant, J. M. Millam, S. S. Iyengar, J. Tomasi, V. Barone, B. Mennucci, M. Cossi, G. Scalmani, N. Rega, G. A. Petersson, H. Nakatsuji, M. Hada, M. Ehara, K. Toyota, R. Fukuda, J. Hasegawa, M. Ishida, T. Nakajima, Y. Honda, O. Kitao, H. Nakai, M. Klene, X. Li, J. E. Knox, H. P. Hratchian, J. B. Cross, V. Bakken, C. Adamo, J. Jaramillo, R. Gomperts, R. E. Stratmann, O. Yazyev, A. J. Austin, R. Cammi, C. Pomelli, J. W. Ochterski, P. Y. Ayala, K. Morokuma, G. A. Voth, P. Salvador, J. J. Dannenberg, V. G. Zakrzewski, S. Dapprich, A. D. Daniels, M. C. Strain, O. Farkas, D. K. Malick, A. D. Rabuck, K. Raghavachari, J. B. Foresman, J. V. Ortiz, Q. Cui, A. G. Baboul, S. Clifford, J. Cioslowski, B. B. Stefanov, G. Liu, A. Liashenko, P. Piskorz, I. Komaromi, R. L. Martin, D. J. Fox, T. Keith, M. A. Al-Laham, C. Y. Peng, A. Nanayakkara, M. Challacombe, P. M. W. Gill, B. Johnson, W. Chen, M. W. Wong, C. Gonzalez and J. A. Pople, Editon edn., 2004.
45. C. F. Guerra, J. G. Snijders, G. te Velde and E. J. Baerends, *Theoretical Chemistry Accounts*, 1998, **99**, 391-403.
46. K. Kitaura and K. Morokuma, *International Journal of Quantum Chemistry*, 1976, **10**, 325-340.
47. T. Ziegler and A. Rauk, *Inorg. Chem.*, 1979, **18**, 1558.
48. G. Cavigliasso and N. Kaltsoyannis, *Inorganic Chemistry*, 2007, **46**, 3557-3565.
49. G. Cavigliasso and N. Kaltsoyannis, *Dalton Transactions*, 2006, 5476-5483.
50. G. Cavigliasso and N. Kaltsoyannis, *Inorganic Chemistry*, 2006, **45**, 6828-6839.
51. K. Pierloot, E. van Besien, E. van Lenthe and E. J. Baerends, *Journal of Chemical Physics*, 2007, **126**.
52. C. Talbot-Eeckelaers, S. J. A. Pope, A. J. Hynes, R. Copping, C. J. Jones, R. J. Taylor, S. Faulkner, D. Sykes, F. R. Livens and I. May, *Journal of the American Chemical Society*, 2007, **129**, 2442-+.
53. R. D. Adams and F. A. Cotton, *Catalysis by Di- and Polynuclear Metal Cluster Complexes*, Wiley - VCH, New York, 1998.
54. F. A. Cotton and R. A. Walton, *Multiple Bonds between Metal Atoms*, 2nd edn., Oxford University Press, New York, 1993.
55. C. Villiers, P. Thuery and M. Ephritikhine, *Acta Crystallogr. Sect. C-Cryst. Struct. Commun.*, 2006, **62**, M243-M245.
56. M. Ephritikhine, *Dalton Transactions*, 2006, 2501-2516.
57. B. O. Roos and L. Gagliardi, *Inorganic Chemistry*, 2006, **45**, 803-807.

58. B. O. Roos, P. A. Malmqvist and L. Gagliardi, *Journal of the American Chemical Society*, 2006, **128**, 17000-17006.
59. R. H. Cayton, K. J. Novogradac and B. E. Bursten, *Inorganic Chemistry*, 1991, **30**, 2265-2272.
60. L. Gagliardi and B. O. Roos, *Nature*, 2005, **433**, 848-851.
61. L. Gagliardi, P. Pyykko and B. O. Roos, *Physical Chemistry Chemical Physics*, 2005, **7**, 2415-2417.
62. G. T. Velde, F. M. Bickelhaupt, E. J. Baerends, C. F. Guerra, S. J. A. Van Gisbergen, J. G. Snijders and T. Ziegler, *Journal of Computational Chemistry*, 2001, **22**, 931-967.
63. F. M. Bickelhaupt and E. J. Baerends, *Reviews in Computational Chemistry, Vol 15*, 2000, **15**, 1-86.
64. A. J. Bridgeman, G. Cavigliasso, L. R. Ireland and J. Rothery, *Journal of the Chemical Society-Dalton Transactions*, 2001, 2095-2108.
65. R. D. Hetterley, E. F. Kozhevnikova and I. V. Kozhevnikov, *Chemical Communications*, 2006, 782-784.
66. J. Berzelius, *Poggendorf's Annalen der Physik*, 1826, **6**.
67. M. T. Pope, *Heteropoly and Isopoly Oxometalates*, Springer-Verlag, Heidelberg, 1983.
68. J. F. Keggin, *Nature*, 1933, **131**.
69. J. S. Anderson, *Nature*, 1937, **140**, 850.
70. I. Lindqvist, *Arkiv for Kemi*, 1953, **5**, 247-250.
71. B. Dawson, *Acta Crystallographica*, 1953, **6**, 113-126.
72. J. M. Poblet, X. Lopez and C. Bo, *Chemical Society Reviews*, 2003, **32**, 297-308.
73. M. T. Pope and A. Muller, *Angewandte Chemie-International Edition in English*, 1991, **30**, 34-48.
74. J. Devemy, M. M. Rohmer, M. Benard and R. Ernenwein, *International Journal of Quantum Chemistry*, 1996, **58**, 267-281.
75. M. M. Rohmer, M. Benard, J. P. Blaudeau, J. M. Maestre and J. M. Poblet, *Coordination Chemistry Reviews*, 1998, **178**, 1019-1049.
76. A. J. Bridgeman, *Chemical Physics*, 2003, **287**, 55-69.
77. A. J. Bridgeman and G. Cavigliasso, *Faraday Discussions*, 2003, **124**, 239-258.
78. A. J. Bridgeman and G. Cavigliasso, *Journal of Physical Chemistry A*, 2003, **107**, 4568-4577.
79. A. J. Bridgeman and G. Cavigliasso, *Chemical Physics*, 2002, **279**, 143-159.
80. A. J. Bridgeman and G. Cavigliasso, *Polyhedron*, 2001, **20**, 2269-2277.
81. A. J. Bridgeman and G. Cavigliasso, *Polyhedron*, 2001, **20**, 3101-3111.
82. A. J. Bridgeman and G. Cavigliasso, *Journal of the Chemical Society-Dalton Transactions*, 2001, 3556-3563.
83. J. M. Maestre, J. P. Sarasa, C. Bo and J. M. Poblet, *Inorganic Chemistry*, 1998, **37**, 3071-3077.
84. J. M. Maestre, J. M. Poblet, C. Bo, N. Casan-Pastor and P. Gomez-Romero, *Inorganic Chemistry*, 1998, **37**, 3444-+.
85. X. Lopez, J. M. Maestre, C. Bo and J. M. Poblet, *Journal of the American Chemical Society*, 2001, **123**, 9571-9576.

86. J. M. Maestre, X. Lopez, C. Bo, J. M. Poblet and N. Casan-Pastor, *Journal of the American Chemical Society*, 2001, **123**, 3749-3758.
87. X. Lopez, C. Bo and J. M. Poblet, *Journal of the American Chemical Society*, 2002, **124**, 12574-12582.
88. J. M. Maestre, X. Lopez, C. Bo, J. M. Poblet and C. Daul, *Inorganic Chemistry*, 2002, **41**, 1883-1888.
89. X. Lopez, C. Bo and J. M. Poblet, *Inorganic Chemistry*, 2003, **42**, 2634-2638.
90. X. Lopez, J. A. Fernandez, S. Romo, J. F. Paul, L. Kazansky and J. M. Poblet, *Journal of Computational Chemistry*, 2004, **25**, 1542-1549.
91. X. Lopez and J. M. Poblet, *Inorganic Chemistry*, 2004, **43**, 6863-6865.
92. X. Lopez, C. de Graaf, J. M. Maestre, M. Beard, M. M. Rohmer, C. Bo and J. M. Poblet, *Journal of Chemical Theory and Computation*, 2005, **1**, 856-861.
93. O. A. Kholdeeva, G. M. Maksimov, R. I. Maksimovskaya, M. P. Vanina, T. A. Trubitsina, D. Y. Naumov, B. A. Kolesov, N. S. Antonova, J. J. Carbo and J. M. Poblet, *Inorganic Chemistry*, 2006, **45**, 7224-7234.
94. X. Lopez, J. A. Fernandez and J. M. Poblet, *Dalton Transactions*, 2006, 1162-1167.
95. X. Lopez, I. A. Weinstock, C. Bo, J. P. Sarasa and J. M. Poblet, *Inorganic Chemistry*, 2006, **45**, 6467-6473.
96. J. A. Fernandez, X. Lopez and J. M. Poblet, *Journal of Molecular Catalysis a-Chemical*, 2007, **262**, 236-242.
97. S. Romo, J. A. Fernandez, J. M. Maestre, B. Keita, L. Nadjo, C. de Graaf and J. M. Poblet, *Inorganic Chemistry*, 2007, **46**, 4022-4027.
98. J. A. Fernandez, X. Lopez, C. Bo, C. de Graaft, E. J. Baerends and J. M. Poblet, *Journal of the American Chemical Society*, 2007, **129**, 12244-12253.
99. A. J. Bridgeman and G. Cavigliasso, *Inorganic Chemistry*, 2002, **41**, 1761-1770.
100. A. J. Bridgeman and G. Cavigliasso, *Journal of Physical Chemistry A*, 2002, **106**, 6114-6120.
101. A. Muller, M. T. Pope, A. Merca, H. Bogge, M. Schmidtmann, J. van Slageren, M. Dressel and D. G. Kurth, *Chemistry-a European Journal*, 2005, **11**, 5849-5854.
102. K. I. M. Ingram, L. J. L. Haller and N. Kaltsoyannis, *Dalton Transactions*, 2006, 2403-2414.
103. K. C. Kim and M. T. Pope, *Journal of the American Chemical Society*, 1999, **121**, 8512-8517.
104. A. J. Gaunt, I. May, R. Copping, A. I. Bhatt, D. Collison, O. D. Fox, K. T. Holman and M. T. Pope, *Dalton Transactions*, 2003, 3009-3014.
105. A. J. Gaunt, I. May, D. Collison, K. T. Holman and M. T. Pope, *Journal of Molecular Structure*, 2003, **656**, 101-106.
106. A. J. Gaunt, I. May, M. Helliwell and S. Richardson, *Journal of the American Chemical Society*, 2002, **124**, 13350-13351.
107. R. Copping, A. J. Gaunt, I. May, M. J. Sarsfield, D. Collison, M. Helliwell, I. S. Denniss and D. C. Apperley, *Dalton Transactions*, 2005, 1256-1262.
108. A. J. Gaunt, I. May, D. Collison and O. D. Fox, *Inorganic Chemistry*, 2003, **42**, 5049-5051.

109. R. Copping, L. Jonasson, A. J. Gaunt, D. Drennan, D. Collison, M. Helliwell, R. J. Pirttijarvi, C. J. Jones, A. Huguet, D. C. Apperley, N. Kaltsoyannis and I. May, *Inorg. Chem.*, 2008, **47**, 5787-5798.
110. E. J. Baerends, J. Autschbach, A. Bérces, F. M. Bickelhaupt, C. Bo, P. M. Boerrigter, L. Cavallo, D. P. Chong, L. Deng, R. M. Dickson, D. E. Ellis, M. van Faassen, L. Fan, T. H. Fischer, C. Fonseca Guerra, S. J. A. van Gisbergen, J. A. Groeneveld, O. V. Gritsenko, M. Grüning, F. E. Harris, P. van den Hoek, C. R. Jacob, H. Jacobsen, L. Jensen, G. van Kessel, F. Kootstra, E. van Lenthe, D. A. McCormack, A. Michalak, J. Neugebauer, V. P. Nicu, V. P. Osinga, S. Patchkovskii, P. H. T. Philipsen, D. Post, C. C. Pye, W. Ravenek, P. Ros, P. R. T. Schipper, G. Schreckenbach, J. G. Snijders, M. Solà, M. Swart, D. Swerhone, G. te Velde, P. Vernooijs, L. Versluis, L. Visscher, O. Visser, F. Wang, T. A. Wesolowski, E. M. van Wezenbeek, G. Wiesenekker, S. K. Wolff, T. K. Woo, A. L. Yakovlev and T. Ziegler, SCM, Vrije Universiteit, Amsterdam, Editon edn., 2007.
111. R. Copping, University of Manchester, 2006.
112. A. J. Gaunt, I. May, M. J. Sarsfield, D. Collison, M. Helliwell and I. S. Denniss, *Dalton Transactions*, 2003, 2767-2771.
113. J. K. Gibson, R. G. Haire, M. Santos, J. Marcalo and A. P. de Matos, *Journal of Physical Chemistry A*, 2005, **109**, 2768-2781.
114. R. G. Denning, *Struct. Bonding*, 1992, **79**, 215.
115. K. Tatsumi and R. Hoffmann, *Inorganic Chemistry*, 1980, **19**, 2656-2658.
116. R. G. Denning, *Journal of Physical Chemistry A*, 2007, **111**, 4125-4143.
117. N. Kaltsoyannis, *Inorg. Chem.*, 2000, **39**, 6009.
118. N. Kaltsoyannis, *Journal of the Chemical Society-Dalton Transactions*, 1997, 1-11.
119. N. Kaltsoyannis, P. J. Hay, J. Li, J.-P. Blaudeau and B. E. Bursten, in *The Chemistry of the Actinide and Transactinide Elements*, eds. L. R. Morss, N. Edelstein and J. Fuger, Springer, Editon edn., 2006, pp. 1893-2012.
120. R. G. Denning, J. C. Green, T. E. Hutchings, C. Dallera, A. Tagliaferri, K. Giarda, N. B. Brookes and L. Braicovich, *Journal of Chemical Physics*, 2002, **117**, 8008-8020.
121. R. G. Denning, *Structure and Bonding*, 1992, **79**, 215-276.
122. K. Pierloot and E. van Besien, *Journal of Chemical Physics*, 2005, **123**.
123. T. Yanai, D. P. Tew and N. C. Handy, *Chemical Physics Letters*, 2004, **393**, 51-57.
124. R. K. Szilagyi, M. Metz and E. I. Solomon, *Journal of Physical Chemistry A*, 2002, **106**, 2994-3007.
125. E. McMillan and P. H. Abelson, *Physical Review*, 1940, **57**, 1185.
126. M. A. Makhyoun, *Inorganic Chemistry*, 1987, **26**, 3592-3595.
127. G. V. Ionova, V. G. Pershina and N. I. Suraeva, *Soviet Radiochemistry*, 1989, **31**, 9-14.
128. G. V. Ionova, V. G. Pershina and N. I. Suraeva, *Soviet Radiochemistry*, 1989, **31**, 379-386.
129. V. G. Pershina, G. V. Ionova and N. I. Suraeva, *Soviet Radiochemistry*, 1989, **31**, 386-391.

130. V. G. Pershina, G. V. Ionova and N. I. Suraeva, *Croatica Chemica Acta*, 1990, **62**, 763-773.
131. V. G. Pershina, G. V. Ionova and N. I. Suraeva, *Zhurnal Neorganicheskoi Khimii*, 1990, **35**, 2066-2070.
132. G. V. Ionova, V. G. Pershina and N. I. Suraeva, *Zhurnal Neorganicheskoi Khimii*, 1991, **36**, 316-319.
133. R. B. Dushin, *Soviet Radiochemistry*, 1990, **32**, 153-158.
134. S. Matsika and R. M. Pitzer, *Journal of Physical Chemistry A*, 2000, **104**, 4064-4068.
135. S. Matsika, Z. Zhang, S. R. Brozell, J. P. Baudeau, Q. Wang and R. M. Pitzer, *Journal of Physical Chemistry A*, 2001, **105**, 3825-3828.
136. B. Bleaney, *Discussions of the Faraday Society*, 1955, 112-118.
137. R. G. Denning, J. O. W. Norris and D. Brown, *Molecular Physics*, 1982, **46**, 287-323.
138. R. G. Denning, J. O. W. Norris and D. Brown, *Molecular Physics*, 1982, **46**, 325-364.
139. Eisenste.Jc and M. H. L. Pryce, *Journal of Research of the National Bureau of Standards Section a-Physics and Chemistry*, 1966, **A 70**, 165-&.
140. Eisenste.Jc and M. H. L. Pryce, *Journal of Research of the National Bureau of Standards Section a-Physics and Chemistry*, 1965, **A 69**, 217-&.
141. S. P. McGlynn and J. K. Smith, *Journal of Molecular Spectroscopy*, 1961, **6**, 188-&.
142. S. Matsika and R. M. Pitzer, *Journal of Physical Chemistry A*, 2001, **105**, 637-645.
143. C. Clavaguera-Sarrio, V. Vallet, D. Maynau and C. J. Marsden, *Journal of Chemical Physics*, 2004, **121**, 5312-5321.
144. F. Real, V. Vallet, C. Marian and U. Wahlgren, *Journal of Chemical Physics*, 2007, **127**.
145. S. Hirata and M. Head-Gordon, *Chemical Physics Letters*, 1999, **314**, 291-299.
146. P. R. T. Schipper, O. V. Gritsenko, S. J. A. van Gisbergen and E. J. Baerends, *Journal of Chemical Physics*, 2000, **112**, 1344-1352.
147. R. Vanleeuwen and E. J. Baerends, *Physical Review A*, 1994, **49**, 2421-2431.
148. M. P. Wilkerson, C. A. Arrington, J. M. Berg and B. L. Scott, *Journal of Alloys and Compounds*, 2007, **444**, 634-639.
149. H. Bolvin, U. Wahlgren, H. Moll, T. Reich, G. Geipel, T. Fanghanel and I. Grenthe, *Journal of Physical Chemistry A*, 2001, **105**, 11441-11445.
150. S. Skanthakumar, M. R. Antonio and L. Soderholm, *Inorganic Chemistry*, 2008, **47**, 4591-4595.
151. M. R. Antonio, L. Soderholm, C. W. Williams, J. P. Blaudeau and B. E. Bursten, *Radiochimica Acta*, 2001, **89**, 17-25.
152. R. G. Denning, J. C. Green, T. E. Hutchings, C. Dallera, A. Tagliaferri, K. Giarda, N. B. Brookes and L. Braicovich, *J. Chem. Phys.*, 2002, in press.
153. M. S. Fred and J. Blaise, *The chemistry of the actinide elements, chapter 15*, Second edn., Chapman and Hall, New York, 1986.
154. W. J. Liu, M. Dolg and P. Fulde, *Journal of Chemical Physics*, 1997, **107**, 3584-3591.

155. D. Seyferth, *Organometallics*, 2004, **23**, 3562-3583.
156. B. O. Roos and P. A. Malmqvist, *Physical Chemistry Chemical Physics*, 2004, **6**, 2919-2927.
157. E. Ruiz, D. R. Salahub and A. Vela, *Journal of the American Chemical Society*, 1995, **117**, 1141-1142.
158. G. A. Shamov and G. Schreckenbach, *Journal of Physical Chemistry A*, 2005, **109**, 10961-10974.
159. G. Schreckenbach, P. J. Hay and R. L. Martin, *Journal of Computational Chemistry*, 1999, **20**, 70-90.
160. B. Y. Liang, L. Andrews, N. Ismail and C. J. Marsden, *Inorganic Chemistry*, 2002, **41**, 2811-2813.
161. K. G. Dyall, *Molecular Physics*, 1999, **96**, 511-518.
162. P. Pyykko, L. J. Laakkonen and K. Tatsumi, *Inorganic Chemistry*, 1989, **28**, 1801-1805.
163. M. F. Zhou and L. Andrews, *Journal of Chemical Physics*, 1999, **111**, 11044-11049.
164. M. Pepper and B. E. Bursten, *Chemical Reviews*, 1991, **91**, 719-741.
165. L. J. L. Haller, N. Kaltsoyannis, M. J. Sarsfield, I. May, S. M. Cornet, M. P. Redmond and M. Helliwell, *Inorganic Chemistry*, 2007, **46**, 4868-4875.
166. S. P. Ionov, C. Rabbe and G. V. Ionova, *Russ. J. Coord. Chem.*, 2002, **28**, 249-258.
167. G. Schreckenbach, P. J. Hay and R. L. Martin, *Inorganic Chemistry*, 1998, **37**, 4442-4451.
168. B. Liang and L. Andrews, *Journal of Physical Chemistry A*, 2002, **106**, 4038-4041.
169. K. I. M. Ingram, N. Kaltsoyannis, A. J. Gaunt and M. P. Neu, *Journal of Alloys and Compounds*, 2007, **444**, 369-375.
170. W. H. Zachariasen, *Acta Crystallographica*, 1949, **2**, 291-296.
171. H. Kohlmann and H. P. Beck, *Zeitschrift Fur Anorganische Und Allgemeine Chemie*, 1997, **623**, 785-790.
172. H. Noel and J. Y. Lemarouille, *Journal of Solid State Chemistry*, 1984, **52**, 197-202.
173. D. R. Boehme, M. C. Nichols, R. L. Snyder and D. P. Matheis, *Journal of Alloys and Compounds*, 1992, **179**, 37-59.
174. D. R. Brown, R. G. Denning and R. H. Jones, *Journal of the Chemical Society-Chemical Communications*, 1994, 2601-2602.
175. D. R. Brown and R. G. Denning, *Inorganic Chemistry*, 1996, **35**, 6158-6163.
176. T. W. Hayton, J. M. Boncella, B. L. Scott, P. D. Palmer, E. R. Batista and P. J. Hay, *Science*, 2005, **310**, 1941-1943.
177. T. W. Hayton, J. M. Boncella, B. L. Scott, E. R. Batista and P. J. Hay, *Journal of the American Chemical Society*, 2006, **128**, 10549-10559.
178. D. S. J. Arney and C. J. Burns, *Journal of the American Chemical Society*, 1993, **115**, 9840-9841.
179. D. S. J. Arney, C. J. Burns and D. C. Smith, *Journal of the American Chemical Society*, 1992, **114**, 10068-10069.

180. C. J. Burns, W. H. Smith, J. C. Huffman and A. P. Sattelberger, *Journal of the American Chemical Society*, 1990, **112**, 3237-3239.
181. N. Kaltsoyannis, *Inorganic Chemistry*, 2000, **39**, 6009-6017.
182. N. Kaltsoyannis, *Abstracts of Papers of the American Chemical Society*, 2000, **220**, U501-U501.
183. L. Belkhiri, R. Lissillour and A. Boucekkine, *Journal of Molecular Structure-Theochem*, 2005, **757**, 155-164.
184. P. J. Stephens, F. J. Devlin, C. F. Chabalowski and M. J. Frisch, *Journal of Physical Chemistry*, 1994, **98**, 11623-11627.
185. A. D. Becke, *Journal of Chemical Physics*, 1993, **98**, 5648-5652.
186. T. H. Dunning Jr and P. J. Hay, Plenum, New York, 1976.
187. W. Kuchle, M. Dolg, H. Stoll and H. Preuss, *Journal of Chemical Physics*, 1994, **100**, 7535-7542.
188. X. Y. Cao, M. Dolg and H. Stoll, *Journal of Chemical Physics*, 2003, **118**, 487-496.
189. S. Larsson and P. Pyykko, *Chemical Physics*, 1986, **101**, 355-369.
190. W. A. de Jong, L. Visscher and W. C. Nieuwpoort, *Journal of Molecular Structure-Theochem*, 1999, **458**, 41-52.
191. L. Pauling, *J. Am. Chem. Soc.*, 1932, **54**, 3570-3582.
192. E. J. Baerends, V. Branchadell and M. Sodupe, *Chemical Physics Letters*, 1997, **265**, 481-489.
193. M. F. Zhou, L. Andrews, N. Ismail and C. Marsden, *Journal of Physical Chemistry A*, 2000, **104**, 5495-5502.